Aspects of Dark Matter Phenomenology

Christopher M^{c}Cabe

Worcester College

University of Oxford

A thesis submitted for the degree of

Doctor of Philosophy

Trinity 2011

This thesis is dedicated to my family:
my wife Caroline, my parents and my siblings.
Their loving support has been unwavering over many years.

The LORD is my light and my salvation
Psalm 27 v1

Aspects of Dark Matter Phenomenology

Christopher M^{c}Cabe, Worcester College

A thesis submitted for the degree of Doctor of Philosophy

Trinity 2011

Abstract

Identifying the relic particles that constitute the cold dark matter in our Universe is an outstanding problem in astro-particle physics. Direct detection experiments are among the most promising methods of detecting particle dark matter through non-gravitational interactions. In this thesis, the usual assumptions made when calculating the event rate at direct detection experiments are examined. Varying astrophysical parameters and the dark matter velocity distribution leads to significant changes in acceptance regions and exclusion curves for scenarios in which the tail of the velocity distribution is sampled; this includes 'light dark matter' (mass $\lesssim 10$ GeV) and 'inelastic dark matter'. The DAMA and CoGeNT collaborations both report an annual modulation in their event rate that they attribute to dark matter. Two analyses of these experiments are performed. In the first, it is shown that these experiments can be compatible with each other and with the constraints from other direct detection experiments. This requires some isospin violation in the couplings of dark matter to protons and neutrons and a small inelastic splitting to boost the modulation fraction. The second analysis provides a comparison of the modulation signals free from all astrophysical parameters, under the assumption that dark matter scatters elastically. Again it is found that some isospin violation and a boosted modulation fraction is required in order that DAMA and CoGeNT are consistent with all experiments. A boosted modulation fraction may arise from a velocity distribution different from the Maxwell-Boltzmann distribution, which is usually assumed. Finally, a supersymmetric theory in which the dark matter candidate is a mixture of left- and right-handed sneutrino is considered. This theory has many novel signatures at colliders, indirect detection and direct detection experiments.

Acknowledgements

First and foremost, I would like to thank my D.Phil supervisor Prof. John March-Russell. As well as suggesting interesting research proposals, he has given me the freedom and encouragement to find my own problems and develop my own interests. I greatly appreciate discussions with him, his suggestions that inevitably improved anything I was working on and his prompting to think through all the details. His knowledge and enthusiasm over vast swathes of physics has been inspirational.

I also owe much to my undergraduate tutors at Worcester College, Prof. Paul Ewart and especially Prof. Fabian Essler, for their initial encouragement to pursue postgraduate studies. I immensely valued the nuggets of advice they continued to offer during my time as a graduate student.

I am thankful for the opportunity to have worked with various people on different projects: Mads Frandsen, Kai Schmidt-Hoberg, Felix Kahlhoefer and especially Matthew McCullough. Some ideas we pursued together have been successful, others less so. However, from each, I have learnt something about how to approach and carry out research problems.

There are many people in theoretical physics who have made my time at Oxford tremendously enjoyable. I have learnt much about a great many things in physics and beyond during discussions at coffee, lunch, in the Dalitz Institute and on Friday evenings in a nearby pub. I feel very privileged to have been part of such an intellectually stimulating environment.

The financial support of the STFC through a Postgraduate Studentship is gratefully acknowledged. I am also appreciative of the additional funding from Worcester College and the EU UniverseNet and BSMOXFORD grants, all of which have greatly enriched my experience.

Finally, but my no means least, I thank my family. Firstly, to my parents and siblings for their support and encouragement throughout all of my education. I am grateful to my father for his interest in science and his numerous books in our roof space on physics, chemistry and mathematics that sparked my own interest in science. Finally, my wife Caroline has probably suffered the most over the past four years. Her loving support and numerous lessons in grammar have benefited me enormously.

Contents

Prologue

The work in this thesis constitutes the body of research carried out for my D.Phil at Oxford. Chapters 2 - 5 and Chapter 7 contain original research and are based on published papers [1, 2, 3, 4, 5]. Also included are two chapters reviewing background information on dark matter and supersymmetry.

Chapter 1 provides a brief overview of dark matter. Some of the experimental evidence that points towards the existence of a large abundance of particle dark matter in our galaxy and throughout the Universe is presented. From this, we distill what this tells us about the nature of dark matter. We develop the Standard Halo Model (SHM), the simplest model of the distribution of dark matter in our galaxy and discuss its limitations. Some of the most studied dark matter candidates are discussed and we detail how a relic abundance is thought to arise for each. Finally, we consider how dark matter might be discovered, focusing particularly on direct detection experiments.

In Chapter 2, we investigate the dependence of the putative signal at the DAMA experiment and the constraints from other direct detection experiments on the local dark matter velocity distribution, when dark matter scatters inelastically. 'Inelastic dark matter' (iDM) was proposed as a way to reconcile the DAMA experiment with the null results from other experiments. To date, most analyses assume a simple galactic halo dark matter velocity distribution that arises from the SHM: a Maxwell-Boltzmann distribution. Direct experimental support for such a distribution is severely lacking and theoretical studies indicate possible significant differences. Therefore, we utilise the dark matter velocity distribution extracted from the Via Lactea and Dark Disc numerical simulations. We also investigate effects of varying the solar circular velocity, the dark matter escape velocity and the DAMA quenching factor within experimental limits. The scattering rate of iDM is more sensitive to the tail of the velocity distribution. As a result, the DAMA results are consistent with all other experiments over an enlarged region of iDM parameter space, when the Via

Lactea velocity distribution is used, with higher mass particles being preferred. However, the Dark Disc does not lead to any improvement. The research in this chapter was carried out in collaboration with John March-Russell and Matthew McCullough and was published in *JHEP* **05**, 071 (2009).

In Chapter 3, the effects of astrophysical uncertainties on the exclusion limits at direct detection experiments are examined for three scenarios: elastic, momentum dependent and inelastically scattering dark matter. We find that varying the dark matter galactic escape velocity and the Sun's circular velocity can lead to significant variations in the exclusion limits for light (mass $\lesssim 10$ GeV) elastic and inelastic scattering dark matter. We also calculate the limits using one hundred velocity distributions extracted from the Via Lactea II and GHALO N-body simulations and find that a Maxwell-Boltzmann distribution with the same astrophysical parameters generally sets less constraining limits. The elastic and momentum dependent limits remain robust for a dark matter mass $\gtrsim 50$ GeV under variations of the astrophysical parameters and the form of the velocity distribution. The research in this chapter was published in *Phys. Rev.* **D82** (2010), 023530.

The CoGeNT collaboration has reported evidence of an annual modulation in its first fifteen months of data. The simplest interpretation of these findings in terms of dark matter–nucleus scatterings is excluded by other direct detection experiments. In Chapter 4, we consider the robustness of these exclusions with respect to assumptions regarding the scattering and test the compatibility of the CoGeNT modulation with the modulation observed by DAMA. We find that isospin-violating inelastic dark matter helps alleviate the tension with the experiments reporting null results and allows marginal compatibility between experiments for particles of mass ~ 8 GeV. Isospin-violation can significantly weaken the XENON constraints, while inelasticity enhances the annual modulation fraction of the signal, bringing the CoGeNT and CDMS results into better agreement. The research in this chapter was carried out in collaboration with Mads T. Frandsen, Felix Kahlhoefer, John March-Russell, Matthew McCullough and Kai Schmidt-Hoberg and was published in *Phys. Rev.* **D84** (2011), 041301(R).

In Chapter 5, we compare the amplitude and phase of the modulation signal observed by CoGeNT with the modulation observed by the DAMA collaboration, assuming that both arise due to elastically scattering dark matter. We directly map the CoGeNT signal to the DAMA detector without specifying any astrophysical parameters and compare this with the signal measured by DAMA. We also compare with constraints from XENON10 and the germanium and silicon data taken by CDMS II. We find that dark matter of mass 5-14 GeV that couples equally to

protons and neutrons is strongly disfavoured, requiring a modulation fraction that is significantly larger than usually expected. Isospin-violating dark matter fares better but still requires a boosted modulation fraction, pointing to deviations from a Maxwell-Boltzmann velocity distribution. The research in this chapter was published in *Phys. Rev.* **D84** (2011), 043525.

Chapter 6 provides a brief introduction to supersymmetry (SUSY). Beginning with the SUSY algebra, we develop the superfield formalism and gradually construct more complicated field theories invariant under SUSY transformations. Starting from theories containing only chiral superfields, we add both Abelian and non-Abelian gauge fields and their associated superpartners. This allows the Minimal Supersymmetric Standard Model (MSSM) to be written down in a relativity straightforward way. We also introduce the 'soft terms', which parameterise the effects of SUSY breaking. We end by touching upon some of the primary motivations that have led to the huge abundance of research carried out into supersymmetric theories.

Finally, in Chapter 7 we study in detail a simple theory of supersymmetric dark matter naturally linked to neutrino flavour physics. The dark matter sector comprises a spectrum of mixed left- and right-handed sneutrino states where both the sneutrino flavour structure and mass splittings are determined by the associated neutrino masses and mixings. Prospects for indirect detection from solar capture are good due to a large sneutrino-nucleon cross section afforded by the inelastic splitting. The solar capture limits exclude an explanation of the modulation observed by DAMA. We find parameter regions where all heavier states will have decayed, leaving only one flavour mixture of sneutrino as the candidate DM. Such regions have a unique 'smoking gun' signature; sneutrino annihilation in the Sun produces a pair of neutrino mass eigenstates free from vacuum oscillations, with the potential for detection at neutrino telescopes through the observation of a hard spectrum of ν_μ and ν_τ (for a normal neutrino hierarchy). Next generation direct detection experiments can explore much of the parameter space through both elastic and inelastic scattering. We show in detail that the observed neutrino masses and mixings can arise as a consequence of supersymmetry breaking effects in the sneutrino dark matter sector, consistent with all experimental constraints. The research in this chapter was carried out in collaboration with John March-Russell and Matthew McCullough and was published in *JHEP* **1003**, 108 (2010).

Chapter 1

Dark Matter

One of the outstanding puzzles in modern physics is to identify the matter that makes up around 79% of the matter and around 22% of the energy density in the Universe. The evidence for this non-baryonic 'dark' matter, which does not appear to emit or absorb electromagnetic radiation of any wavelength, has been steadily growing. The evidence for dark matter has increased to the extent that the primary question motivating research is no longer "Does dark matter exist?" but rather, "What *is* dark matter?".

In Section 1.1 of this chapter, we briefly review some of the key evidence that points to a large abundance of dark matter in our galaxy and throughout the Universe.[1] In Section 1.2, we outline the Standard Halo Model; this is a simple model that predicts the density and velocity distributions of dark matter in the Milky Way. Section 1.3 discusses some of the most theoretically appealing candidates, dwelling particularly on weakly interacting massive particles (WIMPs) and the process of thermal freeze-out. Finally, in Section 1.4 we consider how dark matter might be detected through non-gravitational interactions, focusing particularly on direct detection experiments.

1.1 Dark matter in galaxies and clusters

Historically, some of the earliest evidence for dark matter came from observations of the Coma cluster, which contains roughly one thousand galaxies. Fritz Zwicky used the virial theorem to infer the average mass of a galaxy within the cluster [9, 10]. He found a value about 160 times larger than expected from their luminosity, implying the existence of a large abundance of non-luminous matter.

Perhaps the most well known and robust evidence for dark matter on galactic scales comes from the observations of the rotation curves of spiral galaxies. These

[1] More detailed reviews can be found in [6, 7, 8].

curves show the circular velocity of stars and gas in the galaxy as a function of their distance r from the galactic centre. Most of the luminous matter is contained within a relatively thin disc with a central bulge. Newton's Laws imply that the circular velocity should increase up to some radius $r_{\rm lum}$ (typically a few kpc), which contains most of the luminous matter, before falling as $1/\sqrt{r}$ beyond. However, what is typically observed is that after rising from $r = 0$, the velocity remains constant out far beyond $r_{\rm lum}$ (measurements of the 21 cm emission line of atomic hydrogen, from which the velocity is inferred, typically extend to a few tens of kpc) [11, 12]. This implies the existence of a large halo of non-luminous matter, in addition to the observed disc and central bulge, whose mass interior to r increases linearly with the distance from the galactic centre. Although complicated by our position within the galaxy, astronomers have tried to infer the rotation curve of the Milky Way. Their results are consistent with a flattening of the rotation curve at large radii [13]. This implies that the Milky Way, like other spiral galaxies, has a large dark matter halo. For a recent analysis, see [14, 15].

There is also evidence that dark matter exists on the scales of galaxy clusters. General Relativity predicts that light bends when traveling through the gravitational field of a massive body. This effect can be used to ascertain the mass of this matter, which acts as a lens, even if it were completely non-luminous, since it only relies on the gravitational interaction [16]. There are two regimes of lensing: so called strong and weak lensing. The lensing is said to be strong if an observer sees multiple images or arcs of a distant bright object, such as a galaxy or pulsar. This can occur if the source is fortuitously aligned behind a galaxy cluster (the 'lens'). The mass of the lensing object can be inferred from the resulting image and compared with the mass of luminous matter.

Unfortunately, in many cases the lensing is too weak to produce the multiple images and arcs of the source object associated with strong lensing. However, the source can still be weakly distorted, or 'sheared', appearing more elliptical in shape. Although not identifiable from individual sources, since the source galaxy may be elliptical, observing a large ensemble of sources should average out this 'shape noise', so that information can still be obtained on the intermediate matter distribution. This is weak lensing, and has been used spectacularly to map the mass distribution of the 'Bullet Cluster' (1E0657-558) [17]. This is in fact two clusters that have collided and it provides one of the most visually striking pieces of evidence that particle dark matter exists and only weakly interacts with baryonic matter. The Chandra X-ray observatory has mapped the hot gas, which makes up most of the luminous matter in

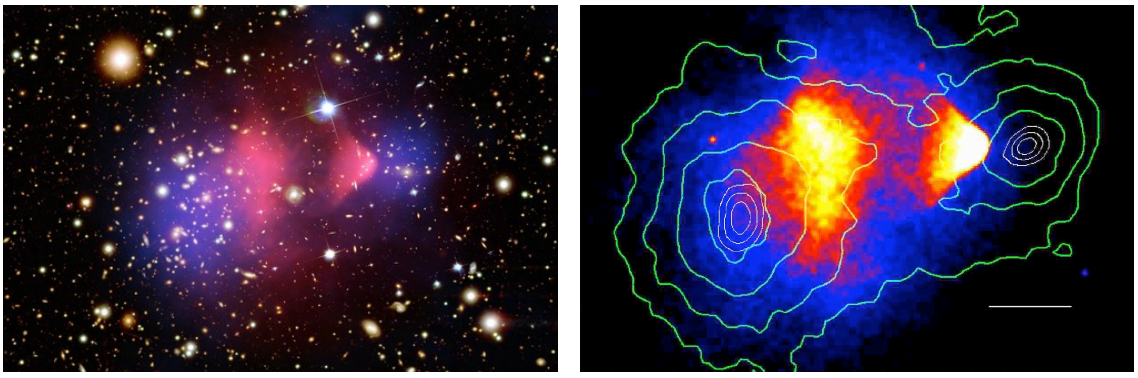

Figure 1.1: Two images of the Bullet Cluster. In the left image, the pink region shows the luminous matter mapped with the Chandra X-ray observatory. The purple region shows the matter distribution mapped with gravitational lensing. In the right image, from [17], the green contours show the matter distribution while the coloured regions show the luminous matter distribution. It is clear that the luminous matter and total matter distribution are displaced. Credit for left image: X-ray: NASA/CXC/CfA/M.Markevitch et al.; Optical: NASA/STScI; Magellan/U.Arizona/D.Clowe et al.; Lensing Map: NASA/STScI; ESO WFI; Magellan/U.Arizona/D.Clowe et al. The right image is reproduced by permission of the AAS.

the cluster. As Fig. 1.1 clearly demonstrates, the baryonic matter has been held up due to electromagnetic interactions while the dark matter has passed straight through. Thus, a separation of the net mass distribution and the luminous matter distribution is observed, implying that most of the matter is dark. A weak upper bound can be placed on the dark matter self interaction cross section [18]. Although dark matter interacts weakly with baryonic matter, it may have sizeable self interactions.

1.1.1 Dark matter on cosmological scales

The evidence presented thus far does not allow us to determine if the dark matter found in galaxies and galaxy clusters is non-baryonic. In fact, galaxies are expected to contain a certain number of non-luminous compact objects composed of baryonic matter, whimsically given the acronym MACHO, standing for massive astrophysical compact halo object. These MACHOs could be black holes, neutron stars, white dwarfs, brown dwarfs, faint red dwarfs or unassociated planets and are difficult to observe. Fortunately, observations of processes from the early Universe do provide insight into this matter.

The energy density of baryons can be determined from comparing observations of the primordial abundance of light elements with the abundance predicted from Big

Bang Nucleosynthesis (BBN) [19]. The predicted abundances from BBN depend on the density of baryons present and well understood Standard Model physics, leading to one of the most reliable probes of the early Universe. During BBN the primordial abundances of deuterium, helium-3, helium-4 and lithium formed from the free protons and neutrons that where present in the early Universe. The abundance of deuterium is a particularly sensitive probe of the baryon density, since there are no known astrophysical sources of this isotope. Therefore, any observed abundance gives a lower bound on the primordial abundance. The observed deuterium abundance can be explained if $\Omega_{\rm B}h^2 \approx 0.02$ [20], where $\Omega_{\rm B}$ is the baryon energy density in terms of the critical density $\rho_c = 3H^2/(8\pi G)$, with Hubble parameter $H = 100 \cdot h$ km s^{-1}Mpc^{-1} and Newton's constant G. Traditionally, h parameterises our uncertainty in the Hubble constant. The WMAP-7 year data finds $h = 0.710 \pm 0.025$ [21].

The position and amplitude of peaks in the power spectrum of cosmic microwave background (CMB) anisotropies are sensitive to both the baryon and dark matter energy densities. For a good review, see [22]. Fitting to the WMAP-7 year data [21] gives $\Omega_{\rm DM}h^2 = 0.1109 \pm 0.0056$ and $\Omega_{\rm B}h^2 = 0.0258^{+0.057}_{-0.056}$, where $\Omega_{\rm DM}$ is the dark matter energy density in terms of the critical density. This value of $\Omega_{\rm B}$ agrees with the result from BBN.

The results from BBN and the CMB imply that baryons only account for $\sim 19\%$ of the matter in the Universe. Since MACHOs are composed of baryonic matter, we can be confident that they do not make up a significant fraction of the observed dark matter. Similar conclusions are borne out in microlensing observations from the Milky Way [23].

Finally, the currently accepted cosmological model predicts that the same quantum fluctuations that seed the anisotropies in the CMB also seed the formation of structure on all scales in the Universe. Comparing the predictions of N-body cosmological simulations [24, 25, 26] with large-scale surveys indicate that most of the dark matter should be cold (that is, non-relativistic) at the onset of galaxy formation. Hot (relativistic) dark matter would disrupt the hierarchical formation of large scale structure, contrary to what is observed.

1.2 Dark matter in the Milky Way: the Standard Halo Model

The most likely place where we will directly probe dark matter is in our galaxy. In particular, dark matter 'direct' and 'indirect' detection experiments, to be discussed in

Section 1.4, depend on the local dark matter velocity distribution and density profile. Therefore, it is important to understand the Milky Way's dark matter distribution. In this section, we wish to review the simplest model of the dark matter in our galaxy, the 'Standard Halo Model' (SHM) [27, 28]. This assumes the dark matter is distributed spherically, isotropically and smoothly. Below, we closely follow the formalism outlined in Chapter 4 of [29], which makes use of distribution functions.

The distribution function $\mathcal{F}(x, v, t)$ is defined such that $\mathcal{F}\, d^3x\, d^3v/M_H$ is the probability that at time t, a randomly chosen dark matter particle has velocity v and position x in the given range. We assume that the halo has reached a steady state, so that $\mathcal{F}$ no longer depends on time. Here we have chosen to divide by M_H, the total mass of the dark matter halo, such that $\mathcal{F}$ is normalised as

$$\int d^3x d^3v\, \mathcal{F}(x, v) = M_H. \tag{1.1}$$

In this case, the dark matter density ρ and velocity distribution f are

$$\rho(x) = \int d^3v\, \mathcal{F}(x, v) \text{ and } f(v) = \frac{1}{M_H} \int d^3x\, \mathcal{F}(x, v). \tag{1.2}$$

We immediately see one advantage of this approach. Starting with a given distribution function $\mathcal{F}$, we can find a self consistent density profile and velocity distribution.

The distribution of the SHM is defined by

$$\mathcal{F}_{\text{SHM}} = \frac{\rho_0}{(2\pi\sigma^2)^{3/2}} \exp\left(\frac{\Psi - \frac{1}{2}v^2}{\sigma^2}\right), \tag{1.3}$$

where ρ_0 and σ are constants and Ψ is the relative potential defined by $\Psi \equiv -\Phi + \Phi_0$. Here Φ is the gravitational potential and Φ_0 is an appropriately chosen constant. Ψ satisfies Poisson's equation

$$\nabla^2\Psi = -4\pi G\rho. \tag{1.4}$$

Using the assumption that the dark matter is distributed spherically, isotropically and smoothly implies Ψ depends solely on r. Integrating Eq. (1.3) over all velocities gives an expression for ρ in terms of Ψ. Substituting this into Poisson's equation, we find

$$\frac{d}{dr}\left(r^2 \frac{d\ln\rho}{dr}\right) = -\frac{4\pi G}{\sigma^2} r^2\rho, \tag{1.5}$$

which has the (singular) solution

$$\rho(r) = \frac{\sigma^2}{2\pi G r^2}. \tag{1.6}$$

Similarly, integrating Eq. (1.3) over position, we obtain the velocity distribution

$$f(v) \propto \exp\left(-\frac{v^2}{2\sigma^2}\right). \tag{1.7}$$

The distribution of velocities in this model is the well-known Maxwell-Boltzmann distribution, with a velocity dispersion $\overline{v^2} = 3\sigma^2$.

It is interesting to note that an equation similar in form to Eq. (1.5) can be obtained starting from the equation of hydrostatic equilibrium for an isothermal gas

$$\frac{dp}{dr} = \frac{k_B T}{m}\frac{d\rho}{dr} = -\rho\frac{d\Phi}{dr} = -\rho\frac{GM(r)}{r^2}. \tag{1.8}$$

Here, k_B is the Boltzmann constant, p and T are the pressure and temperature of the gas, m is the particle mass and $M(r)$ is the mass interior to radius r. Multiplying through by $r^2 m/(\rho k_B T)$ and differentiating with respect to r, leads to an equation identical to Eq. (1.5), when we identify

$$\sigma^2 \equiv \frac{k_B T}{m}\ . \tag{1.9}$$

We thus find that the density and velocity distribution of the SHM correspond to an isothermal self-gravitating sphere of gas.

The mass interior to radius r and the circular speed v_0 are found to be

$$M(r) = \frac{2\sigma^2 r}{G} \ \text{ and } \ v_0(r) = \sqrt{2}\sigma. \tag{1.10}$$

Hence, the SHM predicts that the circular speed is independent of radius. This should not be surprising since observations of a flat circular speed as a function of radius were presented as evidence for dark matter in Section 1.1. We can infer the value of σ from the measured value of v_0. The canonical value of v_0 is 220 km/s, implying $\sigma = 155$ km/s. Hence, the root-mean-square speed of particles in the halo is $\sqrt{\overline{v^2}} \sim 270$ km/s $\sim 10^{-3}c$.

1.2.1 Problems with the Standard Halo Model

The advantage of the SHM is its simplicity. It has, however, many problems. Perhaps the most serious is the infinite size of the halo and the divergence of the mass as $r \to \infty$. This is distinct from real galaxies, which are finite in size and mass.

To account for the finite size of a real halo, the SHM velocity distribution is generally truncated at the escape velocity $v_{\rm esc}$ of the galaxy. This is usually done in

one of two ways: either having a hard cut at $v = v_{\rm esc}$, or smoothly deforming the distribution so that it tends to zero as $v \to v_{\rm esc}$. Mathematically, this is expressed as

$$f(v) \propto \begin{cases} \exp\left(-v^2/v_0^2\right) - \beta \exp\left(-v_{\rm esc}^2/v_0^2\right) & v < v_{\rm esc} \\ 0 & v > v_{\rm esc} \end{cases}, \tag{1.11}$$

with $\beta = 0$ or 1 for the hard cut or smooth deformation respectively. Note that we have used the result for the circular speed, Eq. (1.10), to replace $2\sigma^2$ with v_0^2.

The assumptions input into the SHM, namely that of a smooth halo that is isotropic and spherically symmetric, are also not expected to hold for a real halo. Indeed, simulated halos from dark matter N-body simulations [30, 31, 32] do show departures from these assumptions. In particular, N-body simulations show that the density profile of a typical halo is more faithfully described by the Navarro, Frenk and White (NFW) [33] or Einasto [34] profiles:

$$\rho(r) = \frac{\rho_s}{(r/r_s)(1 + r/r_s)^2} \quad \text{(NFW)} \tag{1.12}$$

$$\rho(r) = \rho_s \exp\left[-\frac{2}{\alpha}\left((r/r_s)^\alpha - 1\right)\right] \quad \text{(Einasto)}, \tag{1.13}$$

where ρ_s is the scale density, r_s is the scale radius and α is a shape parameter for the Einasto profile. N-body simulations find $\alpha \sim 0.16$ [35].

The dark matter velocity distribution extracted from N-body simulations show significant local and global departures from the Maxwell-Boltzmann distribution [36, 37, 38, 39]: many high-resolution simulations have observed 'bumpy' features or 'wiggles' in the velocity distribution, which are attributed to the hierarchical assembly history. In comparison, the SHM predicts a smooth velocity distribution. Secondly, simulations typically find halos with significant anisotropy, as opposed to the isotropic halo of the SHM [40]. Finally, it is found that the Maxwell-Boltzmann distribution tends to under predict the abundance of particles towards the high-energy tail of the distribution, while over predicting the abundance of particles towards the peak of the distribution [38].

There has been one glaring omission in our discussion thus far, namely the influence of the baryonic matter on the dark matter halo. Baryons are able to dissipate energy and contract to the centre of the galaxy, creating a deeper gravitational well, potentially increasing the dark matter density there. It has been observed in simulations that the baryons can cause the dark matter halo to change shape, becoming more oblate than prolate [41, 42]. This seems to agree with measurements of the Milky Way halo, which indicate a slightly more round, oblate halo shape [43]. Numerical

simulations that include baryons are currently being pursued and should increase our understanding of dark matter in the galactic halo.

In later chapters of this thesis, we will return to these departures from the SHM when we consider the results of dark matter direct detection experiments, to be discussed in Section 1.4.

1.3 Candidates for dark matter

Although there is much we don't know about dark matter, the evidence we have presented in Section 1.1 does constrain any particle physics candidate. First of all, any particle must be stable on cosmological time scales in order to have a sizeable abundance today. Secondly, the Bullet Cluster indicates that dark matter must interact more weakly than baryonic matter. In fact, the null results from searches for exotic nuclei on Earth constrain the dark matter to be at most weakly interacting [44]. Thirdly, BBN and the CMB data indicate that it must be non-baryonic. Lastly, in order to explain structure formation, N-body simulations indicate that dark matter must be cold. This last constraint rules out the only candidate from the Standard Model: the neutrino. Bounds on the neutrino mass tell us that at least one species of neutrino is relativistic, so, neutrinos cannot make up all of the dark matter abundance without having a significant effect on the formation of large scale structure.

The lack of other suitable candidates for dark matter within the Standard Model is one of the clearest calls for new physics beyond the Standard Model. It is interesting that many theories that address perceived theoretical problems with the Standard Model often include a dark matter candidate. In the remainder of this section, we outline some of the more popular dark matter candidates and briefly describe the mechanism that leads to the generation of their primordial abundance.

1.3.1 WIMPs

Weakly interacting massive particles (WIMPs) are perhaps the most studied of any dark matter candidate, and is the one we will be primarily concerned with in this thesis. WIMPs are a generic class of particles with masses typically ranging from a few GeV to a few TeV. They are characterised by having an interaction cross section that is of a similar order in magnitude as a weak interaction cross section. Examples of WIMPs are the neutralino or sneutrino in supersymmetric theories, or a Kaluza-Klein (KK) excitation of the photon in theories of extra dimensions.

The relic abundance of WIMPs is determined from the 'freeze-out' mechanism, first discussed in [45, 46, 47, 48]. Consider a massive particle χ which at early times is in chemical and thermal equilibrium with the other constituents of the Universe. If the interaction rate per particle Γ, which keeps the particle in thermal equilibrium, stays above the expansion rate of the Universe (determined by the Hubble constant H), the particle will remain in thermal equilibrium with an exponentially suppressed number density

$$n_\chi^{\rm eq} = g\left(\frac{m_\chi T}{2\pi}\right)^{3/2} \exp(-m_\chi/T). \tag{1.14}$$

Here g is the number of internal degrees of freedom of the particle, m_χ is the particle's mass and T is the temperature. At late times (small temperature), the relic abundance is exponentially small. However, if Γ falls below the expansion rate H, the particle will decouple, or 'freeze-out' from the thermal bath. If the decoupled particle is stable, this mechanism can give rise to a sizable relic cosmological abundance.

More quantitively, the time evolution of the WIMP number density n_χ is described by the Boltzmann equation[2]

$$\frac{dn_\chi}{dt} + 3Hn_\chi = -\langle\sigma_A v\rangle[n_\chi^2 - (n_\chi^{\rm eq})^2]. \tag{1.15}$$

Here $H = \dot{a}/a$ is Hubble's constant, a is the scale factor of the Universe and $\langle\sigma_A v\rangle$ is the thermal average of the WIMP annihilation cross section. This equation is simple to understand: the second term on the left-hand side accounts for the dilution of the number density due to the expansion of the Universe. In the absence of number changing interactions, the right-hand side is zero, so $n_\chi \sim a^{-3}$, as expected for non-relativistic matter. The first term on the right-hand side accounts for the depletion of WIMPs due to annihilation, while the second term accounts for the creation of WIMPs from the inverse reaction.

In solving the Boltzmann equation, it is convenient to introduce the comoving number density

$$Y \equiv \frac{n_\chi}{s} \quad \text{and} \quad Y^{\rm eq} \equiv \frac{n_\chi^{\rm eq}}{s}, \tag{1.16}$$

where $s = 2\pi^2 g_{\star s} T^3/45$ is the entropy density and $g_{\star s}$ counts the number of relativistic degrees of freedom. Conservation of s per comoving volume implies $s \sim a^{-3}$. Since we

[2]The relic density calculation presented here can be significantly changed when coannihilations or resonance enhancements are included. We refer the reader to [49, 50] for further discussion on these processes.

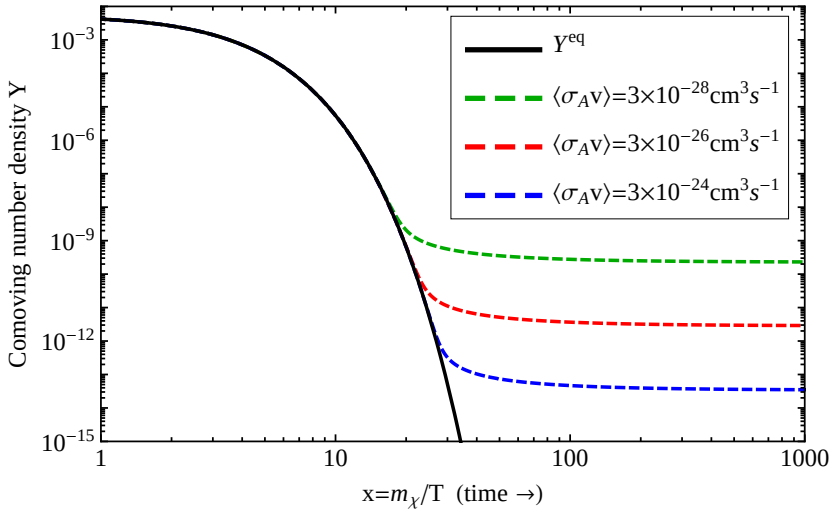

Figure 1.2: Numerical solution of the Boltzmann equation for $m_\chi = 100$ GeV. At early times the number density tracks the equilibrium value (black line). The late time number density decreases as $\langle\sigma_A v\rangle$ increases.

know $n_\chi \sim a^{-3}$, we deduce that Y is unchanged by the expansion of the Universe. It is also convenient to introduce $x \equiv m_\chi/T$, in which case, Eq. (1.15) can be rewritten:

$$\frac{dY}{dx} = -\frac{\langle\sigma_A v\rangle s}{Hx}\left[Y^2 - (Y^{\rm eq})^2\right]. \tag{1.17}$$

This form is more amenable for solving. In general this equation needs to be solved numerically, although good approximations do exist, which typically give results that are accurate to better than $\sim 5\%$.

Figure 1.2 shows the numerical solution of Eq. (1.17) for $m_\chi = 100$ GeV and three choices of $\langle\sigma_A v\rangle$. At early times, the number density closely tracks the equilibrium value. Decoupling from thermal equilibrium occurs at $x_{FO} \approx 25$. As $\langle\sigma_A v\rangle$ increases, the WIMP stays in equilibrium for longer and the resulting relic abundance after freeze-out is smaller.

Good derivations of the approximate solution [51, 52] are presented in [7, 53], so we do not review it here. Rather, we content ourselves with an order of magnitude estimate[3]:

$$\begin{aligned}\Omega_\chi h^2 &\simeq 2.8\times 10^{10}\cdot\frac{m_\chi}{100\ \text{GeV}}\cdot Y(x\to\infty)\\ &\approx \frac{3\times 10^{-27}\ \text{cm}^3\ \text{s}^{-1}}{\langle\sigma_A v\rangle}\\ &\approx 0.1\,\frac{10^{-36}\ \text{cm}^2\cdot c}{\langle\sigma_A v\rangle}\end{aligned} \tag{1.18}$$

[3]We have assumed there is no significant production of entropy following freeze-out.

It is straightforward to check that this approximation is in accord with the numerical results of Fig. 1.2. It is also worth noting that $\Omega_\chi h^2$ is independent of m_χ (up to logarithmic corrections not included here). It is striking that a particle interacting with a typical weak scale cross section predicts a relic density close to the observed value $\Omega_{\rm DM} h^2 \sim 0.1$. This fact has been coined the 'WIMP miracle'.

Of course, one might wonder why a particle with just these properties should appear. Remarkably, solutions of the 'hierarchy problem' of the Standard Model generally predict additional particles with weak scale masses ~ 100 GeV and additional symmetries to stabilise the particle on cosmological timescales. We will return to these issues in more detail in Chapter 6, which deals with supersymmetric theories.

1.3.2 Other candidates

Particles other than WIMPs have, of course, been suggested as the constituent of dark matter. Here I briefly describe these other candidates, each of which clearly represents physics beyond the Standard Model.

1.3.2.1 Asymmetric dark matter

As attractive as the freeze-out mechanism might be, it completely fails to explain the observed baryon abundance, predicting an abundance around ten orders of magnitude smaller than what is observed [54]. Also, it gives no explanation for the observed domination of baryons over anti-baryons in the Universe. Rather, a primordial asymmetry between baryons and anti-baryons is required to explain the baryon abundance observed today, which can not arise from the freeze-out mechanism. The anti-baryons have subsequently annihilated with the baryons, leaving behind an excess of baryonic matter, of which we are made.

The observation that the ratio

$$R_{\rm B}^{\rm DM} = \frac{\Omega_{\rm DM}}{\Omega_{\rm B}} \simeq 4.3 \sim \mathcal{O}(1) \tag{1.19}$$

has motivated the study of models of asymmetric dark matter (ADM). In these models, the abundance is determined from an initial asymmetry between dark matter particles and their anti-particles, as in the case of the baryons. Unlike the freeze-out mechanism, which provides no explanation for the value of the ratio $R_{\rm B}^{\rm DM}$, in models of ADM, the dark matter asymmetry may be linked to the baryon asymmetry, naturally explaining why the ratio $R_{\rm B}^{\rm DM}$ is $\mathcal{O}(1)$. Models of ADM are fairly generic and have been constructed in theories of technicolour [55], in which a 'technibaryon' [56]

is the dark matter candidate, or in supersymmetric theories, in which the sneutrino [57] or additional gauge singlets [58] are the dark matter.

1.3.2.2 The QCD axion

The axion was posited as a consequence of the Peccei-Quinn solution [59, 60] of the 'strong CP problem' in QCD. In the Standard Model, there are no symmetries that forbid the P and CP violating term

$$\frac{\bar{\theta}}{16\pi^2} Tr(G_{\mu\nu}\tilde{G}^{\mu\nu}). \tag{1.20}$$

Here $G^{\mu\nu}$ and $\tilde{G}^{\mu\nu}$ are the $SU(3)$ field strength and dual field strength tensors respectively and $\bar{\theta}$ is a dimensionless parameter, which can *a priori* take values between 0 and 2π. Explicitly breaking CP in this way leads to the generation of an electric dipole moment for the neutron. The experimental upper limit on such an electric dipole moment constrains $|\bar{\theta}| < 3 \times 10^{-10}$. The strong CP problem is to explain the extreme smallness of $\bar{\theta}$.

Peccei and Quinn introduced an additional global chiral $U(1)_{\mathrm{PQ}}$ symmetry to the Standard Model, anomalous under $SU(3)$ and spontaneously broken at a scale f_a. The axion a is the (pseudo)-Nambu-Goldstone boson of the broken $U(1)_{\mathrm{PQ}}$ symmetry [61, 62] and is identified with $\bar{\theta}$ ($a \equiv f_a\bar{\theta}$). QCD instanton effects explicitly break the symmetry and generate a potential for a, which is minimised for $a = 0$. Since $\bar{\theta}$ has been promoted to a dynamical field (a/f_a), its value has been naturally set to zero. This is the attractive feature of the Peccei-Quinn solution. The explicit breaking also leads to the generation of a mass for the axion [63]

$$m_a \sim \frac{m_\pi f_\pi}{f_a} \sim 0.6 \text{ meV} \left(\frac{10^{10} \text{ GeV}}{f_a}\right), \tag{1.21}$$

where m_π and f_π are the pion mass and pion decay constants respectively.

Interactions of the axion with normal matter are suppressed by f_a. *A priori*, the Peccei-Quinn solution works for any value of f_a and historically, the first axion models identified f_a with the scale of electroweak symmetry breaking. However, various laboratory and especially astrophysical bounds, notably from the cooling of red giants and SN 1987A, constrain $f_a \gtrsim 10^9$ GeV. Thus the axion is light and interacts very weakly, potentially making it a dark matter candidate [64, 65, 66].

The experimentally allowed values of f_a imply that axions interact so weakly that a thermal population is never created [53]. However, a non-thermal relic abundance

of axions is created through the 'mis-alignment mechanism'. The axions are produced as a non-relativistic condensate with an abundance today of [67]

$$\Omega_a h^2 \sim 0.09 \left(\frac{f_a}{10^{11}\ \text{GeV}}\right)^{7/6} \left(\frac{\theta_i}{\pi/\sqrt{3}}\right)^2 . \tag{1.22}$$

Here θ_i is the initial value of $\bar{\theta}$ in the early Universe, before the Peccei-Quinn mechanism relaxes it to zero. We thus see that the QCD axion is a viable dark matter candidate for $f_a \gtrsim 10^9$ GeV. Values of $f_a \gtrsim 10^{11}$ GeV are somewhat disfavoured as they require a fine-tuning of θ_i, which many find unpalatable.

Detecting axion dark matter experimentally is very challenging due to the extremely weak coupling with normal matter. The ADMX experiments hopes to detect the axion through its coupling to two photons and is sensitive to values of $f_a \sim 10^{11}$ GeV [68]. More recently, an experimental technique was proposed that can probe values of $f_a \gtrsim 10^{16}$ GeV, but it relies on the development of new technology [69].

1.3.2.3 SuperWIMPs

There are candidates other than the axion that gain an abundance through non-thermal mechanisms. One such class of particles have been coined superWIMPs [70], which are particles that interact with 'super weak' interactions. The leading example of a superWIMP is the gravitino [71], the spin-3/2 superpartner of the graviton.

Consider a WIMP which, after freezing-out from the thermal bath, decays via super weak interactions to a superWIMP. The WIMP bestows its relic abundance to the superWIMP. The two are related via

$$\Omega_{\text{superWIMP}} = \frac{m_{\text{superWIMP}}}{m_{\text{WIMP}}} \Omega_{\text{WIMP}} . \tag{1.23}$$

Even though the superWIMP particle is not itself a WIMP, its abundance is indirectly determined from the 'WIMP miracle'.

Alternatively, if a superWIMP couples through a non-renormalizable interaction, its abundance depends on the reheat temperature T_{R} after inflation. Requiring that gravitinos do not have a relic abundance that is larger than experimentally observed leads to the well known bound $T_{\text{R}} \lesssim 10^{10}$ GeV [72, 73, 74].

1.4 Experimental detection

A noticeable feature of all of the candidates we have considered is that they all interact with normal matter (to varying degrees). This opens up the possibility of directly

or indirectly detecting the dark matter through non-gravitational interactions. In this section we consider some of the experiments designed to search for dark matter through non-gravitational interactions.

1.4.1 Direct detection

Direct detection experiments offer one of the most promising methods of detecting dark matter that interacts with weak scale interactions. These experiments aim to detect the energy deposited by a recoiling nucleus, after a collision with a dark matter particle [75]. In the Earth's frame, the maximum recoil energy of an initially stationary nucleus after a collision with a particle moving at speed v_χ is

$$E_{\mathrm{R}}^{\mathrm{max}} = \frac{2 m_N m_\chi^2 v_\chi^2}{(m_N + m_\chi)^2} \, . \tag{1.24}$$

From Section 1.2, we know the typical speed v_χ of a dark matter particle in the galactic halo is ~ 270 km/s. Thus, for a dark matter particle and nucleus of mass $m_\chi \sim m_N \sim 100$ GeV respectively, the recoil energy of the nucleus is tens of keV and the de Broglie wavelength of the dark matter is $\lambda_{\mathrm{dB}} \sim 10$ fm. This is similar in size to the diameter of a heavy nucleus, which justifies the implicit assumption we have made that DM scatters off the whole nucleus in a direct detection experiment. Designing experiments to detect recoil energies of this magnitude, while reducing energy depositions induced by electron and neutron backgrounds, is extremely challenging. Two main experimental approaches have been rigorously pursued. The first group of experiments significantly reduce the background contribution, while searching for the absolute scattering rate due to dark matter. A variety of target nuclei are used in these experiments, each with different advantages and disadvantages. The second group allow more background events, but search for an annual modulation signal in the event rate that is characteristic of dark matter.[4]

The annual modulation signal arises due to the motion of the Earth relative to the galactic halo and peaks when the Earth is travelling fastest with respect to the halo [27, 28]. Remarkably, two experiments have now detected an annual modulation signal that has many features consistent with a signal arising from dark matter. The DAMA collaboration [76, 77] has observed an annual modulation over thirteen years; first with the DAMA/NaI setup and later with the DAMA/LIBRA upgrade. The large mass of the target material and the long exposure time mean that the

[4] A third approach under development takes into account the direction of the recoiling nucleus, as well as the recoil energy. Due to the (at present) reduced sensitivity of these experiments, we will not consider them further in this thesis.

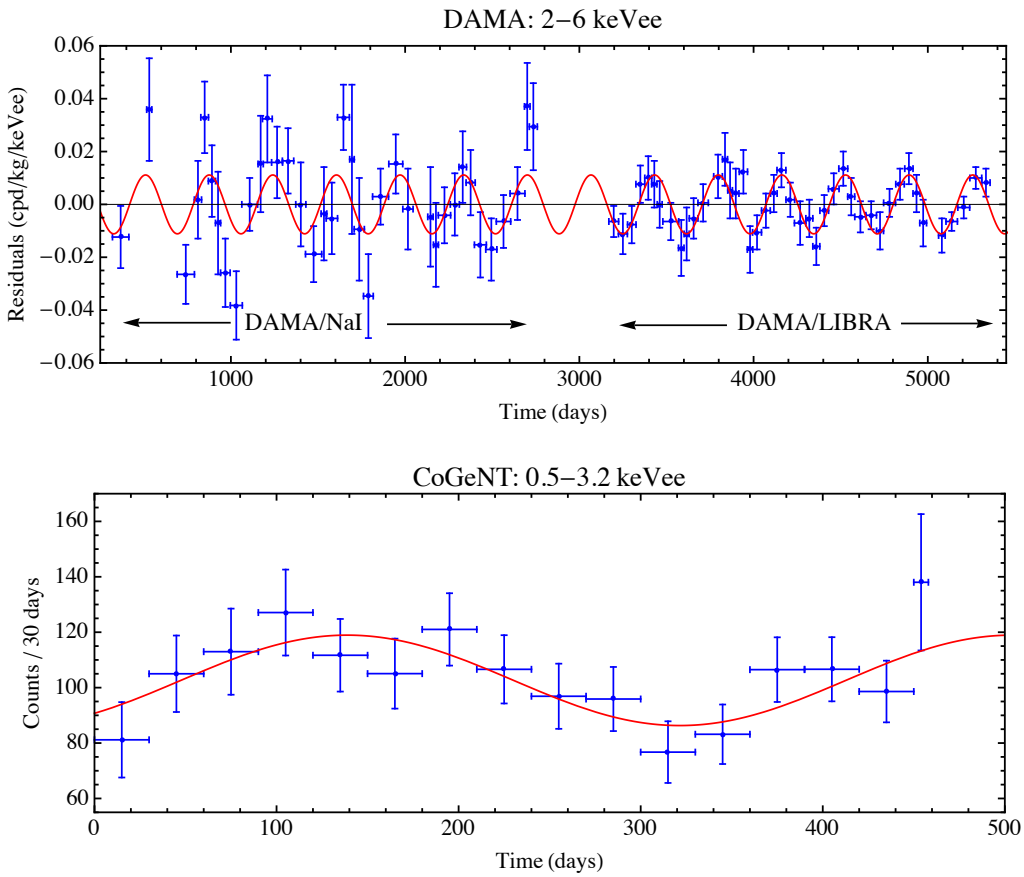

Figure 1.3: The time evolution of the DAMA and CoGeNT event rates. The blue points show the data, while the best-fit line with a period of one year is shown in red. Data taken from Refs. [76, 77] and [78].

statistical nature of the modulation is beyond question. More recently, the CoGeNT collaboration [78] has presented tentative evidence for an annual modulation after analysing fifteen months of data. The event rate for both experiments, measured over time, is presented in Fig. 1.3. The blue points show the measured data, while the best-fit line with a period of one year is shown in red. The DAMA/LIBRA data displays the clearest signs of a modulation.

The simplest explanation of these experiments in terms of dark matter is spin-independent elastic scattering on both protons and neutrons. Unfortunately, this explanation is strongly disfavoured by the null results from other direct detection experiments aiming to detect the absolute scattering rate. Any theory attempting to explain the modulation signals must also be consistent with bounds from the CDMS II [79, 80, 81, 82], CRESST-II [83], SIMPLE [84], XENON10 [85, 86, 87], XENON100 [88, 89, 90], ZEPLIN-II [91] and ZEPLIN-III [92, 93] experiments. In Chapters 2, 4 and 5, we will explore theories that try and reconcile all of these experiments.

1.4.1.1 Calculating the event rate

The differential event rate for DM-nucleus scattering in units of cpd/kg/keV (counts per day/unit nucleus mass/unit exposure time/unit energy) as a function of recoil energy $E_{\rm R}$ is

$$\frac{dR}{dE_{\rm R}} = \frac{\rho_\chi}{m_N m_\chi} \int_{v_{\rm min}}^{\infty} v f_\oplus(\vec{v}, \vec{v}_e) \frac{d\sigma}{dE_{\rm R}} d^3v. \tag{1.25}$$

Here m_χ is the dark matter mass, ρ_χ the local dark matter density, m_N the mass of the target nucleus, $v = |\vec{v}|$, $f_\oplus(\vec{v}, \vec{v}_e)$ the local dark matter velocity distribution in the detector rest frame and $d\sigma/dE_{\rm R}$ the dark matter-nucleus differential cross section. For a nucleus to recoil with an energy $E_{\rm R}$, the incident dark matter particle must have a minimum speed given by

$$\frac{v_{\rm min}}{c} = \sqrt{\frac{1}{2m_N E_{\rm R}}} \left(\frac{m_N E_{\rm R}}{\mu_N} \right) , \tag{1.26}$$

where μ_N is the dark matter-nucleus reduced mass.

As was discussed in Section 1.2, the SHM predicts a truncated Maxwell-Boltzmann velocity distribution in the galactic frame (see Eq. (1.11)). The velocity distribution entering Eq. (1.25) is evaluated in the frame of the detector, therefore we need to transform the galactic velocity distribution $f(\vec{v})$ to the Earth frame. $f_\oplus(\vec{v}, \vec{v}_e)$ and $f(\vec{v})$ are simply related through a Galilean boost

$$f_\oplus(\vec{v}, \vec{v}_e) = f(\vec{v} + \vec{v}_e) , \tag{1.27}$$

where $\vec{v}_e = \vec{v}_\odot + \vec{v}_\oplus$ is the velocity of the Earth relative to the rest frame of the galaxy. $\vec{v}_\odot = \vec{v}_0 + \vec{v}_\circledast$ is the sum of the Sun's circular velocity $\vec{v}_0 \sim (0, 220, 0)$ km/s relative to the galactic centre, and peculiar velocity $\vec{v}_\circledast \sim (11, 12, 7)$ km/s relative to Sun's circular velocity.[5] $\vec{v}_\oplus$ is the Earth's velocity relative to the Sun's rest frame and is given by [94, 95]

$$\vec{v}_\oplus = \langle u_E \rangle (1 - e \sin(\lambda(n) - \lambda_0)) \begin{pmatrix} \cos(\beta_x)\sin(\lambda(n) - \lambda_x) \\ \cos(\beta_y)\sin(\lambda(n) - \lambda_y) \\ \cos(\beta_z)\sin(\lambda(n) - \lambda_z) \end{pmatrix} \text{km/s}, \tag{1.28}$$

where the Earth's orbit has a mean velocity $\langle u_E \rangle = 29.79$ km/s and ellipticity $e = 0.016722$. The quantities β_i, λ_i, define the orientation of the Earth's orbit in galactic coordinates, and $\lambda(n)$ gives the angular position of the Earth's orbit for a given day number n, with $n = 1$ corresponding to 1st January 2000. These quantities are given in [95].

[5] If they are required, precise values of $\vec{v}_0$ and $\vec{v}_\circledast$ will be specified in the relevant chapter.

Generally, a model of dark matter is constructed by writing down a Lagrangian that describes the interaction of dark matter with quarks. Calculating the dark matter-nucleus differential cross section $d\sigma/dE_{\rm R}$ from this Lagrangian is non-trivial as it involves matching the quark fields to the nucleon fields, followed by matching the nucleon fields to the nucleus field. Finally, since the galactic dark matter is non-relativistic, the resulting scattering amplitude and cross section must be evaluated in the non-relativistic limit. When this limit is taken, it has been shown (for example in Ref.[96]) that in general, only spin independent or spin dependent scattering occurs. Below we outline how the matching procedure is carried out for vector and scalar interactions, which lead to spin independent scattering, and axial-vector interactions, which lead to spin dependent scattering.[6] Further details, including a discussion of other interactions, can be found in [6, 97, 98, 99].

1.4.1.2 Calculating cross sections: Vector interactions

The most straightforward case to consider is when dark matter interacts with quarks through a vector interaction. In this case, the Lagrangian is

$$\mathcal{L}^{q}_{\rm vec} = a_q\, \bar{\chi}\gamma^{\mu}\chi\, \bar{q}\gamma_{\mu}q\ , \tag{1.29}$$

where q is the quark field and χ the dark matter field. This dimension-6 operator arises from integrating out a heavy vector mediator, in which case, the coupling constant is $a_q = g_\chi g_q/M^2$, where M is the mass of the vector mediator and g_q and g_χ are the charges of the quarks and dark matter respectively.

The vector current is conserved so the contribution from each valence quark in the nucleon adds coherently and there is no contribution from sea quarks or gluons. Hence, the effective interaction of dark matter with a proton p and neutron n is $\mathcal{L}^{p}_{\rm vec} = f_p\, \bar{\chi}\gamma^{\mu}\chi\, \bar{p}\gamma_{\mu}p$ and $\mathcal{L}^{n}_{\rm vec} = f_n\, \bar{\chi}\gamma^{\mu}\chi\, \bar{n}\gamma_{\mu}n$ respectively, where $f_p = 2a_u + a_d$ and $f_n = a_u + 2a_d$. The ratio f_n/f_p depends on the charges of the quarks and can *a priori* take any value. For example, for the Z boson, $f_n/f_p = -1/(1-4\sin^2\theta_W) \approx -13.2$, where $\sin\theta_W$ is the Weinberg mixing-angle.

To match to the nucleus, we again make use of the conservation of the vector current. For a point like nucleus N, the Lagrangian is simply $\mathcal{L}^{N}_{\rm vec} = a_N\, \bar{\chi}\gamma^{\mu}\chi\, \bar{N}\gamma_{\mu}N$, where $a_N = f_p Z + f_n(A-Z)$, and A and Z are the number of nucleons and protons respectively. From this Lagrangian, the amplitude is

$$\mathcal{M} = a_N\, \bar{u}_{\chi}\gamma^{\mu}u_{\chi}\, \bar{u}_N\gamma_{\mu}u_N\ , \tag{1.30}$$

where u are Dirac spinors. In the non-relativistic limit, $u = \sqrt{m}\begin{pmatrix}\xi\\ \xi\end{pmatrix}$, where ξ is a

[6] Throughout we assume the dark matter is a Dirac fermion.

two-component spinor, normalised such that $\xi^\dagger\xi = 1$. In this limit $\bar{u}_\chi\gamma^\mu u_\chi\,\bar{u}_N\gamma_\mu u_N = 4m_N m_\chi$ (only the time component gives a non-zero contribution). The resulting cross section for a point like nucleus is

$$\sigma^N_{\rm vec} = \frac{a_N^2\mu_N^2}{\pi} = \left(f_p Z + f_n(A-Z)\right)^2 \frac{\mu_N^2}{\pi}\ . \tag{1.31}$$

The de Broglie wavelength of the dark matter is similar in magnitude to the diameter of a nucleus so it is not correct to ignore the finite size of the nucleus. The nuclear form factor $F(E_{\rm R})$ accounts for this correction. The amplitude and differential cross section for a nucleus of finite size is

$$\mathcal{M} = 4a_N m_N m_\chi F(E_{\rm R}) \ \Rightarrow\ \frac{d\sigma_{\rm vec}}{dE_{\rm R}} = \frac{\sigma^N_{\rm vec}}{E^{\rm max}_{\rm R}} F^2(E_{\rm R})\ , \tag{1.32}$$

where $E^{\rm max}_{\rm R} = 2\mu_N^2 v^2/m_N$ is the maximum recoil energy of a nucleus after interacting with an incident dark matter particle with speed v.

The form factor is the Fourier transform of the charge density. It is assumed that all charge densities in the nucleus are proportional to the electric charge density, which is determined from electron-nucleus scattering experiments. Different parameterisations exist but the most commonly used is the Lewin-Smith parameterisation of the Helm form factor [95]

$$F^2(E_{\rm R}) = \left(\frac{3j_1(qR)}{qR}\right)^2 e^{-q^2s^2}, \tag{1.33}$$

where $q = \sqrt{2m_N E_{\rm R}}$ is the momentum transfer, $R = \sqrt{c^2 + \frac{7}{3}\pi^2a^2 - 5s^2}$, $c = 1.23A^{1/3} - 0.60$ fm, $s = 0.9$ fm and $a = 0.52$ fm. This has the advantage of having an analytic form, however, it tends to be too large when the momentum transfer is large. A more accurate form factor that we will use in cases when the momentum transfer is large is the Fermi Two-Parameter form factor, defined by

$$F(q) = \int_0^\infty \frac{\rho_c}{e^{(r-c)/a}+1}\frac{\sin(qr)}{qr}4\pi r^2 dr\ . \tag{1.34}$$

Here ρ_c is chosen so that $F(0) = 1$, while a and c are constants that depend on the target nucleus. Values for various nuclei can be found in Appendix I of Ref.[100].

Direct detection experiments use different target nuclei so it is conventional to state results in terms of the cross section to interact with a neutron σ_n. This is

in order that different experiments can be easily compared. From Eq. (1.31), it is straightforward to see that

$$\frac{\sigma_n}{\mu_{\chi n}^2}\frac{1}{f_n^2} = \frac{\sigma_{\rm vec}^N}{\mu_N^2}\frac{1}{\left(f_p Z + f_n(A-Z)\right)^2} \ , \tag{1.35}$$

where $\mu_{\chi n}$ is the dark matter neutron reduced mass. Therefore, the differential cross section for a nucleus of finite size can be written as

$$\frac{d\sigma_{\rm SI}}{dE_{\rm R}} = \frac{m_N \sigma_n}{2\mu_{\chi n}^2 v^2}\frac{\left(f_p Z + f_n(A-Z)\right)^2}{f_n^2} F^2(E_{\rm R}) \ . \tag{1.36}$$

1.4.1.3 The dark matter-nucleus cross section: Scalar interactions

We can next consider the interaction of dark matter with quarks through a scalar mediator such as the Higgs boson. In this case, the Lagrangian is

$$\mathcal{L}_{\rm scal}^q = a_q \, \bar{\chi}\chi \, \bar{q}q \ . \tag{1.37}$$

Unfortunately, matching to the nucleon fields is not as straightforward as the vector case because the scalar mediator will generally interact with the sea quarks and gluons in addition to the valence quarks. To proceed, we use the fact that the nucleon mass is determined from the trace of the energy momentum tensor [101]. For the proton, we have

$$m_p = \langle p|\theta_\mu^\mu|p\rangle = \langle p|\sum_{q=u,d,s} m_q \bar{q}q + \sum_{Q=c,b,t} m_Q \bar{Q}Q + \frac{\beta(\alpha_s)}{4\alpha_s} G^a_{\mu\nu}G^{a\mu\nu}|p\rangle \ , \tag{1.38}$$

where m_q and m_Q are the 'light' and 'heavy' quark masses respectively and $\beta(\alpha_s) = -7\alpha_s^2/(2\pi)$ is the QCD beta function [102, 103]. The last term arises due to the trace anomaly [104].

There are no heavy valence quarks in the proton so they only enter through virtual states. In particular, a triangle diagram with heavy virtual quarks induces an (additional) effective coupling of dark matter with gluons. Integrating out the heavy quarks Q we find (for each heavy quark) [101]

$$m_Q \bar{Q}Q = -\frac{2}{3}\frac{\alpha_s}{8\pi} G^a_{\mu\nu}G^{a\mu\nu} \ . \tag{1.39}$$

If we define

$$m_p f_{T_q}^{(p)} = \langle p|m_q \bar{q}q|p\rangle \ \text{ and } \ f_{T_Q}^{(p)} = 1 - \sum_{q=u,d,s} f_{T_q}^{(p)} \ , \tag{1.40}$$

then, making use of Eq. (1.39) to rearrange Eq. (1.38), we find

$$m_Q \bar{Q} Q = -\frac{2}{27} m_p f_{T_Q}^{(p)} \ . \tag{1.41}$$

Hence, for the proton, we can define f_p

$$\begin{aligned} f_p \, \bar{p} p &\equiv \langle p | \sum_{q=u,d,s} a_q \bar{q} q + \sum_{Q=c,b,t} a_Q \bar{Q} Q | p \rangle \\ &= \left(\sum_{q=u,d,s} a_q f_{T_q}^{(p)} \frac{m_p}{m_q} + \frac{2}{27} \sum_{Q=c,b,t} a_Q f_{T_Q}^{(p)} \frac{m_p}{m_Q} \right) \bar{p} p \ . \end{aligned} \tag{1.42}$$

By similar reasoning, we can get an expression for f_n. Significant uncertainties exist on the values of f_{T_q}, especially f_{T_s}. They are determined using a combination of chiral perturbation theory and lattice calculations. Recent values can be found in [105]. For the Higgs boson, $f_n/f_p \approx 1$ because the interaction is dominated by the strange quark content of the nucleon, similar in both the proton and the neutron.

From here, matching the proton and neutron fields to the nucleus is relatively straightforward as $\bar{p}p$ and $\bar{n}n$ simply count the number of protons and neutrons respectively. Therefore the amplitude for a point like nucleus is

$$\mathcal{M} = \left(f_p Z + f_n (A - Z) \right) \bar{u}_\chi u_\chi \, \bar{u}_N u_N \ . \tag{1.43}$$

In the non-relativistic limit, $\bar{u}_\chi u_\chi \, \bar{u}_N u_N = 4 m_N m_\chi$, leading to

$$\sigma_{\text{scal}}^N = \left(f_p Z + f_n (A - Z) \right)^2 \frac{\mu_N^2}{\pi} \ \Rightarrow \ \frac{d\sigma_{\text{scal}}}{dE_{\text{R}}} = \frac{\sigma_{\text{scal}}^N}{E_{\text{R}}^{\text{max}}} F^2(E_{\text{R}}) \ . \tag{1.44}$$

By assuming that the mass distribution of the nucleus is the same as the electric charge distribution, we can use the Helm or Fermi Two-Parameter form factors described above. Finally, when the differential cross section is expressed in terms of the neutron cross section σ_n, we get the same functional form as for the vector interaction, namely Eq. (1.36).

1.4.1.4 Calculating cross sections: Axial-vector interactions

The final case we consider is the axial-vector interaction, which can arise from integrating out a vector mediator with axial couplings. The Lagrangian is this case is

$$\mathcal{L}_{\text{ax-vec}}^q = a_q \, \bar{\chi} \gamma^\mu \gamma^5 \chi \, \bar{q} \gamma_\mu \gamma^5 q \ . \tag{1.45}$$

It is instructive to first consider this interaction in the zero momentum transfer limit. We will then generalise the result to the case when the momentum transfer is finite.

In the non-relativistic limit, $\bar{\chi}\gamma^\mu\gamma^5\chi$ reduces to $2m_\chi\,\xi^\dagger_\chi\vec{\sigma}\xi'_\chi \propto \vec{s}_\chi$, where σ^i are the Pauli matrices and $\vec{s}_\chi$ is the spin of χ. Similar reasoning can be applied to the current involving quarks. Therefore, the amplitude for dark matter quark scattering depends on $\vec{s_\chi}\cdot\vec{s_q}$. Although complicated when matching from quarks to the nucleus, the amplitude for dark matter nucleus scattering will still depend on the spin of the dark matter and nucleus.

We consider matching from quarks to the neutron (similar reasoning applies for the proton). We can define $\langle n|\bar{q}\gamma_\mu\gamma^5 q|n\rangle = \Delta_q^{(n)}\bar{n}\gamma_\mu\gamma^5 n$, where $\Delta_q^{(n)}$ give the fraction of spin due to each quark in the neutron. Contributions from charm, bottom and top are zero. Thus the effective Lagrangian for the neutron is $\mathcal{L}^n_{\text{ax-vec}} = a_n\,\bar{\chi}\gamma^\mu\gamma^5\chi\,\bar{n}\gamma_\mu\gamma^5 n$, where $a_n = \sum_{q=u,d,s} a_q\Delta_q^{(n)}$. As discussed in [105], the individual $\Delta_q^{(n)}$ are poorly constrained. Taking the non-relativistic limit, the cross section to scatter off a neutron in the limit of zero momentum transfer is

$$\mathcal{M} = 4a_n m_\chi m_n \xi^\dagger_\chi\sigma^i\xi'_\chi\xi^\dagger_n\sigma^i\xi'_n \;\Rightarrow\; \sigma_n = \frac{3\,a_n^2\,\mu^2_{\chi n}}{\pi}\,. \tag{1.46}$$

Similarly, the cross section for a point-like nucleus at zero momentum transfer is given by

$$\sigma^N_{\text{ax-vec}} = \frac{4\mu_N^2}{\pi}\frac{J_N+1}{J_N}(a_p\langle S_p\rangle + a_n\langle S_n\rangle)^2\,, \tag{1.47}$$

where J_N and $\langle S_{p(n)}\rangle$ are the nuclear spin and expectation value of the spin content of the proton (neutron) in the nucleus respectively. It is useful to define

$$S(0) = \frac{2J_N+1}{\pi}\frac{J_N+1}{J_N}(a_p\langle S_p\rangle + a_n\langle S_n\rangle)^2 \;\Rightarrow\; \sigma^N_{\text{ax-vec}} = \frac{4\mu_N^2}{2J_N+1}S(0)\,. \tag{1.48}$$

When the momentum transfer is non-zero and the finite size of the nucleus is taken into account, the differential cross section is given by

$$\frac{d\sigma_{\text{ax-vec}}}{dE_{\text{R}}} = \frac{1}{E_{\text{R}}^{\text{max}}}\frac{4\mu_N^2}{2J_N+1}S(E_{\text{R}})\,, \tag{1.49}$$

where

$$S(E_{\text{R}}) = a_0^2 S_{00}(E_{\text{R}}) + a_1^2 S_{11}(E_{\text{R}}) + a_0 a_1 S_{01}(E_{\text{R}}) \tag{1.50}$$

are the nuclear structure functions, which vary for different nuclei. We have defined $a_0 = a_p + a_n$ and $a_1 = a_p - a_n$. The functional forms of $S_{00}(E_{\text{R}})$, $S_{01}(E_{\text{R}})$ and $S_{11}(E_{\text{R}})$ for nuclei used in direct detection experiments can be found in [106]. Ultimately, experiments place limits on a_p or a_n, which can be used to put limits on σ_n (or σ_p) through Eq. (1.46).

To summarise, in general, the dark matter-nucleus cross section can be separated into a spin-independent (SI) and spin-dependent (SD) contribution. Expressing everything in terms of the SI and SD cross sections to scatter off a neutron, we have

$$\frac{d\sigma}{dE_{\mathrm{R}}} = \frac{1}{2\mu_{\chi n} v^2}\left(\sigma_n^{\mathrm{SI}} \frac{\left(f_p Z + f_n (A-Z)\right)^2}{f_n^2} F^2(E_{\mathrm{R}}) + \frac{4\pi\sigma_n^{\mathrm{SD}}}{3}\frac{1}{2J_N+1}\frac{S(E_{\mathrm{R}})}{a_n^2}\right) . \quad (1.51)$$

Experiments are typically much more sensitive to spin-independent interactions. This is in part due to the $A^2 \sim 10^4$ (assuming $f_n = f_p = 1$ in Eq. (1.51) enhancement of the spin-independent scattering rate, and in part due to the challenge of scaling up experiments containing nuclei with non-zero spin. For instance, the experiments currently being scaled up contain germanium or xenon nuclei. Only 7.73% of naturally occurring germanium contains an isotope with spin (^{73}Ge) [107]; xenon fares slightly better, containing two isotopes with spin, with abundances of 26.4% (^{129}Xe) and 21.2% (^{131}Xe) [108].

1.4.2 Indirect detection

Indirect detection searches aim to detect the secondary particles produced in the decays or annihilations of dark matter particles. These secondary particles are typically high energy gamma rays, neutrinos, (anti-) electrons and (anti-) protons. The flux of secondary particles depends on the density of dark matter ρ_χ, scaling as ρ_χ and ρ_χ^2 for decays and annihilations respectively. Therefore, the best places to search for signals are in regions where the dark matter density is large, such as the galactic centre or dwarf spheroidal galaxies. While the galactic centre will produce the largest flux of, for instance, gamma rays, extraction of a dark matter signal is complicated by the large background signal, which is difficult to understand in detail. Even though dwarf spheroidal galaxies produce a much smaller flux of gamma rays, they are dominated by dark matter, so extracting a signal originating from dark matter should, in principle, be more straightforward.

Another interesting place where a significant abundance of dark matter can build up is inside astrophysical bodies, such as the Sun. After scattering on one of the nuclei comprising the Sun, the dark matter particles can lose enough kinetic energy to become gravitationally bound. This can lead to two interesting effects.

If a significantly large abundance is captured, dark matter may change the helioseismology and low energy neutrino fluxes [109, 110, 111]. This may happen if the dark matter is, for instance, asymmetric, so that self-annihilations can not occur (there are no anti-particles around to annihilate with).

The second interesting effect occurs when annihilations can proceed. Most neutrinos that are produced in the annihilation (or arise due to subsequent processes resulting from the annihilation) easily escape from the interior of the Sun due to the small neutrino interaction cross section. These high energy neutrinos can be detected at dedicated neutrino observatories on Earth, such as Super-Kamiokande [112] or Ice-Cube [113]. The flux of neutrinos depends on the initial spin-dependent or spin-independent dark matter-nucleon scattering cross section[7], so limits can be placed on these cross sections. Indeed, the neutrino signals from the Sun are rather complementary to direct detection experiments as they are able to put much stronger limits on spin-dependent cross sections (for masses above the energy threshold of the neutrino observatory) [114].

1.4.3 Collider searches

Finally, in the era of the Large Hadron Collider (LHC), we consider what information colliders can provide on particle dark matter. For more detailed reviews, see e.g. [115, 116]. Due to the small interaction cross section and long lifetime, dark matter, if produced in a collision, will escape the detector without depositing any energy or momentum. Therefore, the signature of any dark matter particle at a collider will involve missing (transverse) energy and momentum $\not{E}_T$ [117].

Data from the Tevatron, LHC and LEP have been converted into limits on the dark matter-neutron cross section σ_n [118, 119, 120]. These analyses are particularly useful because they are able to explore parameter space where direct detection experiments are less sensitive; for example, for light ($m_\chi \sim$ 1 GeV) particles, particles that couple dominantly to leptons or particles with spin dependent interactions with nuclei.

As an example of how limits are set, we consider the operator

$$\mathcal{O}_V = \frac{g_\chi g_q}{q^2 - M^2} \bar{\chi}\gamma^\mu \chi \, \bar{q}\gamma_\mu q \, , \tag{1.52}$$

which arises from the exchange of a vector mediator of mass M.[8] When the mediator is exchanged in the t-channel and $M \gg q$, we recover the effective operator considered previously (Eq. (1.29)), which can give rise to a signal at a direct detection experiment. This is represented in the left panel of Fig. 1.4. A direct detection experiment effectively puts a bound on the combination $\sqrt{g_q g_\chi}/M$. Similarly, when the mediator is exchanged in the s-channel, we get the production mechanism for

[7]The dominant nucleus in the Sun is hydrogen, a single proton, which has non-zero spin.
[8]The discussion generalises in a straightforward manner for other operators.

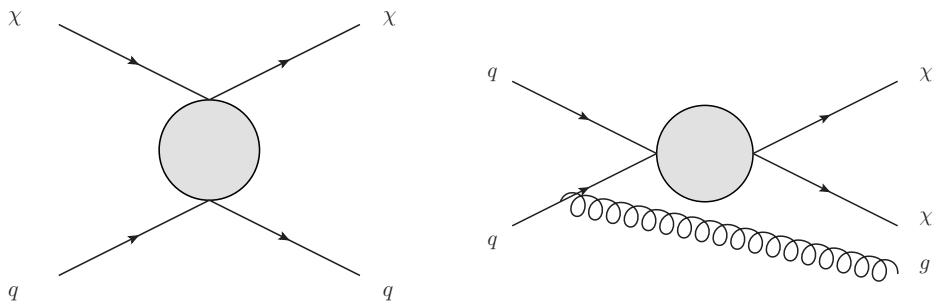

Figure 1.4: Left panel: a typical scattering process at a direct detection experiment. Right panel: production of dark matter and a mono-jet at a collider. The two processes are related by s- and t-channel exchange of a mediator.

dark matter particles at a collider. A signal with only missing energy would not be recorded; a collider needs to trigger on something. Therefore, the case when a photon or gluon (giving rise to a jet) is emitted from one of the initial quarks is used to set limits. Thus, the channels they consider are mono-jet (or mono-photon) plus $\not{E}_T$, represented in the right panel of Fig. 1.4. When $M \gg q$, these collider searches can also be used to put a bound on $\sqrt{g_q g_\chi}/M$. For a vector mediator, this is directly related to the cross section to scatter on a neutron through

$$\sigma_n = \frac{(g_u + 2g_d)^2 g_\chi^2}{M^4} \frac{\mu_{\chi n}^2}{\pi} \,. \tag{1.53}$$

For a model independent statement to be made, it is important that $M \gg q$. At direct detection experiments this is a relatively weak condition since $q \sim 100$ MeV. However, at LEP/Tevatron/LHC, $q \sim 100/100/1000$ GeV respectively. In the case when $M \ll q$ the bounds from colliders can change considerably. If $M > 2m_\chi$ and $q^2 \approx M^2$, the production cross section is resonantly enhanced, while if $M < 2m_\chi$ the production cross section is independent of M. In this case, collider searches place a limit on $g_q g_\chi$ only and since σ_n scales as M^{-4}, for small M, the bound on σ_n is weak.

Unfortunately, data taken solely from colliders will never serve to definitely discover particle dark matter. Particles that live longer than $\sim 10^{-8}$ s (the time it takes to leave the detector) are considered to be 'stable' at the LHC. Thus, there is no way to tell if the particle is stable on cosmological timescales. However, considering data from the LHC in conjunction with direct and indirect searches may help in refining information on the properties of the dark matter. For example, combining experiments may reduce uncertainties on the particle's mass and couplings. Precise measurements of these properties will be crucial in testing the mechanism that is responsible for the dark matter relic abundance.

Chapter 2

Inelastic Dark Matter, Non-Standard Halos and the DAMA/LIBRA Results[1]

Inelastic dark matter (iDM) [122] was proposed as a way to reconcile the positive result from DAMA/NaI with the null result from germanium based detectors. In the iDM scenario, dark matter-nucleon elastic scattering is suppressed, while inelastic scattering from a ground-state dark matter (DM) particle to a slightly higher mass excited particle is allowed and dominates the recoil event rate. As we summarise in Section 2.1, the kinematics of the recoil scattering are changed by the inelastic nature of the collision, and this can bring the DAMA results closer to agreement with the other experiments for three principal reasons:

- Heavier nuclei are favoured.
- The recoil spectrum is changed at low energies.
- The ratio of modulated to unmodulated signal is higher.

Nevertheless the other direct detection experiments still strongly constrain the DM interpretation of DAMA/LIBRA, with, apparently, only a relatively small region of parameter space being allowed [123].

One unchecked assumption that goes into the analysis is that the velocity distribution of the DM in the galactic rest frame is well described by so-called Standard

[1]Two years have passed since the publication of this work. Since then, the XENON and CRESST Collaborations have published significantly stronger exclusion limits [90, 121], which seemingly exclude all of the DAMA regions considered here. Due to the proximity in mass between xenon and iodine nuclei, these new limits suggest that it is unlikely that consistency can be found amongst all experiments, even with more significant deviations of the galactic halo than discussed here.

Halo Model (SHM). The SHM assumes that in the galactic frame the DM distribution is an isotropic isothermal sphere, which leads to an essentially structureless isotropic Maxwell-Boltzmann velocity distribution with dispersion set by the local circular velocity. This is a questionable assumption: Little is known about the phase-space distribution of DM on the scales relevant for direct detection experiments and as we outline in Section 2.2, numerical simulations of DM distributions for Milky-Way-like galaxies lead to results differing from the SHM in potentially significant ways, especially for iDM, which is more sensitive to the DM velocity distribution.

In this chapter, we compare the results obtained using the SHM to those obtained using two recent computer simulations of the DM distribution in a Milky-Way-like galaxy:

- Via Lactea [124] - a Milky Way size DM halo distribution containing 234 million particles.
- Dark Disc [125] - a simulation which contains in addition to the SHM, a slowly rotating disc of DM.

With these less idealised halo models, we find that the iDM scenario allows the DAMA region to be consistent with all other experiments, and that in the Via Lactea distribution, more parameter space can be opened up at high DM masses, compared to the SHM. After reviewing the details of each experiment and describing how we calculate the allowed DAMA region and exclusion curves for the null experiments in Section 2.3, we present our results together with their physical interpretation in Section 2.4.

2.1 Inelastic dark matter

2.1.1 Review of inelastic dark matter

If the dark matter particle can only scatter off nuclei by making a transition to a heavier state, then the altered kinematics of the interaction can lead to significant changes in detection rates for different detectors [122, 123, 126]. If we call the two dark matter states χ_- and χ_+, with mass splitting $\delta \equiv M_{\chi_+} - M_{\chi_-} \sim \mathcal{O}(100\text{ keV})$,

then the minimum velocity to scatter off a nucleus and impart an energy $E_{\rm R}$ is no longer given by Eq. (1.26) but rather by

$$\frac{v_{\rm min}}{c} = \sqrt{\frac{1}{2m_N E_{\rm R}}}\left(\frac{m_N E_{\rm R}}{\mu_N} + \delta\right). \tag{2.1}$$

There are a variety of particle physics models that lead to such phenomenology [122, 127, 128]. The models will not be our concern in this work, rather our focus will be upon the consequences of iDM for direct detection experiments.

In this chapter, we will only be concerned with spin independent scattering. As a result, the differential event rate for DM-nucleus scattering is found by combining Eqs. (1.25) and (1.36), resulting in[2]

$$\frac{dR}{dE_{\rm R}} = \frac{\rho_\chi \sigma_n}{2M_\chi \mu_{\chi n}^2}\frac{(f_p Z + f_n(A-Z))^2}{{f_n}^2}F^2(E_{\rm R})\int_{v_{\rm min}}^{\infty}\frac{f_\oplus(\vec{v},\vec{v}_e)}{v}\,d^3v. \tag{2.2}$$

The local dark matter density ρ_χ is taken as 0.3 GeV/cm^3. The factors f_n and f_p parameterize the relative scattering strength off neutrons and protons. For simplicity and to maintain model-independence we assume that scattering off neutrons and protons is the same and take $f_n = f_p = 1$. (This assumption is not always correct for candidate dark matter particles from specific models). In accordance with [123] we use the Helm form factor for CDMS II, KIMS, XENON10, ZEPLIN-II, and ZEPLIN-III, and the Fermi Two-Parameter form factor for CRESST-II and DAMA/LIBRA. In the left panel of Fig. 2.1 we show the effect of the Helm and Fermi Two-Parameter form factors for scattering off tungsten.

Finally, $f_\oplus(\vec{v},\vec{v}_e)$ is the local velocity distribution of the DM in the Earth rest frame. The default assumption for the dark matter phase space density is the so-called "Standard Halo Model" (SHM), which assumes a local isothermal and isotropic distribution of dark matter leading to a Maxwell-Boltzmann velocity distribution. Changes in this velocity distribution make major differences to the final differential event rate as calculated from Eq.(2.2), especially for iDM. We emphasise that $f_\oplus(\vec{v},\vec{v}_e)$ is poorly constrained by data and not well understood. The primary subject of this work is to investigate the allowed parameter space for iDM taking account of reasonable variations in $f_\oplus(\vec{v},\vec{v}_e)$ motivated by numerical simulations of the DM distribution in our galaxy.

The most important difference between inelastic and standard elastic dark matter is the δ-dependent increase in the minimum relative velocity for scattering with

[2]In this chapter, the DM mass is denoted by M_χ

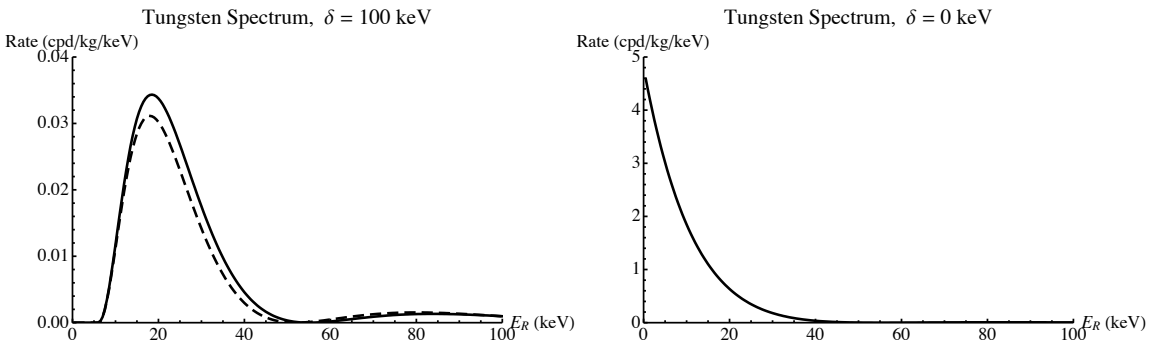

Figure 2.1: The recoil energy spectrum for scattering off tungsten. On the left the inelastic scattering rates are shown for the two choices of form factor: the Fermi Two-Parameter (dashed) and Helm (solid) form factor. Both choices show that iDM leads to a suppression of low-energy events. The right panel shows the recoil energy spectrum for elastic scattering; in this case the difference between the two form factors is negligible. For elastic scattering the recoil spectrum peaks at low $E_{\rm R}$. All calculations assume $M_\chi = 200\,\text{GeV}$, $\sigma_n = 10^{-40}$ cm^2 and $v_{\rm esc} = 500$ km/s.

recoil energy $E_{\rm R}$ (see Eq.(2.1)). The important consequences for direct detection experiments are:

- As only higher velocity portions of the dark matter distribution lead to recoils the overall event rate for a given cross section is lower.

- The spectrum of events is changed, with the greatest qualitative departure from elastic scattering occurring at low energies. As one can see from the left panel of Fig. 2.1 there is a low energy cut off in the recoil spectrum. This is not present for elastic scattering as shown in the right panel of Fig. 2.1.

- Due to the higher minimum velocity, the annual modulation as a fraction of the total signal can be much greater. It is possible that detection of DM occurs solely during the summer months, when the Earth's velocity into the DM wind is greatest, leading to a modulation fraction of 100%. This has important consequences both for DAMA/LIBRA and XENON10.

- As the minimum velocity cut-off, Eq. (2.1), is lower for heavier target nuclei, inelastic scattering leads to higher expected detection rates for heavier elements. This has important consequences for the sensitivity of the CDMS II ($A_{\rm Ge} = 72.64$) and CRESST-II ($A_{\rm W} = 183.84$) experiments.

2.1.2 Overview of consequences of iDM for the various experiments

The minimum velocity for scattering will be much greater for the CDMS II detector compared to DAMA/LIBRA, where the dominant signal is from scattering off germanium and iodine respectively, because germanium is much lighter than iodine. This leads to a weakening of the constraints from CDMS II on the region of parameter space preferred by the DAMA/LIBRA annual modulation signal. In fact for high enough δ the expected rate for CDMS II can be consistent with zero, while still allowing signal at DAMA/LIBRA. The converse effect applies to the CRESST-II experiment, where scattering occurs off tungsten. Here we would expect a higher rate for scattering, which leads to CRESST-II setting the most stringent constraints on the DAMA/LIBRA results.

The three xenon based experiments, XENON10, ZEPLIN-II, and its successor ZEPLIN-III, provide an excellent test of the DAMA/LIBRA results due to the similarity of xenon and iodine masses ($A_{\rm Xe} = 131.293, A_{\rm I} = 126.904$). However the events observed at these detectors lead to consistency with the DAMA/LIBRA preferred region. Also, due to the enhancement of the modulation effect, detectors which took results over the winter period, when signals would be lowest, inevitably set lower constraints than possible if running during the summer months. This applies in particular to the XENON10 experiment. Moreover, the low upper-energy limit (30.2 keV) in the analysed recoil energy spectrum of ZEPLIN-III reduces the sensitivity of this experiment to the iDM scenario, as for a typical δ of 100 keV the xenon recoil spectrum peaks at $\sim$40 keV. We return to the details of the experiments in Section 2.3.

2.2 Dark matter halos

Due to the long range of the gravitational force, and the distribution of matter in our galaxy, one would expect the correct velocity distribution of dark matter particles to deviate from exact Maxwellian and to show some anisotropy. N-body simulations of large numbers of dark matter particles have shown that the SHM may well be incorrect [124, 125].

Here we will consider three models for the local velocity distribution of particles in the dark matter halo. As described in Chapter 1, the Earth's velocity with respect to the galactic rest frame is given by $\vec{v}_e = \vec{v}_\odot + \vec{v}_\oplus$, where $\vec{v}_\odot$ is the Sun's velocity

relative to the galactic rest frame and $\vec{v}_\oplus$ is the Earth's velocity relative to the Sun (Eq. (1.28)). In this chapter we take

$$\vec{v}_\odot = (10.00, 5.23, 7.17) \text{ km/s } + (0, 220, 0) \text{ km/s } . \tag{2.3}$$

One feature common to all of the velocity distributions considered here is that they are truncated at the local escape velocity, $f(|\vec{v}| > v_{\rm esc}) = 0$. There is relatively large error in the known value of the local escape velocity, $498 < v_{\rm esc} < 608$ km/s (90%), with a median of 544 km/s [129]. We have taken $v_{\rm esc} = 550$ km/s in the analysis presented here. In Section 2.4.7 we check that varying $v_{\rm esc}$ between the 90% confidence limits does not change the qualitative features of our results, and therefore the conclusions.

2.2.1 The Standard Halo Model

Details of the Standard Halo Model (SHM) are given in Section 1.2. The velocity distribution is a Maxwell Boltzmann distribution, which in this chapter, we truncate at the escape velocity according to

$$f(\vec{v}) = \begin{cases} \frac{1}{N}[\exp(-v^2/v_0^2) - \exp(-v_{\rm esc}^2/v_0^2)] & v < v_{\rm esc} \\ 0 & v > v_{\rm esc} \end{cases} , \tag{2.4}$$

where $v_0 = 220$ km/s. Combining Eqs. (1.27) and (2.2), we see that the following integral must be performed in $dR/dE_{\rm R}$:

$$g(v_{\rm min}) \equiv \int_{v_{\rm min}}^{\infty} \frac{d^3v}{v} f(\vec{v} + \vec{v}_e). \tag{2.5}$$

In Appendix A we present an analytic expression for $g(v_{\rm min})$ for the SHM velocity distribution, as defined by Eq. (2.4). To the best of our knowledge, this has not previously been presented in the literature.

2.2.2 Via Lactea

Here we use results for the phase space distribution of dark matter in a Milky-Way-like galaxy derived from a simulation containing 234 million particles of dark matter and no baryons; Via Lactea [124] published in 2006.

In [130] the velocity distribution of dark matter particles was fitted to the distribution of individual particles from the Via Lactea simulation [124]. The radial and tangential velocity distributions were fit according to

$$f(v_R) = \frac{1}{N_R} \exp\left[-\left(\frac{v_R^2}{\overline{v}_R^2}\right)^{\alpha_R}\right] \tag{2.6}$$

$$f(v_T) = \frac{2\pi v_T}{N_T} \exp\left[-\left(\frac{v_T^2}{\overline{v}_T^2}\right)^{\alpha_T}\right] \tag{2.7}$$

and the distribution was truncated in the same way as for the SHM. From Fig. 3 in [130] we extracted the values $\alpha_R \approx 1.09$, and $\overline{v}_R/(\sqrt{-U(r_0)}) \approx 0.72$ and $\alpha_T \approx 0.73$, and $\overline{v}_T/(\sqrt{-U(r_0)}) \approx 0.47$ at our radius from the centre of the galaxy, $r_0 \approx 8.5$ kpc. (Although there is uncertainty in our radius from the galactic centre, $r_0 = 8.0 \pm 0.5$ kpc [29], from Fig. 3 in [130] one can see that the values of α_T and $\overline{v}_T$ do not change significantly over the range $7.5 < r_0 < 8.5$ kpc, and the tangential velocity distribution is the main determinant of the event rate). $U(r_0)$ is the gravitational potential.

For completeness we will present results using two values for $\sqrt{-U(r_0)}$. In the Via Lactea halo the average value of $\sqrt{-U(r)}$ between 7 and 9 kpc is 270 km/s;[3] we will refer to results using this value as VL_{270}. Following [130] and in order to allow direct comparison between inelastic and elastic scenarios, we also present results using $\sqrt{-U(r_0)} = 220$ km/s, and refer to these as VL_{220}.

We believe both values for $\sqrt{-U(r_0)}$ are worth studying, given that the Milky Way is baryon dominated at the solar radius, so uncertainties will arise from the lack of baryons in any simulation which contains only dark matter particles. It is also important to remember that the velocity distribution extracted from any DM simulation is for a Milky-Way-like galaxy, and not the Milky-Way itself. Therefore it is important to study the effects of reasonable deviations from results predicted by a simulation.

The deviation from the Gaussian distribution and difference in radial and tangential velocity dispersions have been shown in [130] to affect the expected DAMA/LIBRA modulation signal for elastic dark matter, although not by enough to allow an elastic DM interpretation of the DAMA results.

Due to the smaller tangential velocity dispersion in this model compared to the SHM, one would expect the results for inelastic scattering to be changed for light nuclei. This is because the high minimum velocity for scattering on light nuclei leaves only the high velocity part of the distribution detectable. This smaller velocity dispersion reduces the population of this high velocity region further, leading to a

[3]We thank M. Kuhlen for providing us with this information.

reduced event rate. This effect is particularly interesting as it arises through the combination of iDM and the Via Lactea halo. We discuss this further in Section 2.4.

2.2.3 Dark Disc

Previous simulations of the DM phase space density distribution have modelled the dark matter alone, while at the solar neighbourhood we expect the effects of the baryons, the gas and stars that make up the Milky Way, to be important. Read et al. [125] have performed a series of simulations including the baryons, and have shown that massive satellites, dragged into the disc plane by dynamical friction, are torn apart by tidal forces depositing their stars and dark matter into a thick disc, lying in the same plane as the visible galaxy. Later the influence of this Dark Disc on direct detection of elastic dark matter was examined [131]. Here we investigate the influence of the Dark Disc on iDM detection.

Following [131], we assume the Dark Disc kinematics match the Milky Way's stellar thick disc, whose properties are listed in Table 1 of [125]. This will be a good approximation if the Milky Way's stellar thick disc is mostly composed of accreted, rather than heated stars. We model the Dark Disc as a component of DM additional to the SHM, lagging the rotation of the Sun by 40 km/s in the tangential direction, compared to the SHM which lags by 220 km/s. It is also assumed to have a Maxwellian velocity distribution, with a dispersion of $\vec{\sigma} = (63, 39, 39)$ km/s, and a density in the range $0.5 < \frac{\rho_{\rm Disc}}{\rho_{\rm SHM}} < 2$. We employ these parameter ranges in our study of iDM signals from the Dark Disc.

Due to the smaller relative velocity of the Dark Disc with the Earth, when compared with the SHM, one would expect Dark Disc event rates to be low for high δ as the Dark Disc particles may not have high enough velocity to cross the minimum velocity threshold.

2.3 Experimental information

We now turn to a detailed discussion of the individual direct detection experiments.

2.3.1 DAMA/LIBRA

As the Earth revolves around the Sun, there should be a larger flux of DM in the forward direction incident on the detector around the 2nd June, when the relative velocity of the Earth is at a maximum with respect to the galaxy. Conversely, the

flux incident on the detector should be smallest around the 2nd December when the relative velocity of the Earth is at a minimum with respect to the galaxy. It is the annual modulation in the recoil event rate caused by this velocity modulation that the DAMA collaboration claim to have measured.

The first results from the DAMA/LIBRA set-up, with an exposure of 0.53 ton-yr, have recently been published [76]. These have been combined with the data collected by the DAMA/NaI set-up to give an impressive 0.82 ton-yr total exposure, yielding a modulation signal at 8.2 σ C.L.

For a DM mass $M_\chi > 10$ GeV, this signal appears to be in conflict with other experiments under the assumptions of spin independent, elastic DM-nucleon scattering, with the DM phase space distribution described by the SHM. This has prompted a number of alternative explanations: light DM [132, 133, 134, 135, 136, 137, 138, 139], spin dependent interactions [140], mirror dark matter [141, 142] and iDM [122].

2.3.1.1 Quenching and channeling

DAMA use highly radio-pure NaI(Tl) scintillators as their target material. The light yield of scintillators depends on whether the recoiling nucleus interacts electromagnetically or via the strong nuclear interaction, since only electromagnetic interactions will produce photons. As a result, the measured energy, $E_{\rm M}$, is different from the recoiling energy of the nucleus. This difference is expressed by the quenching factor q defined by $E_{\rm M} = qE_{\rm R}$. We will follow the convention of measuring $E_{\rm R}$ in keV, and $E_{\rm M}$ in keVee (keV electron equivalent). The DAMA collaboration have measured the quenching factor for iodine and sodium for their NaI(Tl) crystals. They obtained the values $q_{\rm Na} = 0.3$ and $q_{\rm I} = 0.09$ [143] with an error of 0.01 on the value of $q_{\rm I}$.[4] Following the analysis of Ref.[123], in our calculations, we use $q_{\rm Na} = 0.3$ and $q_{\rm I} = 0.085$, however in Section 2.4.5 we investigate what effect varying $q_{\rm I}$ within the experimental limits has on our results.

If the nucleus recoils along certain directions in a crystalline structure, and if the recoiling energy is low, no nuclear interactions occur, so the quenching factor, q, equals one. This effect is known as channeling [144]. Since NaI(Tl) is a crystalline material,

[4]The error on $q_{\rm I}$ is from `http://people.roma2.infn.it/~dama/web/nai_que.html`.

we need to include this effect in our calculations. We use the parameterisation given in [130] for the fraction f of channeled events relevant for DAMA[5]

$$f_{\rm Na}(E_{\rm R}) \approx \frac{e^{-E_{\rm R}/18}}{1+0.75E_{\rm R}}, \qquad f_{\rm I}(E_{\rm R}) \approx \frac{e^{-E_{\rm R}/40}}{1+0.65E_{\rm R}}. \tag{2.8}$$

2.3.1.2 Calculating best fit regions

DAMA have released their binned data from the combined DAMA/LIBRA and DAMA/NaI data sets covering the range 2-20 keVee. A clear modulation signal is present below about 8 keVee, while the modulation is consistent with zero at higher energies [76]. The rate in the lowest energy bin, covering the range 2-2.5 keVee, is smaller than in the next bin, covering the range 2.5-3 keVee, suggesting that the rate is falling to zero at low energies. While care should always be taken when examining the data at the edges of the experimental sensitivity, it should be noted that both of these features are found naturally with inelastic scattering.

We use a χ^2 goodness of fit test to analyse the DAMA results. We construct a χ^2 function using the twelve 0.5 keVee width bins between 2.0 - 8.0 keVee and their relative uncertainties. We do not fit to the higher energy bins because, as mentioned above, the inelastic spectrum falls off at high energies.

In our 2D plots, we find the best fit point by minimising the χ^2 function for the two unconstrained parameters, either σ_n and M_χ, or σ_n and δ. For a goodness of fit, we require that the best fit point have $\chi^2_{\rm min} < 10$, given that we have 12 bins and 2 free parameters. Allowed regions at a given confidence limit are obtained by looking for contours $\chi^2 = \chi^2_{\rm min} + \Delta\chi^2$, where $\Delta\chi^2 = 4.61$ or 10.60 for 90% and 99.5% confidence limits respectively.

DAMA have also released the unmodulated rate for a single-hit scintillation as measured by DAMA/LIBRA. Dark matter is expected to scatter no more than once, so we are using the rest of the detector as a veto. No other background subtraction is applied. We can use this data to set a limit by requiring that the calculated unmodulated rate not be larger than the measured rate across the energy range shown in Fig. 1 of [76].

It should be noted that we have not included the effect of the finite energy resolution of the detector in our calculations. We are fitting to the modulated rate from the combined data sets of DAMA/LIBRA and DAMA/NaI, however the energy resolution for DAMA/LIBRA and DAMA/NaI are known to be different [146, 147].

[5]More recently, it has been shown that the expected fraction of channeled events is much smaller than the estimate used here [145]. However, channeling has almost no effect on any of our results.

2.3.2 Null experiments

In this section, we discuss the data used in calculating the regions excluded at 90% confidence level by other direct detection experiments. We adopt a conservative approach and include events that the experiments ascribe to background processes when setting limits. We will find that the most constraining experiment is CRESST-II. Unless otherwise stated, we use the 'p_{max} method' [148], to set our limits. This method has the advantage of setting similarly strong limits as the 'optimum interval method', but is easier to implement. A discussion of how exclusion limits are calculated can be found in Appendix B. Care should be taken when comparing exclusion curves at 90% confidence level and the region allowed by DAMA at 90% confidence limit, since we are using different statistical methods in evaluating them. In calculating the total event rate, we integrate the differential rate over the energy range of the experiment, then find the average value over the running dates given by the collaboration, and finally, we multiply by the exposure. As a final check of our methods, we have reproduced the published exclusion curves from CDMS II and XENON10 in the $\delta = 0$ keV limit.

2.3.2.1 CDMS II

In setting the limits for CDMS II, we use the three runs from the Soudan Underground Laboratory which were sensitive to nuclear recoil energies between 10-100 keV [149, 150, 79]. We only consider scattering from germanium as scattering off silicon is highly suppressed. The published effective germanium exposures are weighted for a DM mass of 60 GeV and averaged over recoil energies 10-100 keV, however these numbers are expected to apply for iDM since their acceptance efficiency is fairly constant over their energy range. The first run took place from 11th October 2003 to 11th January 2004, had an exposure of 19.4 kg-day and saw one event at 64 keV [149]. The second run was from 25th March 2004 to 8th August 2004, had an exposure of 34 kg-day and saw one event at 10.5 keV [150]. The latest five-tower run was between October 2006 and July 2007, had an exposure of 121.3 kg-day and saw no events [79].

2.3.2.2 CRESST-II

For the CRESST-II limits, we use data collected by the Julia and Daisy detectors [151] between 31st January 2004 - 23rd March 2004, and the Verena and Zora detectors [83] between 27th March 2007 - 23rd July 2007. We only consider scattering off the tungsten atoms in the $CaWO_4$ crystals, and include events on or beneath the curve

where 90% of the tungsten recoils are expected. The Julia detector had a tungsten exposure of 6.26 kg-day and we include the four observed events between 10 - 50 keV and an unpublished event above 50 keV[6]. The Daisy detector had a tungsten exposure of 6.84 kg-day and we include the two events between 10-12 keV, the event which lies on the curve where 90% of the tungsten recoils are expected, at approximately 22 keV, the event at approximately 45 keV, and a second unpublished event above 50 keV[6]. The Verena and Zora detectors had a combined tungsten exposure of 30.6 kg-day and we use the seven published events between 10 - 100 keV. To take into account the difference in energy regions, we do not integrate above the energy of the extra events for the Daisy and Julia detectors.

Note that following [123] we have set limits by including the Daisy point which lies on the tungsten curve at 22 keV in Fig. 9 of Ref.[151]. If we redo the analysis by ignoring this point and only including data which lie fully below the curve, we find that CRESST-II just manages to exclude all of the DAMA/LIBRA 99.5% allowed region. This point has such a large impact on the limits set using the 'p_{max} method' because it lies at the peak of the recoil energy spectrum, as can be seen in the left panel of Fig. 2.1.

This shows us that with further data, the CRESST-II experiment has the ability to completely exclude the DAMA/LIBRA region.

2.3.2.3 KIMS

From the null experiments we consider, KIMS [152] is the only one where scattering occurs off iodine, in the CsI(Tl) crystals they employ. Two of the crystals collected experimental data between June 2005 and March 2006, then another two crystals were installed, running between December 2005 and March 2006.[7] In setting limits, we find the average rate and statistical error from the four crystals, and require the calculated rate to be less than the measured rate plus 1.64 times the error in the first five bins, corresponding to the energy range 3-8 keVee. For the quenching factor, we use the parameterization

$$q_{\mathrm{CsI(Tl)}}(E_{\mathrm{R}}) \approx \frac{0.175e^{-E_{\mathrm{R}}/137}}{1+0.00091E_{\mathrm{R}}}. \tag{2.9}$$

This function fits the curve shown in Fig. 13 of [153] to a good accuracy.

[6]Data point provided by H. Kraus. We include it for completeness but it has little effect on our exclusion limits as the expected rate is very small at this energy (see Fig. 2.1).

[7]We thank H. S. Lee for providing us with the KIMS running times.

2.3.2.4 XENON10

XENON10 [154] is a liquid xenon based experiment which ran from 6th October 2006 until 14th February 2007 and had an effective exposure of 316.4 kg-day. In calculating our limits, we include the 10 events used in their analysis in the range 4.5 - 26.9 keV, as well as the 14 events in the range 26.9 - 45 keV. Below 26.9 keV, we use the published acceptances and above 26.9 keV we use the known software cut efficiencies and assume a constant nuclear recoil acceptance of 0.45.[8]

2.3.2.5 ZEPLIN-II

We include only the limits from ZEPLIN-II [155] since ZEPLIN-I [156] is not competitive with the other experiments we consider [123]. ZEPLIN-II is another xenon based experiment with an effective exposure of 225 kg-day and was assumed to run between May and July 2006.[9] In total, 29 events were observed in the range 5 - 20 keVee, which corresponds to a range of 13.9 - 55.6 keV if the published quenching factor $q = 0.36$ is used. In calculating our limits, we use the published efficiencies and we take all observed events as signal.

2.3.2.6 ZEPLIN-III

We also include the first results from the ZEPLIN-III experiment [92], the successor to ZEPLIN-II. ZEPLIN-III is also xenon based and improves on the limits set by ZEPLIN-II as only 7 events were observed, in the range 10.7 - 30.2 keV. The effective exposure was 126.7 kg-day, the data being collected between 27th February 2008 and 20th May 2008. Using Fig. 15 of [92], we extract an approximate quenching factor parameterization:

$$q_{\rm Xe}(E_{\rm M}) \approx (0.142E_{\rm M} + 0.005)\exp[-0.305(E_{\rm M})^{0.564}]. \tag{2.10}$$

We extracted the energies of the 7 observed events from Fig. 12 of [92] and converted to nuclear recoil energies using the above quenching factor.

2.4 Results and discussion

In this section we present our results for iDM in the context of the different halo models.

[8] We thank K. Ni for providing us with this information.

[9] These dates are taken from `http://pppa.group.shef.ac.uk/dm/zeplin2.php`.

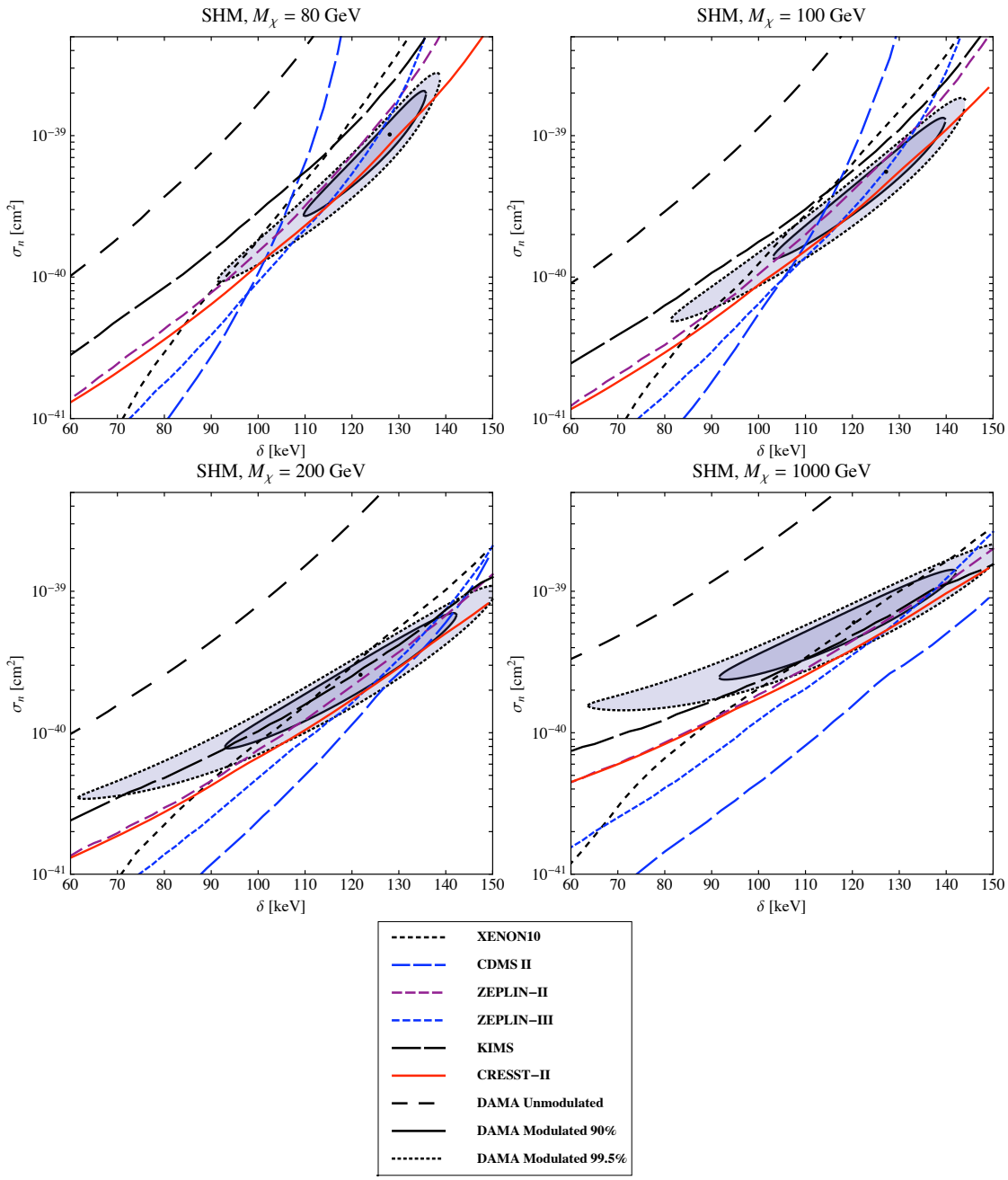

Figure 2.2: Here we show the variation in the exclusion limits set by the experiments as δ is varied and M_χ is held constant. These limits are calculated using the SHM. The preferred region of parameter space for the DAMA results is shown at 90% and 99.5%, and the DAMA best fit point is plotted with a dot. As one can see there is a small region of agreement between all experiments for low masses and $\delta \sim 130$ keV. At higher masses both CRESST-II and CDMS II exclude the DAMA results and the region of agreement with the other experiments is greatly reduced.

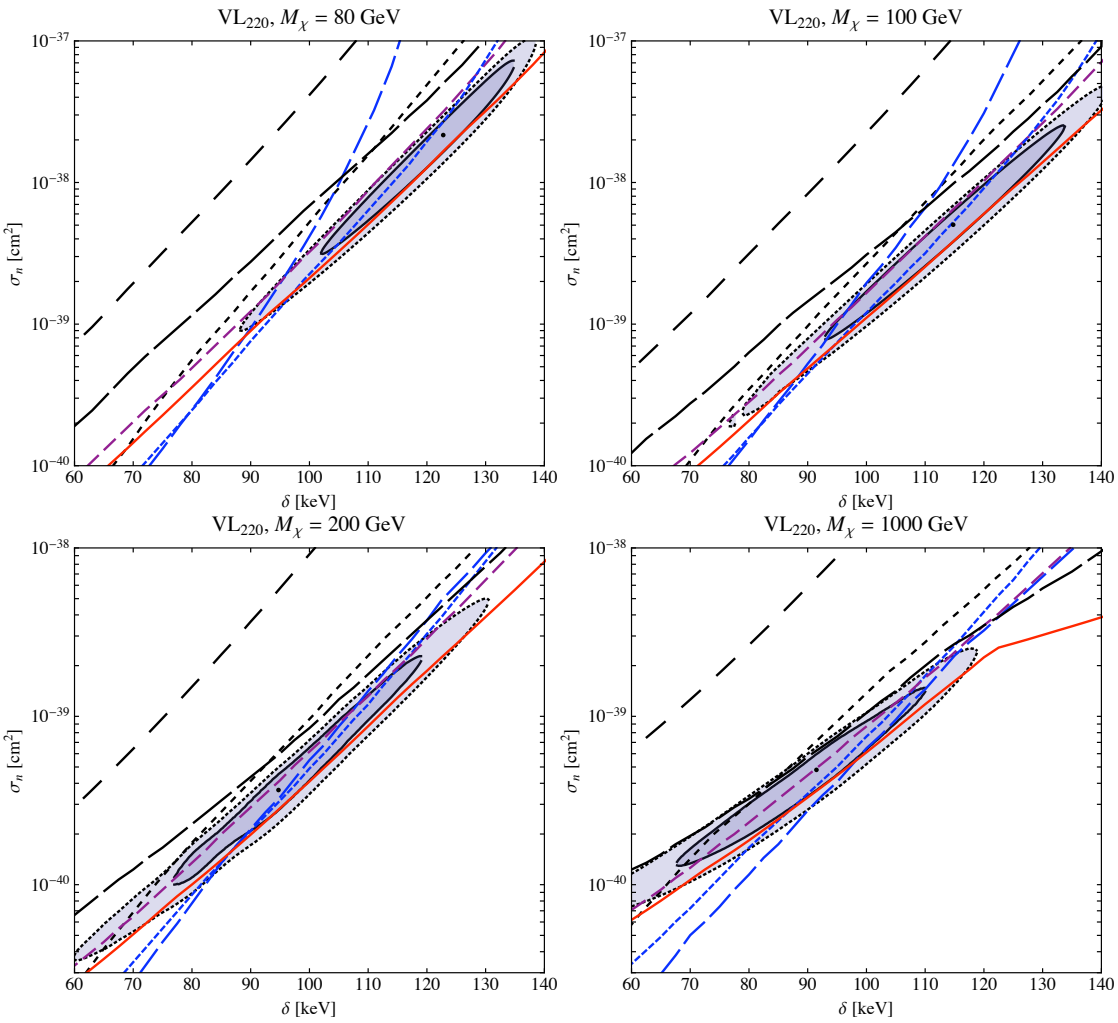

Figure 2.3: Change in limits when the SHM is replaced by the VL_{220} halo, cf, Fig. 2.2. At low masses there is a smaller region of agreement between CRESST-II and DAMA, with CRESST-II almost excluding DAMA at the 90% level over all masses. At high masses, however, CRESST-II and CDMS II are significantly less constraining on the DAMA region than for the SHM, this can be seen by comparing the bottom right panels of both figures. One can also see that the typical cross sections are an order of magnitude higher for the VL_{220} halo at low masses than for the SHM (note also that the lower panels have a different scale for the cross section).

2.4.1 VL_{220} vs SHM

In Figs. 2.2 and 2.3 we present a comparison of the iDM limits on the DAMA/LIBRA preferred region under the assumptions of the SHM and the VL_{220} halo, for a variety of DM masses.

As one can see the allowed cross section limits are generally higher for the VL_{220} halo than the SHM. Also the CRESST-II results are slightly more constraining on

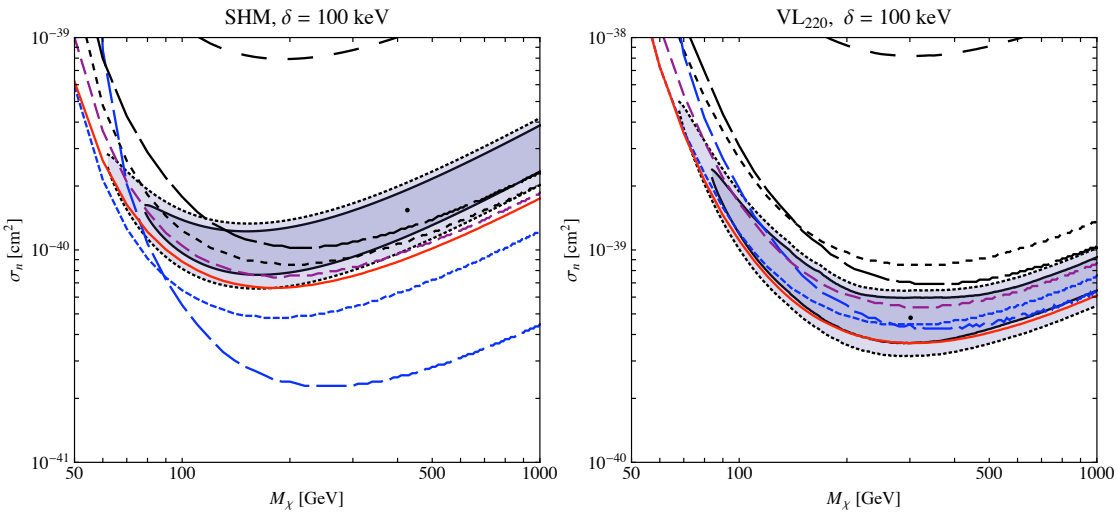

Figure 2.4: The allowed parameter space for fixed $\delta = 100$ keV and varying M_χ. For the SHM (left panel) and this value of δ, CDMS II excludes the DAMA region at 90%. For the VL$_{220}$ halo (right panel) the tightest constraints are set by CRESST-II, and there is agreement between DAMA and CDMS II up to high DM masses. Again one can see that the typical allowed cross sections are an order of magnitude higher for the VL$_{220}$ halo.

the DAMA/LIBRA preferred region at low mass when the VL$_{220}$ halo is used. The most interesting feature to note is that all of the experiments show less disagreement with the DAMA/LIBRA region at high DM masses when the VL$_{220}$ halo is used. This feature is most prominent for the CDMS II exclusion line, but is true for all experiments to some degree.

This feature is made more explicit by observing how the limits change as a function of M_χ for fixed δ. In Fig. 2.4 we show the exclusion limits for $\delta = 100$ keV and 50 GeV $< M_\chi <$ 1000 GeV.

In this case all experiments are less constraining on DAMA/LIBRA at high mass, however the CDMS II limits completely rule out the entire DAMA/LIBRA preferred region under the assumptions of the SHM, yet for the VL$_{220}$ halo there is agreement up to $M_\chi \sim \mathcal{O}$(TeV). This can be explained by a combined effect of iDM and the VL$_{220}$ velocity distribution, as noted in Section 2.2.

Looking quantitatively at this effect we can take the example of germanium in the CDMS II detector. As the inelasticity has pushed the minimum velocity up significantly we need only consider the tangential velocity distributions (in the Earth's frame), as they are centred around $v_{\rm circ} \sim 220$ km/s whereas the radial velocity distribution is centred around $v_{0r} \sim 0$ km/s. Therefore the high velocity components scattering on the germanium will be from the tangential component of the halos.

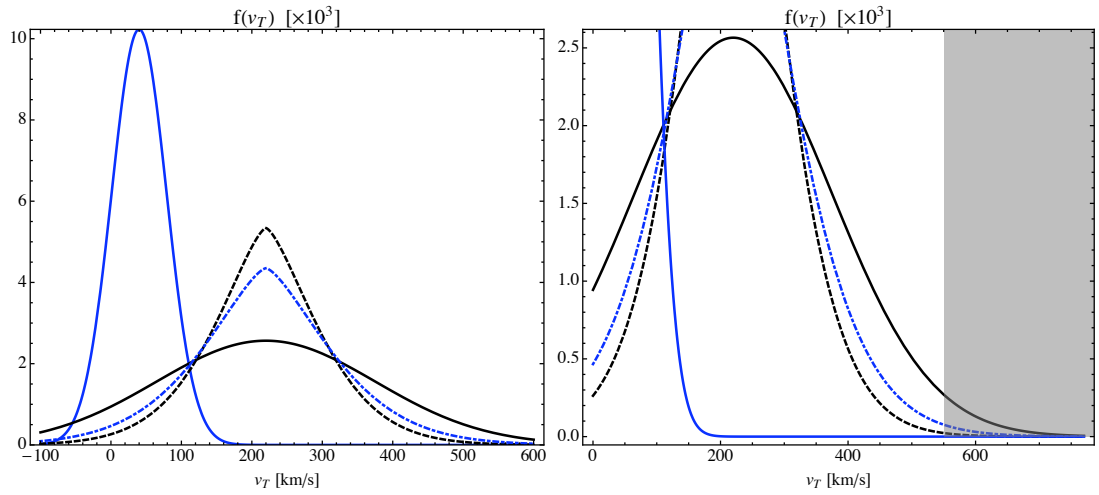

Figure 2.5: Left Panel: Tangential velocity distributions in the Earth rest frame. The solid black and blue lines show the SHM and Dark Disc distributions and the dashed and dot-dashed lines show the VL_{220} and VL_{270} distributions respectively. The Dark Disc distribution is peaked at 40 km/s. Right Panel: Detectable particle distributions in a germanium detector as a function of tangential velocity. The detectable region is shaded in grey. The left edge of the grey region corresponds to $M_\chi = 500$ GeV.

The CDMS II detector is sensitive to the energy range 10 keV $< E_\mathrm{R} <$ 100 keV, and if we consider 50 GeV $< M_\chi <$ 500 GeV, then for $\delta = 100$ keV the minimum velocity lies in the range 550 km/s $< v_\mathrm{min} <$ 1006 km/s. As the escape velocity is taken as $v_\mathrm{esc} = 550$ km/s in the halo rest frame, then the highest velocity particles observed in the Earth's frame have $v_\mathrm{max} \sim 770$ km/s. Therefore the observable particles will have velocities 550 km/s $< v_\mathrm{obs} <$ 770 km/s. In Fig. 2.5 we plot the two different tangential velocity distributions and the region over which v_min varies as M_χ is increased.

As one can see the detectable particle number in the SHM distribution grows significantly as M_χ is increased and v_min decreases, leading to stronger limits on the cross section from the CDMS II results. However, for the VL_{220} distribution this growth in the number of detectable particles is not nearly as pronounced, due to the reduced width of the distribution, and this leads to much slower variation in CDMS II exclusion limits as M_χ is varied, and overall to much weaker limits than from the SHM. As stated above this effect is due to the combination of iDM, which increases the minimum velocity relative to elastic scattering, and the VL_{220} velocity distribution, which is much smaller than the SHM at high velocities.

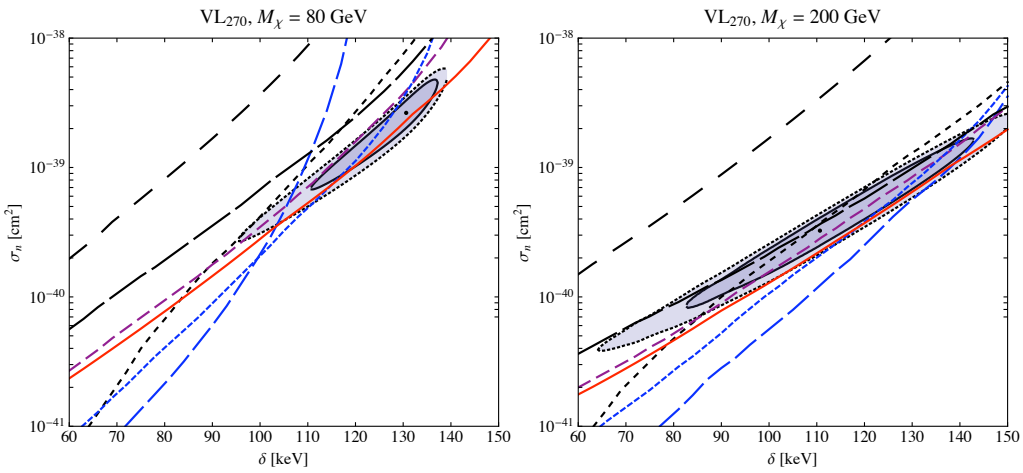

Figure 2.6: Exclusion limits for VL_{270}. These results are similar to those presented in Fig. 2.2. We see that there are still allowed regions of the DAMA parameter space at the 90% confidence level for DM masses lower than 200 GeV and $\delta \sim 130$ keV, however these typically occur at larger cross sections than in Fig. 2.2.

2.4.2 VL_{270} vs SHM

In Figs. 2.6 and 2.7, we present the exclusion limits for VL_{270}. Comparing Fig. 2.6 with Figs. 2.2 and 2.3, and Fig. 2.7 with Fig. 2.4, we see that although the exclusion limits from VL_{270} typically occur at a larger cross section than the SHM, the DAMA allowed region is much closer to that from the SHM than VL_{220}.

With reference to Fig. 2.5, we see that the departure from the SHM velocity distribution is greater for the VL_{220} distribution compared to the VL_{270} distribution, particularly in the high velocity region. However, the tail of the distribution is still much less populated in VL_{220} and VL_{270} compared to the SHM, which explains why the exclusion limits for VL_{220} and VL_{270} typically occur at larger cross sections than for the SHM. The increased population in the VL_{270} tail, relative to the VL_{220} tail, and the small change in particle numbers over the region of $v_{\rm min}$ of interest leads to stronger exclusion limits at high DM masses compared to VL_{220}. This shows that even a small change in the dispersion can lead to relatively large changes in allowed parameter space.

2.4.3 The Dark Disc and iDM

In Fig. 2.8 we plot the exclusion limits as a function of δ for the SHM and SHM + Dark Disc. As a fiducial choice we have taken $R = \frac{\rho_{\rm Disc}}{\rho_{\rm SHM}} = 1$.

One can immediately see that the Dark Disc only influences the limits at very low δ. Increasing the density of the Dark Disc will change the limits at low δ but not

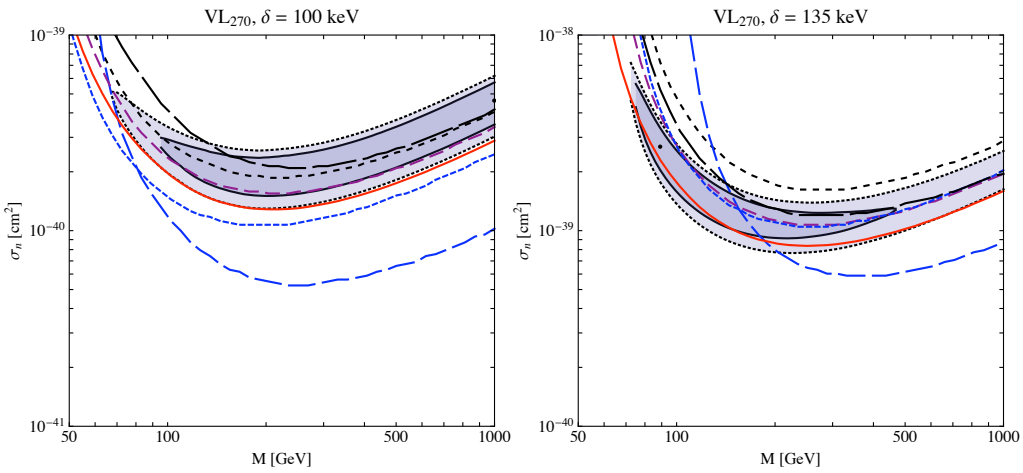

Figure 2.7: The allowed parameter space for fixed $\delta = 100$ keV and $\delta = 135$ keV while varying M_χ. Comparing with Fig. 2.4, we see that these results are similar to those obtained for the SHM, the difference being that the exclusion curves are typically at larger cross sections. While all of the DAMA parameter space is excluded at $\delta = 100$ keV (the right panel), there is clearly some allowed parameter space at $\delta = 135$ keV (the left panel) for DM masses less than 200 GeV.

the value of δ at which the disc is detectable. The fact that the Dark Disc is not detectable at high δ is due to the increased minimum velocity required for scattering. As the disc lags the motion of the Sun by 40 km/s, and has velocity dispersion of 39 km/s in the tangential direction, 99% of disc particles will only have a relative velocity up to $v_{DD} \sim 135$ km/s. If the minimum velocity for scattering is above this the Dark Disc will have little effect on event rates. This effect is demonstrated in Fig. 2.9.

One can see that for heavier DM masses the effect of the Dark Disc would increase, but would still only be found for $\delta < 20$ keV. These results would suggest that possible sub-halo components which are rotating roughly in the same way as the visible galactic plane would have little or no effect on inelastic scattering event rates, whereas the effect on elastic scattering rates should be pronounced. This effect could have interesting consequences for clumpy dark matter.

2.4.4 Discussion

Variations in the regions of parameter space consistent with all experiments in Figs. 2.2, 2.3 and 2.6 show that precise statements about the consistency of DAMA/LIBRA with other direct detection experiments depend sensitively on the precise details of the velocity distribution of the DM in our galaxy. Since the solar

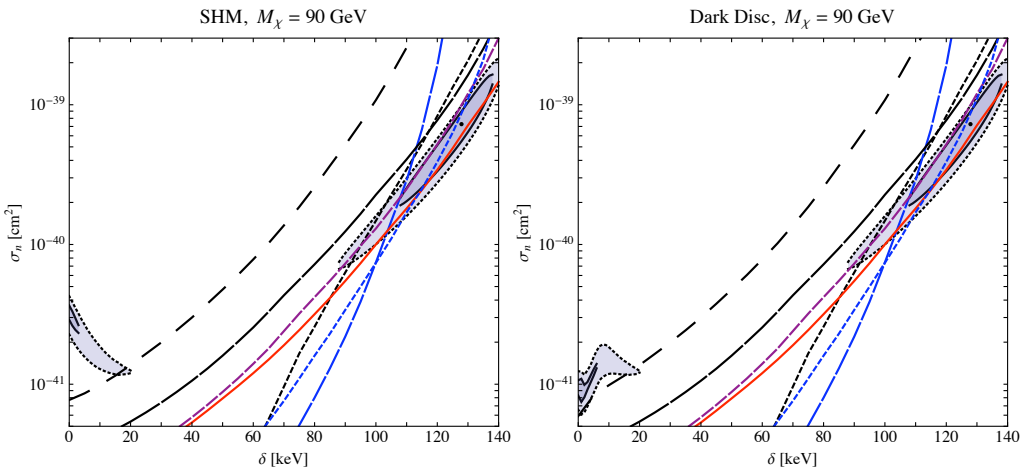

Figure 2.8: Exclusion limits for the SHM (left panel) and the SHM + Dark Disc (right panel) for a DM mass of 90 GeV. The only major differences occur at relatively low δ where one can see the region corresponding to DAMA channeled events is deformed when the Dark Disc is included. However, this region of parameter space is completely excluded by the other experiments.

neighbourhood is baryon dominated we would expect the DM velocity distribution to be influenced by the effect of baryons. Although the Dark Disc simulation is an important first step in this direction, since it looks at one possible effect of the baryons, in this case the velocity distribution of the halo is taken to be the SHM with an added Maxwellian component, as opposed to a velocity distribution resulting from a cosmological simulation with baryons and dark matter included from the outset. As this added Dark Disc component contributes negligibly to iDM scattering in the region of parameter space of interest, the limits set for iDM are identical for the SHM and SHM + Dark Disc scenarios. Therefore this uncertainty will remain until such a time when the velocity distribution resulting from a cosmological simulation with baryons included is obtained. Also, we emphasise again that any velocity distribution obtained from a simulation will have an inherent uncertainty since it is a Milky-Way-like galaxy, and not the Milky Way itself.

In light of recent results from the indirect detection experiments PAMELA [157] and ATIC [158], it is interesting to note that with the VL220 velocity distribution, the DAMA region is consistent with DM masses $M_\chi \sim 1$ TeV, as shown in Figs. 2.3 and 2.4. In the context of the SHM, regions of agreement between DAMA/LIBRA and other experiments only exist at DM masses too small to allow a DM annihilation interpretation of the ATIC results. For the VL220 distribution this may be possible and models attempting to explain the DAMA/LIBRA, PAMELA and ATIC anomalies may be consistent with experiment.

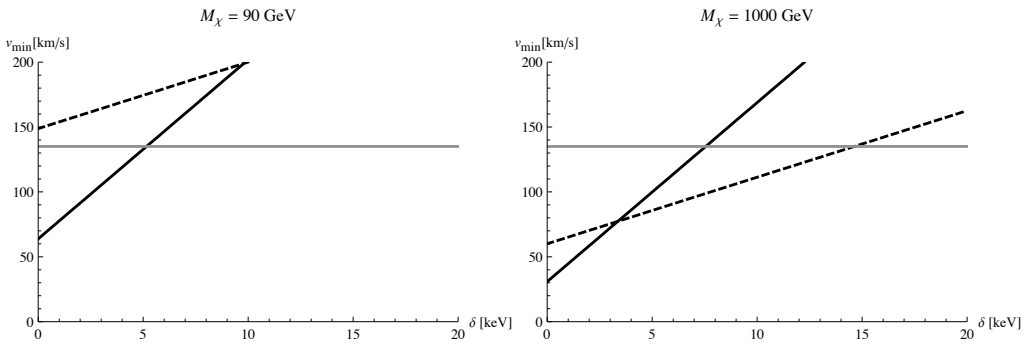

Figure 2.9: The minimum velocity for scattering at CRESST-II (dashed) and DAMA (solid). The velocities are calculated using Eq. (2.1) and taking the experimental energy threshold. The DAMA line corresponds to channeled scattering and the grey line is roughly the maximum velocity at which the Dark Disk particles would be found. For $\delta \geq 15$ keV very few particles in the Dark Disc will scatter.

As our analysis has been purely phenomenological, keeping M_χ, σ_n and δ as free parameters, comparison with specific models of iDM is possible, however a detailed analysis of any specific model is beyond the scope of this work.

2.4.5 Iodine quenching factor

The iodine quenching factor is $q_{\rm I} = 0.09 \pm 0.01$.[10] As changing the value of the quenching factor will stretch the recoil spectrum as a function of recoil energy it is interesting to see what effect varying the quenching factor has on the DAMA/LIBRA preferred region of parameter space, and whether this strongly influences the agreement with other experiments. The effect of this variation is illustrated in Fig. 2.10.

As one can see, the overall effect can be significant, and the DAMA/LIBRA preferred region can shift by a relatively large amount. For the lower quenching factor there is a region of agreement between all experiments at the 90% confidence level, whereas for the higher quenching factor there is disagreement between DAMA/LIBRA and the CRESST-II and CDMS II experiments at almost a 99.5% level for the SHM.

As this effect is so pronounced it would be interesting if the DAMA collaboration are able to put tighter bounds on the quenching factors in their experiment. For elastic scattering the uncertainty is not so significant as it is the channeled event regions where $q_{\rm I} = 1$ that show best agreement with the other experiments. However, as inelastic scattering finds greatest agreement for the region of parameter space

[10] This value and error are quoted on `http://people.roma2.infn.it/~dama/web/nai_que.html`.

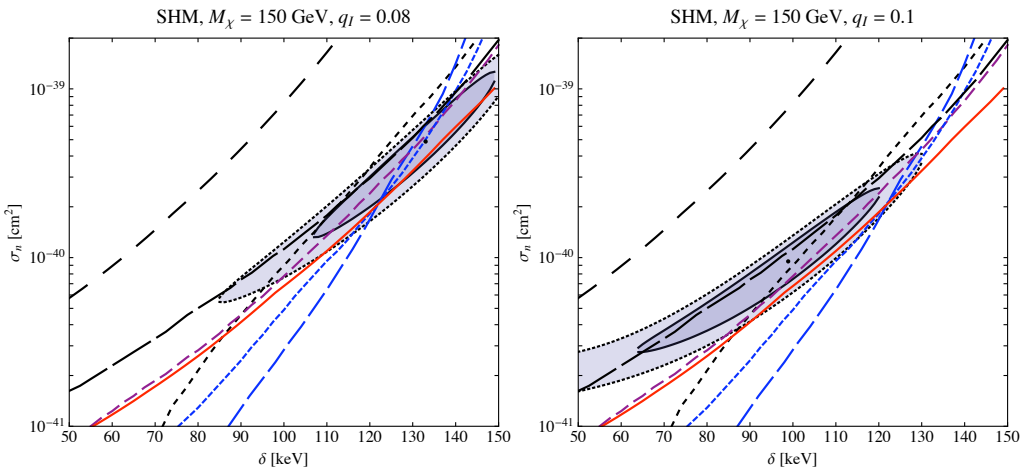

Figure 2.10: The exclusion limits with an iodine quenching factor of $q_{\rm I} = 0.08$ (left panel) and $q_{\rm I} = 0.1$ (right panel), for a DM mass of 150 GeV and using the SHM. One can see that the preferred region of parameter space for the DAMA results can move by $\Delta(\delta) \sim 30$ keV and $\Delta(\sigma_n) \sim 5 \times 10^{-40}$ cm^2, leading to agreement with or exclusion by the other experiments.

corresponding to quenched events, the value of the quenching factor is of much greater importance.

2.4.6 Circular velocity

In [29] the Sun's circular velocity about the centre of the Milky Way is given as $v_{\rm circ} = 220 \pm 20$ km/s. In the iDM scenario, the majority of observed events are expected to be from scattering off DM at the high end of the tangential velocity distribution, so it is expected that varying the circular velocity will have an effect on the exclusion limits set by detectors. In Fig. 2.11 we plot the exclusion curves for DM of mass $M_\chi = 125$ GeV for $v_{\rm circ} = 200, 240$ km/s.

As expected this variation does affect the exclusion limits, however there is little overall change in the qualitative features. Unlike with the Dark Disc this variation occurs over all ranges of δ. Due to the enhancement of the signal, through increasing the number of particles with $v > v_{\rm min}$, increasing the circular velocity of the Sun generally leads to marginally stronger upper limits on cross sections for iDM.

2.4.7 Local galactic escape velocity

The RAVE survey have measured the escape velocity to lie within the range $498 < v_{\rm esc} < 608$ km/s at 90% confidence [129]. In this chapter, we have taken the fiducial value $v_{\rm esc} = 550$ km/s, however the experiments are only sensitive to the

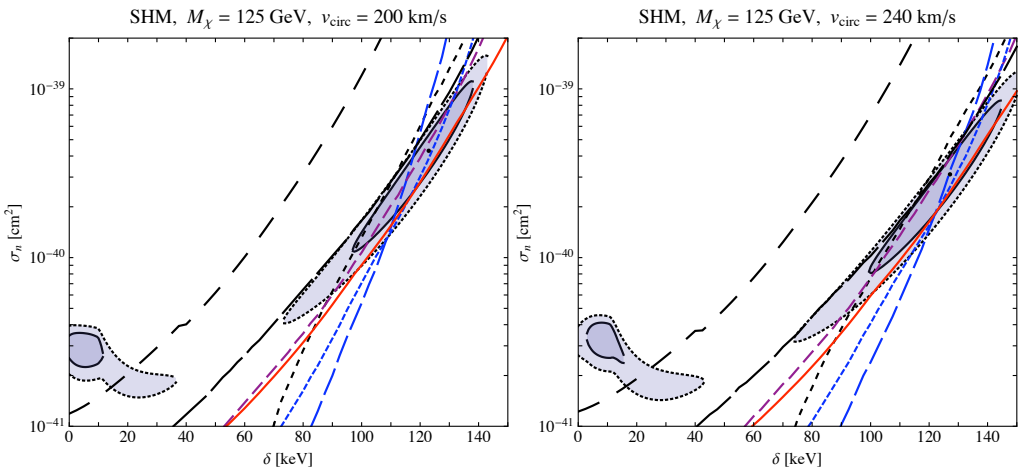

Figure 2.11: The exclusion limits for a local circular velocity of $v_{\rm circ} = 200$ km/s (left panel) and $v_{\rm circ} = 220$ km/s (right panel), for DM of mass 125 GeV and using the SHM. One can see that the limits change a small amount and that the overall agreement with the DAMA results is slightly better for a lower circular velocity. However, the overall qualitative effect of changing the circular velocity is relatively small.

tails of the velocity distribution, which depend on the escape velocity. In Fig. 2.12 we illustrate what the effect of varying the escape velocity within the range allowed by the RAVE survey has on the experimental limits.

The limit which shows the largest change is from CDMS II, although all experimental limits show some variation, particularly at lower masses. This effect can be understood with reference to Fig. 2.5. At lower masses, the minimum velocity is closer to the escape velocity, therefore for lower escape velocities, the range of integration is smaller, hence the limits are weaker. At higher masses, the relative change in varying the escape velocity is lower because the range of integration is larger, so the difference for all experiments is smaller.

2.5 Conclusions

We have shown, in the context of iDM, that the region of agreement between the DAMA data and results from other experiments is sensitive to the uncertainties present in the galactic DM velocity distribution. In particular we have found that the other direct detection experiments, including the most recent ZEPLIN-II and III, CRESST-II, XENON10, KIMS, and CDMS-II data sets, do not exclude the region of parameter space preferred by the DAMA results up to DM masses $M_\chi \sim 1$ TeV when the VL_{220} velocity distribution is used (see Figs. 2.3 and 2.4), while for the VL_{270} velocity distribution, DM masses $M_\chi \leq 200$ GeV are allowed (see Figs. 2.6 and 2.7).

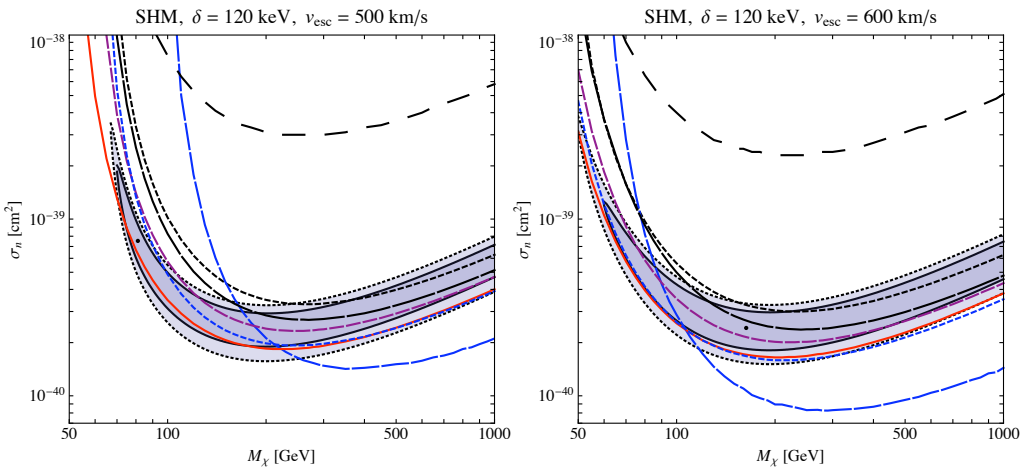

Figure 2.12: Exclusion limits for the SHM for $v_{\rm esc} = 500$ km/s (left panel) and $v_{\rm esc} = 600$ km/s (right panel). There is better agreement between experiments for lower escape velocity and the limits from CDMS II show the most sensitivity to $v_{\rm esc}$.

Furthermore, we have also argued that the region of agreement between experiments is very sensitive to the quenching factor used to interpret the DAMA data (see Fig. 2.10), and also to the local galactic escape velocity (see Fig. 2.12), both of which presently have $\sim$10% uncertainties, and somewhat to the Sun's circular velocity (see Fig. 2.11).

Independent of experimental set-ups we have also shown that, in the iDM scenario, detectors would be insensitive to DM traveling with a small velocity relative to the Sun due to the increased minimum velocity for scattering. This would lead to dark matter clumps or streams being undetectable if rotating in the galactic plane, as in the Dark Disc halo model, or streaming with a small relative velocity (see Fig. 2.8).

New data from heavy element experiments such as CRESST-II and XENON100 could have the potential to completely exclude the DAMA preferred region for iDM, especially if taken during the modulation maximum. In particular, if the planned EURECA experiment were to use a tungsten detector it would provide significant limits on both the elastic and iDM scattering cross sections. Furthermore because of the low energy cut-off in the recoil energy spectrum for iDM, it is important that the experiments increase their sensitivity at higher recoil energies, where the iDM recoil spectrum peaks.

Without a better understanding of the details of the velocity distribution in our galaxy, including the effects of the baryons, precise statements about the consistency of various direct detection experiments are not possible.

Chapter 3

The Astrophysical Uncertainties Of Dark Matter Direct Detection Experiments

As well as depending on particle physics models, the recoil spectrum and scattering rate at dark matter (DM) direct detection experiments depend on the astrophysical parameters and the form of the local velocity distribution the particle DM in the galactic halo takes. Unfortunately, these parameters still suffer from large uncertainties, while high resolution numerical N-body simulations have shown that the velocity distribution deviates significantly from the default choice, namely, a Maxwell-Boltzmann distribution.

Given this, in this chapter we investigate the effect of astrophysical uncertainties on three scenarios: elastic spin independent scattering; and, as proxies for the many varied models, inelastic and momentum dependent (aka form factor) spin independent scattering. In Fig. 3.1 we have plotted the differential scattering rate at a germanium detector to illustrate the differences between the three scenarios. We vary the galactic escape velocity, the Sun's velocity relative to the galactic centre, and the local DM density within their experimental errors. We then compare the exclusion limits for these scenarios assuming a Maxwell-Boltzmann velocity distribution with those extracted from two of the highest resolution DM N-body simulations, Via Lactea II and GHALO. We particularly focus on four experiments with different target nuclei which span a large range of atomic number A to compare the relative change at different experiments: CDMS II-Si; CDMS II-Ge; XENON10; and CRESST-II, with silicon ($A = 28$), germanium ($A = 72$), xenon ($A = 131$) and tungsten ($A = 184$) target nuclei respectively.[1] In Appendix C we summarise the relevant experimental details.

[1]Since we are seeking to understand the effects of the astrophysical uncertainties, we do not

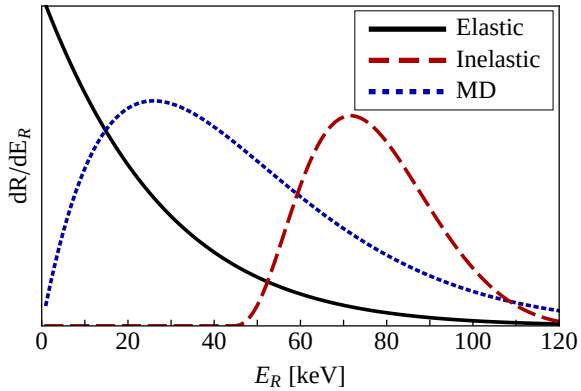

Figure 3.1: The differential scattering rate at a germanium detector for $M_\chi = 100$ GeV for elastic, inelastic and momentum dependent (MD) spin-independent scattering. The normalisation of each curve is different.

In particular, we call attention to the reanalysed early CDMS II runs and discuss uncertainties affecting the XENON10 exclusion limits at low masses.

3.1 Review of standard formalism

The differential scattering rate at direct detection experiments is given by Eq. (1.25).[2] In this chapter we only consider spin independent scattering so the differential cross section $d\sigma/dE_{\rm R}$ is given by Eq. (1.36). For simplicity, we assume $f_n/f_p = 1$ throughout this chapter, but one should bear in mind that in specific particle physics models, this may not be the case. Fortunately the rescaling of the cross section for different values of f_n and f_p is trivial. For tungsten and xenon we use the Fermi Two-Parameter form factor while for germanium and silicon, we use the Helm form factor.

For dark matter that scatters elastically, the minimum speed $v_{\rm min}$ that the incident DM particle must have in order that a nucleus recoils with energy $E_{\rm R}$ is given by Eq. (1.26). We also consider inelastic dark matter, which alters this formula to Eq. (2.1). As we saw in the previous chapter, inelastic scattering of the DM to a state ~ 100 keV heavier [122] changes the phenomenology in three principal ways: it leads to a suppression of scattering rates at low mass target nuclei experiments; the ratio of the modulated to unmodulated scattering rate increases; and the recoil spectrum at low recoil energies is kinematical suppressed. Although often invoked as a way of reconciling the modulation signal seen by DAMA with the null results at

specifically address whether astrophysical uncertainties can improve the fit between the CoGeNT and DAMA signals. For analyses in this direction, see [159, 160].

[2]In this chapter the mass of the DM and nucleus is denoted by M_χ and M_N respectively.

other experiments [126, 123, 1, 91, 161], the latest results from XENON100 [90] and CRESST-II [121] rule out this interpretation. However, having this splitting is natural in many models [162, 163, 164, 127, 128, 165, 5, 166, 167, 168] and leads to much other interesting phenomenology, for example through capture in astrophysical bodies [169, 170, 171, 172, 173]. Therefore, we emphasise that even if inelastic scattering can not reconcile the DAMA result with other experiments, it remains an interesting and viable possibility worth exploring.

In momentum dependent scattering [174, 175], the differential cross section is suppressed by additional powers of $q^2 = 2M_N E_{\rm R}$. This leads to a suppression of the exclusion limits from experiments which rely on having a sensitivity at low recoil energies, in our case XENON10 and CDMS II-Si. This dependence can arise for example, from the Lagrangian $\mathcal{L} = ia_q \bar{\chi}\gamma^5\chi\bar{q}q$. This could result from integrating out a pseudoscalar so matching to a point like nucleus closely follows the case of the scalar interaction discussed in Section 1.4.1.3. The matrix element is this case is $\mathcal{M} = ia_N \bar{u}_\chi \gamma^5 u_\chi \, \bar{u}_N u_N$. Taking the non-relativistic limit, we find as before that $\bar{u}_N u_N = 2M_N$. However, at this order $\bar{u}_\chi \gamma^5 u_\chi = 0$. Therefore, we need to account for higher order terms in the non-relativistic expansion of u_χ. Doing so, we find

$$u_\chi = \sqrt{M_\chi} \begin{pmatrix} (1 - \frac{\vec{p}\cdot\vec{\sigma}}{2M_\chi})\,\xi \\ (1 + \frac{\vec{p}\cdot\vec{\sigma}}{2M_\chi})\,\xi \end{pmatrix} \;\Rightarrow\; \bar{u}_\chi \gamma^5 u_\chi = \vec{q}\cdot\xi^\dagger \vec{\sigma}\,\xi' \,, \tag{3.1}$$

where $q^2 = |\vec{q}|^2$ is the momentum transfer. As a result, the square of the amplitude is

$$\frac{1}{4}\sum_{\rm spins} |\mathcal{M}|^2 = 2a_N^2 M_N^2 M_\chi^2 \, \frac{q^2}{M_\chi^2} \,. \tag{3.2}$$

We can see that this is suppressed by an extra factor of q^2 compared with the cases we have previously considered. Therefore, if those operators that have previously been considered in Chapter 1 are not present and $\mathcal{L} = ia_q \bar{\chi}\gamma^5\chi\bar{q}q$ is the leading order interaction, the DM will scatter with an interaction that is momentum dependent. Following [175], in this chapter we parameterise the momentum dependence by replacing the differential cross section (Eq. (1.36)) with

$$\frac{d\sigma}{dE_{\rm R}} \to \frac{q^2}{q_{\rm ref}^2} \cdot \frac{d\sigma}{dE_{\rm R}} \,, \tag{3.3}$$

where $q_{\rm ref} = 100$ MeV is the typical scale of the momentum transfer at direct detection experiments.

3.1.1 Astrophysical formalism

The simplest model of the DM distribution is the Standard Halo Model (SHM), described in detail in Section 1.2. This assumes an isotropic, isothermal sphere for the DM distribution and leads to a Maxwell-Boltzmann velocity distribution in the galactic frame. Throughout this chapter, we use the distribution given in Eq. (1.11), with $\beta = 1$ to smoothly truncate the distribution at $v_{\rm esc}$. High resolution N-body simulations of the galactic DM structure have shown that the DM velocity distribution departs from the SHM [176, 38, 36], and the effects can be large, especially in scenarios such as inelastic DM where only the high velocity tail of the velocity distribution is sampled [177, 178, 94, 179, 134, 180, 130, 1, 37]. Therefore in Section 3.3 we explore how the exclusion limits vary when we use data from the Via Lactea II [30] and GHALO [31] simulations, two of the highest resolution simulations of galactic DM structure.

3.2 Astrophysical Uncertainties

The quantities entering into this calculation from astrophysics are: ρ_χ, the local DM density, with canonical value $\rho_\chi = 0.3$ GeV/cm^3; the Sun's circular velocity with respect to the galactic rest frame with fiducial value $\vec{v}_0 = (0, 220, 0)$ km/s; the Sun's peculiar velocity relative to the Sun's circular velocity, which is usually given by $\vec{v}_\circledast = (10.0, 5.25, 7.17)$ km/s [181]; and the escape velocity $v_{\rm esc}$, which is often chosen in the range from 500 km/s to 650 km/s. In this section we will discuss recent determinations of these parameters and investigate the changes in the exclusion limits when we vary them within their allowed ranges, for elastic, momentum dependent and inelastic scattering DM with $\delta = 130$ keV.

3.2.1 The galactic escape velocity

The RAVE survey [129] has determined a 90% confidence interval for the galactic escape velocity of 498 km/s $< v_{\rm esc} <$ 608 km/s with a median likelihood of 544 km/s. In Fig. 3.2 we plot the exclusion limits for CDMS II-Si in brown, CDMS II-Ge in blue, CRESST-II in green and XENON10 in red for elastically scattering (left and right upper panels), momentum dependent (lower left panel) and inelastically scattering DM with a mass splitting $\delta = 130$ keV (lower right panel) for three values of $v_{\rm esc}$; 498 km/s (dotted); 544 km/s (solid); and 608 km/s (dashed) while keeping $\rho_\chi = 0.3$ GeV/cm^3 and $v_0 = 220$ km/s fixed. For clarity, we have only shown the limits for CDMS II-Si

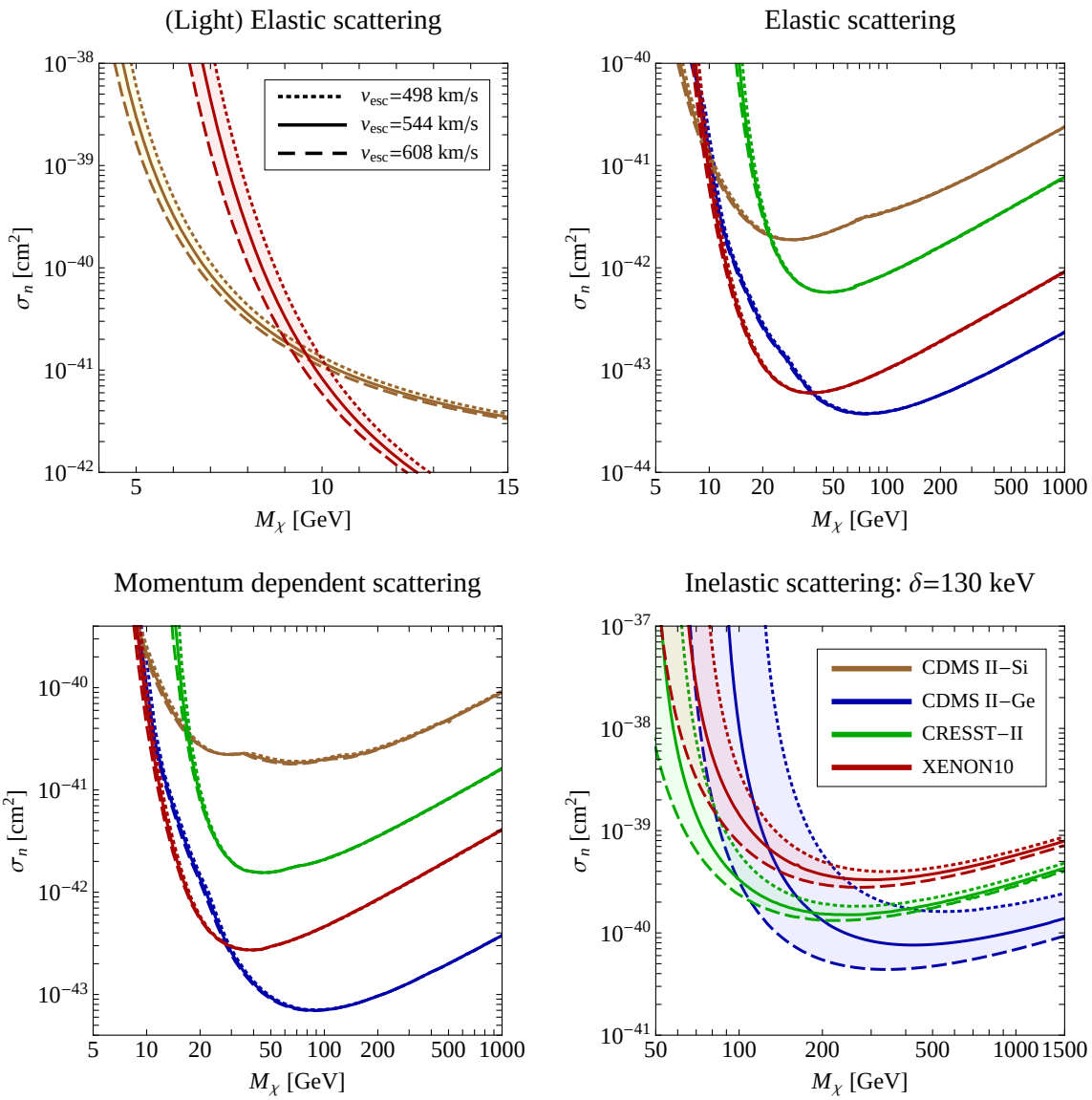

Figure 3.2: Varying v_{esc} within the 90% confidence limit found by the RAVE survey: $v_{esc} = 498$ km/s (dotted), 544 km/s (solid) and 608 km/s (dashed). Varying v_{esc} has a negligible effect on the limits for momentum dependent and elastically scattering DM except at low masses, where the limits are shifted horizontally by ~ 0.5 GeV. For inelastically scattering DM, the effect is much larger, especially for CDMS II-Ge. The two principal features to note are a shift left (right) and down (up) when v_{esc} is increased (decreased).

and XENON10 at low masses (upper left panel), since the CDMS II-Ge limits behave similarly to those from XENON10 in this mass range. CDMS II-Si is not able to set any limits for inelastic DM with $\delta = 130$ keV since its low mass means the minimum speed required to scatter off a nucleus is higher than the galactic escape velocity.

The limits for momentum dependent and elastically scattering DM are very in-

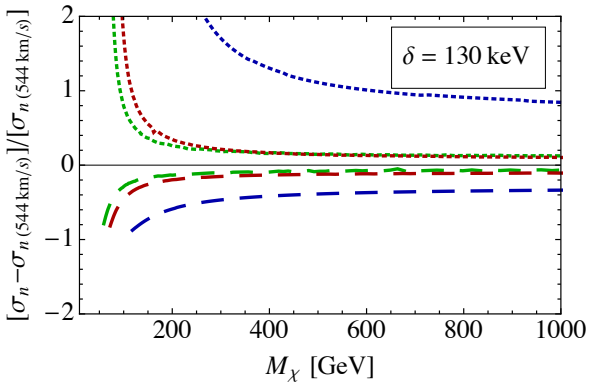

Figure 3.3: The fractional change in σ_n relative to value at $v_{\rm esc} = 544$ km/s for $v_{\rm esc} = 498$ km/s (dotted) and $v_{\rm esc} = 608$ km/s (dashed) for inelastically scattering DM with $\delta = 130$ keV. The blue, red and green lines show the change for CDMS II-Ge, XENON10 and CRESST-II respectively.

sensitive to $v_{\rm esc}$ for all experiments and it is only for masses $M_\chi \lesssim 10$ GeV that the three lines can be separately resolved. In comparison, inelastically scattering DM is much more sensitive, with two principal features to note: the curves shift left (right) and down (up) when $v_{\rm esc}$ is increased (decreased).

In Fig. 3.3 the fractional change in σ_n relative to the value at $v_{\rm esc} = 544$ km/s is plotted as a function of mass for the inelastically scattering case. The dotted and dashed lines show the ratio for $v_{\rm esc} = 498$ km/s and 608 km/s respectively. We see that the XENON10 and CRESST-II limits change in a similar way, varying by $< 20\%$ at high masses, and remaining fairly constant until ~ 100 GeV, when a very rapid increase occurs. In comparison, decreasing the escape speed dramatically weakens the CDMS II-Ge limits, by 80% at high masses ($M_\chi \sim 1000$ GeV) and larger at lower masses. Increasing $v_{\rm esc}$ has a less dramatic effect with a change of $\sim 40\%$ for CDMS II-Ge until ~ 150 GeV when a rapid increase happens. These effects are simple to understand qualitatively and quantitively.

We will first explain why the curves move vertically in Fig. 3.2. If there is a lower escape velocity, there will be fewer particles in the halo capable of scattering, therefore a larger σ_n is required to produce the same number of events at a given experiment. Since the Maxwell-Boltzmann distribution is exponentially suppressed at high velocities, decreasing $v_{\rm esc}$ will have a very small effect in the number of particles able to scatter, unless $v_{\rm min}$ is close to $v_{\rm esc}$, in which case the fractional change can be substantial. For elastic and momentum dependent scattering DM, this occurs at $M_\chi \lesssim 10$ GeV, and is true for all masses when $\delta = 130$ keV. CDMS II-Ge is particularly affected relative to XENON10 and CRESST-II because its germanium

target is much lighter than xenon and tungsten, so $v_{\rm min}$ is higher, and much closer to $v_{\rm esc}$. Similarly if $v_{\rm esc}$ is raised, there are extra particles in the halo which can scatter, so a lower σ_n will produce the same number of events in an experiment. Due to the exponential suppression of the Maxwell-Boltzmann distribution, increasing $v_{\rm esc}$ has a smaller affect than decreasing it by a similar amount.

Unfortunately, the intricacies of the '$\rm p_{max}$' method [148] for setting exclusion limits prevents very accurate estimates. However, we can give a quantitive estimate which should serve as a useful guide to the size of shift expected when $v_{\rm esc}$ is varied. Since the combination $\sigma_n g(v_{\rm min})$ enters $dR/dE_{\rm R}$ (from Eqs. (2.2) and (2.5)), the vertical shift is given by

$$\Delta\sigma_j^i \equiv \frac{\sigma_{n(i)} - \sigma_{n(j)}}{\sigma_{n(j)}} = \frac{g(v_{\rm min})_{(j)} - g(v_{\rm min})_{(i)}}{g(v_{\rm min})_{(i)}} \ , \tag{3.4}$$

where an analytic expression for $g(v_{\rm min})$ is given by Eq. (A-5).

For example, for CRESST-II with $v_{\rm min}$ from Eq. (2.1), $M_\chi = 500$ GeV, $\delta = 130$ keV, and $E_{\rm R} = 25$ keV [3], we find $\Delta\sigma^{498\ {\rm km/s}}_{544\ {\rm km/s}} = 0.13$ and $\Delta\sigma^{608\ {\rm km/s}}_{544\ {\rm km/s}} = -0.08$, in good agreement with the values 0.15 and -0.08 presented in Fig. 3.3. In comparison for CDMS II-Ge, with $M_\chi = 500$ GeV, $\delta = 130$ keV and $E_{\rm R} = 80$ keV [3], we find $\Delta\sigma^{498\ {\rm km/s}}_{544\ {\rm km/s}} = 0.75$ and $\Delta\sigma^{608\ {\rm km/s}}_{544\ {\rm km/s}} = -0.29$. This compares to the values of 1.1 and -0.39 shown in Fig. 3.3, a difference of around 40%.

To understand the horizontal shift, we will consider the energy of the recoiling nucleus, which is ultimately what experiments measure. In the Earth frame, the nuclear recoil energy is given by

$$E_{\rm R} = \frac{2\mu_N^2 v_\chi^2 \cos^2\theta_R}{M_N} \ , \tag{3.5}$$

where v_χ is the DM speed in the Earth's frame and θ_R is the nuclear recoil angle. If the recoil energy is the same, we expect a similar signal at an experiment. Increasing $v_{\rm esc}$ will increase the average speed of DM particles in the halo, but this increase will only be perceptible if $v_{\rm min}$ is close to $v_{\rm esc}$, as for inelastic and light DM. When the average speed increases, the average kinetic energy will be the same for a lighter DM particle, and since we expect the nuclear recoil energy to depend on a simple way on the dark matter's initial kinetic energy, the exclusion curves shift to the left.[4]

[3] The peak energy of the recoil spectrum $dR/dE_{\rm R}$ [123]

[4] A similar argument is presented in [182, 183]

Quantitively, the mass shift is found from differentiating Eq. (3.5), leading to

$$\frac{\Delta M_\chi}{M_\chi} = -(1 + \frac{M_\chi}{M_N})\frac{\Delta v_\chi}{v_\chi} \ , \tag{3.6}$$

where $\Delta M_\chi = M_{\chi 2} - M_{\chi 1}$, and $\Delta v_\chi = v_{\chi 2} - v_{\chi 1}$ corresponds to the shift in the average speed of the DM responsible for measurable events.

For CDMS II-Ge with $\delta = 130$ keV, $M_\chi = 90$ GeV, the only particles which can scatter have a speed $v_\chi \sim v_{\rm esc} + v_e = 800$ km/s. Changing $v_{\rm esc}$ from 544 km/s by ± 64 km/s leads to $\Delta v_\chi = \pm 64$ km/s, which from Eq. (3.6) gives $\Delta M_\chi \sim \mp 17$ GeV, in reasonable agreement with what we find in Fig. 3.2. For the elastic case $\Delta v_\chi \sim 0$ because the average speed doesn't depend sensitively on the escape speed, unless $v_{\rm min} \sim v_{\rm esc} + v_e$ which occurs at $M_\chi \sim 10$ GeV. For XENON10 at $M_\chi = 7$ GeV, $\delta = 0$ keV, $v_\chi = 800$ km/s and $\Delta v_\chi = \pm 64$ km/s, this leads to $\Delta M_\chi \sim \mp 0.6$ GeV, again in reasonable agreement with Fig. 3.2.

3.2.2 The Sun's peculiar velocity

The peculiar velocity $\vec{v}_\circledast = (U, V, W)_\circledast$ is often assumed to be well known: $\vec{v}_\circledast = (10.0, 5.25, 7.17)$ km/s with small errors ~ 0.5 km/s [181]. However three recent papers have suggested that $V_\circledast$ may have been underestimated by ~ 7 km/s [184, 185, 186]. Ref.[186] found that the classical determination in [181] underestimated $V_\circledast$ by ignoring the metallicity gradient in the Milky Way disc. Furthermore when $\vec{v}_\circledast$ is increased, [184] and [185] found better fits to the observations of masers in high mass star forming regions and the Milky Way distribution functions respectively. Therefore unless otherwise stated, in the remainder of this chapter we will use this newly determined value for the Sun's peculiar velocity: $\vec{v}_\circledast = (11.1, 12.24, 7.25)$ km/s with uncertainties $\sim (1, 2, 0.5)$ km/s.

3.2.3 The Sun's circular velocity

The Sun's circular velocity can be determined in a number of ways, which give slightly different values from the fiducial value of $v_0 = 220$ km/s. The ratio of the total velocity of the Sun about the galactic centre to the distance of the Sun from the galactic centre has been determined from the apparent proper motion of Sgr A* to be $v_\odot/R_0 = (v_0 + V_\circledast)/R_0 = 30.2 \pm 0.2$ km s^{-1}kpc^{-1} [187]. Unfortunately R_0 is still poorly determined with the most recent studies of stellar orbits obtaining $R_0 = 8.4 \pm 0.4$ kpc [188] and $R_0 = 8.33 \pm 0.35$ kpc [189]. Combining these results, and using the new value of $V_\circledast = 12.24$ km/s, we find $v_0 = 242 \pm 12$ km/s and

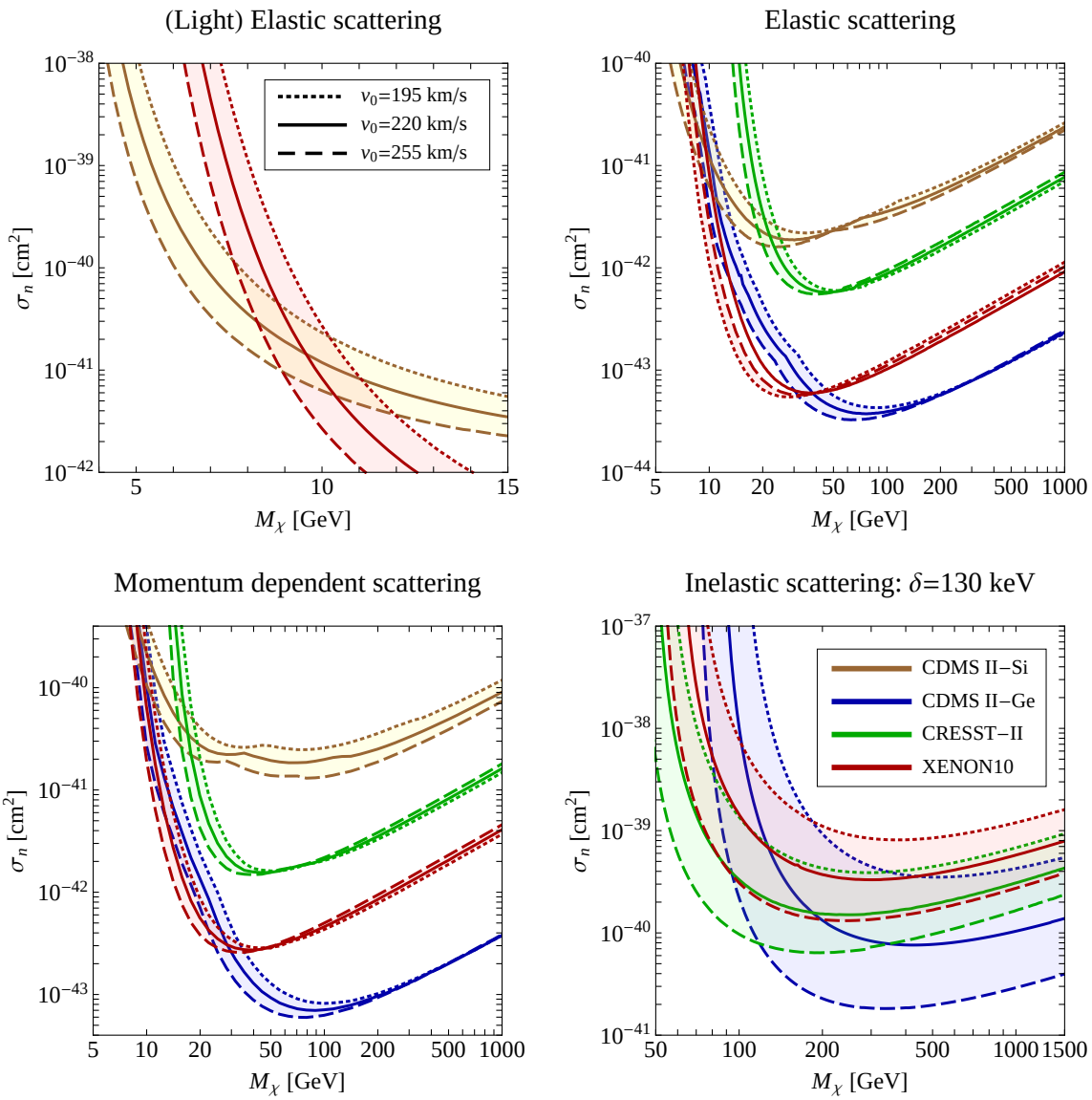

Figure 3.4: The exclusion limits for $v_0 = 195$ km/s (dotted), $v_0 = 220$ km/s (solid) and $v_0 = 255$ km/s (dashed). Varying v_0 leads to a larger vertical shift in the exclusion limits compared to varying $v_{\rm esc}$ for all panels (cf. Fig. 3.2). The horizontal shift for all experiments at masses ~ 10 GeV for elastic and momentum dependent scattering is $\sim 1-2$ GeV, larger than when $v_{\rm esc}$ is varied (cf. Fig. 3.2). In contrast, when varying v_0 in the inelastic case, the horizontal shift is smaller compared to varying $v_{\rm esc}$.

$v_0 = 239 \pm 11$ km/s respectively. This is in comparison to the analysis of the GD-1 stellar stream which found $v_0 = 221 \pm 18$ km/s [190], and the best fit to masers in the high mass forming regions which found the range $v_0 = 225 \pm 29$ km/s [184]. Wary of the possibility of unknown systematic errors affecting one of these measurements of v_0, we take a conservative approach by giving the same weight to each and hence, in

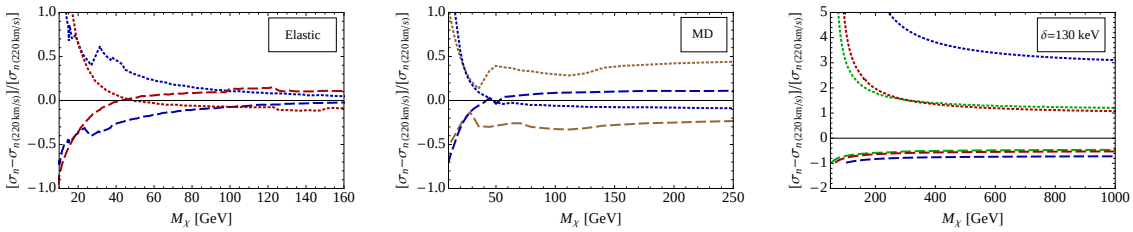

Figure 3.5: The fractional change in σ_n relative to value at $v_0 = 220$ km/s for $v_0 = 195$ km/s (dotted) and $v_0 = 255$ km/s (dashed) for elastically (left panel), momentum dependent (middle panel) and inelastically scattering DM with $\delta = 130$ keV (right panel). The blue, brown, red and green lines show the change for CDMS II-Ge, CDMS II-Si, XENON10 and CRESST-II respectively. For clarity we only show the change for CDMS II-Ge and XENON10 in the left panel and CDMS II-Ge and CDMS II-Si in the middle panel.

Fig. 3.4 we investigate how the exclusion limits change for three values of v_0; 195 km/s (dotted); 220 km/s (solid); and 255 km/s (dashed), while keeping $\rho_\chi = 0.3$ GeV/cm^3 and $v_{\rm esc} = 544$ km/s fixed. Again the left and right upper panels shows elastically scattering DM while the lower left and right panels show momentum dependent and inelastically scattering DM for $\delta = 130$ keV. We see that varying v_0 has more of an effect on σ_n than changing $v_{\rm esc}$ for all cases (cf. Fig. 3.2), and that once again there are two principal features to note: increasing (decreasing) v_0 causes the exclusion curves to shift down (up) and left (right).

Changing v_0 has two effects: v_0 is needed to boost from the galactic frame to the Earth frame (Eq. (1.27)), so increasing v_0 means there are more particles at speeds above $v_{\rm min}$ available to scatter in the Earth's frame; and in the SHM, v_0 determines the DM dispersion velocity ($\sigma_{\rm dis} \equiv \sqrt{\frac{3}{2}} v_0$), so increasing v_0 also increases the range of the speed of particles in the halo, with more at higher and lower speeds. Therefore if $v_{\rm min}$ is close to $v_{\rm esc}$, as for inelastic DM and light DM, changing v_0 has a similar effect to changing $v_{\rm esc}$ since it also increases or decreases the number of particles which can scatter. However since we are not just changing the tail of an exponential distribution, but rather its overall shape and position, the effect of changing v_0 is larger than varying $v_{\rm esc}$. This is demonstrated in the right panel of Fig. 3.5 where we have plotted the fractional change in σ_n relative to the value at $v_0 = 220$ km/s for $v_0 = 195$ km/s (dotted) and $v_0 = 255$ km/s (dashed) assuming $\delta = 130$ keV. Comparing this to Fig. 3.3, we see that it has the same features, but the effects are exaggerated.

The left and middle panels of Fig. 3.5 show the fractional change in σ_n relative to

the value at $v_0 = 220$ km/s for $v_0 = 195$ km/s (dotted) and $v_0 = 255$ km/s (dashed), assuming elastic and momentum dependent scattering. For clarity, in the left panel we have only plotted the fractional change for CDMS II-Ge (blue) and XENON10 (red) since the fractional changes for CRESST-II and CDMS II-Si are similar to those of XENON10. In the middle panel, we have only plotted the change for CDMS II-Ge and CDMS II-Si. In the top panel, for masses > 75 GeV, the fractional change in σ_n when increasing or decreasing v_0 remains at $\sim 10\%$ for all experiments. However, for lower masses, the fractional change at all experiments increases dramatically, reaching $\sim 100\%$ at 10 GeV. This sudden increase is caused by the horizontal shift in the exclusion limits which occurs for the same reasons as outlined in Section 3.2.1. In the middle panel, the CDMS II-Ge curves are similar to those in the left panel (although not shown, XENON10 and CRESST-II are also similar), but those for CDMS II-Si are quite different. This is because for momentum dependent scattering, the events at higher recoil energies are more important. To scatter with a larger recoil energy, a larger speed is required. For CDMS II-Si, this minimum speed is close to $v_{\rm esc}$, so the limits are effected more when v_0 is varied, compared with elastic scattering.

We can use the formulae from Section 3.2.1 to estimate the vertical and horizontal shifts of the exclusion curves for inelastic scattering. In particular for XENON10 at $M_\chi = 400$ GeV, $\delta = 130$ keV and $E_{\rm R} = 35$ keV [3], we find $\Delta\sigma^{195\ {\rm km/s}}_{220\ {\rm km/s}} = 1.59$ and $\Delta\sigma^{255\ {\rm km/s}}_{220\ {\rm km/s}} = -0.56$, in good agreement with the values 1.32 and -0.60 presented in the bottom panel of Fig. 3.5, while for the horizontal shift at $M_\chi = 65$ GeV, $\delta = 130$ keV, $\Delta v_\chi = \pm 35$ km/s and $v_\chi \sim 700$ km/s we find $\Delta M_\chi \sim \mp 5$ GeV. For XENON10 at $M_\chi = 12$ GeV, $\delta = 0$ keV, $\Delta v_\chi = \pm 35$ km/s and $v_\chi \sim 500$ km/s we find $\Delta M_\chi \sim \mp 1$ GeV. These estimates are all in reasonable agreement with what is observed in Fig. 3.4.

3.2.4 The local dark matter density

We next consider the local DM density ρ_χ. Unfortunately, this is the least well known astrophysical parameter with an often quoted uncertainty of a factor of 2 or 3 in the fiducial value $\rho_\chi = 0.3$ GeV/cm^3 [191, 192]. Two recent studies using different techniques found $\rho_\chi = 0.3 \pm 0.1$ GeV/cm^3 [193] and $\rho_\chi = 0.43 \pm 0.15$ GeV/cm^3 [194], consistent with $\rho_\chi = 0.3$ GeV/cm^3 with an error of a factor of 2. Dark matter N-body simulations from the Aquarius Project have shown that ρ_χ should be very smooth at the Sun's position, varying by less than 15% at the 99.9% confidence level from the average value over an ellipsoidal shell at the Sun's position [36]. Therefore we can

be reasonably confident that the Earth is not sitting in a particularly over or under dense region of the halo.

Since the combination $\rho_\chi \sigma_n$ enters into $dR/dE_{\rm R}$ (Eq. (2.2)), the error in ρ_χ corresponds directly to an uncertainty of a factor of 2 in the DM-neutron cross section σ_n, affecting all experiments equally.

3.2.5 Discussion: The correlation between v_0 and ρ_χ

We have followed the standard procedure of varying these astrophysical parameters independently, however, Refs. [187, 184] found that there is a strong correlation between the Sun's circular speed v_0 and the distance from the galactic centre R_0: $v_0/R_0 \approx 29$ kms^{-1}kpc^{-1}. Since ρ_χ also depends on R_0, a more careful approach should take into account the change in ρ_χ as we vary v_0. Here we estimate this correction.

Assuming $v_0 = 230$ km/s and $\rho_\chi = 0.3$ GeV/cm^3 at $R_0 = 8$ kpc, and assuming ρ_χ follows an NFW profile, when $\Delta R_0 = \pm 1$ kpc, we find $\Delta v_0 \approx \pm 30$ km/s and $\Delta\rho_\chi/\rho_\chi \approx \mp 20\%$, similar to the range of v_0 explored in Section 3.2.3. Therefore for higher (lower) values of v_0, the exclusion curves in Fig. 3.4 are shifted upwards (downwards) by an additional $\sim 20\%$. Comparing with Figs. 3.4 and 3.5, we see that this correction is of a similar size to what we found for $\Delta\sigma_n/\sigma_n$ when independently varying v_0 for the elastic and momentum dependent scattering case when $M_\chi \gtrsim 30$ GeV, although the spread in the limits remains small. For light and inelastic DM, the change when varying v_0 independently is $\sim 200\%$, therefore the spread in limits shown in Fig. 3.4 is overestimated by $\sim 10\%$, but still remains significant.

3.3 Uncertainties in the form of the dark matter velocity distribution

In the previous section we investigated the effect of astrophysical uncertainties whilst always assuming a Maxwell-Boltzmann distribution for the DM velocity distribution. Dark matter numerical N-body simulations have shown that a typical velocity distribution exhibits global (the overall shape) and local departures ('bumpy' features) from a Maxwell-Boltzmann distribution, and in this section we wish to investigate how these affect exclusion limits.

We use data extracted from the Via Lactea II (VLII) [30] and GHALO [31] simulations.[5] To facilitate a more direct comparison between the VLII and GHALO simulations, we use the GHALO_s data from [38] in which the maximum circular speed in the GHALO simulation has been rescaled to agree with that from VLII. As explained in [38], the lack of baryons in the simulations means that the dispersion of the extracted velocity distribution is lower than expected from a galaxy which contains baryons and DM, because it is expected that the baryons will create a deeper gravitational potential well, increasing the velocity dispersion. Since we are interested in departures from a Maxwellian distribution, we will compare the simulation limits with those from a Maxwell-Boltzmann distribution with the same dispersion. This corresponds to using $v_0 = 184$ km/s in Eq. (1.11). In the previous section we found that different astrophysical parameters can lead to significant deviations in the exclusion limits, therefore we will match these as closely as possible so that we are just observing the effects of the simulation distributions. Following [38] we take $\rho_\chi = 0.3$ GeV/cm^3, $\vec{v}_\odot = (10.0, 220 + 5.25, 7.17)$ km/s and $v_\text{esc} = 550$ km/s and 586 km/s for VLII and GHALO_s respectively.

With the simulation data, it is possible to examine the effects of local structure in the DM velocity distribution. This was done in [38] by extracting the velocity distribution for one hundred spheres of radii 1.5 kpc and 1 kpc for VLII and GHALO_s respectively, centred at a distance of 8.5 kpc from the galactic centre. In Fig. 3.6 the thin bands show the exclusion curves from Via Lactea II (left panels) and GHALO_s (right panels) assuming elastic and momentum dependent scattering for all one hundred spheres for CDMS II-Si (yellow), CDMS II-Ge (blue), CRESST-II (green) and XENON10 (red). We have checked the robustness of these bands by comparing the strongest and weakest limit with the sixteenth strongest and sixteenth weakest limit at each mass, and find that the limits are essentially the same. The dashed line shows the limits derived from a Maxwell-Boltzmann distribution with the astrophysical and dispersion parameters above. We find that VLII and GHALO_s produce similar limits, which are generally more stringent than those from a Maxwell-Boltzmann distribution.

The inelastically scattering case has been studied in detail in [38], therefore in Fig. 3.7 we only plot the limits for CRESST-II for $\delta = 130$ keV (for CDMS II-Ge and XENON10 we find a similar spread in the limits). To give an estimate of what the typical limits are, we have plotted the limits excluding five and sixteen maximum and minimum cross sections at each mass as the blue dashed and red dotted bands

[5] This data is available from `http://astro.berkeley.edu/~mqk/dmdd/`.

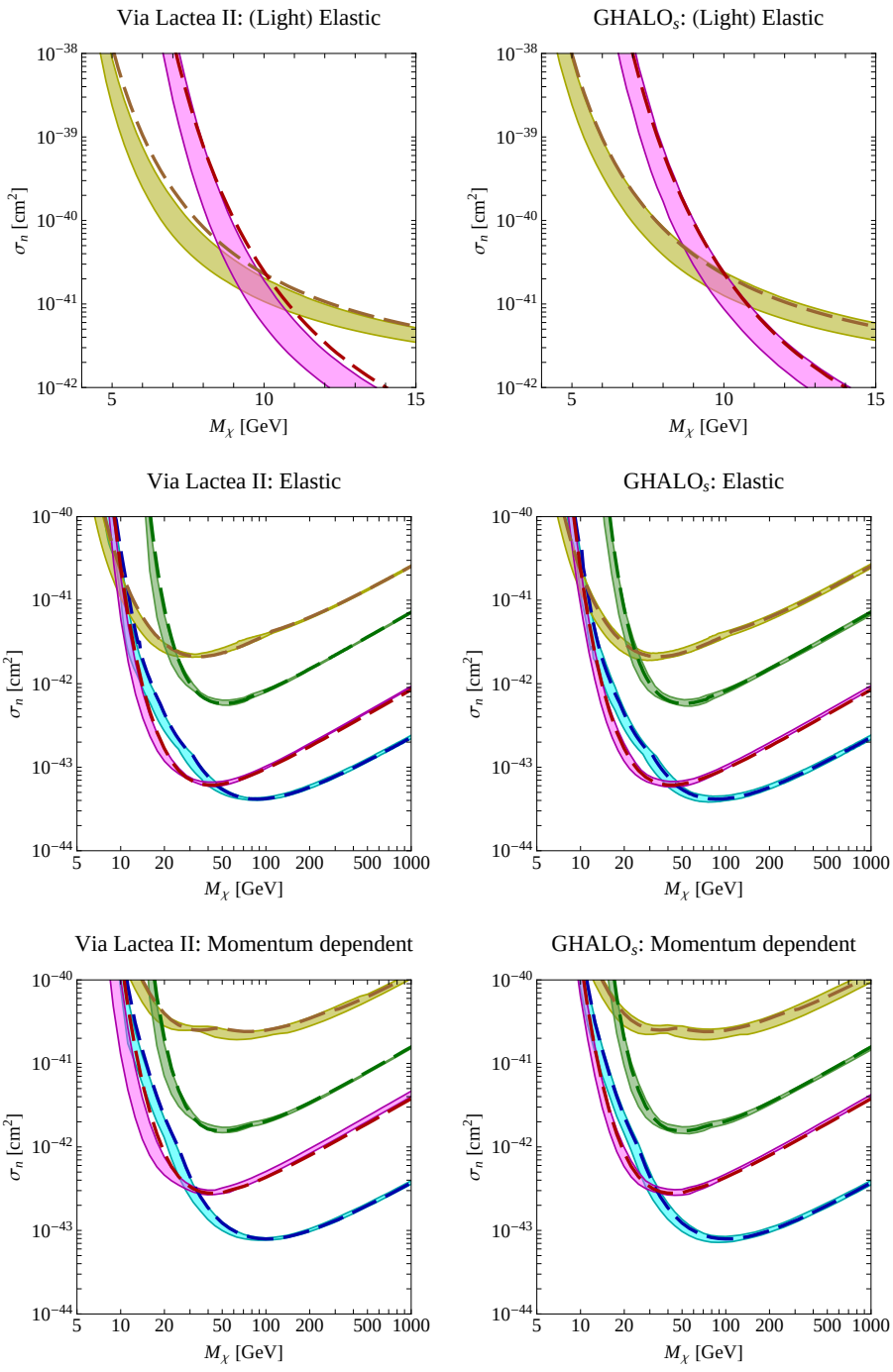

Figure 3.6: The exclusion limits from the Via Lactea II (left panels) and GHALO$_s$ (right panels) simulations. The legend is the same as Fig. 3.4. The solid bands shows the range of limits from the velocity distribution of 100 random spheres centred at 8.5 kpc. For comparison, the dashed line show the limits from a Maxwell-Boltzmann velocity distribution with the same astrophysical parameters as found in the simulation halos. The Maxwell-Boltzmann distribution generally sets less constraining limits on σ_n.

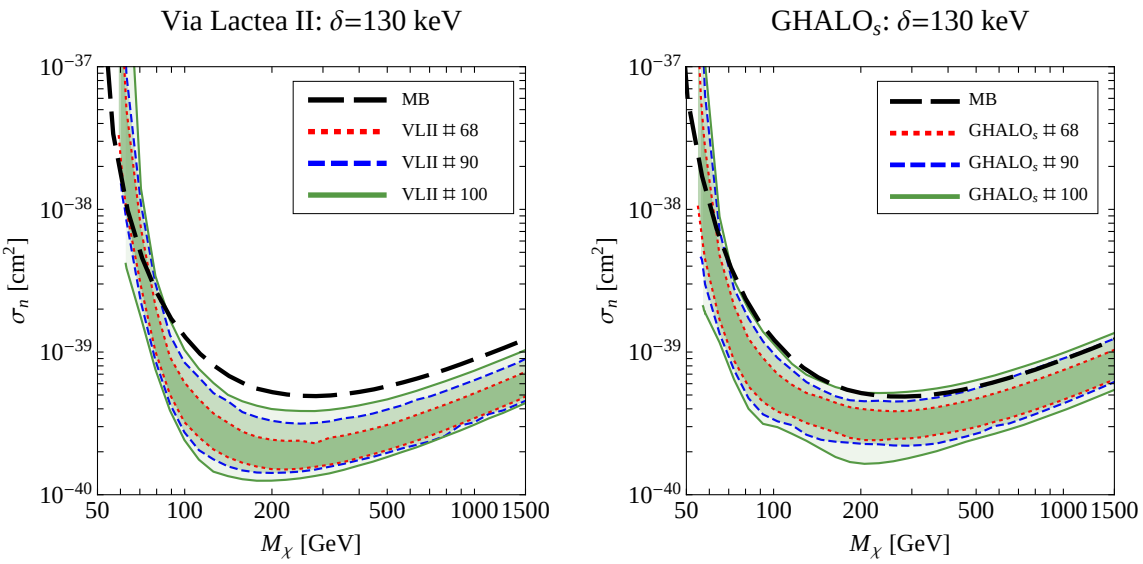

Figure 3.7: The exclusion limits for CRESST-II, assuming inelastic scattering from 100 random spheres from the Via Lactea II (left panel) and GHALOs (right panel) simulations. The dotted red and dashed blue lines indicate the range of limits when we exclude five and sixteen of the highest and lowest cross sections at each mass. For comparison, the long-dashed black line shows the limits from a Maxwell-Boltzmann distribution with the same astrophysical parameters and dispersion. At $M_\chi \sim 60$ GeV, we find that some of the spheres are not able to set any limits. As in Fig. 3.6, we find that the Maxwell-Boltzmann distribution generally sets less constraining limits on σ_n.

respectively. As we might expect, the inelastic case shows much more of a spread in the cross section compared to the elastic case, and the limits from VLII and GHALO$_s$ show some differences. Interesting features to note are the bumpy features in the GHALO$_s$ exclusion limits, and near threshold we find that some spheres can not set any limits for both VLII and GHALO$_s$. The black dashed line shows the exclusion limits from a Maxwell-Boltzmann distribution which as in the elastic case, is typically more conservative than the limits from the simulations.

We emphasise here that we have not been comparing the simulation limits with the SHM, in which the circular speed enters Eq. (1.11) but rather to a best fit Maxwell-Boltzmann distribution which has the same velocity dispersion. Until simulations include baryonic effects, which will increase the dispersion, we urge caution in making direct comparisons to the SHM. The velocity distributions from the simulations are interesting since they show that the overall shape of the limits can change, rather than causing a spread about a central value as we found when varying the astrophysical parameters (cf Figs. 3.4 and 3.7). Furthermore since different experiments vary by

different amounts, when comparing exclusion curves at one experiment with preferred regions of parameter space at another (for example, comparing CDMS II-Ge to the DAMA/LIBRA or CoGeNT preferred region), one should bear in mind that different velocity distributions may affect the limits from different experiments by differing amounts.

3.4 Conclusions

If we are to understand the nature of DM, it is vital that we have a full understanding of the astrophysical uncertainties affecting DM direct detection experiments. For spin-independent elastic and momentum dependent scattering with $M_\chi \gtrsim 50$ GeV, we have shown that the exclusion limits are robust against variations in the galactic escape velocity $v_{\rm esc}$ and the Sun's circular speed about the centre of the galaxy v_0 (right upper and left lower panels of Figs. 3.2 and 3.4) and under realistic variations in the form of the velocity distribution (middle and bottom panels of Fig. 3.6), with uncertainty $\sim 10\%$. The major uncertainty in this mass range arises from the error in the local DM density (a factor of 2).

In comparison, for lighter masses, we found that uncertainties in v_0 and $v_{\rm esc}$ and the velocity distributions from the numerical simulations can shift the exclusion curves horizontally by ~ 1 GeV at masses $M_\chi \sim 10$ GeV (upper left panels of Figs. 3.2, 3.4 and 3.6). Similarly for inelastically scattering DM, we found the vertical shift in the exclusion curves when varying v_0 or $v_{\rm esc}$ is large ($\sim 100\%$), with lighter target experiments such as CDMS II being particularly affected. Variations in the velocity distribution can also lead to significant changes, as we explicitly demonstrated in Fig. 3.7 for the CRESST-II experiment.

Inelastic and light DM are particularly sensitive to astrophysical uncertainties because the minimum speed needed to scatter is just below the galactic escape speed, so experiments only sample the tail of the velocity distribution. Even though the recoil spectrum for momentum dependent DM is different from elastically scattering DM (Fig. 3.1) they both respond to astrophysical uncertainties in a similar fashion for germanium, xenon and tungsten targets, because $v_{\rm min}$ remains far from $v_{\rm esc}$. Therefore, models that only sample the tail of the velocity distribution should carefully examine the effect of astrophysical uncertainties on their limits.

Chapter 4

On the DAMA and CoGeNT Modulations

Among the most promising strategies for the identification of particle dark matter (DM) are direct detection experiments, which aim to observe the scattering of DM particles off target nuclei. While the recoil energy spectrum has no features that allow for an unambiguous identification of a DM signal, a characteristic annual modulation of the differential event rate is expected due to the motion of the Earth relative to the Galactic halo [27, 28].

Two DM direct detection experiments, namely DAMA [77] and CoGeNT [195, 78], have published data demonstrating evidence for such an annual modulation. The combined results from DAMA/NaI and DAMA/LIBRA have a statistical significance exceeding 8σ. CoGeNT has taken data for over a year and also observes an annual modulation with a significance of 2.8σ [78]. The simplest explanation of these experiments in terms of DM is spin-independent elastic scattering on both protons and neutrons of a light, $\mathcal{O}(10)$ GeV DM particle [196, 197]. However, this explanation is strongly disfavoured by other null results, most notably by the CDMS [82], XENON10 [87] and XENON100 [89] experiments.

Various proposals towards reconciling all experiments have been put forward. First of all, doubts have been raised concerning experimental details, such as the proper calibration of the nuclear recoil energy scale and the correct assessment of the various quenching factors (see e.g. [198]). Secondly, significant astrophysical uncertainties are present in all analyses, which may considerably change the implications of the data [1, 2]. Finally, it may well be that the DM-atom interaction is not solely with the nucleus or that the DM-nucleus interaction is more complicated than generally assumed.

In this chapter we will primarily focus on the third option in the context of nuclear recoils. Of particular interest is the combination of two effects that have been recently considered as possibilities to alleviate the tension between the various experiments: Isospin-violating dark matter (IVDM) [199, 160, 200] and inelastic dark matter (iDM) [122, 126, 123, 161, 201]. In fact, if one assumes that DM scatters differently on protons and neutrons, then for a particular choice of the proton to neutron scattering fractions, it is possible to weaken the limits from XENON, which would otherwise give the strongest constraints.[1] On the other hand, inelastic scattering of the DM particle can enhance the annual modulation signal and reduce the tension between CDMS and CoGeNT, which cannot be reduced by isospin-violating couplings.

We only take the annual modulation of the signal measured by DAMA and CoGeNT as a hint of DM. We make the important assumption that the background does not modulate, and that the modulation is entirely due to DM interactions. We do not fit to the unmodulated spectrum as it is very difficult to interpret an exponentially falling energy spectrum in the presence of an unknown background in terms of a DM particle. Rather we can use the unmodulated recoil spectra for the sole purpose of calculating exclusion limits to constrain the parameter region consistent with annual modulation.

4.1 Direct Detection of Dark Matter

In this chapter, we consider spin independent inelastic scattering, therefore the differential event rate is given by Eq. (2.2). We will allow the possibility of inelastic scattering so the minimum speed is given by Eq. (2.1). Throughout we take $v_0 = 220$ km/s, $v_{\rm esc} = 544$ km/s and $\rho_\chi = 0.3$ GeV/cm^3.

For DAMA, we fit to the latest data [77] and take the sodium quenching factor to be $Q_{\rm Na} = 0.3$. In one case we consider $Q_{\rm Na} = 0.43$, within the range $Q_{\rm Na} = 0.3 \pm 0.13$, deemed representative of experimental uncertainties in [202]. We do not include channeling in our calculations [145]. We find that scattering off of sodium dominates that of iodine in the low mass DM region that we consider. We use the detector resolution from [147] for DAMA/NaI and [146] for DAMA/LIBRA and weight them appropriately.

For the CoGeNT parameter regions shown in Fig. 4.1, we use modulation amplitudes of 1.20 ± 0.65, 0.54 ± 0.19 and 0.08 ± 0.16 events/kg/day/keVee for $0.5 - 0.9$,

[1] Note that it is not possible to completely suppress scattering on xenon due to the presence of different isotopes, as emphasised in [200].

$0.9-3.0$ and $3.0-4.5$ keVee respectively. We use the detector resolution and efficiency given in [195, 78] and use a quenching factor for germanium of 0.2.

A DM explanation of a signal in DAMA and CoGeNT must be confronted with the exclusion limits obtained by the XENON and CDMS collaborations. While heavy DM is most strongly constrained by the recent results of XENON100 [89], an even stronger bound for low mass DM can be obtained from a dedicated low threshold analysis of the XENON10 data [87]. For the XENON experiments we assume a detector resolution dominated by Poisson fluctuations and take $\mathcal{L}_{\rm eff}$ and $\mathcal{Q}_y$ from the respective papers. For the XENON10 data, we include the S2 width cut and assume the absence of fluctuations at the low energy threshold (i.e. impose a cut-off).

The ratio f_n/f_p depends on the underlying model of DM and generally differs from one. Equation (2.2) implies that if the DM scattering satisfies $f_n/f_p = Z/(Z-A)$ for a given nuclear isotope, this isotope would then give no constraint. In practice, experiments consist of targets with more than one isotope, so they can still yield some constraints. As considered in [160, 200] the choice $f_n/f_p \sim -0.7$ reduces the sensitivity of xenon experiments by three orders of magnitude. Here, instead of treating f_n/f_p as a free parameter, we fix the ratio in such a way that the constraint from xenon is reduced as much as possible.

The most restrictive limit from CDMS results from a low-energy analysis of the CDMS II data from the Soudan Underground Laboratory [82]. In this chapter we only include the detector with the best ionisation resolution (T1Z5), treating all observed events as potential DM signals. We find that the constraint obtained with this simplification agrees well with the limit published by CDMS. Since both CoGeNT and CDMS are germanium target experiments they cannot be reconciled using isospin-violating couplings. Inelastic scattering increases the modulation fraction, and hence reduces the tension between CDMS and CoGeNT. However, for scattering on sodium in DAMA, the tension between DAMA and CDMS increases as germanium is greater in mass. Thus, we must require $\delta \lesssim 15$ keV in order for DAMA not to be excluded by CDMS.

Exothermic dark matter [203] has been proposed as a way to reduce the tension between DAMA and CDMS. However, the possibility of down-scattering will reduce the modulation fraction and therefore bring the CoGeNT modulation into disagreement with the constraint from the absolute rate and the CDMS bound. Therefore, we only consider $\delta > 0$, corresponding to endothermic inelastic dark matter.

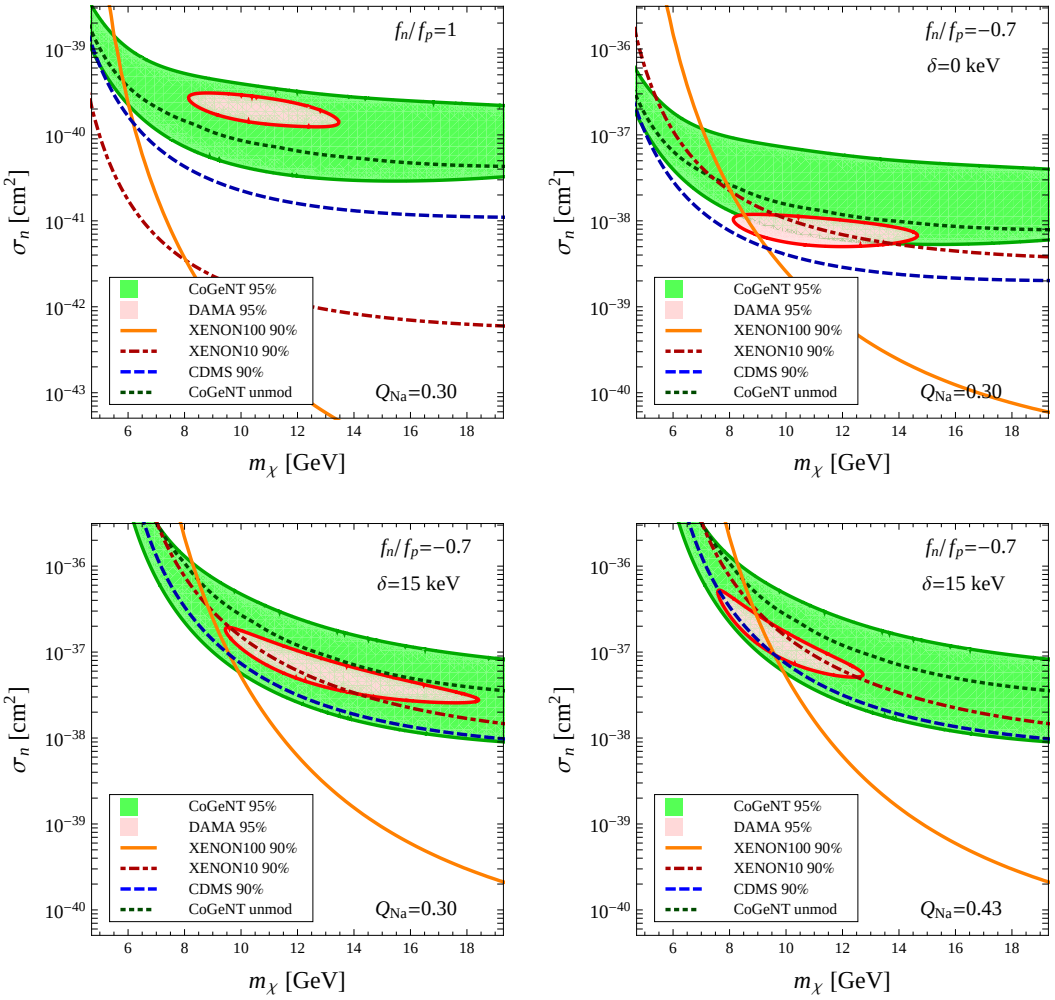

Figure 4.1: Allowed parameter regions for DAMA and CoGeNT (coloured regions) as well as exclusion limits from XENON10, XENON100, CDMS II and the unmodulated CoGeNT signal. In the upper panels, $\delta = 0$ keV and $f_n/f_p = 1$ (left) and $f_n/f_p = -0.7$ (right). The lower panels have $\delta = 15$ keV and $f_n/f_p = -0.7$ (left and right). In the lower right panel we have taken the sodium quenching factor to be $Q_{\rm Na} = 0.43$. In the other panels we take the standard value $Q_{\rm Na} = 0.3$. Notice the upper left panel uses a different scale for σ_n. It is clear that employing the IVDM and iDM mechanisms significantly weakens the constraints from null searches, and allows for a small region of agreement when the sodium quenching factor is varied within a reasonable range.

In Fig. 4.1 we show how the combination of the iDM and IVDM mechanisms can reduce but not completely resolve the apparent conflict between the annual modulation observed in both CoGeNT and DAMA with exclusion limits from other detectors.[2] Any alteration of these limits due to uncertainties in low-energy efficiencies,

[2]Note that we do not perform a parameter estimation, but show the regions that give a sufficiently small χ^2 corresponding to a satisfactory goodness-of-fit for the annual modulations.

astrophysical parameters, quenching factors, or inclusion of channelling could weaken the limits sufficiently to allow a DM interpretation of the CoGeNT and DAMA annual modulation. As a demonstration, we consider a larger value of the sodium quenching factor and find better agreement as shown in the lower right panel of Fig. 4.1. In fact, it should be noted that our 95% best-fit and 90% exclusion regions do not take into account uncertainties in all such astrophysical and experimental parameters, and therefore are not truly 90% regions.

4.2 Future constraints from direct detection experiments

Even with $f_n/f_p = -0.7$, the XENON100 limit remains strong and cannot be suppressed much further due to the different isotopes present in natural liquid xenon. Consequently, additional data from XENON100, as well as a dedicated S2 only analysis with lower threshold may provide strong constraints for isospin-violating inelastic DM. The CDMS collaboration has also collected data from detectors with a silicon target. From the unpublished data presented in [204], we find a limit which is more constraining than the CDMS germanium low threshold analysis. We have not included this in Fig. 4.1 because of uncertainties related to the calibration of the silicon nuclear recoil energy scale [204, 202][3]. We encourage the CDMS collaboration to perform a dedicated analysis of the Soudan silicon data.

4.3 Other constraints and implications for the dark sector

Mono-jet [205, 206, 118] and di-jet searches at the Tevatron constrain the DM couplings to quarks. For light DM the Tevatron limits on mono-jet production are relevant, but sensitive to the mass of the particle mediating the DM interaction with quarks [118]. Assuming the mediator is heavy compared to the typical momentum transfer at the Tevatron, the limits can be as strong as $\sigma_n \sim 10^{-39}\,\mathrm{cm}^2$. However, if the mediator is light, or if the coupling is not by a vector current, the constraints weaken. For example, a mediator of mass $M \sim 10$ GeV interacting via a vector current allows $\sigma_n \sim 3 \times 10^{-34}\,\mathrm{cm}^2$ easily allowing our best fit CoGeNT and DAMA regions.

[3]We thank J. P. Filippini for clarifying uncertainties associated with the silicon data.

The couplings of the mediator to quarks g_q are separately constrained. In the case of a vector mediator with a mass in the range $M \gtrsim 10$ GeV the constraints are $g_q \lesssim 0.1$ from meson decay measurements [207] which easily satisfies the constraints from the di-jet measurements at Tevatron. The DM-neutron scattering cross section may be written as $\sigma_n \sim f_n^2\, g_\chi^2\, \mu_{\chi n}^2/(\pi M^4)$, where g_χ is the DM mediator coupling and the effective coupling constants via the vector current $\bar{q}\gamma^\mu q$, for the neutron (proton) are $f_n = g_u + 2g_d$ ($f_p = 2g_u + g_d$). We can then reach the required DAMA and CoGeNT cross section $\sigma_n \sim 10^{-37}\,\mathrm{cm}^2$ with $g_q \sim g_\chi \sim 5 \times 10^{-2}$, within the above bounds. If the light dark matter results from strong dynamics in another sector saturating the perturbativity bound $g_\chi \sim \sqrt{4\pi}$ [208] couplings to quarks as small as $g_q \sim 10^{-3}$ are allowed.

If the DM has no particle–anti-particle asymmetry, additional constraints from searches for the annihilation products apply. For example, there are constraints coming from neutrino telescopes searching for the annihilation products of DM accreted in stars. In particular, annihilations of light DM captured in the Sun are constrained by SuperKamiokande which excludes the DAMA/CoGeNT regions shown in Fig. 4.1 for DM annihilating into the $c\bar{c}, b\bar{b}, \tau\bar{\tau}, \nu\bar{\nu}, 4\tau$ channels (even with velocity suppressed annihilations) [209]. Note that also inelastic, annihilating DM is constrained by capture and annihilation in the Sun [169, 170] and compact stars [172, 173] and for the small splittings we are considering the above mentioned limits still apply.

An attractive framework which avoids the annihilation constraints is asymmetric dark matter (ADM), where a particle-antiparticle asymmetry $\eta_\chi = (n_\chi - n_{\bar{\chi}})/s$ in DM, similar to that in baryons η_B, provides a natural link between their observed energy densities. If some process shares or co-generates the two asymmetries ensuring $\eta_\chi \sim \eta_B$, then the observed cosmological DM energy density is realised for $m_\chi \sim 1 - 10$ GeV. Consequently, ADM offers a motivation for the low DM mass favoured by the DAMA and CoGeNT data, and naturally avoids the constraints from annihilation in the Sun [209].

Note added: After this work was completed, the CRESST-II Colloboration released data showing an excess of events at low energies [210]. Light DM-nuclei scattering can offer an explanation of this excess with m_χ and σ_n taking values close to those required for an explanation of the DAMA and CoGeNT signals. Unfortunately, a preliminary investigation of this data indicates that including an inelastic splitting does not lead to an improvement in the agreement between CRESST-II, DAMA and CoGeNT or to a reduction in the tension with XENON100.

Chapter 5

DAMA and CoGeNT without astrophysical uncertainties

As discussed in the previous chapter, the DAMA and CoGeNT Collaborations have detected an annual modulation signal that has many features consistent with a signal arising from particle dark matter (DM). In this chapter, we assume both signals arise due to DM and study the consistency of the two signals assuming the DM scatters elastically. In particular, we consider whether the phase and amplitude of the modulations are consistent. Previous studies [3, 211, 212, 213, 214] have shown that DAMA and CoGeNT can be in agreement for DM of mass $\sim$ 5–14 GeV that scatters elastically via a spin independent interaction, albeit with tension from the CDMS II [82], XENON10 [87], XENON100 [89] and SIMPLE [84] experiments.[1] However, it is well known that interpreting the signals at direct detection experiments is sensitive to many uncertainties, particularly uncertainties in astrophysical parameters (see e.g. [1, 2, 38, 39, 130, 218, 219]). Therefore, we follow the approach of [220], which specifies how to directly map experimental signals from one detector to another, allowing a comparison without specifying any astrophysical parameters. Given the modulation observed at CoGeNT, we calculate the peak day and modulation amplitude expected at DAMA, which we compare with that observed at DAMA. The phase and amplitude will be the same if both modulations arise from DM. We finish by considering constraints from the low threshold analysis of CDMS II [82, 81] and XENON10 [87].

5.1 A formalism free from astrophysics

Following the approach of [220], we wish to map the differential event rate into $v_{\rm min}$ space. As we will show, when the $v_{\rm min}$ space probed by two different experiments

[1] See [215, 216, 217] for a critical discussion of these experiments.

is the same, we can compare them directly without making any assumptions about any astrophysical parameters. This allows us to map the peak day and amplitude of the CoGeNT modulation onto the DAMA detector, which can be compared with the signal that DAMA observes. Below we briefly recap the relevant theory from [220].

First, let us rewrite the differential event rate for elastic spin independent DM-nucleus scattering (Eq. (2.2)) as

$$\frac{dR(t)}{dE_{\rm R}} = \frac{\rho_\chi \sigma_n}{2 m_\chi \mu_{\chi n}^2} \frac{C_T}{f_n^2} F^2(E_{\rm R}) \epsilon(E_{\rm R}) g(v_{\rm min}, t). \tag{5.1}$$

Here, $\epsilon(E_{\rm R})$ is the efficiency of the detector, which in general depends on $E_{\rm R}$, and we have defined $C_T \equiv \kappa \left(f_p Z + f_n (A - Z)\right)^2$, where κ is the detector mass fraction of the target nucleus. For all elements we will consider, we use the Helm form factor. $g(v_{\rm min}, t)$, previously defined in Eq. (2.5), encodes all the information about the DM velocity distribution while $v_{\rm min}$, defined in Eq. (1.26), is the minimum speed an incident DM particle must have for a nucleus to recoil with energy $E_{\rm R}$. We can invert Eq. (1.26) to consider $E_{\rm R}$ as a function of $v_{\rm min}$; that is,

$$E_{\rm R}(v_{\rm min}) = \frac{2 \mu_N^2 v_{\rm min}}{m_N} \ . \tag{5.2}$$

This allows us to rewrite Eq. (5.1) in $v_{\rm min}$ space:

$$R(t) = \frac{2 \rho_\chi \sigma_n}{m_N m_\chi} \frac{\mu_N^2}{\mu_{\chi n}^2} \frac{C_T}{f_n^2} \int_{v_{\rm low}}^{v_{\rm high}} F^2(v) \epsilon(v)\, v\, g(v, t)\, dv \tag{5.3}$$

$$\approx \frac{2 \rho_\chi \sigma_n}{m_N m_\chi} \frac{\mu_N^2}{\mu_{\chi n}^2} \frac{C_T}{f_n^2} \bar{F}^2(v) \bar{\epsilon}(v) \int_{v_{\rm low}}^{v_{\rm high}} v\, g(v, t)\, dv \ . \tag{5.4}$$

The efficiency $\epsilon(E_{\rm R})$ and form factor $F(E_{\rm R})$ are almost flat across the range of recoil energies we consider at DAMA, CoGeNT and later CDMS II. Therefore, we remove them from the integral and evaluate them at the average value across the domain of integration. The error introduced by this approximation is less than a few percent.

All of the physics that determines the peak day of the modulation is encapsulated in the integral $\int_{v_{\rm low}}^{v_{\rm high}} v g(v, t) dv$. By arranging to have the same integration limits for DAMA and CoGeNT, the respective modulations will have the same peak day if they both arise from DM scattering. Given an energy range at DAMA (D), we can use Eq. (5.2) to find the energy range at CoGeNT (C) which spans the same $v_{\rm min}$ space. Doing so we find

$$[E_{\rm low}^{\rm C}, E_{\rm high}^{\rm C}] = \frac{\mu_{\rm C}^2 m_N^{\rm D}}{\mu_{\rm D}^2 m_N^{\rm C}} [E_{\rm low}^{\rm D}, E_{\rm high}^{\rm D}]. \tag{5.5}$$

Given the modulation amplitude $\Delta R = (R(t_{\rm max}) - R(t_{\rm min}))/2$ observed by CoGeNT (in cpd/kg), and a specific choice of m_χ and C_T, we can invert Eq. (5.4) to solve

for $\int_{v_{\rm low}}^{v_{\rm high}} vg(v,t)dv$. This allows us to calculate the amplitude expected at DAMA (in cpd/kg)

$$\Delta R^{\rm D}_{\rm expec} = \frac{\bar{\epsilon}_{\rm D}(E^{\rm D}_{\rm R})\bar{F}^2_{\rm D}(E^{\rm D}_{\rm R})}{\bar{\epsilon}_{\rm C}(E^{\rm C}_{\rm R})\bar{F}^2_{\rm C}(E^{\rm C}_{\rm R})}\frac{C^{\rm D}_T}{C^{\rm C}_T}\frac{m^{\rm C}_N\mu^2_{\rm D}}{m^{\rm D}_N\mu^2_{\rm C}}\Delta R^{\rm C}_{\rm obs}\ . \tag{5.6}$$

We compare this with what is observed at DAMA. If both modulations arise from DM scattering, the expected and observed amplitude will be the same. Since no astrophysical parameters enter into this formula, the two experiments can be compared free from astrophysical uncertainties.

5.2 Comparing DAMA and CoGeNT

For the purposes of this analysis, we assume the DM only scatters off the sodium nuclei at DAMA. This is a very good approximation for the light DM that we consider. DAMA presents their time-dependent results in fixed energy ranges: 2-4 keVee, 2-5 keVee and 2-6 keVee. This can be converted to keV by dividing by the quenching factor for sodium, which we take as $q_{\rm Na} = 0.3$. Varying $q_{\rm Na}$ does not lead to significant differences in our results. We do not include channelling, as theoretical calculations indicate this is small [145].

The CoGeNT Collaboration has released the time-stamped data for independent analysis. We bin their data in the energy range that spans the same $v_{\rm min}$ space as DAMA. Statistics at CoGeNT are limited, therefore we concentrate on the 2-6 keVee bin at DAMA, as this corresponds to the largest energy range at CoGeNT and will therefore contain the most events. To convert from keV to keVee at CoGeNT, we use $E[\text{keVee}] = 0.199E[\text{keV}]^{1.12}$. For each energy range, we divide the 458 days of data into 15 time bins with a width of 30 days, and one final bin with a width of 8 days, correcting, when appropriate, for periods when the detector was not running.

In Fig. 5.1 we show the peak day found at DAMA and CoGeNT. The regions between the red lines indicate the preferred regions at 1σ (solid), 90% (dashed) and 2σ (dotted) after fitting to the residual events as a function of time measured by DAMA/NaI [76] and DAMA/LIBRA [77] over thirteen annual cycles. For each mass, we bin the data at CoGeNT in the relevant range determined from Eq. (5.5) and plot the results in blue. For both DAMA and CoGeNT, we fix the period of the modulation to be one year and consider variations of the phase that satisfy $\chi^2 \leq \chi^2_{\rm min} + \Delta\chi^2$. The variation in the peak day for different values of m_χ is expected, since for each mass the data are binned in a different energy range. As well as purely statistical fluctuations in the observed count rate, N-body simulations have shown that variations in the

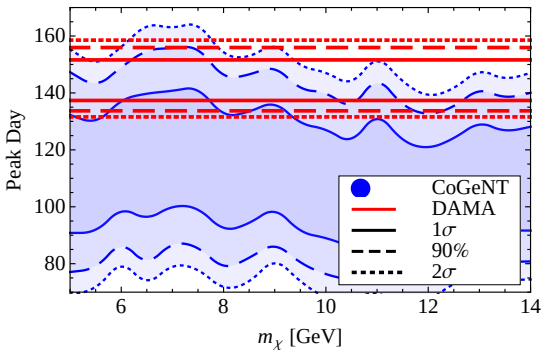

Figure 5.1: The peak day of the modulation signals measured by DAMA (red) and CoGeNT (blue) for different values of m_χ. At DAMA, we fit to the data in the 2-6 keVee energy range while at CoGeNT, we fit to the data in the energy range determined using Eq. (5.5). It is clear that the CoGeNT modulation generally peaks earlier in the year than DAMA's modulation signal, although there is agreement at 1σ for $m_\chi \sim 7$ GeV. The SHM predicts that the modulation peaks on Day 152 = 2nd June. These results are independent of the value of f_n/f_p.

peak day as a function of energy should be expected [38] and are also observed by DAMA (see Fig. 9 of [77]). Generally, the CoGeNT modulation peaks earlier in the year than DAMA. It is only for $m_\chi \sim 7$ GeV that there is agreement at 1σ.

Figure 5.2 shows the 1σ (solid), 90% (dashed) and 2σ (dotted) contours in the peak day against modulation amplitude plane for $m_\chi = 7$ GeV (left panels) and $m_\chi = 12$ GeV (right panels). In the upper panels, we choose $f_n/f_p = 1$ while in the lower panels $f_n/f_p = -0.7$. The choice $f_n/f_p = -0.7$ is phenomenologically motivated by the desire to suppress the event rate at xenon experiments [199, 160, 200, 3, 221]. Given the modulation amplitude measured at CoGeNT, we show in blue the preferred region calculated using Eq. (5.6) for the expected amplitude at DAMA. The red region shows the fit to the DAMA data measured over thirteen cycles. In our fits, we fix the period to be one year and subtract a constant rate at CoGeNT, determined from the value which minimises the χ^2. We proceed to find the values of the modulation amplitude and peak day that satisfy $\chi^2 \leq \chi^2_{\rm min} + \Delta\chi^2$.

The energy ranges at CoGeNT for $m_\chi = 7$ GeV and $m_\chi = 12$ GeV, determined from Eq. (5.5), are 0.70 – 2.38 keVee and 0.87 – 2.96 keVee respectively. In these energy ranges, the presence of an annual modulation is preferred over a constant event rate at 2.0σ and 2.4σ respectively. The purple solid horizontal line indicates the constraint from the unmodulated rate measured by CoGeNT. We integrate the unmodulated rate in the energy range, calculated using Eq. (5.5), after subtracting the L-shell EC contribution and a constant background. We map this onto the DAMA

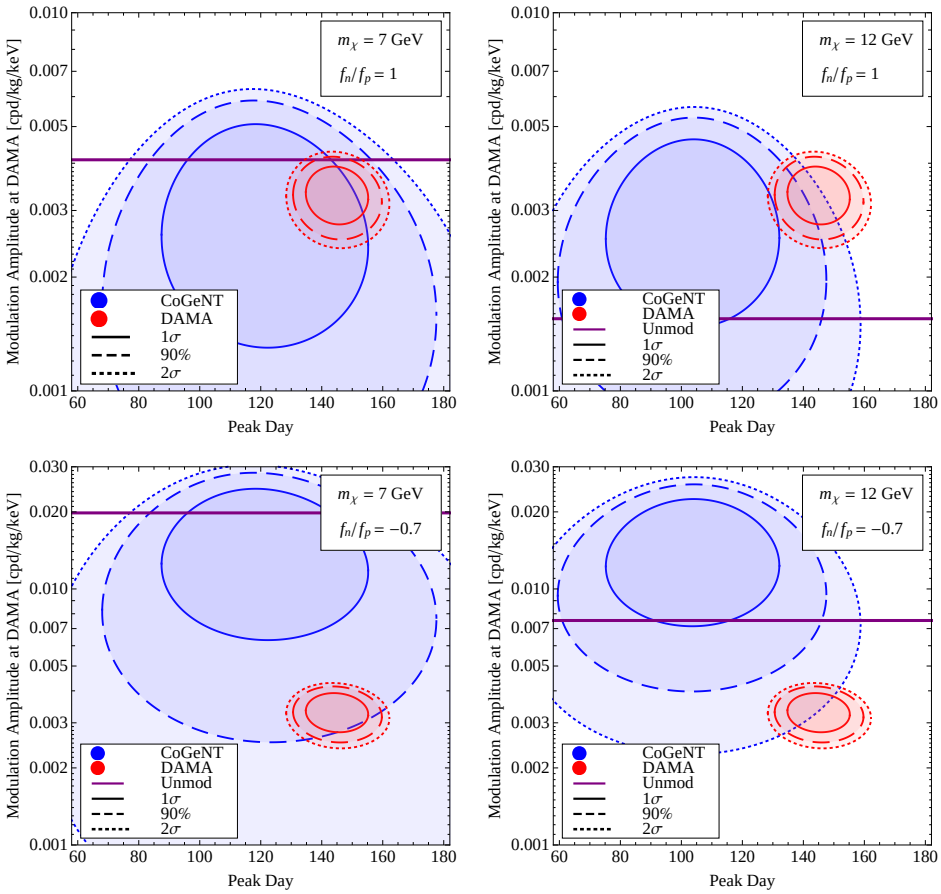

Figure 5.2: Best fit regions for DAMA and CoGeNT from a two parameter fit to the amplitude and peak day of the respective modulation signals. Day 152 = 2nd June. The blue region shows the amplitude and peak day expected at the DAMA detector based on what CoGeNT observe. The red contours show the regions obtained from fitting to the 2-6 keVee DAMA data in [76, 77]. In the left (right) panels $m_\chi = 7\,(12)$ GeV. In the upper (lower) panels $f_n/f_p = 1\,(-0.7)$. The purple solid line indicates the unmodulated rate at CoGeNT. Modulation amplitudes above this line are excluded. Note the lower panels have a different scale for the modulation amplitude.

detector using Eq. (5.6). A modulation amplitude above this line predicts a modulated rate which is larger than the unmodulated rate. A modulation amplitude above this line is excluded since it would predict a negative event rate in the winter. Although the regions favoured by CoGeNT are large due to the low statistics, we can already see that $m_\chi \sim 7$ GeV is preferred over 12 GeV and that the fit is worse for $f_n/f_p = -0.7$, where a larger modulation amplitude is generally predicted.

For 7 GeV and $f_n/f_p = 1$ (upper left panel), we see that there is good agreement between the DAMA and CoGeNT modulation amplitude and peak day. However, the modulation amplitude is close to the unmodulated limit, so a large modulation

fraction ($\sim$ 70%) is required to be consistent. We will return to this issue in the next section. For $f_n/f_p = -0.7$ (lower left panel), the best fit modulation amplitude predicted by CoGeNT is much larger than that observed by DAMA. However, the 90% regions do overlap and a smaller modulation fraction ($\sim$ 15%) is required to be consistent with the unmodulated rate. For 12 GeV and $f_n/f_p = 1$ (upper right panel), the CoGeNT unmodulated rate excludes all of the DAMA region. For $f_n/f_p = -0.7$ (lower right panel) it is only the DAMA and CoGeNT 2σ regions that are in agreement. We thus conclude that a 12 GeV DM particle with $f_n/f_p = 1$ or -0.7 is disfavoured, before applying constraints from other experiments.

5.3 Other constraints

CDMS II has analysed data over a similar energy range as CoGeNT in its low threshold Soudan Underground Laboratory germanium analysis [82] and Stanford Underground Facility silicon analysis [81].[2] Limits on an annual modulation signal have not been published but we can restrict the unmodulated rate, which we use to constrain the modulation fraction, defined as

$$\frac{R(t_{\rm max}) - R(t_{\rm min})}{R(t_{\rm max}) + R(t_{\rm min})}. \tag{5.7}$$

For the germanium analysis, we use the 35 kg-days of data collected between October 2006 and September 2008 from the T1Z5 detector, which has the best ionisation resolution. For the silicon analysis, we use the 24.64 kg-days collected between December 2001 and June 2002. To set conservative limits, we assume that all of the observed events arise due to DM. In Fig. 5.3, the 90% lower confidence limits on the modulation fraction for $f_n/f_p = 1$ (dotted) and $f_n/f_p = -0.7$ (solid) are shown. The blue (green) lines are from the germanium (silicon) analysis. We assume the modulation amplitude at DAMA is 0.0028 cpd/kg/keV, which we see from Fig. 5.2, is on the lower edge of the CoGeNT 90% region for $m_\chi = 7$ GeV. For each value of the mass, we use Eq. (5.5) to find the energy range at CDMS II which spans the same $v_{\rm min}$ space as the 2-6 keVee range at DAMA. As the energy range varies for each mass, discrete jumps occur whenever a measured event at CDMS II enters or leaves the energy range. For comparison, the purple dashed horizontal line shows the modulation fraction predicted from the SHM. We see that the modulation fraction required at

[2]Unpublished silicon data has also been presented in [204]. We do not consider it here due to uncertainties in calibrating the energy scale for nuclear recoils near threshold. We thank J. P. Filippini for discussions on this point.

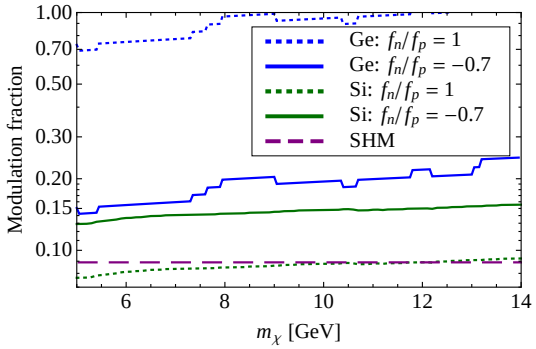

Figure 5.3: The 90% lower confidence limit on the fractional modulation required to be compatible with CDMS II. The blue (green) lines indicate constraints from the Ge (Si) analysis. The dotted (solid) line is for $f_n/f_p = 1\,(-0.7)$. For comparison, the purple horizontal dashed line shows the modulation fraction from the SHM.

DAMA and CoGeNT to be compatible with CDMS II-germanium is larger for both choices of f_n/f_p, while for CDMS II-silicon, is larger for $f_n/f_p = -0.7$.

The 2-6 keVee range at DAMA corresponds to 1.84-5.52 keV at a xenon-target experiment (for m_χ=7 GeV). We do not consider limits from XENON100 [89], as $\mathcal{L}_{\rm eff}$ has not been measured below 3 keV [222]. However, we can apply the limits from the S2 only analysis of XENON10 [87], which has a low energy threshold of 1.4 keV. The 15 kg-days of data were collected between 23rd August and 14th September. Since this is approximately half way between the maximum and minimum of the CoGeNT and DAMA modulation signals, we assume the measured rate is the same as the unmodulated rate. We use the parameterization for $\mathcal{Q}_{\rm y}$ given in [87] and assume all events arise due to DM. We do not apply the edge (in z) event rejection. For each mass, we again use Eq. (5.5) to find the energy range that spans the same $v_{\rm min}$ space as the 2-6 keVee range at DAMA, and assume a modulation amplitude of 0.0028 cpd/kg/keV. For $f_n/f_p = 1$, we find the required modulation fraction is $> 100\%$ for all masses we consider. Hence, under the assumptions we have made, XENON10 excludes all parameter space. For $f_n/f_p = -0.7$ the constraints are severely weakened; a modulation fraction greater than $\sim 2\%$ is required over the whole mass range, which is easily achievable.

5.4 Summary and Conclusions

We have presented a comparison of the CoGeNT and DAMA modulation signals free from astrophysical uncertainties, having assumed that both modulation signals arise due to elastically scattering DM. We found that the peak day of the CoGeNT

modulation is always earlier than the peak day of the DAMA modulation. The 1σ confidence regions do overlap in some parameter space, but the best fit points typically differ by ~ 30 days. The SHM, which assumes the DM is distributed isotropically, predicts a peak day close to 2nd June. If CoGeNT continue to measure a peak day at the lower edge of the DAMA confidence regions (around mid-May), there will be interesting consequences for DM galactic halo models.

For DM that couples equally to protons and neutrons ($f_n/f_p = 1$), we found the measured modulation amplitude at DAMA is consistent with that expected based on the CoGeNT results. However, the XENON10 S2 analysis excludes the whole mass range in question. Even if we were to ignore the XENON10 analysis, tension remains with the unmodulated CoGeNT rate and the constraint from CDMS II-germanium, which both require large modulation fractions. For $m_\chi = 12$ GeV, the CoGeNT unmodulated rate excludes the DAMA modulation signal. Moreover, for all masses we consider, the modulation fraction needs to be larger than $\sim 70\%$ to be consistent with the low energy analysis of CDMS II-germanium. The SHM predicts $\sim 9\%$, which is significantly smaller. Such large deviations from the SHM seem unrealistic. Therefore, based on the constraints from XENON10, CDMS II and the CoGeNT unmodulated rate, we conclude that elastically scattering DM with $f_n/f_p = 1$ is unlikely to be the source of the DAMA and CoGeNT modulation signals.

We also considered DM with isospin violating couplings $f_n/f_p = -0.7$. For this choice, the expected modulation amplitude at DAMA, calculated from the CoGeNT measurement, is generically higher than that observed at DAMA. For $m_\chi = 12$ GeV, we find that only the 2σ CoGeNT and DAMA regions overlap. However, for $m_\chi = 7$ GeV, amplitudes at the lower end of the CoGeNT 90% region are compatible. Furthermore, the CDMS II germanium and silicon constraints on the modulation fraction are milder, typically requiring modulation fractions $\sim 15\%$. This is still larger than that from the SHM, so if the DAMA and CoGeNT signals do arise from DM, the constraints from CDMS II indicate the galactic halo model must deviate from the SHM.

It is clear that the evidence for a modulation in the CoGeNT data is still tentative and that more data is required to definitively confirm a modulation. Fortunately, the CoGeNT-4 upgrade should provide much more data and significantly shrink the CoGeNT best fit regions. With more data, the approach presented here will serve as a useful complementary test on the consistency of DAMA and CoGeNT. In comparison to the usual method of displaying results in the $\sigma_n - m_\chi$ plane, this approach has the advantage that the results do not depend on any astrophysical parameters.

Chapter 6

Supersymmetry

In this chapter we provide a brief introduction to ($\mathcal{N} = 1$) supersymmetry (SUSY) [223, 224, 225].[1] Our ultimate goal is the construction of the minimal supersymmetric Standard Model (MSSM). As well as being much studied in its own right, it often serves as the starting point in the construction of new supersymmetric theories. On our journey to the MSSM, we will find it fruitful to introduce the superspace formalism, in which manifestly supersymmetric Lagrangians can be written down with relative ease. Since SUSY is manifestly not an exact symmetry of nature (where are the super-particles?), we must introduce the soft SUSY breaking terms, which parameterise the breaking of SUSY in a 'safe' way. This we do in Section 6.4. Finally, we end by mentioning the successes of SUSY, both theoretical and phenomenological. There are many good introductions to SUSY. The ones that have most influenced this chapter are [227, 228, 229, 230, 231].[2]

6.1 SUSY: A voyage through superspace

In this section we give a brief mathematical introduction to SUSY. SUSY is special as it is the only consistent non-trivial extension of the Poincaré group consistent with quantum field theories [232]. In addition to the usual Poincaré commutation relations, the Poincaré algebra can be extended (to a Super-Poincaré algebra) by

[1] A historical account of the development of SUSY can be found in [226].

[2] In particular, we follow the conventions of [229].

including the fermionic symmetry generators Q_A and $\overline{Q}_{\dot{A}}$, where $A, \dot{A} = \{1, 2\}$. The most important additional terms for our discussion are[3]

$$\{Q_A, Q_B\} = \{\overline{Q}_{\dot{A}}, \overline{Q}_{\dot{B}}\} = 0 \tag{6.1}$$

$$\{Q_A, \overline{Q}_{\dot{B}}\} = 2\sigma^{\mu}_{A\dot{B}} P_\mu \ , \quad \{\overline{Q}^{\dot{A}}, Q^B\} = 2\bar{\sigma}^{\mu A\dot{B}} P_\mu \ . \tag{6.2}$$

Here P_μ is the generator of translations, $\sigma^{\mu}_{A\dot{B}} \equiv (I, \vec{\sigma})$ and $\bar{\sigma}^{\mu A\dot{B}} \equiv (I, -\vec{\sigma})$, where $\vec{\sigma}$ are the usual Pauli matrices and I the identity matrix.

At this point it is useful to introduce four fermionic coordinates: θ^A and $\overline{\theta}_{\dot{A}}$. These are Grassmann variables satisfying

$$\{\theta^A, \theta^B\} = \{\theta^A, \overline{\theta}_{\dot{A}}\} = \{\overline{\theta}_{\dot{A}}, \overline{\theta}_{\dot{B}}\} = 0 \ . \tag{6.3}$$

By combining these 4-fermionic coordinates with the usual spatial and time dimensions, we can generalise 4-dimensional Minkowski space to an 8-dimensional superspace [233], with coordinates $(x^\mu, \theta^A, \overline{\theta}_{\dot{A}})$. It is also natural to generalise the usual notion of fields to superfields, which can be understood in terms of their finite power series expansion in θ and $\overline{\theta}$. Due to their Grassmann nature, powers of θ ($\overline{\theta}$) higher than $\theta\theta$ ($\overline{\theta}\overline{\theta}$) vanish.[4]

The action of the symmetry generators on a superfield can be reproduced using differential operator representations. In a similar manner to the usual relation $P^\mu = i\partial^\mu$, the fermionic generators can be represented by

$$Q_A = -i(\partial_A + i\sigma^{\mu}_{A\dot{B}} \overline{\theta}^{\dot{B}} \partial_\mu) \tag{6.4}$$

$$\overline{Q}_{\dot{A}} = i(\overline{\partial}_{\dot{A}} + i\theta^B \sigma^{\mu}_{B\dot{A}} \partial_\mu) \ , \tag{6.5}$$

where $\partial_A = \partial/\partial\theta^A$ and $\overline{\partial}_{\dot{A}} = \partial/\partial\overline{\theta}^{\dot{A}}$. These relations can be explicitly verified by substituting into Eqs. (6.1) and (6.2).

The fermionic coordinates allow us to rewrite Eq. (6.2) as a commutation relation

$$[\theta Q, \bar{\theta}\bar{Q}] = 2\theta\sigma^\mu\bar{\theta}P_\mu \tag{6.6}$$

Using the standard technique for Lie groups of exponentiating the generators, a general group element (ignoring Lorentz transformations) can be written as

$$L(x^\mu, \theta^A, \overline{\theta}_{\dot{A}}) = e^{i(-x^\mu P_\mu + \theta Q + \bar{\theta}\bar{Q})} \tag{6.7}$$

[3]For the full super-Poincaré algebra, see, for example, [227]

[4]We use the standard summation convention $\theta\theta = \theta^A\theta_A$ and $\bar{\theta}\bar{\theta} = \bar{\theta}_{\dot{A}}\bar{\theta}^{\dot{A}}$.

Hence, an infinitesimal SUSY transformation is $\delta_S(\alpha,\bar{\alpha}) = i(\alpha Q + \bar{\alpha}\bar{Q})$. It is convenient to introduce SUSY covariant derivatives, which transform covariantly under a SUSY transformation[5]

$$\mathcal{D}_A \equiv \partial_A - i\sigma^\mu_{A\dot{B}}\bar{\theta}^{\dot{B}}\partial_\mu \tag{6.8}$$

$$\overline{\mathcal{D}}_{\dot{A}} = -\bar{\partial}_{\dot{A}} + i\theta^B\sigma^\mu_{B\dot{A}}\partial_\mu \tag{6.9}$$

So far everything we have written holds for an arbitrary superfield. However, to describe chiral fermions and gauge bosons, we need only consider two irreducible representations of the SUSY algebra: the chiral and vector superfields. We consider each in turn.

6.1.1 Chiral superfields

In general, superfields do not transform under irreducible representations. However, irreducible representations can be found by imposing constraints. The first constraint we consider defines the left- (right-) chiral superfield $\Phi(\Phi^\dagger)$:

$$\overline{\mathcal{D}}_{\dot{A}}\Phi(x,\theta,\overline{\theta}) = 0 \;\text{ and }\; \mathcal{D}_A\Phi^\dagger(x,\theta,\overline{\theta}) = 0\ . \tag{6.10}$$

It should be clear from Eq. (6.9) that $\overline{\mathcal{D}}_{\dot{A}}\theta = 0$. It is also straightforward to verify that $\overline{\mathcal{D}}_{\dot{A}}y^\mu = 0$, where $y^\mu = x^\mu - i\theta\sigma^\mu\bar{\theta}$. Therefore, any function of these variables will satisfy $\overline{\mathcal{D}}_{\dot{A}}\Phi = 0$. Hence, a left-chiral superfield can be expressed as

$$\Phi(y,\theta) = \phi(y) + \sqrt{2}\theta\psi(y) + \theta\theta F(y)\ . \tag{6.11}$$

Here, ϕ is complex scalar field (usually called a sfermion), ψ_A a complex left-handed Weyl spinor and F an auxiliary complex scalar field. It is straightforward to find $\Phi(x,\theta,\overline{\theta})$ by substituting for y^μ and Taylor expanding. It is not particularly illuminating so we do not explicitly show it here.

Similarly, the right-chiral superfields are in general a function of $\overline{\theta}$ and $\bar{y}^\mu = x^\mu + i\theta\sigma^\mu\bar{\theta}$, so that $\Phi^\dagger(\bar{y},\bar{\theta}) = \phi^\star(\bar{y}) + \sqrt{2}\bar{\theta}\bar{\psi}(\bar{y}) + \bar{\theta}\bar{\theta}F^\star(\bar{y})$. We note that a product of left- (right-) chiral superfields is also a left- (right-) chiral superfield. This is not the case for a general product of left- and right-chiral superfields.

[5]That is, they satisfy $[D_A,\delta_s] = [\overline{D}_{\dot{A}},\delta_s] = 0$.

Applying an infinitesimal SUSY transformation to a left-chiral superfield, one finds that the components transform as

$$\delta_S\phi(x) = \sqrt{2}\alpha\psi(x) \qquad \text{(boson} \to \text{fermion)}, \tag{6.12}$$

$$\delta_S\psi_A(x) = \sqrt{2}\alpha_A F(x) - \sqrt{2}i\sigma^\mu_{A\dot{B}}\bar{\alpha}^{\dot{B}}\partial_\mu\phi(x) \qquad \text{(fermion} \to \text{boson)}, \tag{6.13}$$

$$\delta_S F(x) = \sqrt{2}i\partial_\mu(\psi(x)\sigma^\mu\bar{\alpha}) \qquad \text{(F} \to \text{total derivative)}. \tag{6.14}$$

Eq. (6.14) shows that the $\theta\theta$ term (the 'F-term') transforms as a total derivative. This implies $\int d^4x F(x)$ is invariant under SUSY transformations, assuming, as usual, that boundary terms vanish. This fact will be important when we come to construct field theories invariant under SUSY transformations.

6.1.2 Vector superfields

We have defined the chiral superfields, capable of describing the chiral fermions found in nature. We next consider vector superfields, which, as we will show, contain the gauge fields. Vector superfields satisfy the reality constraint

$$V(x,\theta,\bar{\theta}) = V^\dagger(x,\theta,\bar{\theta}) \ . \tag{6.15}$$

They can be constructed from chiral superfields Λ: in particular, the combination $i\Lambda - i\Lambda^\dagger$ satisfies Eq. (6.15). This allows us to define a 'supergauge transformation'

$$V \to V + i\Lambda - i\Lambda^\dagger. \tag{6.16}$$

The reality constraint Eq. (6.15) holds after this transformation, so V remains a vector superfield. This gauge freedom allows us to choose a gauge, called the 'Wess-Zumino gauge', in which only the physical fields remain. With this choice, the vector superfield is

$$V_{\rm WZ}(x,\theta,\bar{\theta}) = \theta\sigma^\mu\bar{\theta}A_\mu(x) + \theta\theta\,\bar{\theta}\bar{\lambda}(x) + \bar{\theta}\bar{\theta}\,\theta\lambda(x) + \frac{1}{2}\theta\theta\,\bar{\theta}\bar{\theta}D(x) \ . \tag{6.17}$$

Here A_μ is a gauge field, λ a Weyl fermion (usually called a gaugino) and D an auxiliary real scalar field. We can again consider an infinitesimal SUSY transformation on these fields. Being succinct, we only display the important result

$$\delta_S D(x) = i\partial_\mu(\lambda\sigma^\mu\bar{\alpha} + \bar{\lambda}\bar{\sigma}^\mu\alpha) \ , \tag{6.18}$$

which shows that the D-term, like the F-term, transforms as a total derivative. We will use this result to build SUSY invariant field theories, which we turn to next.

6.2 Building a supersymmetric Lagrangian

In this section we present the steps employed in constructing the Lagrangian of a supersymmetric field theory. By definition, we want the action to be invariant under SUSY transformations:

$$\delta_S \int d^4x\, \mathcal{L}(x) = 0 \ . \tag{6.19}$$

This occurs if the Lagrangian transforms as a total derivative. Here we use the knowledge gained in the previous section, namely, that F-terms and D-terms transform as total derivatives under SUSY transformations. Thus Lagrangians constructed from F- and D-terms will transform in the required way. This is the key insight in constructing supersymmetric field theories. The simplest way to extract the D-term or F-term uses integration over Grassmann variables. By definition:

$$\begin{aligned} \int d^2\theta\ \left[f(x) + \theta^A g_A(x) + \theta\theta\, h(x)\right] &\equiv h(x) \\ \int d^2\bar{\theta}\, [f(x) + \bar{\theta}_{\dot{A}} g^{\dot{A}}(x) + \bar{\theta}\bar{\theta}\, h(x)] &\equiv h(x) \\ \int d^4\theta\, [f(x) + \cdots + \theta\theta\, \bar{\theta}\bar{\theta}\, h(x)] &\equiv h(x) \end{aligned} \tag{6.20}$$

for arbitrary functions of $f(x)$, $g(x)$ and $h(x)$. Thus a general Lagrangian can be written as

$$\mathcal{L} = \int d^4\theta\, \Delta_D + \left[\int d^2\theta\, \Delta_F + h.c.\right] \ , \tag{6.21}$$

where Δ_D and Δ_F are general combinations of vector and chiral superfields respectively.

Ultimately we would like to construct theories with chiral fermions and (non-) Abelian gauge bosons since these are observed in nature. In the following, we will gradually increase the complexity of the theories we consider until we have included all the interactions found in the Standard Model. We begin with the simplest theory, containing only chiral superfields.

6.2.1 Theories with interacting chiral superfields

A general Lagrangian with chiral superfields can be written as

$$\mathcal{L} = \int d^4\theta\, K(\Phi_i, \Phi_j^\dagger) + \left[\int d^2\theta\, \mathcal{W}(\Phi_i) + h.c.\right] \ , \tag{6.22}$$

where $K(\Phi_i, \Phi_j^\dagger)$ and $\mathcal{W}(\Phi_i)$ are known as the Kähler potential and superpotential respectively. The fact that $\mathcal{W}$ depends only on Φ_i and not $\Phi_i^\dagger$ is known as holomorphy.

It lies behind many of the powerful results obtained in supersymmetric theories (see, for example, [234]). It is useful to consider the expansion of $\mathcal{W}$ in powers of θ:

$$\begin{aligned}\mathcal{W}(\Phi_i) &\equiv \mathcal{W}(\phi_i + \sqrt{2}\theta\psi_i + \theta\theta\, F_i) \\ &= \mathcal{W}(\phi_i) + \frac{\partial \mathcal{W}}{\partial \phi_i}\sqrt{2}\theta\psi_i + \theta\theta\left[\frac{\partial \mathcal{W}}{\partial \phi_i}F_i - \frac{1}{2}\frac{\partial^2 \mathcal{W}}{\partial \phi_i \partial \phi_j}\psi_i\psi_j\right] \ .\end{aligned} \tag{6.23}$$

After integrating over the Grassmann variables, only the term in square brackets remains.

For the Kähler potential, we consider the simple choice $K = \Phi_i^\dagger \Phi_i$. The integration over Grassmann variables gives

$$\int d^4\theta\, \Phi_i^\dagger \Phi_i = \partial_\mu \phi_i^\star \partial^\mu \phi_i + i\bar{\psi}_i \bar{\sigma}^\mu \partial_\mu \psi_i + F_i^\star F_i \ . \tag{6.24}$$

We recognise the first two terms as the kinetic term for a complex scalar and Weyl fermion respectively. The auxiliary field F may be eliminated from Eqs. (6.23) and (6.24) through its Euler-Lagrange equation, which gives

$$F_i^\star = -\frac{\partial \mathcal{W}}{\partial \phi_i} \ . \tag{6.25}$$

Substituting everywhere for F_i allows us to express the Lagrangian solely in terms of the dynamical fields

$$\begin{aligned}\mathcal{L} &= \int d^4\theta\, \Phi_i^\dagger \Phi_i + \left[\int d^2\theta\, \mathcal{W}(\Phi_i) + h.c.\right] \\ &= \partial_\mu \phi_i^\star \partial^\mu \phi_i + i\bar{\psi}_i \bar{\sigma}^\mu \partial_\mu \psi_i - \left[\frac{1}{2}\frac{\partial^2 \mathcal{W}}{\partial \phi_i \partial \phi_j}\psi_i\psi_j + h.c.\right] - V(\phi, \phi^\star) \ .\end{aligned} \tag{6.26}$$

Here we have defined the scalar potential $V(\phi, \phi^\star)$,

$$V(\phi, \phi^\star) = \left|\frac{\partial \mathcal{W}}{\partial \phi_i}\right|^2 = F_i^\star F_i \ . \tag{6.27}$$

As an explicit example, we consider the Wess-Zumino model [235], a simple theory with one chiral superfield in which

$$K = \Phi^\dagger \Phi \quad \text{and} \quad \mathcal{W} = \frac{m}{2}\Phi^2 + \frac{g}{3}\Phi^3 \ . \tag{6.28}$$

Using the techniques we have developed, the component form Lagrangian is

$$\begin{aligned}\mathcal{L} = \partial_\mu \phi_i^\star \partial^\mu \phi_i + i\bar{\psi}_i \bar{\sigma}^\mu \partial_\mu \psi_i - \frac{1}{2}m(\psi\psi + \bar{\psi}\bar{\psi}) \\ - g(\phi\psi\psi + \phi^\star \bar{\psi}\bar{\psi}) - \left|m\phi + g\phi^2\right|^2 \ .\end{aligned} \tag{6.29}$$

We see there is a complex scalar and Weyl fermion each of mass m, a Yukawa interaction with coupling g and a quartic scalar interaction with coupling g^2. That these relations hold in supersymmetric theories is important, as we will see when we consider the 'hierarchy problem' in Section 6.5.1.

6.2.2 Abelian gauge theories

A $U(1)$ gauge transformation of the chiral superfields is defined by

$$\Phi_i' = e^{-2iq_i\Lambda(x,\theta,\bar{\theta})}\Phi_i \quad \text{with} \quad \overline{\mathcal{D}}_{\dot{A}}\Lambda = 0 \ , \tag{6.30}$$

$$\Phi_i'^{\dagger} = e^{2iq_i\Lambda(x,\theta,\bar{\theta})^{\dagger}}\Phi_i^{\dagger} \quad \text{with} \quad \mathcal{D}_A\Lambda^{\dagger} = 0 \ , \tag{6.31}$$

where q_i is the gauge coupling. The condition imposed on Λ ensures the chiral nature of Φ remains after the gauge transformation. One can easily check that the kinetic term $\Phi_i^{\dagger}\Phi_i$ is not gauge invariant. However, if we introduce a gauge vector superfield V,[6] which transforms as in Eq. (6.16) under a gauge transformation, then the combination $\Phi_i^{\dagger}\exp(2q_iV)\Phi_i$ is gauge invariant. After some lengthy algebra, it can be shown that

$$\begin{aligned}\int d^4\theta\, \Phi_i^{\dagger}e^{2q_iV}\Phi_i = |\mathcal{D}_\mu\phi_i|^2 + i\bar{\psi}_i\bar{\sigma}^\mu\mathcal{D}_\mu\psi_i + F_i^{\star}F_i \\ + q_iD\,|\phi_i|^2 - \sqrt{2}q_i(\bar{\lambda}\bar{\psi}_i\phi_i + h.c.) \ ,\end{aligned} \tag{6.32}$$

where $\mathcal{D}_\mu = \partial_\mu + iq_iA_\mu$ is the familiar $U(1)$ covariant derivative. We see that this contains the correct kinetic terms for the complex scalar and Weyl fermion, as well as a gaugino-fermion-sfermion Yukawa interaction.

The generalisation of the gauge field strength is

$$W_A = -\frac{1}{4}\bar{\mathcal{D}}\bar{\mathcal{D}}\mathcal{D}_AV \qquad (\overline{W}_{\dot{A}} = -\frac{1}{4}\mathcal{D}\mathcal{D}\bar{\mathcal{D}}_{\dot{A}}V) \ . \tag{6.33}$$

It is straightforward to check that this object is chiral and gauge invariant.[7] After some more lengthy algebra, it can be shown that

$$\int d^2\theta\,\frac{1}{4}W^AW_A + \int d^2\bar{\theta}\,\frac{1}{4}\overline{W}_{\dot{A}}\overline{W}^{\dot{A}} = -\frac{1}{4}F^{\mu\nu}F_{\mu\nu} + i\bar{\lambda}\bar{\sigma}^\mu\partial_\mu\lambda + \frac{1}{2}D^2 \ , \tag{6.34}$$

which we recognise as the usual kinetic term for the $U(1)$ gauge field with $F^{\mu\nu} = \partial^\mu A^\nu - \partial^\nu A^\mu$, a kinetic term for the gaugino and a non-derivative term for the auxiliary field D.

[6] Throughout we work in the Wess-Zumino gauge.

[7] Use that $\mathcal{D}_A\mathcal{D}_B\mathcal{D}_C = 0$, $\overline{\mathcal{D}}_{\dot{A}}\Phi = 0$ and $\{\mathcal{D}_A, \overline{\mathcal{D}}_{\dot{A}}\} = 0$.

As with the F-term, the auxiliary field D can be eliminated from Eqs. (6.32) and (6.34) via its Euler-Lagrange equation. Doing so we find

$$D = -q_i \left|\phi_i\right|^2 \ . \tag{6.35}$$

Bringing everything together, the Lagrangian solely in terms of the dynamical fields is

$$\begin{aligned}\mathcal{L} &= \int d^4\theta\, \Phi_i^\dagger e^{2q_i V}\Phi_i + \left[\int d^2\theta\, \left\{\mathcal{W}(\Phi_i) + \frac{1}{4}W^A W_A\right\} + h.c.\right] \\ &= \left|\mathcal{D}_\mu\phi_i\right|^2 + i\bar{\psi}_i\bar{\sigma}^\mu\mathcal{D}_\mu\psi_i - \frac{1}{4}F^{\mu\nu}F_{\mu\nu} + i\bar{\lambda}\bar{\sigma}^\mu\partial_\mu\lambda \\ &\quad - \sqrt{2}q_i(\bar{\lambda}\bar{\psi}_i\phi_i + h.c.) - \left(\frac{1}{2}\frac{\partial^2\mathcal{W}}{\partial\phi_i\partial\phi_j}\psi_i\psi_j + h.c.\right) - V(\phi,\phi^\star)\ .\end{aligned} \tag{6.36}$$

In this case, the scalar potential $V(\phi,\phi^\star)$ is given by

$$V(\phi,\phi^\star) = F_i^\star F_i + \frac{1}{2}D^2\ . \tag{6.37}$$

6.2.3 Non-Abelian gauge theories

The generalisation of the Abelian case to the non-Abelian case is straightforward. The generators T^a of the gauge group satisfy the algebra $[T^a, T^b] = if_{abc}T^c$, where f_{abc} are the structure constants and we normalise such that $\mathrm{Tr}[T^aT^b] = \frac{1}{2}\delta^{ab}$. The generalisation of the gauge transformations of the chiral and vector superfields are

$$\begin{aligned}\Phi_i^{'} &= e^{-2ig\Lambda_{ij}}\Phi_j \quad \text{with} \quad \overline{\mathcal{D}}_{\dot{A}}\Lambda = 0\ , \\ \Phi_i^{'\dagger} &= \Phi_j^\dagger e^{2ig\Lambda_{ji}^\dagger} \quad \text{with} \quad \mathcal{D}_A\Lambda^\dagger = 0\ , \\ e^{2gV_{ij}^{'}} &= e^{-2ig\Lambda_{ik}^\dagger}e^{2gV_{kl}}e^{2ig\Lambda_{lj}}\ ,\end{aligned} \tag{6.38}$$

where g is the gauge coupling and we have defined the matrices $\Lambda_{ij} = T_{ij}^a\Lambda^a$ and $V_{ij} = T_{ij}^aV^a$.

The field strength tensor in the non-Abelian case is defined by

$$W_A = -\frac{1}{4}\bar{\mathcal{D}}\bar{\mathcal{D}}e^{-2gV}\mathcal{D}_A e^{2gV} \qquad (\overline{W}_{\dot{A}} = -\frac{1}{4}\mathcal{D}\mathcal{D}e^{2gV}\bar{\mathcal{D}}_{\dot{A}}e^{-2gV})\ . \tag{6.39}$$

In this case, W_A is not invariant under a gauge transformation but rather transforms as

$$W_A \to e^{-2ig\Lambda}W_A e^{2ig\Lambda} \qquad \left(\overline{W}_{\dot{A}} \to e^{2ig\Lambda}\overline{W}_{\dot{A}}e^{-2ig\Lambda}\right)\ . \tag{6.40}$$

However, it is straightforward to verify that the term $\mathrm{Tr}\left[W^AW_A\right]$ is gauge invariant.

In the Wess-Zumino gauge, terms V^n with $n > 2$ vanish, therefore it is convenient to consider the expansion of Eq. (6.39) in powers of V. Defining W_A^a by

$$W_A = 2gW_A^a T^a \tag{6.41}$$

and carrying out the expansion, we find

$$W_A^a = -\frac{1}{4}\bar{\mathcal{D}}\bar{\mathcal{D}}\left[\mathcal{D}_A V^a + igf^{abc}\left(\mathcal{D}_{\mathcal{A}} V^b\right) V^c\right] \ . \tag{6.42}$$

Finally, expressing the Lagrangian solely in terms of the dynamical fields

$$\begin{aligned}\mathcal{L} &= \int d^4\theta\, \Phi_i^\dagger e^{2gV_{ij}}\Phi_j + \left[\int d^2\theta\, \left\{\mathcal{W}(\Phi_i) + \frac{1}{4}W^{aA}W_A^a\right\} + h.c.\right] \\ &= (\mathcal{D}_{ij}^\mu\phi_j)^\dagger(\mathcal{D}_{\mu ik}\phi_k) + i\bar{\psi}_i\bar{\sigma}^\mu\mathcal{D}_{\mu ij}\psi_j - \frac{1}{4}F^{a\mu\nu}F_{\mu\nu}^a + i\lambda^a\sigma^\mu\tilde{\mathcal{D}}_\mu\bar{\lambda}^a \\ &\quad - \sqrt{2}g(\bar{\lambda}^a\bar{\psi}_i T_{ij}^a\phi_j + h.c.) - \left(\frac{1}{2}\frac{\partial^2\mathcal{W}}{\partial\phi_i\partial\phi_j}\psi_i\psi_j + h.c.\right) - V(\phi,\phi^\star)\ ,\end{aligned} \tag{6.43}$$

where $F_{\mu\nu}^a = \partial_\mu A_\nu^a - \partial_\nu A_\mu^a - gf^{abc}A_\mu^b A_\nu^c$, $\mathcal{D}_{ij}^\mu = \delta_{ij}\partial^\mu + igA^{\mu a}T_{ij}^a$ and $\tilde{\mathcal{D}}_\mu\bar{\lambda}^a = \partial_\mu\bar{\lambda}^a - gf^{abc}A_\mu^b\bar{\lambda}^c$. In this case, the scalar potential $V(\phi,\phi^\star)$ is given by

$$V(\phi,\phi^\star) = F_i^\star F_i + \frac{1}{2}D^a D^a \ , \tag{6.44}$$

where $D^a = -g\phi_i^\dagger T_{ij}^a\phi_j$.

This completes our discussion of theories containing the matter and gauge fields found in nature. With the all of the formalism now in place, we turn to consider the supersymmetric generalisation of the Standard Model.

6.3 The MSSM

We are now in a position to write down the supersymmetric part of the minimal supersymmetric Standard Model (MSSM) [236]. The model is minimal in that it adds the fewest additional particles to the Standard Model; in additional to adding the superpartner of every known particle, an extra Higgs doublet is also required for reasons we will explain below.

The gauge symmetry group of the Standard Model is $SU(3) \times SU(2)_L \times U(1)_Y$ [237, 238, 239]. Therefore, in the MSSM we include three vector superfields, one for each gauge group, to accommodate the experimentally observed gauge bosons. We upgrade all of the matter fields of the Standard Model to chiral superfields. In Table 6.1, the fundamental superfields and component fields of the MSSM are listed,

Superfield	Component fields	$SU(3)$	$SU(2)_L$	$U(1)_Y$	Nomenclature
L_i	$\ell_{iL} = (\nu_{iL},\, e_{iL})$ $\tilde{\ell}_{iL} = (\tilde{\nu}_{iL},\, \tilde{e}_{iL})$	1	2	-1	Leptons
$\bar{E}_i$	e^c_{iL} $\tilde{e}^\star_{iR}$	1	1	2	& Sleptons
Q_i	$q_{iL} = (u_{iL},\, d_{iL})$ $\tilde{q}_{iL} = (\tilde{u}_{iL},\, \tilde{d}_{iL})$	3	2	$\frac{1}{3}$	Quarks
$\bar{U}_i$	u^c_{iL} $\tilde{u}^\star_{iR}$	$\bar{3}$	1	$-\frac{4}{3}$	&
$\bar{D}_i$	d^c_{iL} $\tilde{d}^\star_{iR}$	$\bar{3}$	1	$\frac{2}{3}$	Squarks
H_u	$H_u = (H_u^+,\, H_u^0)$ $\tilde{H}_u = (\tilde{H}_u^+,\, \tilde{H}_u^0)$	1	2	1	Higgs fields
H_d	$H_d = (H_d^0,\, H_d^-)$ $\tilde{H}_d = (\tilde{H}_d^0,\, \tilde{H}_d^-)$	1	2	-1	& Higgsinos
V_Y	B_μ $\tilde{B}$	1	1	0	B boson & Bino
V_W^a	W_μ $\tilde{W}^a$	1	3	0	W boson & Winos
V_G^a	G_μ $\tilde{G}^a$	8	1	0	Gluons & Gluinos

Table 6.1: The chiral and vector superfields of the MSSM with their associated gauge charges.

together with their charges under the gauge groups.[8] As with the Standard Model, there are three generations of quarks and leptons (and their superpartners), labelled by the subscript i in Table 6.1.

As in the Standard Model, the electroweak symmetry $SU(2)_L \times U(1)_Y$ is broken to electromagnetism $U(1)_{\rm EM}$ through the Higgs mechanism [240, 241, 242]. However, unlike in the Standard Model, two Higgs doublets are required. In the Standard Model, H_u and $H_u^\star$ can be used to give masses to all of the fermions. This is not

[8]The hypercharge Y of each field is related to the electromagnetic charge and the third component of left isospin T_3 though $Q = T_3 + \frac{Y}{2}$.

possible in the MSSM; a second Higgs doublet with hypercharge $-1/2$ is required to give mass to the leptons and down quark. This is for two reasons. The first reason is due to the holomorphy of the superpotential, which forbids the use of both H_u and $H_u^\star$. The second reason is for anomaly cancellation. In a theory with chiral fermions, it is possible that gauge anomalies are present in the theory [243]. With one Higgs chiral superfield, the MSSM would have one additional chiral fermion and a gauge anomaly would exist. However, adding a second Higgs chiral superfield with opposite hyper charge adds one more chiral fermion, and all anomalies cancel.

The extra Higgs doublet means there will be five massive Higgs bosons (three degrees of freedom from the original eight are 'eaten' in the Higgs mechanism) in the particle spectrum, as opposed to the single one in the Standard Model. After electroweak symmetry breaking, the neutral Higginos $\tilde{H}_u^0$ and $\tilde{H}_d^0$ mix with the neutral gauginos $\tilde{B}$ and $\tilde{W}$ to form four neutralinos $\tilde{\chi}_i^0$. Similarly, the charged components $\tilde{H}_u^\pm$, $\tilde{H}_d^\pm$ and $\tilde{W}^\pm$ mix to form charginos $\tilde{\chi}_i^\pm$.

The Lagrangian of the MSSM consists of kinetic terms for the gauge and matter fields as well as the superpotential. The kinetic pieces can be written down using the formalism constructed in the previous sections, therefore, here we only explicitly write down the superpotential. It is constructed by writing down all terms permitted by the gauge symmetries[9]

$$\mathcal{W} = \mu H_u \cdot H_d - y_{ij}^e H_d \cdot L_i \bar{E}_j - y_{ij}^d H_d \cdot Q_i \bar{D}_j - y_{ij}^u Q_i \cdot H_u \bar{U}_j + \mathcal{W}_{RPV} \ , \tag{6.45}$$

where y are the Yukawa couplings and μ is a mass term. Any of the terms from

$$\mathcal{W}_{RPV} \in \{L_i \cdot H_u,\ L_i \cdot L_j \bar{E}_k,\ L_i \cdot Q_j \bar{D}_k,\ \bar{U}_i \bar{D}_j \bar{D}_k\} \tag{6.46}$$

are also consistent with the gauge symmetries, but lead to phenomenological problems since they violate lepton or baryon number. For example, when $\bar{U}_i \bar{D}_j \bar{D}_k$ and $L_i \cdot Q_j \bar{D}_k$ are included in the superpotential, the proton can decay via $p \to \pi^0 e^+$. We can use dimensional analysis to estimate the proton lifetime. Assuming order one couplings, we find

$$\tau_p \sim \frac{m_{\tilde{q}}^4}{m_p^5} \sim \left(\frac{1 \text{ TeV}}{m_{\tilde{q}}}\right)^4 10^{-9} \text{ s} \ , \tag{6.47}$$

where m_p and $m_{\tilde{q}}$ are the proton and squark masses respectively. Given the experimental limit $\tau_p > 8 \times 10^{33}$ years [244], at least one of these terms must have an extremely small coupling in the superpotential.

[9] We use the notation $A \cdot B \equiv \epsilon_{CD} A^C B^D$, where $\epsilon_{11} = \epsilon_{22} = 0$ and $\epsilon_{21} = -\epsilon_{12} = 1$.

R-parity is the standard way to forbid all of the operators in Eq. (6.46).[10] This is a discrete $\mathbb{Z}_2$ symmetry under which all Standard Model particles are even and all superpartners odd. For a given field, R-parity can be calculated from $(-1)^{3(B-L)+2S}$, where B, L and S are baryon number, lepton number and the spin of the field. The R-parity of the chiral superfield is the same as the R-parity of the scalar component. Only terms which are even under the R-parity are kept in the superpotential.

The presence of R-parity has important implications for dark matter. The lightest particle that is odd under R-parity is stable. Since only superpartners are R-parity odd, SUSY naturally predicts that the lightest supersymmetric particle (LSP) is stable on cosmological time scales. Furthermore, if the LSP only interacts through the weak interactions (as the sneutrinos and neutralinos do), we have a natural WIMP candidate.

6.4 Supersymmetry breaking

Exact SUSY implies that a particle and its superpartner have the same mass. Since we have not observed a selectron at 511 keV, or any other particles degenerate in mass but with a different spin, we must conclude that SUSY, if a symmetry of nature, is broken. In this section we discuss the conditions required to break (global) SUSY.

The condition for the vacuum $|\Omega\rangle$ to be invariant under a SUSY transformation is

$$\delta_s|\Omega\rangle = i(\alpha^A Q_A + \bar{\alpha}_{\dot{A}}\overline{Q}^{\dot{A}})|\Omega\rangle = 0 \ . \tag{6.48}$$

This implies $Q_A|\Omega\rangle = 0$ and $\overline{Q}^{\dot{A}}|\Omega\rangle = 0$ if SUSY is a symmetry of the vacuum.

The relation $\sigma^{\mu}_{A\dot{B}}\bar{\sigma}^{\nu\dot{B}A} = 2\eta^{\mu\nu}$ allows us to invert the SUSY algebra (Eq. (6.2)), solving for P_μ. The vacuum expectation value (vev) of the Hamiltonian can therefore be written as

$$\langle\Omega|H|\Omega\rangle = \langle\Omega|P_0|\Omega\rangle = \frac{1}{4}\langle\Omega|\{Q_1, \overline{Q}_{\dot{1}}\} + \{Q_2, \overline{Q}_{\dot{2}}\}|\Omega\rangle \ . \tag{6.49}$$

It follows that if the vacuum has a non-zero vev, $Q_A|\Omega\rangle \neq 0$ or $\overline{Q}^{\dot{A}}|\Omega\rangle \neq 0$ and (global) SUSY is not a symmetry of the vacuum.

The Lagrangian for a general theory with a non-Abelian gauge symmetry and chiral fields is given in Eq. (6.43). The only fields that can have a non-zero vev, without breaking Lorentz invariance, are the scalar fields. Thus, if the Hamiltonian

[10] There is one other discrete anomaly free symmetry that can forbid the dangerous terms that lead to proton decay. This is baryon triality [245]. We do not discuss is further because it does not lead to a sparticle that is stable on cosmological time scales.

has a non-zero vev, we should look to the scalar potential of the theory, given in Eq. (6.44). As this is a sum of squares, a non-zero value of F_i or D^a will lead to a vev for the Hamiltonian, and thus, a theory in which SUSY is spontaneously broken. These two types of breaking, when $\langle\Omega|F|\Omega\rangle \neq 0$ or $\langle\Omega|D|\Omega\rangle \neq 0$, are usually called F-term and D-term breaking respectively.

6.4.1 Soft breaking

There are many ways in which SUSY can be broken (see [246] for an introduction). Therefore, most phenomenological analyses do not explicitly give the details of the SUSY breaking but rather, parameterise the effects by including 'soft terms' in the Lagrangian. A special property of SUSY theories, which we will consider in more detail in the next section, is they do not have quadratic divergences. Here 'soft' means that the additional terms do not reintroduce any quadratic diverges to the theory. The full set of soft terms was classified in [247]. They are

- Scalar mass terms: $-m^2_{\phi_i} |\phi_i|^2$
- Gaugino mass terms: $-M_{\lambda_i} \lambda^a_i \lambda_{ai}$
- Trilinear scalar A-terms: $-A_{ijk}\phi_i\phi_j\phi_k$
- Bilinear scalar B-terms: $-B_{ij}\phi_i\phi_j + h.c.$
- Linear scalar C-terms: $-C_i\phi_i$.

The MSSM does not have any gauge singlet scalars so cannot have any C-terms. The only B-term arises in the Higgs sector: $-B_\mu H^0_u H^0_d + h.c.$. Each scalar particle and gaugino gets a mass term, and there are many A-terms allowed by gauge invariance.

The large number of soft terms introduces many additional free parameters to the MSSM compared to the Standard Model. However, once the soft terms and the μ term in the superpotential are specified, all of the phenomenology of the MSSM is in principle, completely determined.

6.5 The attractiveness of SUSY

Much research has been carried out into supersymmetric theories and their consequences and it is probably the most expected 'Beyond the Standard Model' theory to be discovered at the LHC. We end this chapter by considering some of the reasons for its popularity.

We have already mentioned some of the mathematical reasons why SUSY has attracted so much attention: it is the only non-trivial extension of the Poincaré group and powerful results arise from holomorphy of the superpotential. SUSY has also played an essential and central role in string theory, although string theory does not provide a reason for why the symmetry should remain unbroken to the electroweak scale.

Of course, mathematical elegance does not guarantee that SUSY has anything to do with nature. However, there are phenomenological reasons to believe that SUSY is a symmetry of nature that is softly broken at the weak scale. We briefly outline these reasons.

6.5.1 The hierarchy problem

The hierarchy problem is probably the best reason why there is a 'good' chance that SUSY will soon be discovered. It is the most serious problem with the Standard Model and its resolution requires new physics at $\mathcal{O}(1)$ TeV [248]. In high energy physics, there are at least two fundamental scales: $M_{\text{Planck}} \sim 10^{19}$ GeV, the scale of quantum gravity and $M_{\text{Weak}} \sim 10^2$ GeV, the electroweak symmetry breaking scale of the Standard Model. Understanding the large disparity of these scales and how such a large difference can remain stable against quantum corrections is the hierarchy problem.

To demonstrate the influence of the high energy scale on low energy phenomenology, we consider the one loop correction to a scalar boson's mass m_H from a fermion running in a loop. To make contact with the Standard Model, we will imagine that the scalar is the Higgs boson and the fermion is the top quark. The one loop correction is

$$\delta m_H^2 \sim \mathcal{O}\left(-\frac{y^2}{16\pi^2}\Lambda^2\right) \ , \tag{6.50}$$

where y is a Yukawa coupling and Λ is the ultraviolet cutoff for the theory. In the Standard Model, this would be M_{Planck}. This correction, quadratic in the UV cutoff, drives the scalar mass close to the highest scale in the theory.

SUSY helps to tame this problem by introducing additional scalars in the theory with quartic interactions y^2 (see end of Section 6.2.1). The correction from these scalar bosons comes in with a different sign due to the different statistics

$$\delta m_H^2 \sim \mathcal{O}\left(\frac{y^2}{16\pi^2}\Lambda^2\right) \tag{6.51}$$

and exactly cancels the contribution from the fermion. In fact, SUSY cancels all

quadratic divergences to all orders in perturbation theory. When SUSY is softly broken, the terms do not cancel exactly, but rather we find

$$\delta m_H^2 \sim \mathcal{O}\left(\frac{y^2}{16\pi^2}(m_f^2 - m_{\tilde{f}}^2)\right) \ , \tag{6.52}$$

where m_f and $m_{\tilde{f}}$ are the fermion mass and sfermion mass respectively. Thus, in order that the correction should not be too large, the sfermion mass should not be very different from the fermion mass.

6.5.2 Gauge coupling unification and radiative electroweak symmetry breaking

In the 1970s it was realised that the Standard Model gauge groups could be simply embedded into a single gauge group (a grand unified theory or GUT) such as $SU(5)$ [249]. Furthermore, the renormalisation group (RG) equations showed that the couplings approached each other at a high scale [250]. In SUSY GUTs, the addition of sparticles at $\mathcal{O}(1$ TeV) changes the running [251]. Precision measurements from LEP indicated that the unification of couplings is much more precise in supersymmetric theories, unifying at $\sim 2 \times 10^{16}$ GeV [252].

In the Standard Model, a negative mass squared for the Higgs particle is required for electroweak symmetry breaking to occur. While in the Standard Model this condition seems rather ad hoc, since the mass squared is introduced by hand, SUSY can provide a more natural explanation for why the electroweak symmetry is broken. Starting with positive masses for all of the scalar particles at the GUT scale, the large top Yukawa coupling tends to drive the mass squared of H_u^0 and H_d^0 apart as the masses evolve to low energies via the RG equations. Over a large region of parameter space, the low energy parameters satisfy the conditions necessary to break the electroweak symmetry. Thus, SUSY can provide a dynamical explanation for electroweak symmetry breaking [253].

6.5.3 Dark matter

Finally, as we have already mentioned, supersymmetric theories can provide a natural WIMP dark matter candidate. Although much attention has been focussed on the neutralino, in simple extensions of the MSSM, the sneutrino can also provide a good dark matter candidate. We will explore this in detail in Chapter 7.

Chapter 7

Neutrino-Flavoured Sneutrino Dark Matter

The substantial observational evidence for non-baryonic dark matter (DM) is one of the clearest calls for new physics beyond-the-Standard-Model, specifically the existence of an exotic stable or very-long-lived massive particle or particles. All this evidence, however, is indirect in form, and to-date does not fix the nature of the DM particle beyond requiring it to be colour and electromagnetically neutral and relatively weakly self-interacting. Despite this ignorance, one particular candidate has tended, until recently, to dominate theoretical speculation—the neutralino of the minimal supersymmetric (SUSY) extension of the Standard Model, the MSSM. Although the neutralino is the lightest supersymmetric particle (LSP) over substantial regions of parameter space, and thus stable if R-parity conservation is assumed, the increasing reach of both direct DM searches and collider constraints on the MSSM now pushes MSSM neutralino DM into uncomfortable corners, as has been widely recognised. The problems are two-fold: First, direct search experiments probe WIMP-nucleon cross sections orders of magnitude smaller than canonical weak scale cross sections; and second, given the direct search and collider constraints, the standard freeze-out mechanism of dark-matter-genesis generically generates a substantial excess of MSSM neutralino DM, limiting the allowed neutralino parameter space to special 'fine-tuned' regions of parameter space with coannihilations or resonances. Overall, neutralino DM matter works much less naturally than it did in the early 1990s after the excitement of the LEP-I results pointing to SUSY unification.

An independent reason to possibly doubt the standard MSSM neutralino story is that it is based on an assumption of simplicity of the dark sector that is probably not warranted given our experience of normal matter. In the observable sector

there is an extraordinary richness of stable or very long-lived massive states, including more than one hundred essentially stable nuclear isotopes (on the timescale of the Hubble time), a stable charged lepton, and three essentially stable neutrino mass eigenstates of various flavour compositions. This is despite the fact that all global discrete and continuous symmetries such as individual lepton number, as well as total lepton and baryon numbers are violated (by at least neutrino mixing plus the electroweak anomaly, and likely GUT-suppressed interactions too which violate $B - L$ also). There is no reason why we should expect the DM sector to be any less complicated than the observed world, and in a sense the observation of massive neutrinos already directly supports this hypothesis—the WIMP dark sector is already composed of at least a four-component cocktail of the three massive neutrino species plus one more WIMP.

Motivated by these arguments, in this chapter we investigate the physics of a very slight modification of the usual SUSY LSP hypothesis that naturally and simply accommodates a much more structured and varied DM sector (and in fact one that has attractive and potentially testable connections to neutrino flavour physics). Specifically we study what we consider to be one of the simplest alternatives to standard SUSY neutralino DM, though maintaining the SUSY framework that naturally possesses the well-known successes of weak-scale SUSY theories, such as precision gauge coupling unification and a solution to the hierarchy problem, namely, mixed lhd-rhd sneutrinos.

Sneutrinos are potentially interesting alternate SUSY DM candidates since, unlike Majorana neutralinos, they can carry flavour quantum numbers while being charge and colour neutral, In addition they are the LSP in reasonably large regions of parameter space.[1] The traditional reason why sneutrinos have not been considered a good DM candidate is that pure lhd, ie, $SU(2)_L$-active, sneutrinos have too large an annihilation cross section, and thus too small a freeze-out relic density to be the observed DM. However this problem is easily solved if one posits the existence of weak-scale rhd, ie, $SU(2)_L$-sterile, sneutrinos which mix with the lhd states once electroweak symmetry and SUSY is broken. Because of the observed family replication it is most

[1] Another attractive feature of considering such sneutrino DM is that it might afford a dynamical explanation of the baryon-to-dark-matter ratio $\Omega_b/\Omega_{DM} \simeq 1/5$ as the DM can now possess a lepton number asymmetry connected to the baryon-number-asymmetry, in contradistinction to Majorana neutralino DM matter which can carry no such asymmetry. We will not pursue these ideas in this work, but see [254, 57, 255, 256, 257, 258, 259, 260, 261, 262, 263, 58, 264, 265] for studies along these lines.

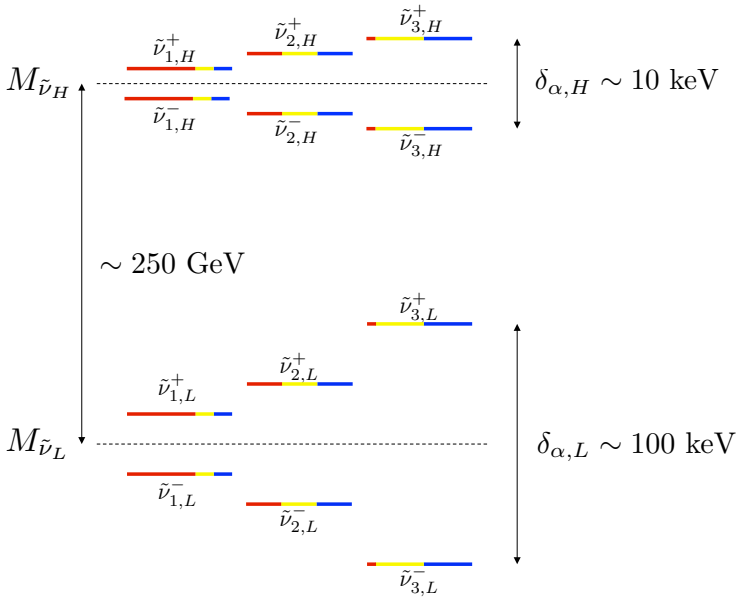

Figure 7.1: The spectrum of sneutrino masses after lifting of scalar and pseudoscalar mass degeneracy by the mass term M_B^2. The red, yellow and blue lines represent, respectively, the electron, muon and tau lepton number flavour components, which mirrors the neutrino flavour structure (here we have assumed the normal neutrino mass hierarchy). Note that the 12 real degrees of freedom split into a heavy sector and a light sector of 6 states each, with further fine structure splittings among these two groups, and the splittings between scalar and pseudoscalar components are proportional to the neutrino masses. This diagram is not to scale.

natural to posit three rhd sneutrinos, one associated with each lepton flavour, in addition to the three standard lhd sneutrinos.

Therefore we are led to a model with six weak-scale sneutrinos, that mix with each other and form, as we will argue in detail, a structured DM sector carrying lepton flavour quantum numbers identical to that carried by the neutrino mass eigenstates observed in neutrino oscillation experiments. In addition, each of these complex scalars splits into CP-odd and CP-even components, so the full spectrum of DM states is thus twelve real degrees of freedom with a variety of masses.

Shortening the story of the subsequent sections, what we find is a successful model comprising an entire sector of mixed sneutrino DM with the novel feature that the sneutrino flavour structure is identical to that of the neutrinos. Further to this the sneutrinos have mass splittings between scalar and pseudoscalar components that are proportional to the neutrino masses (see Fig. 7.1). In addition to these interesting features we find regions of parameter space where the splittings are large enough

that all states will have decayed down, leaving only one flavour of sneutrino as the candidate DM. These regions of parameter space potentially have a unique 'smoking gun' signature as pair annihilations of these sneutrinos through neutralino exchange produce just one neutrino mass eigenstate ν_3 (for the normal neutrino mass hierarchy), free from vacuum oscillations, that has the potential for detection at future neutrino telescopes through the observation of a hard spectrum of ν_μ and ν_τ but not ν_e. These neutrinos would have energy equal to the sneutrino mass and could arise from annihilations in the Sun.

Since we require rhd sneutrinos at the weak scale our model also possesses sterile rhd neutrinos at this scale or below. Naively one may therefore think that, as the rhd neutrinos are not superheavy, it is impossible to generate, eg, by the see-saw mechanism, an acceptable spectrum of light neutrinos as observed in neutrino oscillation experiments. However as originally show by Arkani-Hamed *etal* [127, 266] and Borzumati *etal* [267, 268] and amplified on and extended by later authors (see, eg, [122, 126, 128, 269, 270]) this is not the case. In fact there occurs a new and extremely attractive mechanism of neutrino mass generation linked to supersymmetry breaking, in a sense generalizing the Giudice-Masiero mechanism for generating the μ-term—the Higgsino mass term—in the MSSM. This model of neutrino masses allows for new explanations of the origin of the neutrino mass and flavour structure [127, 266, 128, 270] and elegantly accommodates such nice features as weak-scale resonant leptogenesis [269]. Since our main focus in this work is the novel sneutrino DM phenomenology we only very quickly summarize the physics of neutrino mass generation in as far as it impacts the sneutrino sector, and we strongly encourage the reader to refer to these other papers for more details.

Before we start, one other feature that deserves discussion is the fact that this class of models was the original and motivating example of inelastic DM [122, 126], providing a possible explanation of the reported DAMA/LIBRA [76] signals consistent with the exclusions reported by other direct DM detection experiments. Since these original models involving sneutrinos, the idea of inelastic DM has been implemented in many more set ups, and has been much studied (see, eg, [162] and references therein). This inelastic scattering also changes the phenomenology of DM solar capture and we include the exclusion limits from Refs. [169, 170] on the nucleon scattering cross-section. These can be more constraining than the current generation of direct detection experiments over large regions of parameter space.

There are many previous studies of sneutrino DM, see eg, [271, 272, 273, 274, 275, 276, 277, 165, 278, 279, 280, 281, 282, 283, 284, 285, 286, 287], though most do

not consider connecting the sneutrino and neutrino flavour structure. For treatments of sneutrino DM taking limits from the generation of neutrino masses we refer the reader to [277, 165, 287].

The previous work most closely related to that considered here is Ref.[287] where the flavour structure of the sneutrinos is also considered. However our model has the novel feature that the neutrino and sneutrino flavour structures are exactly the same, allowing a predictive 'smoking gun' signature for sneutrino annihilations into neutrinos, as discussed in Section 7.3.1. Another important difference is that in our model there is an interplay between two terms contributing to the neutrino mass generation (see the off-diagonal entries of Eq. (7.4)) that allow us to fit the observed neutrino masses consistent with successful sneutrino DM over a significant region of parameter space. Finally, our analysis includes the important limits arising from solar capture, which excludes the possibility of an inelastic DM explanation of DAMA/LIBRA using mixed sneutrinos.

In Section 7.1 we first discuss the specific model, outlining the generation of neutrino masses and the origin of the identical neutrino and sneutrino flavour structure, as well as the resulting mass spectrum of the sneutrino states. We then go on in Section 7.2 to present the decay lifetimes for the different flavoured sneutrino states and consider the DM phenomenology of the sneutrinos, showing the regions of parameter space where they are good DM candidates. In Section 7.3 the potential unique signatures of this model are considered, while our conclusions are contained in Section 7.4.

7.1 The Model

We start by summarizing the relevant field content and effective Lagrangian of the model we employ—that of [128], to which we refer the reader for additional details.

7.1.1 Field content and interactions

To the field content of the MSSM we append three $SU(3) \times SU(2)_L \times U(1)_Y$-sterile neutrinos and their sneutrino superpartners, $\tilde{n}_i$, which combine into the chiral superfields N_i. Here $i = 1, 2, 3$ labels the generation. The terms arising from the superpotential are

$$\Delta\mathcal{L} = \int d^2\theta \left(\lambda_{ij} L_i \cdot H_u N_j + \frac{1}{2} M_N N_i N_i \right). \tag{7.1}$$

The SUSY-preserving superpotential term for the rhd neutrino mass, $M_N N_i N_i$, arises from a higher-dimension Kahler term involving a SUSY-breaking spurion F-component, in analogy with the Giudice-Masiero mechanism for the μ-term, thus giving rhd neutrino masses at the weak scale $M_N \sim m_I^2/M \sim$ TeV. (Here $m_I \sim 10^{10} - 10^{11}$ GeV is the intermediate scale at which SUSY is broken in the hidden sector, while M is the reduced Planck scale.) The Yukawa coupling λ_{ij} between the lhd lepton doublet superfields, L_i, and the rhd neutrino supermultiplets, N_i, also arises from a Kahler term involving a spurion F-component and is suppressed in magnitude by a factor of $|\lambda_{ij}| \sim m_I/M \sim 10^{-7} - 10^{-8}$. These suppressions are justified with an R-symmetry, with explicit charges given in [128], which gives a natural motivation for these terms.

In addition to the usual soft-SUSY breaking terms of the MSSM there are also SUSY-breaking terms of the form

$$-\Delta\mathcal{L} = m_{\tilde{n}}^2 \, |\tilde{n}_i|^2 + A \, \tilde{L}_i \tilde{n}_i h_u + \frac{1}{2} \lambda_{ij} \, M_B^2 \, \tilde{n}_i \tilde{n}_j + h.c. \; . \tag{7.2}$$

Namely, TeV-scale, but flavour diagonal, soft mass and trilinear scalar A-terms, and a small but significant rhd sneutrino lepton-number violating B-term with coefficient $B_{ij}^2 \sim \lambda_{ij} M_B^2 \sim m_I^2 (m_I/M)^3 \sim (\text{TeV}^5/M)^{1/2} \sim (100 \text{ MeV})^2$ and flavour structure identical to that of the neutrino Yukawa coupling, which we assume to be real. Again this structure of suppressions and lepton flavour breaking can be justified by the R-symmetry and flavour structure properties of the SUSY-breaking spurions. More complicated flavour breaking patterns, for instance those with non-diagonal A-terms, are also possible, but Eq. (7.1) and (7.2) is the simplest structure that leads to a successful spectrum of masses and mixings in the neutrino sector (as we quickly recall in Section 7.1.3). It also leads to a simple and direct connection between the neutrino and sneutrino flavour structure and masses.

7.1.2 Sneutrino Masses

In total we have six complex sneutrino fields, however these are split into scalar and pseudoscalar components by the sneutrino B-term in Eq. (7.2), leaving twelve mass eigenstates. After electroweak symmetry breaking the sneutrino mass matrix has the form

$$M_{ij}^2 = \begin{pmatrix} M_L^2 \mathbb{1}_3 & Av \sin\beta \mathbb{1}_3 & 0 & \lambda_{ij} M_N v \sin\beta \\ Av \sin\beta \mathbb{1}_3 & M_R^2 \mathbb{1}_3 & \lambda_{ij} M_N v \sin\beta & \lambda_{ij} M_B^2 \\ 0 & \lambda_{ij} M_N v \sin\beta & M_L^2 \mathbb{1}_3 & Av \sin\beta \mathbb{1}_3 \\ \lambda_{ij} M_N v \sin\beta & \lambda_{ij} M_B^2 & Av \sin\beta \mathbb{1}_3 & M_R^2 \mathbb{1}_3 \end{pmatrix} , \tag{7.3}$$

where the basis is $(\tilde{\boldsymbol{\nu}}^*, \tilde{\boldsymbol{n}}, \tilde{\boldsymbol{\nu}}, \tilde{\boldsymbol{n}}^*)$. Due to the flavour diagonality of the unsuppressed terms after electroweak symmetry breaking, this 12×12 sneutrino mass matrix is made up of a total of sixteen 3×3 blocks which are either proportional to the identity matrix (from the A-term, Majorana mass F-term and D-terms), or λ_{ij} (from the B-term and the rhd sneutrino F-term). Therefore the sneutrino flavour structure is completely determined by the matrix that diagonalises λ_{ij}, which we will call U_λ.

After diagonalisation of the flavour structure the sneutrino mass matrix is in the form of sixteen diagonal 3×3 blocks, which by further rotations can be manipulated (detailed in Appendix D) into the simple block-diagonal form of six 2×2 matrices, three for the scalars and pseudoscalars each

$$M^2_{\tilde{\nu}^+_\alpha} = \begin{pmatrix} M_L^2 & Av\sin\beta + \lambda_\alpha a_\nu M_B^2 \\ Av\sin\beta + \lambda_\alpha a_\nu M_B^2 & M_R^2 + \lambda_\alpha M_B^2 \end{pmatrix} \tag{7.4}$$

$$M^2_{\tilde{\nu}^-_\alpha} = \begin{pmatrix} M_L^2 & Av\sin\beta - \lambda_\alpha a_\nu M_B^2 \\ Av\sin\beta - \lambda_\alpha a_\nu M_B^2 & M_R^2 - \lambda_\alpha M_B^2 \end{pmatrix} . \tag{7.5}$$

Here $\tilde{\nu}^+$ and $\tilde{\nu}^-$ denote the scalar and pseudoscalar components respectively. The subscript $\alpha = \{1, 2, 3\}$ denotes the mixed flavour sneutrino mass eigenstate (note the change from Latin to Greek indices on going from weak to mass eigenstates), λ_α are the eigenvalues of the λ_{ij} matrix, $M_L^2 = m_{\tilde{L}}^2 + \frac{1}{2}M_Z^2\cos2\beta$ and $M_R^2 = m_{\tilde{n}}^2 + M_N^2$, where $m_{\tilde{L}}$ and $m_{\tilde{n}}$ are the usual soft mass terms, and, $v = 174$ GeV, is the Higgs expectation value. We have also defined

$$a_\nu = \frac{vM_N\sin\beta}{M_B^2} , \tag{7.6}$$

which gives a measure of the relative size of the B-term and F-term contributions to the splitting of the CP-eigenstate masses.

These 2×2 matrices can then be diagonalised to complete the exact sneutrino rotation matrix U. Further, in this form one can see there are twelve mass eigenstates: two $\tilde{\nu}^+$ and two $\tilde{\nu}^-$ for each flavour, and both the heavy and light $\tilde{\nu}^+$ and $\tilde{\nu}^-$ states for each flavour have their masses split due to λ_{ij}, becoming degenerate in the limit $\lambda_\alpha \to 0$. Expanding to first order in the small parameter λ_α the splitting between the light $\tilde{\nu}_L^+$ and $\tilde{\nu}_L^-$ components for each flavour is given by

$$\delta_{\alpha,L} = M_{\tilde{\nu}^+_{\alpha,L}} - M_{\tilde{\nu}^-_{\alpha,L}} = \lambda_\alpha\frac{M_B^2}{M_{\tilde{\nu}_L}}(\cos^2\theta - a_\nu\sin2\theta) \sim 100 \text{ keV} , \tag{7.7}$$

where $M_{\tilde{\nu}_L}$ and θ are the lightest mass eigenstate and the rotation angle which diagonalises the 2×2 matrices in Eq. (7.4) in the limit $\lambda_\alpha \to 0$. Similarly, the splitting between the $\tilde{\nu}_H^+$ and $\tilde{\nu}_H^-$ components is given by $\delta_{\alpha,H} = M_{\tilde{\nu}^+_{\alpha,H}} - M_{\tilde{\nu}^-_{\alpha,H}} =$

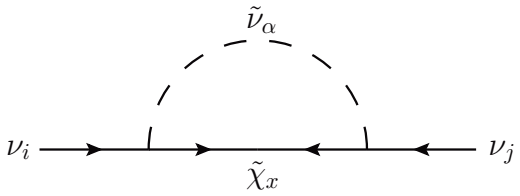

Figure 7.2: Feynman diagram corresponding to the radiative neutrino mass generation.

$\lambda_\alpha \frac{M_B^2}{M_{\tilde{\nu}_H}}(\sin^2\theta + a_\nu \sin 2\theta) \sim 10$ keV, where $M_{\tilde{\nu}_L}$ is the heavy mass eigenstate in the limit $\lambda_\alpha \to 0$. Therefore we are left with a sneutrino mass spectrum as shown schematically in Fig. 7.1.

7.1.3 Neutrino Masses

As the Majorana mass for the rhd neutrinos ($M_N \sim 1$ TeV) is very small compared to the standard seesaw set-up ($M_N \sim 10^{10} - 10^{15}$ GeV) one would naturally expect the seesaw contribution to the light neutrino masses to be large. However, here this contribution is suppressed by the square of the small neutrino Yukawa coupling ($\lambda^2 \sim 10^{-14} - 10^{-16}$) and instead the dominant Majorana masses for the neutrinos arise radiatively through loops involving sneutrinos and neutralinos. This is due to the combination of the lifting of the degeneracy between $\tilde{\nu}^+$ and $\tilde{\nu}^-$ sneutrino states and the Majorana nature of the neutralinos and can be seen schematically through loop diagrams involving perturbative mass-insertions, as in [128]. However, as it is possible to solve for the sneutrino masses and mixing matrices analytically, the exact one-loop contribution to the neutrino masses can be calculated from the Feynman diagram in Fig. 7.2.

Correspondingly, the neutrino masses are given by

$$M_{\nu_{ij}} = \frac{1}{2}\left(\frac{M_Z}{4\pi v}\right)^2 \sum_{\alpha=1}^{12}\sum_{x=1}^{4} m_{\chi_x}(N_{x1}\sin\theta_W - N_{x2}\cos\theta_W)^2 U^\dagger_{i,\alpha} L(r_\alpha, m_{\chi_x}) U_{\alpha,j+6} \ , \quad (7.8)$$

where α runs over the twelve sneutrino mass eigenstates, N_{xy} are the neutralino mixing matrices, m_{χ_x} the neutralino masses, $r_\alpha = M_\alpha/m_{\chi_x}$ and[2]

$$L(r, m_{\chi_x}) = \frac{r^2\ln(r^2)}{1-r^2} + 1 + \ln\left(\frac{\Lambda^2}{m^2_{\chi_x}}\right) \ . \quad (7.9)$$

The parameter dependence and flavour structure of the neutrino masses is more

[2]As $\sum_{\alpha=1}^{12} U_{\alpha,i}{U^\dagger}_{j,\alpha} = \delta_{ij}$ the last two terms vanish when summing over the sneutrinos as they are independent of the sneutrino masses and α.

apparent by expanding the previous exact one-loop formula to first order in the λ_{ij} matrix. This gives

$$\begin{aligned} M_{\nu_{ij}} = \lambda_{ij} \left(\frac{M_Z M_B}{4\pi v} \right)^2 \sum_{x=1}^{4} \frac{1}{m_{\chi_x}} (N_{x1} \sin\theta_W - N_{x2} \cos\theta_W)^2 \\ \cdot \left\{ \sin^2\theta (\cos^2\theta - a_\nu \sin 2\theta) L_1(x_x, y_x) \right. \\ \left. + \cos^2\theta (\sin^2\theta + a_\nu \sin 2\theta) L_2(x_x, y_x) \right\} \ , \end{aligned} \tag{7.10}$$

where L_1 and L_2, defined in Appendix D, are the loop contributions from the sneutrino soft mass term and the F-term contributions. The parameter a_ν, defined in Eq. (7.6), gives the freedom to generate neutrino masses that aren't too large by cancelling these two contributions off each other. Once the overall scale of the neutrino masses is set the mass splittings and mixing angles are determined by the matrix λ_{ij}.

From Eq. (7.10) we can see that the neutrino masses are proportional to the eigenvalues of λ_{ij}. Combining this with Eq. (7.7), it is clear thar $\delta_\alpha \propto M_{\nu_\alpha}$. In order to obtain the correct neutrino masses it is necessary that $\lambda_\alpha/\lambda_\beta = M_{\nu_\alpha}/M_{\nu_\beta}$ and therefore $\delta_\alpha/\delta_\beta = M_{\nu_\alpha}/M_{\nu_\beta}$. Once these ratios and all other parameters are set, then the overall magnitude of the neutrino masses depends on the parameter a_ν. We allow a_ν to take values $-1 < a_\nu < 1$, and find that for reasonable values of this parameter, neutrino masses below cosmological bounds and with $M_{\nu_3} > \sqrt{\Delta m^2_{12} + \Delta m^2_{23}}$ are obtained. This will be discussed in more detail in Section 7.2.3.

It is clear from Eq. (7.10), and is shown to all orders in λ_{ij} in Appendix D, that the flavour structure of the neutrino mass matrix takes a simple form. The PMNS neutrino mixing matrix is given simply by $U_{PMNS} \equiv U_\lambda$, where U_λ was defined previously as the matrix which diagonalizes λ_{ij}, and also completely determines the flavour structure of the sneutrinos. Therefore the flavour structure of the neutrinos is automatically identical to that of the sneutrinos in this model. This enables us to make definite statements about possible 'smoking gun' signatures.

Hence, in order to reproduce the measured neutrino mixing and mass parameters the form of λ_{ij} is completely known, up to an overall normalisation factor which is absorbed into M_B^2. Since $\delta_\alpha \propto M_{\nu_\alpha}$, the largest sneutrino splitting δ_α is in correspondence with the largest neutrino mass. For the normal neutrino mass hierarchy, we know the heaviest neutrino's flavour structure is almost exactly half μ and τ, therefore we know the four sneutrino states $\tilde{\nu}_3$ (two heavy scalar and pseudoscalar, and two light scalar and pseudoscalar states) must also have this flavour structure. This is shown schematically in Fig. 7.1.

7.2 Dark Matter

In the previous section we have derived the sneutrino mass spectrum and shown that, as well as giving mass to the neutrinos, they also pass on their flavour structure to the neutrinos. In this section we would like to apply current experimental constraints to find the regions of parameter space where the flavoured sneutrinos are a good DM candidate.[3]

As explained above, the sneutrino spectrum is split into two groups of six particles with the same flavour structure as the neutrinos. In this section we will only be concerned with the possible transitions of the six lightest particles as the heavier ones very rapidly decay. We will find that there are three general possibilities for the current DM composition: 1) In a Hubble time all of the heavier sneutrinos could have decayed to the lightest state, $\tilde{\nu}^-_{3,L}$, which makes up all of the measured DM relic density; 2) The three lightest species survive to the present day, each making up a third of the measured relic density; 3) An intermediate situation where one or more of the heavier sneutrino states have decayed (or are currently decaying) down to the lighter states, but a non-trivial cocktail of different flavoured sneutrinos remains. For pedagogical clarity, we shall assume in the following that the neutrinos follow the normal mass hierarchy, however we will briefly highlight the differences if the inverted mass hierarchy is assumed at the end of this section.

7.2.1 Stable and meta-stable sneutrino spectrum and decays

The lifetime of the lighter six states is a sensitive function of the splittings δ_1 and Δ_1, (defined in Fig. 7.3), which as shown in Eq. (7.7) depend on the ratio a_ν. As we will show later, there are regions of the parameter space of a_ν where the lifetime of the decays of $\tilde{\nu}^-_{1,L}$ and $\tilde{\nu}^-_{2,L}$ to $\tilde{\nu}^-_{3,L}$ are longer than the age of the Universe. In this case, the DM is comprised of equal abundances of all three states $\tilde{\nu}^-_{1,L}$, $\tilde{\nu}^-_{2,L}$ and $\tilde{\nu}^-_{3,L}$, and is therefore overall flavour neutral. However there are also portions of parameter space where the states will have decayed to only $\tilde{\nu}^-_{3,L}$, leading to one flavour of sneutrino as the DM candidate with potential signatures linked to the mixing properties of neutrinos.

Initially we consider the decay of the lightest scalar particle, $\tilde{\nu}^+_{1,L}$, as shown in Fig. 7.3. The particle can decay by $\nu\nu$ emission through intermediate Z exchange to

[3]For all of our studies we take the current total DM density to be given by the WMAP5+BAO+SN value $\Omega h^2 = 0.1143 \pm 0.0034$[288].

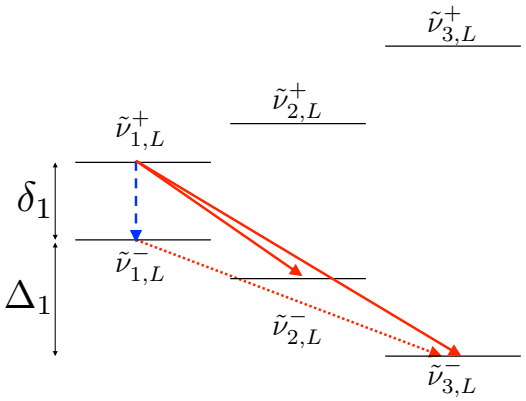

Figure 7.3: The six lightest sneutrino mass eigenstates (splittings not to scale). $\tilde{\nu}^+_{1,L}$ can decay to $\tilde{\nu}^-_{1,L}$ by $\nu\nu$ emission through intermediate Z exchange, as shown by the blue line, or to any of the lighter states by $\nu\nu$ emission through a neutralino (red lines). $\tilde{\nu}^-_{1,L}$ and $\tilde{\nu}^-_{2,L}$ can decay to $\tilde{\nu}^-_{3,L}$ through an intermediate neutralino exchange. For some regions of parameter space, these decays will be longer than the age of the Universe.

the pseudoscalar particle of the same flavour, $\tilde{\nu}^-_{1,L}$, or by $\nu\nu$ emission through an intermediate neutralino exchange to any of the lighter pseudoscalar particles. Typically the dominant decay mode is through the Z-boson,

$$\Gamma_Z^{\tilde{\nu}^+_{1,L}} = \sin^4\theta \frac{G_F^2\,\delta_1^5}{20\pi^3} \sim (9\times 10^4 \text{ yrs})^{-1} \left(\frac{\sin\theta}{0.1}\right)^4 \left(\frac{\delta_1}{100 \text{ keV}}\right)^5 , \tag{7.11}$$

and is around an order of magnitude faster than neutralino-mediated decay. The associated $\tilde{\nu}^+_{1,L}$ lifetime is, for all reasonable parameters, short enough that no $\tilde{\nu}^+_{\alpha,L}$ states survive to the current day. Although these decays occur after Big Bang Nucleosynthesis there are no changes in the predicted light element abundances as the mass splittings are small and there is no hadronic energy injection.

There are similarly no constraints from spectral distortions in the CMB [289] from the energy injection due to Z-mediated decays to two photons, as the loop-suppressed branching fraction into photons is too small for these features to be observable. We estimate this branching fraction as $f_{\gamma\gamma} \simeq 1.3\times 10^{-12}(\frac{\delta}{100 \text{ keV}})^4$ and for each sneutrino decay this leads to an energy release per CMB photon at least ten orders of magnitude below the bounds given in [289].

We will now consider the decays of the pseudoscalar particles, and in particular, the decay of $\tilde{\nu}^-_{1,L}$ to $\tilde{\nu}^-_{3,L}$, as indicated by the dotted red arrow in Fig. 7.3, since it will be the fastest of the possible decays. If this lifetime is longer than the age of the

universe, the lifetime for $\tilde{\nu}^-_{2,L}$ to decay to $\tilde{\nu}^-_{3,L}$ will also be longer. These decays can only occur by $\nu\nu$ emission through an intermediate neutralino. The decay width for typical parameters is

$$\Gamma_\chi^{\tilde{\nu}^-_{1,L}} = \chi \sin^4\theta \left(\frac{M_z}{v}\right)^4 \frac{\Delta_1^5}{960\pi^3 m_{\chi_1}^2 M_{\tilde{\nu}_L}^2} \tag{7.12}$$

$$\sim (10^{10}\text{ yrs})^{-1} \left(\frac{\chi}{0.22}\right) \left(\frac{\sin\theta}{0.1}\right)^4 \cdot \left(\frac{\Delta_1}{25\text{ keV}}\right)^5 \left(\frac{100\text{ GeV}}{M_{\tilde{\nu}_L}}\right)^2 \left(\frac{200\text{ GeV}}{m_{\chi_1}}\right)^2 , \tag{7.13}$$

where

$$\chi = \left(\sum_x \frac{m_{\chi_1}}{m_{\chi_x}} (N_{x1}\sin\theta_W - N_{x2}\cos\theta_W)^2\right)^2 + \left(\sum_x \frac{m_{\chi_1} M_{\tilde{\nu}_L}}{m_{\chi_x}^2} |N_{x1}\sin\theta_W - N_{x2}\cos\theta_W|^2\right)^2 \tag{7.14}$$

depends on the neutralino mixing matrix, N_{xy}, and neutralino masses, m_{χ_x}.

The decay width Eq. (7.13) is in the range where, depending upon parameters, the pseudoscalar $\tilde{\nu}^-_{1,L}$ states can either have essentially all decayed by the present epoch, or can be substantially still present, or can be currently decaying. For the purposes of matching to the observed DM density, however, this ambiguity is immaterial as each heavier state decays to one only marginally lighter state. The same is true for the decays of the $\tilde{\nu}^+_{\alpha,L}$ states, so in computing the total freeze-out relic density it is a good approximation to sum the contribution of all six light states ignoring the later effect of decays.

7.2.2 DM relic density and experimental constraints

Although various thermal and non-thermal mechanisms for generating the observed DM relic density are possible, we assume that the relic density is generated by the standard thermal freeze-out process. In particular we do not here consider the possibility of using the calculable and IR-dominated thermal freeze-in process recently advocated by Hall *etal* [290], as this would apply for supersymmetric theories with Dirac neutrino masses, rather than the model outlined in Section 7.1.

The three main processes which contribute to the freeze-out relic density calculation are shown in Fig. 7.4. We performed the calculation using micrOMEGAs 2.2 [97] with model files created using LanHEP 3.0.4 [291] and the results are shown as the

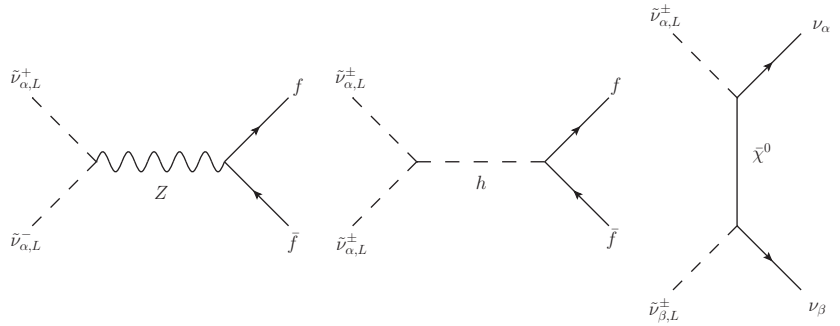

Figure 7.4: The dominant processes which set the sneutrino relic density.

solid green curves in Figs. 7.5, 7.6 and 7.7. Coannihilation between the six lightest sneutrinos, which is obviously important since they are almost degenerate in mass, is automatically included in micrOMEGAs. The dashed black and purple lines show the limits from the current generation of direct detection experiments on the DM-nucleon scattering cross section, or equivalently from using Eqs. (7.15) and (7.16), on the mixing angle $\sin\theta$. An interesting feature of this model is the possibility of two signals at future direct detection experiments; the DM can up-scatter inelastically via Z exchange, for example from $\tilde{\nu}^-_{3,L}$ to $\tilde{\nu}^+_{3,L}$, and therefore is sensitive to the small mass splitting $\delta_{\alpha,L}$, or can elastically scatter by Higgs exchange. This also means that we can constrain the parameter space in two regions due to the different kinematics of each collision. The elastic cross section is larger at smaller masses $M_{\tilde{\nu}_L}$, while the inelastic cross section limit is stronger for smaller $\delta_{\alpha,L}$, as we will explicitly demonstrate later. The cross section for coherent scattering off a nucleus at zero momentum transfer by Z exchange is

$$\sigma^Z_N = \sin^4\theta \frac{G_F^2\,\mu^2}{2\pi}\left((A-Z)-(1-4\sin^2\theta_W)Z\right)^2 \ . \tag{7.15}$$

Here μ is the reduced mass for the sneutrino-nucleus, Z the proton number and A, the number of protons and neutrons in the nucleus. The cross section for elastic scattering off a nucleon by Higgs exchange in the decoupling limit is given by

$$\sigma^h_n = \frac{g^2_{hnn}}{8\pi m_h^4}\left(\frac{m_n}{m_n+M_{\tilde{\nu}_L}}\right)^2\left(A\sin\beta\sin 2\theta - \frac{M_Z^2}{v}\cos 2\beta\sin^2\theta\right)^2 , \tag{7.16}$$

where m_n is the nucleon mass and $g_{hnn} = \frac{m_n}{\sqrt{2}v}\left(\sum_q^{u,d,s} f_{T_q} + \frac{2}{27}\sum_Q^{c,b,t} f_{T_G}\right)$. We use the values of f_{T_q} and f_{T_G} from Ref.[277] which give $g_{hnn} = 1.43\times 10^{-3}$.

The red dot-dashed lines show the indirect detection limits on $\sin\theta$ from the DM capture, and subsequent annihilation into neutrinos, by the Sun. At the masses

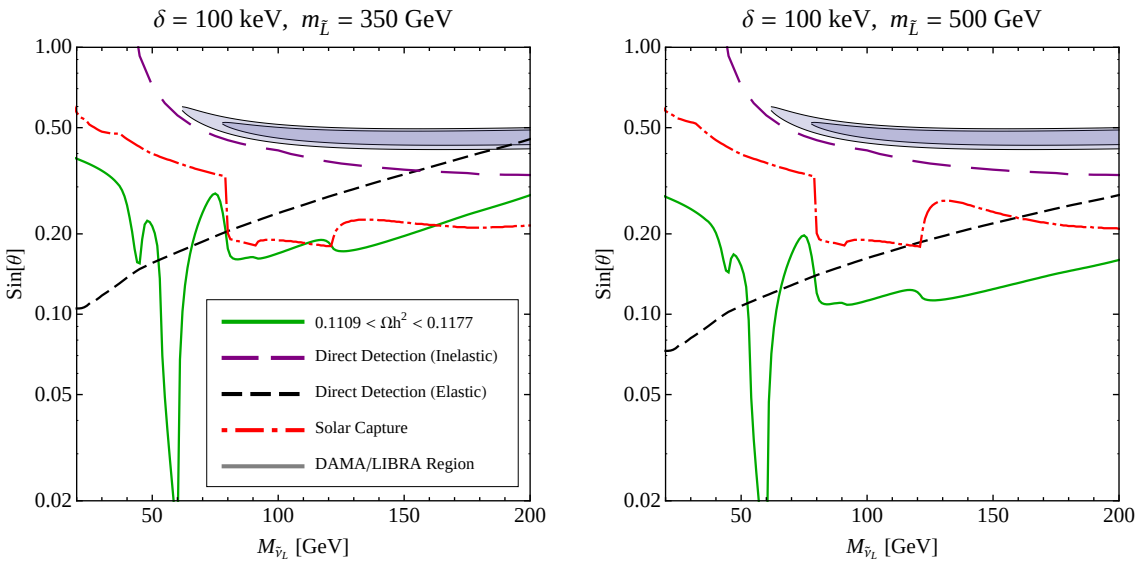

Figure 7.5: Exclusion curves and thermal relic density constraints in the $\sin\theta$ - $M_{\tilde{\nu}_L}$ plane for $M_1 = \mu = 250$ GeV, $M_2 = 500$ GeV and $\tan\beta = 10$, and with Higgs mass 121 GeV. The green solid line indicates the value of $\sin\theta$ where the observed DM relic density is generated thermally. The dashed lines give the exclusion curves from direct detection experiments and the shaded regions show the values of $\sin\theta$ which fit the DAMA/LIBRA experiment at 90% and 99% confidence levels. The dot-dashed curve gives the exclusion curve from the measurement of solar neutrinos from Super-Kamiokande. The green solid line below the dashed and dash-dotted lines indicate parameters where the sneutrinos are a good thermal DM candidate. The two features below 60 GeV on this thermal relic density curve correspond to the Higgs- and Z-funnel regions. The Z-funnel is a co-annihilation effect and so would be absent from indirect detection signals. Note that, with the exception of the Higgs-funnel region, the elastic direct detection, and solar capture indirect detection limits are close to the region of parameter space required for a successful thermally generated relic density.

we consider, the limits are set from the observation of solar neutrinos by Super-Kamiokande [112]. Note that the solar capture and annihilation limits are the most constraining limits over a sizeable region of parameter space.

In the limit $\lambda_\alpha \to 0$, the sneutrino masses and mixings are determined by M_L, M_R, A and $\tan\beta$, however we find it more intuitive to trade in M_L, M_R and A for $m_{\tilde{L}}$, $M_{\tilde{\nu}_L}$ and θ. Furthermore, once a_ν and one of the $\delta_{\alpha,L}$ are specified, and M_1, M_2 and μ are chosen so that the neutralino masses m_{χ_x} and mixing angles N_{xy} can be computed, the absolute neutrino masses can be calculated from Eq. (7.10) and the other two $\delta_{\alpha,L}$ can be found from the ratio $\delta_{\alpha,L}/\delta_{\beta,L} = M_{\nu_\alpha}/M_{\nu_\beta}$. At the top of each

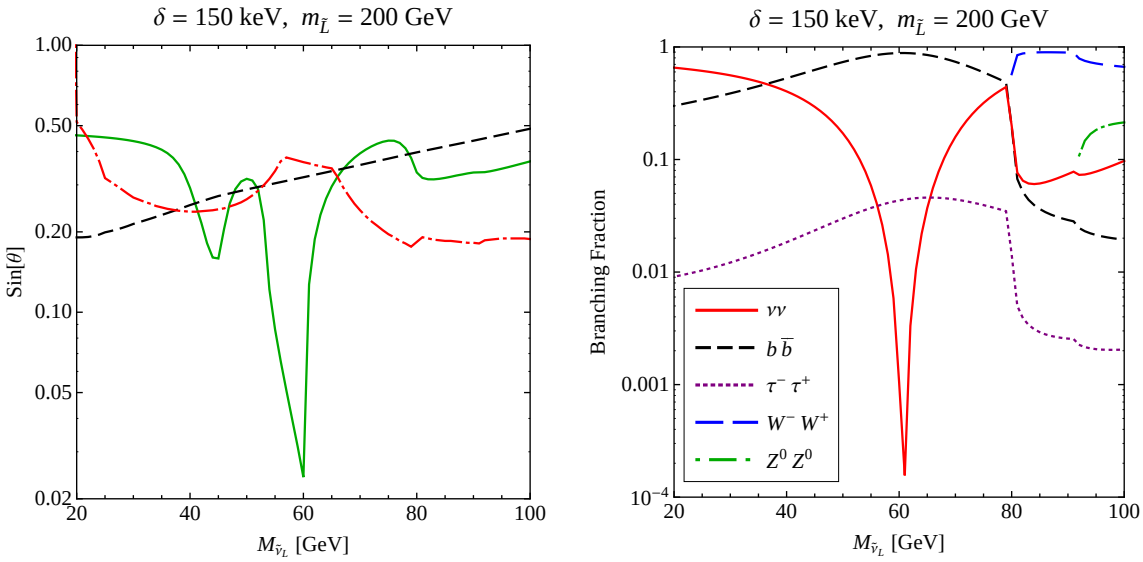

Figure 7.6: Left panel: Exclusion curves and thermal relic density constraints for $M_1 = \mu = 150$ GeV, $M_2 = 300$ GeV and $\tan\beta = 10$. As well as the Higgs-funnel region at ~ 60 GeV, the Z-funnel region at ~ 45 GeV is now also viable. Again, note that, with the exception of the Higgs-funnel region, the elastic direct detection, and solar capture indirect detection limits are close to the region of parameter space required for a successful thermally generated relic density. Right panel: The branching fractions for the same parameters as in the left panel. For each value of $M_{\tilde{\nu}_L}$, we have chosen $\sin\theta$ to give the correct thermal relic density. At low masses the branching fractions to neutrinos dominates, and at masses just below the W mass is substantial. At masses above the W mass, that to W^+W^- dominates.

figure we have displayed the value of $m_{\tilde{L}}$ and δ we have fixed. Note that δ always refers to the smallest $\delta_{\alpha,L}$ from the sneutrinos which have not decayed.

For all further calculations we fix the MSSM parameters at the weak scale. We set $\tan\beta = 10$, the pseudoscalar Higgs mass $M_A = 500$ GeV, the rhd slepton soft mass $m_{\tilde{E}} = 250$ GeV, the top soft coupling $A_t = -1$ TeV and all other soft parameters to 1 TeV giving a Higgs mass of 121 GeV. M_1, M_2 and μ are varied in different plots but we maintain the relation $M_2 = 2M_1$.

The dominant channel which contributes to the relic density is through the Higgs s-channel because of the large A-terms. An especially noticeable feature in the relic density curve in Figs. 7.5, 7.6 and 7.7 is the Higgs-funnel at half the Higgs mass ~ 60 GeV. A similar effect can be seen at ~ 45 GeV, the Z-funnel, but is much smaller because it is suppressed by $\sin^4\theta$ rather than $\sin^2 2\theta$, cf. Eqs. (7.15) and (7.16). The annihilation through the neutralino t-channel is important at lower mass (< 45 GeV)

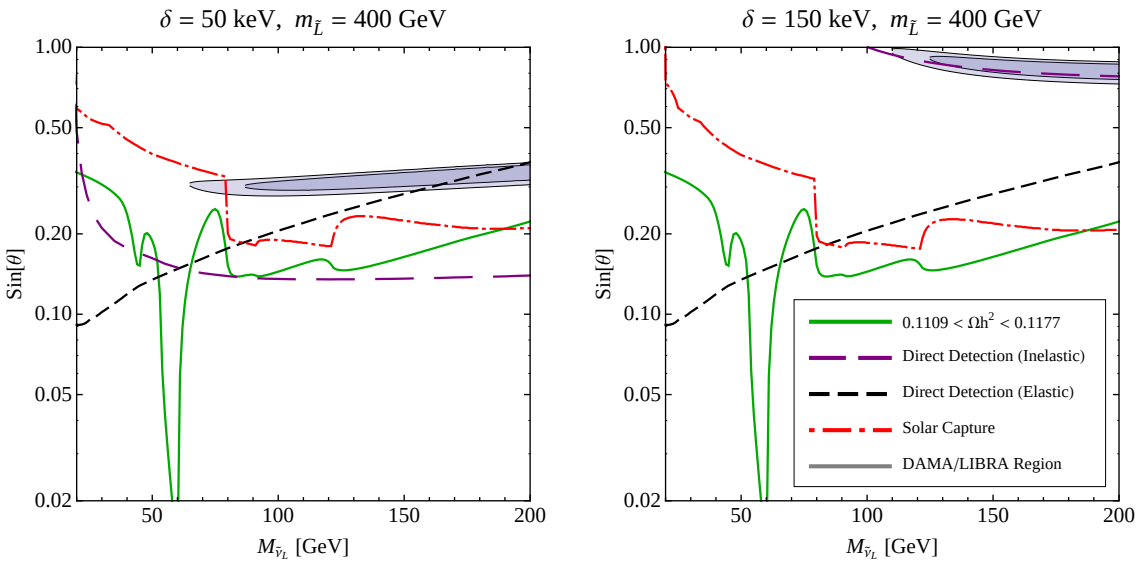

Figure 7.7: The effect of changing δ while keeping everything else fixed. The relic density and elastic direct detection curves remain the same, while there is a small change at low masses in the solar capture limits. The major change is in the inelastic direct detection limits which change considerably due to the different kinematics of the collision with the target nucleus.

and just below the W mass, where, from the right panel of Fig. 7.6, we see that the branching fraction into neutrinos can be large.

As $m_{\tilde{L}}$ increases with θ and $M_{\tilde{\nu}_L}$ held constant, the A-term increases, so smaller values of $\sin\theta$ are required to ensure the sneutrinos do not over-annihilate producing a relic density below the measured value. From Eq. (7.16), we can also see that this increase in the A-term is the reason why the elastic direct detection limits become stronger as $m_{\tilde{L}}$ is increased.

For $m_{\tilde{L}} < 350$ GeV, the only region of parameter space not excluded from elastic direct detection and solar limits is below the W mass; as well as the Higgs-funnel region, the left panel of Fig. 7.6 demonstrates that the Z-funnel region at ~ 45 GeV also opens up. For $m_{\tilde{L}} > 500$ GeV, the elastic direct detection limits and relic density curve move to lower values of $\sin\theta$ together so that no new lower values of $M_{\tilde{\nu}_L}$ are allowed.

Changing δ has virtually no effect on the relic density calculation and the elastic direct detection limits, while the change in the solar limits is very minor. However as Fig. 7.7 shows, the major difference is in the inelastic direct detection limits which change considerably.

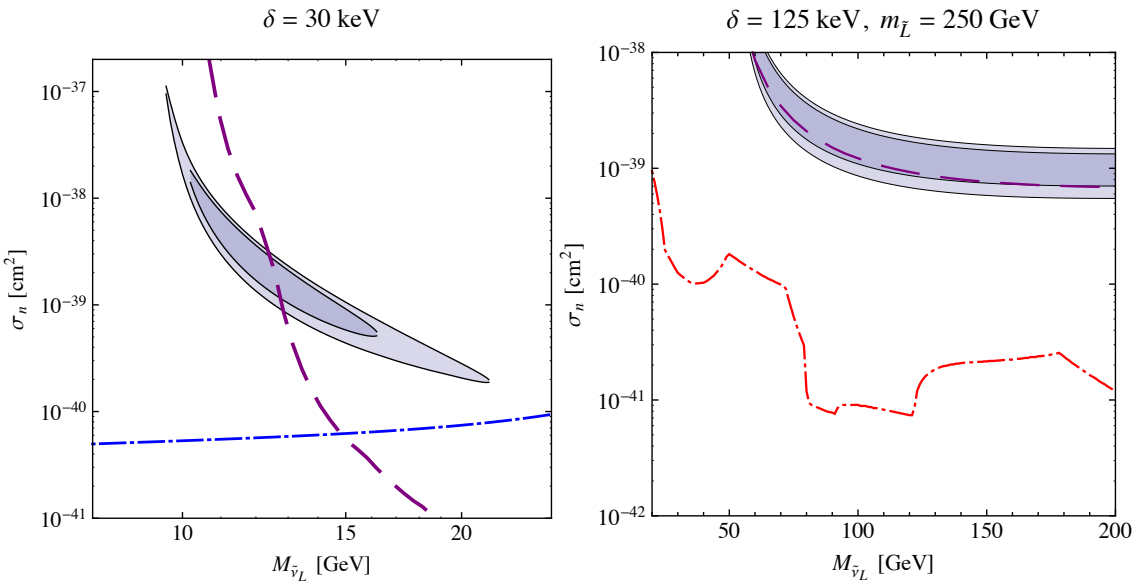

Figure 7.8: The grey shaded regions show the values of the scattering cross section σ_n which fit the DAMA/LIBRA experiment at 90% and 99% confidence levels. Also shown are the best direct detection limits (purple dashed). In the left panel we concentrate on the low mass DAMA/LIBRA region with $\delta = 30$ keV. The blue dot-dashed line is the constraint arising from the sneutrino contribution to the invisible Z width. Regions above this line are excluded. In the right panel, we concentrate on the high mass DAMA/LIBRA region with $\delta = 125$ keV. The red dot-dashed line show the constraints from solar capture. Regions above the line are excluded. Clearly the invisible Z-width and solar capture limits completely exclude both the low and high mass DAMA/LIBRA regions in this model.

The somewhat erratic appearance of the solar limits in Figs. 7.5, 7.6, 7.7 and 7.8 is because we have only plotted the strongest constraint arising from the different possible annihilation channels; $\nu\nu$, $\tau\tau$, $b\bar{b}$, W^+W^-, ZZ and hh. Typically we found that for $M_{\tilde{\nu}_L} < M_W$, the limits from annihilation into $\nu\nu$ dominate except for when $M_{\tilde{\nu}_L} \sim M_h/2$, where the $\tau\tau$ limits dominate. This is because the neutrinos are produced through t-channel neutralino exchange which are not enhanced in the Higgs-funnel, as other massive particles are. For $M_{\tilde{\nu}_L} > M_W$, the W^+W^- limits typically dominate. The branching fractions were calculated using micrOMEGAs and we used the limits on the annihilation branching fraction derived using the methods in [169]. We have also only shown the strongest limits from the direct detection experiments. We assume the Standard Halo Model and refer the reader to Ref.[1] for details on how these limits were calculated and the experimental details.

Since our model naturally includes a splitting of order 100 keV, it is natural to

ask whether this is consistent with the inelastic DM [122] explanation of the positive annual modulation signal measured by the DAMA/LIBRA [76] experiment and the null results from the other direct detection experiments (notably CDMS II [79] and XENON10 [154]). There are two regions of parameter space where the DAMA/LIBRA experiment may still (just) be consistent with the other direct detection experiments; the low mass region with a splitting $\delta \sim 30$ keV; and a higher mass region with a splitting $\delta \sim 125$ keV [123, 1, 162, 91, 161]. However, as we demonstrate in Fig. 7.8, both the low and high mass regions are conclusively excluded in our model. In the left panel of Fig. 7.8, the shaded regions show the (channeled) DAMA/LIBRA 90% and 99% confidence regions with a splitting $\delta = 30$ keV, while the dashed purple line shows the best limit from direct detection experiments (the excluded region lies to the right of this line). The blue dot-dashed line shows the limits from the invisible Z-width (the excluded region lies above this line). The contribution from the six lightest sneutrinos to the invisible Z-width is $\Delta\Gamma_Z = \frac{3\sin^4\theta}{2}(1-(2M_{\tilde{\nu}_L}/M_Z)^2)^{3/2}\ \Gamma_\nu$, where $\Gamma_\nu = 167$ MeV is the invisible Z-width into one species of neutrino. We adopt the LEP bound $\Delta\Gamma_Z < 2$ MeV [277]. We see that the invisible R-symmetry-width constraint completely excludes all of the low mass DAMA/LIBRA parameter space. In the right panel of Fig. 7.8 we show the limits on the high mass DAMA/LIBRA region for $\delta = 125$ keV. We find that when the solar capture limits from Refs. [169, 170] are included, the DAMA/LIBRA region is conclusively excluded.

7.2.3 The allowed a_ν parameter space

For a given set of the parameters $\{m_{\tilde{L}}, \mu, M_1, M_2, \tan\beta\}$ one can see from Figs. 7.5, 7.6 and 7.7 that the allowed values of $\sin\theta$ and $M_{\tilde{\nu}_L}$ are tightly constrained by limits from direct and indirect detection. Although non-thermal mechanisms for generating a relic density are possible, we also impose that the correct relic density is generated thermally and this reduces the allowed parameter space further. Therefore once $M_{\tilde{\nu}_L}$ is chosen, $\sin\theta$ is set by this constraint.

Finally it remains to constrain the parameter a_ν which contributes to the inelastic splittings and the neutrino masses through Eqs. (7.7) and (7.10). For a given splitting $\delta_{3,L}$ the allowed parameter space for a_ν is determined by the requirement that the neutrino masses satisfy both the cosmological bound, $\sum m_\nu < 0.61$ eV [292], and the mass bound $M_{\nu_3} > \sqrt{\Delta m^2_{12} + \Delta m^2_{23}}$.

In Fig. 7.9 we show the allowed values of a_ν for a given parameter set with varying WIMP mass $M_{\tilde{\nu}_L}$. For a typical set of soft mass and electroweak parameters it is in

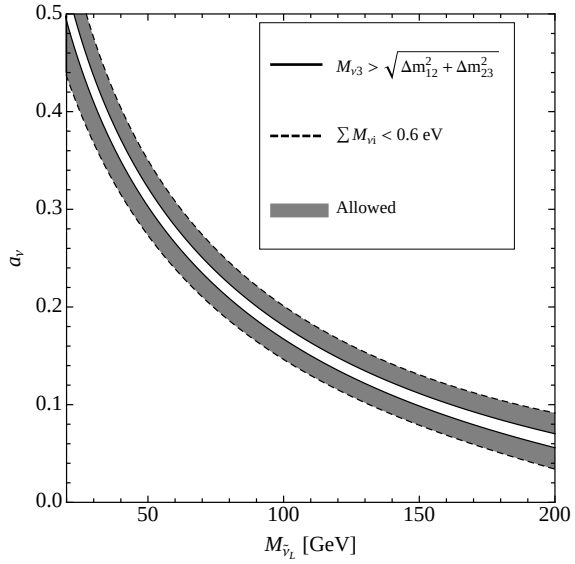

Figure 7.9: Regions of parameter space for the a_ν parameter for which the neutrino masses satisfy both cosmological and mass-splitting bounds. The other parameters are $\mu = M_1 = 250$GeV, $M_2 = 500$GeV, $m_{\tilde{L}} = 350$ GeV, $\sin\theta = 0.2$, $\tan\beta = 10$ and $\delta = 100$ keV.

general possible to find a value of a_ν for which the neutrino masses satisfy the bounds, although the allowed region may become small.

We have shown that within this model it is possible to generate all of the observed neutrino parameters and satisfy cosmological mass-sum bounds. Concurrently the mixed sneutrinos have the same flavour structure as the neutrinos and are good DM candidates capable of providing the observed relic density and avoiding current direct and indirect detection limits.

It is now interesting to consider properties of the sneutrinos that could lead to a positive identification at future experiments. A potentially unambiguous annihilation signal could arise if the DM sneutrinos have all decayed down to the lowest state.

By choosing the same parameter set as that used to generate Fig. 7.5 and varying values of $\sin\theta$ and WIMP mass, we have calculated the fraction of the allowed parameter space of the parameter a_ν for which the sneutrinos will all have decayed down to the lightest state. The results for two different values of δ are shown in Fig. 7.10. From this it seems that, for this model of DM, the fraction of parameter space for which the DM sneutrinos are made up of one state lies in the range $5 - 30\%$ for WIMP masses above M_W and the range $0 - 45\%$ for masses below M_W.

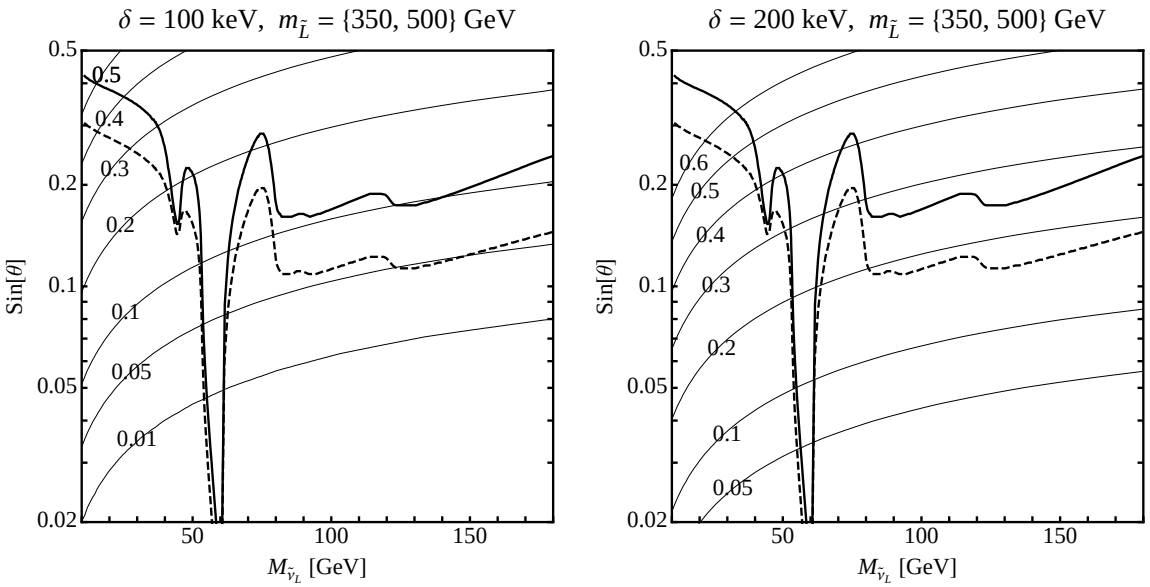

Figure 7.10: Contours of constant fraction of a_ν parameter space for which the sneutrinos have decayed down to the lightest state (i.e. constant fraction of allowed values of a_ν for which $\tau_{\tilde{\nu}^-_{2,L}\to\tilde{\nu}^-_{3,L}} < 10^{10}$ yrs). For comparison the regions where the observed relic density is produced are superimposed. The SUSY-breaking parameters are $\mu = M_1 = 250$ GeV, $M_2 = 500$ GeV, $\tan\beta = 10$ and the solid and dashed lines are for $m_{\tilde{L}} = 350$ and 500 GeV.

7.2.4 Neutrino mass hierarchy

This model does not have a preference for the neutrino mass hierarchy, since it is equally capable of generating either. In the discussion above we have assumed the normal mass hierarchy. Here we highlight how the phenomenology changes if the inverted hierarchy is assumed. Since $\delta_{\alpha,L} \propto M_{\nu_\alpha}$, the $\delta_{\alpha,L}$ follow the neutrino mass hierarchy so that in the normal hierarchy, $\delta_{3,L}$ is the largest splitting. This is much bigger than $\delta_{2,L}$ and $\delta_{1,L}$, which are expected to always be close together because $\delta^2_{2,L} - \delta^2_{1,L} \propto \Delta m^2_{21}$, which is known to be small from solar neutrino measurements. Conversely in the inverted hierarchy, $\delta_{3,L}$ will be the smallest splitting, $\delta_{2,L}$ will be the largest, but $\delta_{1,L}$ will be similar because Δm^2_{21} is small. Therefore even if $\tilde{\nu}^-_{3,L}$ has decayed, we expect to have a significant fraction of both $\tilde{\nu}^-_{1,L}$ and $\tilde{\nu}^-_{2,L}$ and the overall flavour structure of the DM will depend precisely on the relative abundances of $\tilde{\nu}^-_{1,L}$ and $\tilde{\nu}^-_{2,L}$.

7.3 Detection and Identification

7.3.1 Indirect Detection

Mixed sneutrinos present an interesting scenario for indirect detection through neutrino annihilation products for three reasons:

- The inelastic splitting allows for a comparatively large WIMP-nucleon scattering cross section, σ_n, due to the kinematic suppression of scattering at direct detection experiments. However, the large escape velocity of the Sun implies a typical WIMP kinetic energy in the Sun greater than this inelastic splitting, thus allowing a relatively large solar capture rate.

- Sneutrino annihilation can proceed via t-channel neutralino exchange to two neutrinos which propagate relatively unhindered (with some attenuation in the Sun, see e.g. [293]) to the Earth. These neutrinos could be detected in future neutrino telescopes as a hard spectrum centred at the sneutrino mass, although this hard spectrum may lie below the flux of neutrinos from annihilations to other SM particles. This is illustrated in Fig. 7.11.

- If the DM were made up of all three lowest lying states then annihilations to neutrinos would result in equal numbers of ν_e, ν_μ and ν_τ, with the directional flux of hard ν_μ equalling roughly one third of the total flux of hard neutrinos. If the sneutrinos have all decayed down to the lightest state then the hard spectrum of neutrinos would be comprised solely of the ν_3 mass eigenstate, and the ν_μ flux would equal roughly one half of the total flux for the normal hierarchy neutrino structure. In the vacuum none of the neutrinos would oscillate as they are produced in the mass eigenstates $\nu_{1,2,3}$. Moreover, if annihilations are purely to ν_3 states in the Sun, MSW effects would be negligible due to the small ν_e component of ν_3.

As the WIMP-nucleon scattering cross section is typically large, sneutrino capture and annihilation in astrophysical bodies provides the most promising scenario for indirect detection. However it should be noted that neutrino signals from annihilation in the galactic halo are not subject to the large uncertainties relating to the DM structure in the centre of the galaxy [294], and a dedicated analysis by neutrino telescope collaborations could place interesting limits on thermal relic WIMPs from annihilations resulting in final state neutrinos.

Due to the suppressed capture rate in the Earth from the inelastic splitting, we will only discuss potential signals from sneutrino capture in the Sun. Although a thorough treatment of limits from upcoming neutrino telescopes is best left until after the collection of data, it is interesting to speculate about the detection potential. Compared to existing Super-Kamiokande limits [112] projections of the performance of the completed IceCube + DeepCore detector indicate an order of magnitude increase in sensitivity to ν_μ from the Sun for WIMP masses ~ 100 GeV [295]. An order of magnitude increase in sensitivity to σ_n corresponds to an increase in the limits on $\sin\theta$ by a factor ~ 1.8. As the regions where the observed relic density is generated are already close to current indirect detection limits then inspection of Figs. 7.5, 7.6 and 7.7 would suggest that the completed IceCube detector will be sensitive to large portions of parameter space of this model for $m_{\tilde{L}} < 500$ GeV.

In Fig. 7.11 we plot the neutrino spectrum at the Earth for various sneutrino masses where current direct and indirect detection bounds are just satisfied. Inspecting Fig. 7.6 one can see that when $M_{\tilde{\nu}_L} > M_W$ (respectively M_Z) then W (and Z) bosons are the dominant annihilation products, while for $M_{\tilde{\nu}_L} \sim M_h/2$ then $\bar{b}b$ dominate due to the Higgs resonance. Neutrinos from both these annihilations swamp the hard spectrum of neutrinos from neutralino exchange. However when the sneutrino masses lie out of these ranges the sharp peak from annihilation to neutrinos can be seen where the annihilation to neutrinos is at its greatest. Observation of such a feature would constitute a compelling case for sneutrino DM as direct annihilation of neutralinos to neutrinos is forbidden due to their Majorana nature. As described in Ref. [281], the peak from annihilations to neutrinos would lead to a linear component in the muon energy spectrum at IceCube and, if large enough, could be distinguished from annihilation to other Standard Model particles which give a non-linear muon energy spectrum. Further, if the flavour content of this component or alternatively just that of the highest energy neutrinos could be determined and was found to be non-democratic, then this would be an indication of neutrino-flavoured sneutrino DM.

We emphasise that if the sneutrinos have all decayed down to the lightest state then the prediction of this model for the ratios of the flavour content of the hard neutrino spectrum from annihilations through neutralinos is $\sim (0, 1/2, 1/2)$, in the basis (f_e, f_μ, f_τ), exactly matching the flavour content of the heaviest neutrino in the normal hierarchy. If the inverted hierarchy is assumed and the sneutrinos have decayed down to the two lightest states, which are very long lived due to their small mass splitting, the flavour content would be expected to take the form $\sim (1, 1/2, 1/2)$.

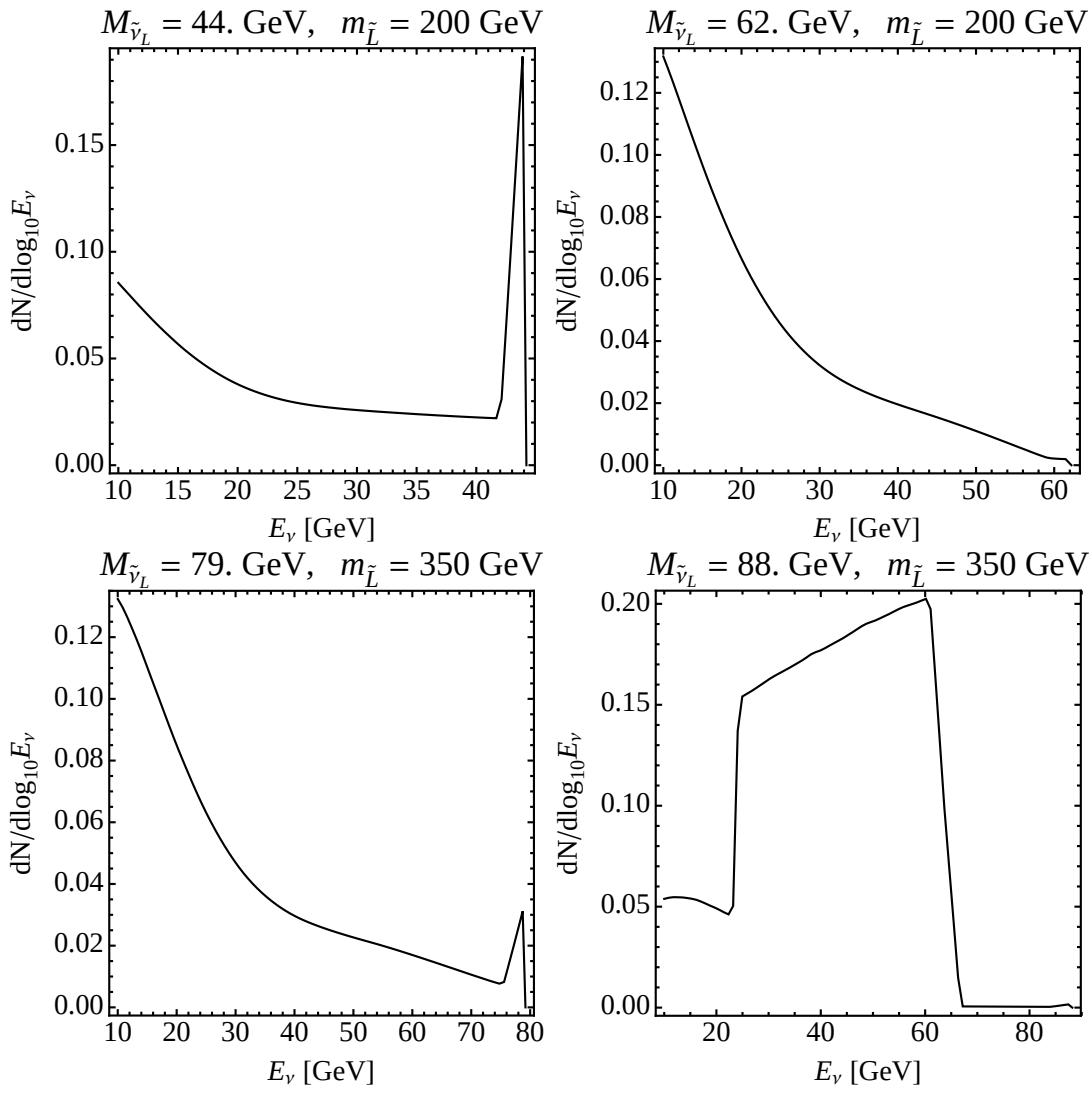

Figure 7.11: The spectrum of neutrinos from the Sun per sneutrino annihilation for two sets of parameters lying just below current indirect detection bounds. The SUSY-breaking parameters are as in Fig. 7.6 and $m_{\tilde{L}}$ is varied in order to stay just below current indirect detection bounds for higher sneutrino masses. The neutrino spectrum is evaluated using the branching fractions calculated using micrOMEGAs 2.2 [97] along with the oscillation and propagation code publicly available [296]. For the two lhd panels the hard feature corresponds to two-body annihilation and gives neutrinos at energy $M_{\tilde{\nu}_L}$. The branching fraction to neutrinos is large away from the Higgs-funnel and below the W mass, as shown in the rhd panel of Fig. 7.6. Note that these are raw spectra. In the rhd panels we illustrate cases where the direct 2-neutrino final state branching fraction is small, the spectrum of neutrinos being dominated by secondary decays of annihilation products.

7.3.2 Direct detection

Referring the reader back to Figs. 7.5, 7.6 and 7.7 one can see that current direct detection bounds are close to large portions of parameter space for this model, whether for elastic scattering via Higgs exchange or inelastic scattering when the splitting δ is smaller than $\sim$ 100 keV. Therefore the prospects for the direct detection of sneutrino DM are good as future direct detection experiments such as EURECA [297], XENON100 [298] and LUX [299] are expected to have significant increases in detection sensitivity.

Regardless of the size of the inelastic splitting the elastic scattering via Higgs exchange is unavoidable and future direct detection experiments should be capable of placing strong limits or possibly observing a positive detection signal with this channel. Also, if the inelastic splitting isn't too large ($\delta \lesssim 150$ keV) then there is also good potential for observing inelastic scattering, which could be discriminated against elastic scattering by the shape of the event spectrum, thus giving a unique window onto the size of the inelastic splitting among sneutrino states.

Therefore upcoming direct and indirect detection experiments will provide a complementary test of the validity of this model of DM.

7.3.3 Collider Signatures

Due to the small mass splittings of the six lightest sneutrino states, to a good approximation all six states would be produced in equal multiplicity at the LHC, making a determination of flavour structures at the LHC very difficult. However it may be possible to identify sneutrinos as the LSP. The LHC signatures of mixed sneutrinos have been studied previously [165] where it was found that mixed sneutrinos can be distinguished from the MSSM over large regions of parameter space. If the NLSP is a right-handed slepton then large lepton multiplicities may result from the decays of more massive sparticles. In particular, decays of the lightest neutralino lead to opposite-sign, same-flavour dilepton signatures. This can be distinguished from similar MSSM scenarios by observing the shape of the dilepton invariant mass distribution [165]. For large $\sin\theta$ decay chains starting with squarks can lead to jet-lepton signatures which are present in the MSSM, but could be distinguished by observing sneutrino-charged slepton mass splittings which arise only through electroweak symmetry breaking in the MSSM [165].

Finally, if the sneutrinos were to lie in the Z-funnel region, $M_{\tilde{\nu}_L} \sim 45$ GeV, as in the left panel of Fig. 7.6, Higgs searches at the LHC and ILC could be dramatically

altered because the large A-term implies that the dominant decay of the Higgs will be to two sneutrinos. For the parameters of Fig. 7.6 and $\sin\theta = 0.2$, the Higgs decay width Γ_h will increase by an order of magnitude from $\Gamma_h \sim 5$ MeV to $\Gamma_h \sim 50$ MeV. Although not directly measurable at the ILC, this could be determined indirectly from $\Gamma_h = \Gamma(H \to WW^*)/Br(H \to WW^*)$ where $Br(H \to WW^*)$ is directly measured and $\Gamma(H \to WW^*)$ is estimated from the measurement of the WWH coupling [300]. The branching fractions for the decays to SM particles, in particular, $b\bar{b}$ and $\gamma\gamma$ would also be lower by an order of magnitude, making Higgs searches at the LHC more difficult. Therefore, it seems that this model of mixed sneutrino DM has signals at colliders, and is testable through direct and indirect detection experiments over much of the parameter space.

7.4 Conclusions

The model detailed herein constitutes a viable model of both DM and neutrino mass generation in which the DM is comprised of mixed lhd-rhd sneutrinos in the same flavour mixtures as the neutrino mass eigenstates. We have shown in detail that it is possible that the observed neutrino masses and mixings arise as a consequence of supersymmetry breaking effects in the sneutrino sector, consistent with all experimental constraints. The prospects for indirect detection of the associate sneutrino DM from solar capture are good, owing to the large sneutrino-nucleon cross-section afforded by the inelastic splitting of Z-coupled states as shown in Figs. 7.5, 7.6, and 7.7. For some regions of the allowed parameter space, a potential 'smoking gun' signature of this model would be monochromatic, non-oscillating, neutrinos comprised of just one mass eigenstate which originate from sneutrino annihilation in the Sun, see Fig. 7.11. The current generation of direct detection experiments place strong limits at low sneutrino masses and at high mass if the inelastic splitting is small, and next generation experiments can explore much of the parameter space, see Figs. 7.5, 7.6, and 7.7. There is a prospect of seeing both elastic and inelastic scattering in these experiments, allowing the size of the sneutrino splitting $\delta_{\alpha,L}$ to be directly measured. Despite being one of the earliest examples of inelastic DM, limits from solar capture completely exclude this model as an explanation of DAMA/LIBRA. The mixed lhd-rhd sneutrinos can have signatures at the LHC, and can change aspects of Higgs physics. Finally, we have shown that a simple extension of the MSSM leads to a much richer structure in the DM sector linking different areas of beyond-the-Standard-Model physics, namely dark matter and neutrino physics.

Epilogue

The nature and properties of particle dark matter remain mysterious. However, there are intriguing hints that a few direct detection experiments may have detected it through non-gravitational interactions.

The modulation signal observed by the DAMA collaboration remains a puzzle. Although it has many features consistent with a signal arising due to the scattering of dark matter particles, the exclusion limits from *many* other experiments challenge this interpretation. More recently, the CoGeNT collaboration has also presented tentative evidence for a signal that it attributes to dark matter. It is by no means clear that the 'excess' of events reported in the unmodulated rate is caused by dark matter, as an understanding of the background at low energies is completely lacking. However, the modulation signal is much more intriguing, as there are no known reasons why the background should modulate with properties similar to those expected of a signal arising from dark matter. Unfortunately, at this stage, the statistical evidence for the modulation is weak and it appears to have some puzzling features; the peak day of the modulation is about a month earlier than expected and the modulation fraction is larger than predicted. Furthermore, a reported excess of events in the oxygen band observed by the CRESST collaboration has also been claimed as evidence for dark matter. Again however, there are doubts as to how well the background is understood.

Unfortunately, the signals from the three experiments are not quite consistent with each other. They are also strongly excluded by other experiments under the standard assumptions of light dark matter described by a Maxwell-Boltzmann velocity distribution, which scatters elastically with a spin-independent interaction and with equal couplings to protons and neutrons. The challenge facing theorists is to come up with and test new models that allow a consistent explanation. It is clear that we must move beyond the simple assumptions underlying the dark matter velocity distribution and its interaction with nuclei. In this thesis we have considered such extensions and have sought to understand the robustness of potential experimental signals.

In Chapter 2, inelastic dark matter was considered as a way of reconciling DAMA with the constants from other experiments. Since inelastic dark matter is particularly sensitive to the tail of the local dark matter velocity distribution, we examined the sensitivity of these results when the distribution is varied, using data extracted from the Via Lactea and Dark Disc numerical simulations. Although we found that the velocity distribution from the Via Lactea simulation did lessen the tension with other experiments, more recent results from the CRESST and XENON100 experiments now cast doubt on this form of inelastic dark matter as an explanation for DAMA.

In Chapter 4, the consistency of the CoGeNT modulation signal was compared with the DAMA modulation signal. At first sight, both signals appear to be in conflict with the exclusion curves from XENON10, XENON100 and CDMS. However, with some isospin violation to reduce the XENON constraints, and an increased modulation fraction provided by an inelastic splitting to reduce the tension with CDMS, a small region of parameter space that is consistent emerges. The inelastic splitting required here is much smaller than that considered in Chapter 2 but its effects are similar.

The effects of astrophysical uncertainties on the exclusion curves set by direct detection experiments were considered in Chapter 3. It is important that the effects of these uncertainties are well understood before interpreting any signal. Scenarios that sample the tail of the velocity distribution are particularly sensitive to variations in astrophysical parameters; this includes light dark matter (masses $\lesssim 10$ GeV) and inelastic dark matter, precisely the properties that may be required to explain the DAMA, CoGeNT and CRESST signals. For these reasons, in Chapter 5, a formalism that does not depend on any astrophysical parameters was used to compare the modulations at CoGeNT and DAMA. Although the CoGeNT best fit regions are large due to low number of observed events, non-trivial conclusions can still be drawn; isospin conserving elastically scattering dark matter is almost certainly excluded. Isospin violation to reduce the constraints from CDMS and XENON helps, but a larger than expected modulation fraction is required. If the signals do arise from dark matter, this points to deviations from a Maxwell-Boltzmann velocity distribution.

In Chapter 7, a theory of supersymmetric dark matter was considered. Supersymmetry is a compelling theory, especially as it can solve the hierarchy problem in the electroweak sector. Discrete symmetries such as R-parity, motivated to avoid dangerous operators that allow rapid proton decay, can give an explanation for why supersymmetric dark matter is stable. The sneutrino is an interesting, somewhat overlooked candidate as it is experimentally excluded as a dark matter candidate in

the MSSM. However, as was shown in Chapter 7, a simple extension of the MSSM allows this to be a dark matter candidate again, with interesting phenomenology linked to flavour physics in the neutrino sector.

This is a very exciting time in the field. The anomalous signals at DAMA, CoGeNT and CRESST may be due to dark matter scattering through non-gravitational interactions. However, the constraints from other direct detection experiments make it clear that the positive signals can not be explained in terms of the usual simple assumptions. Meanwhile, the LHC is rapidly collecting data and should soon provide us with a better understanding of the mechanism behind the breaking of the electroweak symmetry. If the WIMP paradigm for dark matter is correct, the LHC should also be capable of directly producing dark matter particles. The lack of any observed deviations from the Standard Model at the LHC only adds to the tension; new physics may be just around the corner. Clearly supersymmetry has many theoretical benefits but in this era of experimental data, it will be experiments that judge whether nature has taken advantage of it.

Appendix A: Formula for $g(v_{\mathbf{min}})$

Here we present an analytic formula for $g(v_{\rm min})$, defined by

$$g(v_{\rm min}) = \int_{v_{\rm min}}^{\infty} \frac{d^3v}{v} f(\vec{v} + \vec{v}_e), \tag{A-1}$$

where

$$f(\vec{v}) = \begin{cases} \frac{1}{N}\left(e^{-v^2/v_0^2} - \beta e^{-v_{\rm esc}^2/v_0^2}\right) & v < v_{\rm esc} \\ 0 & v > v_{\rm esc} \end{cases} \tag{A-2}$$

and $\beta = 0$ or 1, depending on whether the exponential cutoff is desired. An analytic formula for $g(v_{\rm min})$ with $\beta = 0$ was presented in [301] and we agree with their results in this limit. In Chapter 3, we take $\beta = 1$. It is convenient to define $x_{\rm esc} = v_{\rm esc}/v_0$, $x_{\rm min} = v_{\rm min}/v_0$ and $x_{\rm e} = v_{\rm e}/v_0$, where $v_i = |\vec{v}_i|$.

The normalisation constant N is given by:

$$N = \pi^{3/2} v_0^3 \left[{\rm erf}(x_{\rm esc}) - \frac{4}{\sqrt{\pi}} e^{-x_{\rm esc}^2} \left(\frac{x_{\rm esc}}{2} + \frac{\beta x_{\rm esc}^3}{3} \right) \right] . \tag{A-3}$$

If $x_{\rm e} + x_{\rm min} < x_{\rm esc}$:

$$\begin{aligned} g(v_{\rm min}) = \frac{\pi^{3/2} v_0^2}{2N x_{\rm e}} \Bigg[& {\rm erf}(x_{\rm min} + x_e) - {\rm erf}(x_{\rm min} - x_e) \\ & - \frac{4x_{\rm e}}{\sqrt{\pi}} e^{-x_{\rm esc}^2} \left(1 + \beta(x_{\rm esc}^2 - \frac{x_e^2}{3} - x_{\rm min}^2) \right) \Bigg] . \end{aligned} \tag{A-4}$$

If $x_{\rm min} > |x_{\rm esc} - x_{\rm e}|$ and $x_{\rm e} + x_{\rm esc} > x_{\rm min}$:

$$\begin{aligned} g(v_{\rm min}) = \frac{\pi^{3/2} v_0^2}{2N x_{\rm e}} \Bigg[& {\rm erf}(x_{\rm esc}) + {\rm erf}(x_{\rm e} - x_{\rm min}) - \frac{2}{\sqrt{\pi}} e^{-x_{\rm esc}^2} \\ & \cdot \left(x_{\rm esc} + x_{\rm e} - x_{\rm min} - \frac{\beta}{3}(x_{\rm e} - 2x_{\rm esc} - x_{\rm min})(x_{\rm esc} + x_e - x_{\rm min})^2 \right) \Bigg] . \end{aligned} \tag{A-5}$$

If $x_{\rm e} > x_{\rm min} + x_{\rm esc}$:

$$g(v_{\rm min}) = \frac{1}{v_0 x_{\rm e}} . \tag{A-6}$$

If $x_{\rm e} + x_{\rm esc} < x_{\rm min}$:

$$g(v_{\rm min}) = 0 . \tag{A-7}$$

Appendix B: Exclusion limits

In this appendix we briefly describe three methods commonly used to set an exclusion limit in the $m_\chi - \sigma_n$ plane from data collected by a dark matter direct detection experiment. After running for a set period of time and after applying various cuts to reduce background events, a direct detection experiment reports the number of events n that are observed in a predefined energy range $[E_{\rm low}, E_{\rm high}]$. To set an exclusion limit at the 90% confidence level (C.L.), we wish to find the number of events μ such that 90% of these experiments would have observed more than n events.

For a given mass m_χ, the expected number of events N in an energy range $[E_1, E_2]$ is calculated by integrating Eq. (1.25) between E_1 and E_2 and multiplying by the experiment's exposure $\mathfrak{E}$, usually given in kg days. The only free parameter that enters N is the cross section σ_n. Thus, to set a limit, σ_n is varied until $N = \mu$.

Direct detection experiments are essentially counting experiments looking for a small number of nuclear recoils that arise independently from each other. Hence, the three methods we will discuss to determine μ rely on Poisson statistics. The first method, the 'Poisson method', is the simplest and tends to give the weakest limit. The other two methods, 'maximum gap' and '$\rm p_{max}$', were developed by S. Yellin [148] and work well in the presence of an unknown background. When no events are observed, they reduce to the Poisson method. After describing each method, the resulting exclusion limits derived with data collected by the XENON100 experiment [89] is shown. We will see that the $\rm p_{max}$ method tends to set the strongest limit.

Poisson method

The Poisson distribution tells us the probability of observing exactly n events if the expected number is μ. It is simply

$$P(n|\mu) = \frac{\mu^n e^{-\mu}}{n!} \, . \tag{B-1}$$

The Poisson method takes into account all events n observed in the energy range $[E_{\rm low}, E_{\rm high}]$ and assumes that all events arise from dark matter scattering. To set an

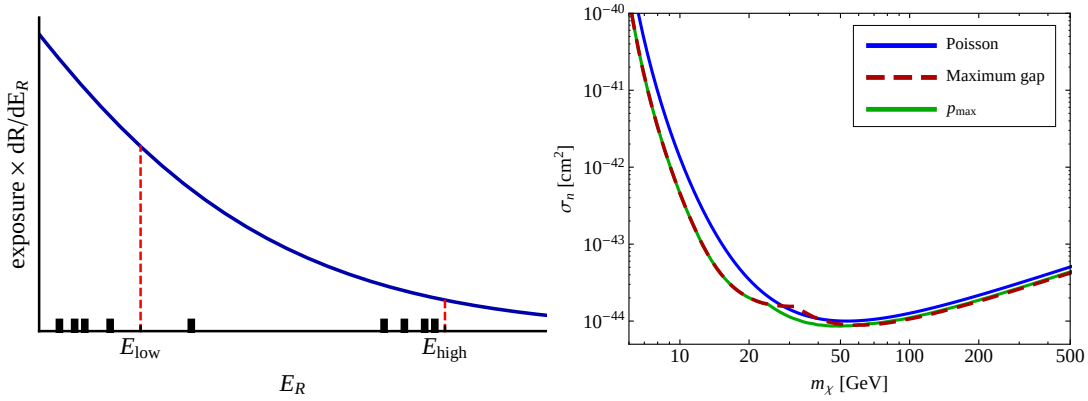

Figure B-1: Left panel: The typical differential rate at a direct detection experiment. The black dots represent observed events. The red dotted lines at $E_{\rm low}$ and $E_{\rm high}$ represent that energy range of the experiment. Right panel: The limits for the XENON100 experiment using the three methods. $\rm p_{max}$ tends to set the strongest limit.

exclusion limit at the 90% C.L., we need to find the expected number of events μ such that 90% of the experiments would have observed more than n events. Mathematically, this is just

$$\sum_{m=n+1}^{\infty} P(m|\mu) = 0.9 \quad \Longrightarrow \quad \sum_{m=0}^{n} \frac{\mu^m\, e^{-\mu}}{m!} = 0.1\ , \tag{B-2}$$

where we have used $\sum_{m=0}^{\infty} P(m|\mu) = 1$ and Eq. (B-1). For example, if an experiment observes no events ($n = 0$), then $\mu = 2.303$.

Yellin's methods

The Poisson method does not work well in the presence of background events. Ideally, the number of background events would be known and a method such as Feldman Cousins [302] could be used. In reality, the backgrounds at direct detection experiments are usually poorly understood and are difficult to model theoretically. A conservative approach is too accept all events, assume they all arise from dark matter and use the Poisson method. Better methods were developed by Yellin. In his approach, the spectral shape of expected events, in addition to the number of observed events are used to set a limit.

To illustrate his approach, in Figure B-1 we show a typical differential event spectrum expected of dark matter. The energy interval in which dark matter is searched for is $[E_{\rm low}, E_{\rm high}]$, denoted by the dashed red lines. The small black rectangles represent observed events that pass all cuts. An interesting feature is the presence of

four events near $E_{\rm high}$. Given the recoil spectrum predicted by dark matter, a cluster of events here, without additional events at lower energy, indicate that it is probable that at least some of these events arise from a background source. The Poisson method does not account for the additional information gleaned from the spectral information. A limit would simply be set taking into account all five events in the energy range. Yellin's methods do take into account the spectral information. The limit is set by choosing the energy interval with the fewest events, while paying the appropriate statistical penalty for the freedom to choose the interval.

Maximum gap

A gap x_i is defined to be the number of events in the energy interval $[E_i, E_{i+1}]$:

$$x_i = \mathfrak{E} \cdot \int_{E_i}^{E_{i+1}} \frac{dR}{dE_{\rm R}}\, dE_{\rm R} \ . \tag{B-3}$$

Here $i = 0, \ldots, n$, where n is the number of observed events. E_i for $i = 1, \ldots, n$ are the event energies, while $E_0 = E_{\rm low}$ and $E_{n+1} = E_{\rm high}$. The maximum gap x is defined as the largest x_i and is used to set the limit. σ_n is excluded at the 90% C.L. if 90% of experiments give a smaller maximum gap. In Appendix A of Ref.[148], this is shown to occur whenever

$$C_0 = \sum_{k=0}^{m} \frac{(kx - N)^k e^{-kx}}{k!} \left(1 + \frac{k}{N - kx}\right) \ , \tag{B-4}$$

where N is the total number of expected events in the interval $[E_{\rm low}, E_{\rm high}]$, m is the greatest integer $\leq N/x$, and $C_0 = 0.9$ for a 90% confidence level.

$\mathbf{p_{max}}$

We can generalise the maximum gap to also consider intervals that include $1, 2, \ldots, n$ events. Here, we calculate all

$$p_k(x) = \sum_{m=0}^{k} \frac{x^m\, e^{-x}}{m!} \tag{B-5}$$

for all intervals with k events. $\mathrm{p_{max}}$ is defined as the maximum $p_k(x)$ over all possible intervals. σ_n is excluded at the 90% C.L. when $\mathrm{p_{max}} = \tilde{\mathrm{p}}_{\rm max}(0.9, N)$ where N is the total number of expected events in the interval $[E_{\rm low}, E_{\rm high}]$. Unfortunately an analytic expression for $\tilde{\mathrm{p}}_{\rm max}(0.9, N)$ is unavailable and it must be evaluated numerically. Tabulated values are given on Yellin's website.[1]

[1] `http://www.slac.stanford.edu/~yellin/ULsoftware.html`.

Appendix C: Details of the experiments considered in Chapter 3

In this appendix we discuss the four experiments which we will use as our reference experiments in Chapter 3, and highlight particular uncertainties associated with each. These experiments all publish unbinned data, so we use Yellin's 'p_{max}' method [148] to calculate the limit on the dark matter-nucleon cross section, since it generally provides a stronger constraint than unbinned methods for the case of an unknown background. It produces similar limits to the 'optimum interval' method used by CDMS II, the 'maximum gap' method used by CRESST-II and XENON10 (in their elastic dark matter (DM) analysis), and was later used by XENON10 (in their inelastic DM reanalysis).

CDMS II-Ge

We initially consider the four published running periods (runs 118, 119, 123-124 and 125-128) by the CDMS II collaboration for scattering off germanium in the energy range $10 - 100$ keV [149, 150, 79, 80]. The first analysis saw one event at 10.5 keV; the second, one event at 64 keV; the third, no events; and the fourth, notably saw two events at 12.3 keV and 15.5 keV.

It was realised that there was an error in the published analysis of the first two runs (118 and 119) and a combined reanalysis was performed, which had redesigned cuts, and lowered the energy threshold from 10 keV to 5 keV [303]. After the cuts were applied, it was found that the two events at 10.5 keV and 64 keV were no longer present, but two new events at 5.3 keV and 7.3 keV passed all the cuts. These were not thought to be real DM events. The 5.3 keV event is very close to the energy threshold so was thought to be from background leakage, while the 7.3 keV event had an unphysical negative phonon delay, but was passed because of a pathology in

the cut definitions. We follow CDMS by using this reanalysis when setting limits rather than the two published runs.[1] It should be noted that due to the lower energy threshold of these first two runs (5 keV rather than 10 keV), CDMS II-Ge is able to place stronger limits on light DM than is often calculated. Similarly, the removal of the event at 64 keV leads to stronger limits being set on inelastic DM since this event lies near the peak of the differential recoil spectrum [123].

In the analysis of the final run, an improved measurement of the germanium detector mass found a 9% decrease in the effective exposure. In addition, a correction of the neutron systematic errors led to a 4.5% increase in the effective exposure. We therefore multiply the published exposures (excluding the final run analysis) by 0.955. The effective germanium exposure of the combined analysis of runs 118 and 119 is given in Figure 10.1 of [303]. For the exposure of the 2008 analysis (runs 123-124), we use 0.995×397.8 kg-days and use the fit to the efficiency from [136]. For the 2009 analysis (runs 125-128), we use an exposure of 612 kg-days and use the efficiency found in the online supplementary material of [80].

CDMS II-Si

The silicon data from the first two runs was also reanalysed and two events at 34.9 keV and 94.1 keV passed all the cuts [303]. The 2008 analysis saw no events [204]. These runs had a low energy threshold of 5 keV and 7 keV respectively, so again, are capable of setting strong limits at low masses.

The effective silicon exposure of the combined analysis of runs 118 and 119 is given in Figure 10.1 of [303]. For the exposure of the 2008 analysis, we use 53.47 kg-days and fit to the efficiency from Fig. 5.13 of [304].

CRESST-II

CRESST-II have released data from two modules from the prototype phase [151] and two modules from the commissioning phase [83]. Here we only include the seven events in the energy range $10 - 100$ keV from the commissioning phase, since there was a significant upgrade to the experiment after the prototype phase. Combining the data leads to significantly weaker limits [161].

[1] We have checked the exclusion limits without the unphysical event at 7.3 keV and the differences are small.

XENON10

Finally we consider the liquid xenon based experiment XENON10, which combines scintillation and ionisation measurements to infer the nucleus recoil energy $E_{\rm R}$. There have been two analyses performed; the first considered only elastically scattering DM [154] and saw 10 events in the energy range $4.5-26.9$ keV; the second analysis, which used the same data but with redesigned cuts considered inelastically scattering DM [86] and saw 13 events in an energy range extended to 75 keV. We use an energy resolution for XENON10 given in [136].

The quantity $\mathcal{L}_{\rm eff}$ is needed to convert from the measured scintillation energy (measured in keVee), to the nuclear recoil energy (measured in keV). Unfortunately $\mathcal{L}_{\rm eff}$ is poorly determined and presents the largest systematic uncertainty in the results of the XENON10 experiment. The original analysis, and the energies quoted above assume a constant value $\mathcal{L}_{\rm eff} = 0.19$, however more recently, [305, 306, 307] have determined that $\mathcal{L}_{\rm eff}$ decreases at low energies, but there is still some uncertainty in its value. Refs. [305, 306] found $\mathcal{L}_{\rm eff} \sim 0.15$ for $E_{\rm R} < 10$ keV, while Ref. [307] found that it continues to decrease from $\mathcal{L}_{\rm eff} \sim 0.15$ at $E_{\rm R} = 10$ keV to $\mathcal{L}_{\rm eff} \sim 0.10$ at $E_{\rm R} = 5$ keV. At $M_\chi \sim 10$ GeV, the exclusion limits from $\mathcal{L}_{\rm eff} = 0.19$ and $\mathcal{L}_{\rm eff}$ from Manzur et al. differ by more than an order of magnitude [307].

When setting limits in this paper, we use the average value of $\mathcal{L}_{\rm eff}$ from [305, 306, 307] and use the elastic analysis to set exclusion limits for momentum dependent and elastically scattering DM, and the inelastic analysis when setting limits for inelastically scattering DM.

We end this section by mentioning another liquid xenon based experiment, ZEPLIN-III [92], which uses a value of $\mathcal{L}_{\rm eff}$ which is smaller at low recoil energy than the three measurements mentioned above. Therefore in contrast to XENON10, we would expect the ZEPLIN-III limits to be stronger at low masses if they were to use $\mathcal{L}_{\rm eff}$ from Manzur et al. However we don't reproduce their limits here since they take into account background subtraction which is beyond our capabilities.

Appendix D: Mass and mixing formulae for Chapter 7

Sneutrino Masses and Mixings

After electroweak symmetry breaking the sneutrino mass matrix has the form

$$M_{ij}^2 = \begin{pmatrix} M_L^2\mathbb{1}_3 & Av\sin\beta\mathbb{1}_3 & 0 & \lambda_{ij}M_N v\sin\beta \\ Av\sin\beta\mathbb{1}_3 & M_R^2\mathbb{1}_3 & \lambda_{ij}M_N v\sin\beta & \lambda_{ij}M_B^2 \\ 0 & \lambda_{ij}M_N v\sin\beta & M_L^2\mathbb{1}_3 & Av\sin\beta\mathbb{1}_3 \\ \lambda_{ij}M_N v\sin\beta & \lambda_{ij}M_B^2 & Av\sin\beta\mathbb{1}_3 & M_R^2\mathbb{1}_3 \end{pmatrix}, \qquad \text{(D-1)}$$

where the basis is $(\tilde{\boldsymbol{\nu}}^*, \tilde{\boldsymbol{n}}, \tilde{\boldsymbol{\nu}}, \tilde{\boldsymbol{n}}^*)$ and individual terms are defined in Section 7.1.2. If U_λ is the matrix that diagonalises the λ matrix as $U_\lambda \cdot \lambda \cdot U_\lambda^\dagger = \mathrm{Diag}(\lambda_1, \lambda_2, \lambda_3)$, and P_6 is a permutation matrix given by

$$P_6 = \begin{pmatrix} 1 & 0 & 0 & 0 & 0 & 0 \\ 0 & 0 & 0 & 1 & 0 & 0 \\ 0 & 1 & 0 & 0 & 0 & 0 \\ 0 & 0 & 0 & 0 & 1 & 0 \\ 0 & 0 & 1 & 0 & 0 & 0 \\ 0 & 0 & 0 & 0 & 0 & 1 \end{pmatrix}, \qquad \text{(D-2)}$$

which rotates 6×6 matrices made up of four diagonal 3×3 blocks down to three 2×2 matrices along the diagonal, then the product

$$U = \frac{1}{\sqrt{2}} \begin{pmatrix} P_6 & 0 \\ 0 & P_6 \end{pmatrix} \cdot \begin{pmatrix} \mathbb{1}_6 & -\mathbb{1}_6 \\ i\mathbb{1}_6 & i\mathbb{1}_6 \end{pmatrix} \cdot \begin{pmatrix} \mathbb{1}_2 \otimes U_\lambda & 0 \\ 0 & \mathbb{1}_2 \otimes U_\lambda \end{pmatrix} \qquad \text{(D-3)}$$

rotates the sneutrino mass matrix down to the block-diagonal form of six 2×2 matrices described in Section 7.1.2.

Neutrino Masses and Mixings

From the form of the neutrino mass formula one can see that the neutrino mass matrix is diagonalized by the matrix U_λ to all orders. Considering just the mixing part of

Eq. (7.8) we have the term

$$M_{\nu_{ij}} \propto \sum_{\alpha=1}^{12} U^{\dagger}_{i,\alpha} L(r_\alpha, m_{\chi_x}) U_{\alpha,j+6} \ . \tag{D-4}$$

$L(r_\alpha, m_{\chi_x})$ is a diagonal matrix and as P_6 is a permutation matrix, $P_6^{\dagger} \cdot \mathrm{Diag}(6\times 6) \cdot P_6$ is also diagonal. Therefore the only non-diagonal contribution to the neutrino mass matrix is from the U_λ part of the sneutrino mixing matrix and $U_\lambda \cdot M_\nu \cdot U_\lambda^{\dagger}$ must be diagonal.

Perturbative Mass Formula

Here we give the full form of Eq. (7.10). Defining $x_x = M_{\tilde{\nu}_L}/m_{\chi_x}$ and $y_x = M_{\tilde{\nu}_H}/m_{\chi_x}$, then

$$\begin{aligned} M_{\nu_{ij}} = \lambda_{ij} \left(\frac{M_Z M_B}{4\pi v}\right)^2 \sum_{x=1}^{4} \frac{1}{M_{\chi_x}} (N_{x1}\sin\theta_W - N_{x2}\cos\theta_W)^2 \\ \cdot \left\{ \sin^2\theta(\cos^2\theta - a_\nu \sin 2\theta) L_1(x_x, y_x) \right. \\ \left. + \cos^2\theta(\sin^2\theta + a_\nu \sin 2\theta) L_2(x_x, y_x) \right\} \ , \end{aligned} \tag{D-5}$$

where

$$L_1(x,y) = \frac{1}{x^2-y^2}\left(\frac{x^2\ln x^2}{1-x^2} - \frac{y^2 \ln y^2}{1-y^2}\right) - \frac{1}{1-y^2}\left(1 + \frac{\ln y^2}{1-y^2}\right) \tag{D-6}$$

and

$$L_2(x,y) = \frac{1}{x^2-y^2}\left(\frac{x^2\ln x^2}{1-x^2} - \frac{y^2 \ln y^2}{1-y^2}\right) - \frac{1}{1-x^2}\left(1 + \frac{\ln x^2}{1-x^2}\right) \ . \tag{D-7}$$

Bibliography

[1] J. March-Russell, C. McCabe, and M. McCullough, *Inelastic Dark Matter, Non-Standard Halos and the DAMA/LIBRA Results*, *JHEP* **05** (2009) 071, [arXiv:0812.1931].

[2] C. McCabe, *The Astrophysical Uncertainties Of Dark Matter Direct Detection Experiments*, *Phys. Rev.* **D82** (2010) 023530, [arXiv:1005.0579].

[3] M. T. Frandsen *et al.*, *On the DAMA and CoGeNT Modulations*, *Phys. Rev.* **D84** (2011) 041301(R), [arXiv:1105.3734].

[4] C. McCabe, *DAMA and CoGeNT without astrophysical uncertainties*, *Phys. Rev.* **D84** (2011) 043525, [arXiv:1107.0741].

[5] J. March-Russell, C. McCabe, and M. McCullough, *Neutrino-Flavoured Sneutrino Dark Matter*, *JHEP* **03** (2010) 108, [arXiv:0911.4489].

[6] G. Jungman, M. Kamionkowski, and K. Griest, *Supersymmetric dark matter*, *Phys. Rept.* **267** (1996) 195–373, [hep-ph/9506380].

[7] G. Bertone, D. Hooper, and J. Silk, *Particle dark matter: Evidence, candidates and constraints*, *Phys. Rept.* **405** (2005) 279–390, [hep-ph/0404175].

[8] M. Roos, *Dark Matter: The evidence from astronomy, astrophysics and cosmology*, arXiv:1001.0316.

[9] F. Zwicky, *Die Rotverschiebung von extragalaktischen Nebeln*, *Helvetica Physica Acta* **6** (1933) 110–127.

[10] F. Zwicky, *On the Masses of Nebulae and of Clusters of Nebulae*, *Astrophys. J.* **86** (1937) 217–246.

[11] V. C. Rubin and W. K. Ford, Jr., *Rotation of the Andromeda Nebula from a Spectroscopic Survey of Emission Regions*, *Astrophys. J.* **159** (1970) 379–403.

[12] Y. Sofue and V. Rubin, *Rotation Curves of Spiral Galaxies*, *Ann. Rev. Astron. Astrophys.* **39** (2001) 137–174, [astro-ph/0010594].

[13] M. R. Merrifield, *The rotation curve of the Milky Way to 2.5 R_0 from the thickness of the H I layer*, *Astron. J.* **103** (1992) 1552–1563.

[14] **SDSS** Collaboration, X. X. Xue *et al.*, *The Milky Way's Circular Velocity Curve to 60 kpc and an Estimate of the Dark Matter Halo Mass from Kinematics of 2400 SDSS Blue Horizontal Branch Stars*, *Astrophys. J.* **684** (2008) 1143–1158, [arXiv:0801.1232].

[15] Y. Sofue, M. Honma, and T. Omodaka, *Unified Rotation Curve of the Galaxy – Decomposition into de Vaucouleurs Bulge, Disk, Dark Halo, and the 9-kpc Rotation Dip –*, arXiv:0811.0859.

[16] R. Narayan and M. Bartelmann, *Lectures on gravitational lensing*, astro-ph/9606001.

[17] D. Clowe *et al.*, *A direct empirical proof of the existence of dark matter*, *Astrophys. J.* **648** (2006) L109–L113, [astro-ph/0608407].

[18] S. W. Randall, M. Markevitch, D. Clowe, A. H. Gonzalez, and M. Bradac, *Constraints on the Self-Interaction Cross-Section of Dark Matter from Numerical Simulations of the Merging Galaxy Cluster 1E 0657-5*, *Astrophys. J.* **679** (2008) 1173–1180, [arXiv:0704.0261].

[19] R. A. Alpher, H. Bethe, and G. Gamow, *The origin of chemical elements*, *Phys. Rev.* **73** (1948) 803–804.

[20] R. H. Cyburt, B. D. Fields, and K. A. Olive, *Primordial Nucleosynthesis in Light of WMAP*, *Phys. Lett.* **B567** (2003) 227–234, [astro-ph/0302431].

[21] D. Larson *et al.*, *Seven-Year Wilkinson Microwave Anisotropy Probe (WMAP) Observations: Power Spectra and WMAP-Derived Parameters*, *Astrophys. J. Suppl.* **192** (2011) 16, [arXiv:1001.4635].

[22] W. Hu and S. Dodelson, *Cosmic Microwave Background Anisotropies*, *Ann. Rev. Astron. Astrophys.* **40** (2002) 171–216, [astro-ph/0110414].

[23] E. I. Gates, G. Gyuk, and M. S. Turner, *Microlensing and halo cold dark matter*, *Phys. Rev. Lett.* **74** (1995) 3724–3727, [astro-ph/9411073].

[24] M. Davis, G. Efstathiou, C. S. Frenk, and S. D. M. White, *The evolution of large-scale structure in a universe dominated by cold dark matter*, *Astrophys. J.* **292** (1985) 371–394.

[25] S. D. M. White, C. S. Frenk, M. Davis, and G. Efstathiou, *Clusters, filaments, and voids in a universe dominated by cold dark matter*, *Astrophys. J.* **313** (1987) 505–516.

[26] C. S. Frenk, S. D. M. White, M. Davis, and G. Efstathiou, *The formation of dark halos in a universe dominated by cold dark matter*, *Astrophys. J.* **327** (1988) 507–525.

[27] A. K. Drukier, K. Freese, and D. N. Spergel, *Detecting Cold Dark Matter Candidates*, *Phys. Rev.* **D33** (1986) 3495–3508.

[28] K. Freese, J. A. Frieman, and A. Gould, *Signal Modulation in Cold Dark Matter Detection*, *Phys. Rev.* **D37** (1988) 3388.

[29] J. Binney and S. Tremaine, *Galactic Dynamics (Second Edition)*, *Princeton University Press* (2008).

[30] J. Diemand *et al.*, *Clumps and streams in the local dark matter distribution*, *Nature* **454** (2008) 735–738, [arXiv:0805.1244].

[31] J. Stadel *et al.*, *Quantifying the heart of darkness with GHALO - a multi-billion particle simulation of our galactic halo*, arXiv:0808.2981.

[32] V. Springel *et al.*, *The Aquarius Project: the subhalos of galactic halos*, *Mon. Not. Roy. Astron. Soc.* **391** (2008) 1685–1711, [arXiv:0809.0898].

[33] J. F. Navarro, C. S. Frenk, and S. D. M. White, *The Structure of Cold Dark Matter Halos*, *Astrophys. J.* **462** (1996) 563–575, [astro-ph/9508025].

[34] J. Einasto, *Kinematics and dynamics of stellar systems*, *Trudy Inst. Astroz. Alma-Ata* **51** (1965) 87.

[35] J. F. Navarro *et al.*, *The Diversity and Similarity of Cold Dark Matter Halos*, *MNRAS* **402** (2008) 21–34, [arXiv:0810.1522].

[36] M. Vogelsberger *et al.*, *Phase-space structure in the local dark matter distribution and its signature in direct detection experiments*, *MNRAS* **395** (2009) 797–811, [arXiv:0812.0362].

[37] F. S. Ling, E. Nezri, E. Athanassoula, and R. Teyssier, *Dark Matter Direct Detection Signals inferred from a Cosmological N-body Simulation with Baryons*, *JCAP* **1002** (2010) 012, [arXiv:0909.2028].

[38] M. Kuhlen *et al.*, *Dark Matter Direct Detection with Non-Maxwellian Velocity Structure*, *JCAP* **1002** (2010) 030, [arXiv:0912.2358].

[39] M. Lisanti, L. E. Strigari, J. G. Wacker, and R. H. Wechsler, *The Dark Matter at the End of the Galaxy*, *Phys. Rev.* **D83** (2011) 023519, [arXiv:1010.4300].

[40] C. A. Vera-Ciro *et al.*, *The Shape of Dark Matter Haloes in the Aquarius Simulations: Evolution and Memory*, arXiv:1104.1566.

[41] M. Gustafsson, M. Fairbairn, and J. Sommer-Larsen, *Baryonic Pinching of Galactic Dark Matter Haloes*, *Phys. Rev.* **D74** (2006) 123522, [astro-ph/0608634].

[42] V. P. Debattista *et al.*, *The Causes of Halo Shape Changes Induced by Cooling Baryons: Disks Versus Substructures*, arXiv:0707.0737.

[43] M. Fellhauer *et al.*, *The origin of the bifurcation in the Sagittarius stream*, *Astrophys. J.* **651** (2006) 167–173, [astro-ph/0605026].

[44] T. Yamagata, Y. Takamori, and H. Utsunomiya, *Search for anomalously heavy hydrogen in deep sea water at 4000-m*, *Phys.Rev.* **D47** (1993) 1231–1234.

[45] Y. B. Zel'dovich, *Magnetic model of universe*, *Zh. Eksp. Teor. Fiz.* **48** (1965) 986.

[46] Y. B. Zel'dovich, L. B. Okun, and S. B. Pikelner, *Quarks: the astrophysical and physical-chemistry aspects (Translation)*, *Usp. Fiz. Nauk.* **84** (1965) 113.

[47] H. Y. Chiu, *Symmetry between particle and anti-particle populations in the universe*, *Phys. Rev. Lett.* **17** (1966) 712.

[48] B. W. Lee and S. Weinberg, *Cosmological Lower Bound on Heavy Neutrino Masses*, *Phys.Rev.Lett.* **39** (1977) 165–168.

[49] K. Griest and D. Seckel, *Three exceptions in the calculation of relic abundances*, *Phys. Rev.* **D43** (1991) 3191–3203.

[50] J. Edsjo and P. Gondolo, *Neutralino Relic Density including Coannihilations*, *Phys. Rev.* **D56** (1997) 1879–1894, [hep-ph/9704361].

[51] J. Bernstein, L. S. Brown, and G. Feinberg, *The Cosmological Heavy Neutrino Problem Revisited*, *Phys. Rev.* **D32** (1985) 3261.

[52] R. J. Scherrer and M. S. Turner, *On the Relic, Cosmic Abundance of Stable Weakly Interacting Massive Particles*, *Phys. Rev.* **D33** (1986) 1585.

[53] E. W. Kolb and M. Turner, *The Early Universe*, *Frontiers in Physics, Westview Press* (1990).

[54] R. J. Scherrer and M. S. Turner, *Erratum: On the Relic, Cosmic Abundance of Stable Weakly Interacting Massive Particles*, *Phys. Rev.* **D34** (1986) 3263.

[55] S. Nussinov, *Technocosmology: Could a Technibaryon excess provide a 'natural' missing mass candidate?*, *Phys. Lett.* **B165** (1985) 55.

[56] A. Belyaev, M. T. Frandsen, S. Sarkar, and F. Sannino, *Mixed dark matter from technicolor*, *Phys. Rev.* **D83** (2011) 015007, [arXiv:1007.4839].

[57] D. Hooper, J. March-Russell, and S. M. West, *Asymmetric sneutrino dark matter and the Ω_b/Ω_{DM} puzzle*, *Phys. Lett.* **B605** (2005) 228–236, [hep-ph/0410114].

[58] D. E. Kaplan, M. A. Luty, and K. M. Zurek, *Asymmetric Dark Matter*, *Phys. Rev.* **D79** (2009) 115016, [arXiv:0901.4117].

[59] R. D. Peccei and H. R. Quinn, *Constraints Imposed by CP Conservation in the Presence of Instantons*, *Phys. Rev.* **D16** (1977) 1791–1797.

[60] R. D. Peccei and H. R. Quinn, *CP Conservation in the Presence of Instantons*, *Phys. Rev. Lett.* **38** (1977) 1440–1443.

[61] F. Wilczek, *Problem of Strong p and t Invariance in the Presence of Instantons*, *Phys. Rev. Lett.* **40** (1978) 279–282.

[62] S. Weinberg, *A New Light Boson?*, *Phys. Rev. Lett.* **40** (1978) 223–226.

[63] P. Ramond, *Journeys Beyond the Standard Model*, *Frontiers in Physics, Westview Press* (2004).

[64] J. Preskill, M. B. Wise, and F. Wilczek, *Cosmology of the invisible axion*, *Phys. Lett.* **B120** (1983) 127–132.

[65] L. F. Abbott and P. Sikivie, *A cosmological bound on the invisible axion*, *Phys. Lett.* **B120** (1983) 133–136.

[66] M. Dine and W. Fischler, *The not-so-harmless axion*, *Phys. Lett.* **B120** (1983) 137–141.

[67] P. Fox, A. Pierce, and S. D. Thomas, *Probing a QCD string axion with precision cosmological measurements*, hep-th/0409059.

[68] **The ADMX** Collaboration, S. J. Asztalos *et al.*, *A SQUID-based microwave cavity search for dark-matter axions*, *Phys. Rev. Lett.* **104** (2010) 041301, [arXiv:0910.5914].

[69] P. W. Graham and S. Rajendran, *Axion Dark Matter Detection with Cold Molecules*, *Phys. Rev.* **D84** (2011) 055013, [arXiv:1101.2691].

[70] J. L. Feng, A. Rajaraman, and F. Takayama, *Superweakly-interacting massive particles*, *Phys. Rev. Lett.* **91** (2003) 011302, [hep-ph/0302215].

[71] J. L. Feng, S. Su, and F. Takayama, *SuperWIMP gravitino dark matter from slepton and sneutrino decays*, *Phys. Rev.* **D70** (2004) 063514, [hep-ph/0404198].

[72] M. Khlopov and A. D. Linde, *Is It Easy to Save the Gravitino?*, *Phys.Lett.* **B138** (1984) 265–268.

[73] J. R. Ellis, J. E. Kim, and D. V. Nanopoulos, *Cosmological Gravitino Regeneration and Decay*, *Phys.Lett.* **B145** (1984) 181.

[74] M. Bolz, A. Brandenburg, and W. Buchmuller, *Thermal Production of Gravitinos*, *Nucl. Phys.* **B606** (2001) 518–544, [hep-ph/0012052].

[75] M. W. Goodman and E. Witten, *Detectability of certain dark-matter candidates*, *Phys. Rev.* **D31** (1985) 3059.

[76] **DAMA** Collaboration, R. Bernabei *et al.*, *First results from DAMA/LIBRA and the combined results with DAMA/NaI*, *Eur. Phys. J.* **C56** (2008) 333–355, [arXiv:0804.2741].

[77] R. Bernabei *et al.*, *New results from DAMA/LIBRA*, *Eur. Phys. J.* **C67** (2010) 39–49, [arXiv:1002.1028].

[78] C. E. Aalseth *et al.*, *Search for an Annual Modulation in a P-type Point Contact Germanium Dark Matter Detector*, arXiv:1106.0650.

[79] **CDMS** Collaboration, Z. Ahmed *et al.*, *Search for Weakly Interacting Massive Particles with the First Five-Tower Data from the Cryogenic Dark Matter Search at the Soudan Underground Laboratory*, *Phys. Rev. Lett.* **102** (2009) 011301, [arXiv:0802.3530].

[80] **The CDMS-II** Collaboration, Z. Ahmed *et al.*, *Dark Matter Search Results from the CDMS II Experiment*, *Science* **327** (2010) 1619–1621, [arXiv:0912.3592].

[81] **CDMS** Collaboration, D. S. Akerib *et al.*, *Low-threshold analysis of CDMS shallow-site data*, *Phys. Rev.* **D82** (2010) 122004, [arXiv:1010.4290].

[82] **CDMS-II** Collaboration, Z. Ahmed *et al.*, *Results from a Low-Energy Analysis of the CDMS II Germanium Data*, *Phys. Rev. Lett.* **106** (2011) 131302, [arXiv:1011.2482].

[83] G. Angloher *et al.*, *Commissioning Run of the CRESST-II Dark Matter Search*, *Astroparticle Physics* **31** (2009) 270–276, [arXiv:0809.1829].

[84] M. Felizardo *et al.*, *Final Analysis and Results of the Phase II SIMPLE Dark Matter Search*, arXiv:1106.3014.

[85] **XENON** Collaboration, U. Oberlack, *First limits on WIMP dark matter from the XENON10 experiment*, *J. Phys. Conf. Ser.* **110** (2008) 062020.

[86] **XENON10** Collaboration, J. Angle *et al.*, *Constraints on inelastic dark matter from XENON10*, *Phys. Rev.* **D80** (2009) 115005, [arXiv:0910.3698].

[87] **XENON10** Collaboration, J. Angle *et al.*, *A search for light dark matter in XENON10 data*, *Phys. Rev. Lett.* **107** (2011) 051301, [arXiv:1104.3088].

[88] **XENON100 Collaboration** Collaboration, E. Aprile *et al.*, *Likelihood Approach to the First Dark Matter Results from XENON100*, *Phys.Rev.* **D84** (2011) 052003, [arXiv:1103.0303].

[89] **XENON100 Collaboration** Collaboration, E. Aprile *et al.*, *Dark Matter Results from 100 Live Days of XENON100 Data*, *Phys.Rev.Lett.* **107** (2011) 131302, [arXiv:1104.2549].

[90] **XENON100** Collaboration, E. Aprile *et al.*, *Implications on Inelastic Dark Matter from 100 Live Days of XENON100 Data*, arXiv:1104.3121.

[91] D. B. Cline, W. Ooi, and H. Wang, *Constraints on Inelastic Dark Matter Signal using ZEPLIN- II Results*, arXiv:0906.4119.

[92] V. N. Lebedenko *et al.*, *Result from the First Science Run of the ZEPLIN-III Dark Matter Search Experiment*, *Phys. Rev.* **D80** (2009) 052010, [arXiv:0812.1150].

[93] **ZEPLIN-III** Collaboration, D. Y. Akimov *et al.*, *Limits on inelastic dark matter from ZEPLIN-III*, *Phys. Lett.* **B692** (2010) 180–183, [arXiv:1003.5626].

[94] A. M. Green, *Effect of realistic astrophysical inputs on the phase and shape of the WIMP annual modulation signal*, *Phys. Rev.* **D68** (2003) 023004, [astro-ph/0304446].

[95] J. D. Lewin and P. F. Smith, *Review of mathematics, numerical factors, and corrections for dark matter experiments based on elastic nuclear recoil*, *Astropart. Phys.* **6** (1996) 87–112.

[96] A. Kurylov and M. Kamionkowski, *Generalized analysis of weakly interacting massive particle searches*, *Phys.Rev.* **D69** (2004) 063503, [hep-ph/0307185].

[97] G. Belanger, F. Boudjema, A. Pukhov, and A. Semenov, *Dark matter direct detection rate in a generic model with micrOMEGAs 2.2*, *Comput.Phys.Commun.* **180** (2009) 747–767, [arXiv:0803.2360].

[98] J. Fan, M. Reece, and L.-T. Wang, *Non-relativistic effective theory of dark matter direct detection*, *JCAP* **1011** (2010) 042, [arXiv:1008.1591].

[99] J.-M. Zheng, Z.-H. Yu, J.-W. Shao, X.-J. Bi, Z. Li, *et al.*, *Constraining the interaction strength between dark matter and visible matter: I. fermionic dark matter*, *Nucl.Phys.* **B854** (2012) 350–374, [arXiv:1012.2022].

[100] G. Duda, A. Kemper, and P. Gondolo, *Model independent form factors for spin independent neutralino nucleon scattering from elastic electron scattering data*, *JCAP* **0704** (2007) 012, [hep-ph/0608035].

[101] M. A. Shifman, A. Vainshtein, and V. I. Zakharov, *Remarks on Higgs Boson Interactions with Nucleons*, *Phys.Lett.* **B78** (1978) 443.

[102] D. Gross and F. Wilczek, *Ultraviolet Behavior of Nonabelian Gauge Theories*, *Phys.Rev.Lett.* **30** (1973) 1343–1346.

[103] H. Politzer, *Reliable Perturbative Results for Strong Interactions?*, *Phys.Rev.Lett.* **30** (1973) 1346–1349.

[104] R. Crewther, *Nonperturbative evaluation of the anomalies in low-energy theorems*, *Phys.Rev.Lett.* **28** (1972) 1421.

[105] J. R. Ellis, K. A. Olive, and C. Savage, *Hadronic Uncertainties in the Elastic Scattering of Supersymmetric Dark Matter*, *Phys.Rev.* **D77** (2008) 065026, [arXiv:0801.3656].

[106] V. A. Bednyakov and F. Simkovic, *Nuclear spin structure in dark matter search: The finite momentum transfer limit*, *Phys. Part. Nucl.* **37** (2006) S106–S128, [hep-ph/0608097].

[107] **CDMS** Collaboration, D. S. Akerib *et al.*, *Limits on spin-dependent WIMP nucleon interactions from the Cryogenic Dark Matter Search*, *Phys. Rev.* **D73** (2006) 011102, [astro-ph/0509269].

[108] J. Angle *et al.*, *Limits on spin-dependent WIMP-nucleon cross-sections from the XENON10 experiment*, *Phys. Rev. Lett.* **101** (2008) 091301, [arXiv:0805.2939].

[109] M. T. Frandsen and S. Sarkar, *Asymmetric dark matter and the Sun*, *Phys. Rev. Lett.* **105** (2010) 011301, [arXiv:1003.4505].

[110] D. T. Cumberbatch, J. A. Guzik, J. Silk, L. S. Watson, and S. M. West, *Light WIMPs in the Sun: Constraints from Helioseismology*, *Phys. Rev.* **D82** (2010) 103503, [arXiv:1005.5102].

[111] M. Taoso, F. Iocco, G. Meynet, G. Bertone, and P. Eggenberger, *Effect of low mass dark matter particles on the Sun*, *Phys. Rev.* **D82** (2010) 083509, [arXiv:1005.5711].

[112] **Super-Kamiokande** Collaboration, S. Desai *et al.*, *Search for dark matter WIMPs using upward through-going muons in Super-Kamiokande*, *Phys. Rev.* **D70** (2004) 083523, [hep-ex/0404025].

[113] K. Helbing and f. t. I. Collaboration, *IceCube as a discovery observatory for physics beyond the standard model*, arXiv:1107.5227.

[114] C. d. l. Heros, *Dark matter searches with IceCube*, arXiv:1012.0184.

[115] E. A. Baltz, M. Battaglia, M. E. Peskin, and T. Wizansky, *Determination of dark matter properties at high-energy colliders*, *Phys. Rev.* **D74** (2006) 103521, [hep-ph/0602187].

[116] G. Kane and S. Watson, *Dark Matter and LHC: What is the Connection?*, *Mod. Phys. Lett.* **A23** (2008) 2103–2123, [arXiv:0807.2244].

[117] G. F. Giudice, B. Gripaios, and R. Mahbubani, *Counting dark matter particles in LHC events*, arXiv:1108.1800.

[118] Y. Bai, P. J. Fox, and R. Harnik, *The Tevatron at the Frontier of Dark Matter Direct Detection*, *JHEP* **12** (2010) 048, [arXiv:1005.3797].

[119] P. J. Fox, R. Harnik, J. Kopp, and Y. Tsai, *LEP Shines Light on Dark Matter*, *Phys. Rev.* **D84** (2011) 014028, [arXiv:1103.0240].

[120] P. J. Fox, R. Harnik, J. Kopp, and Y. Tsai, *Missing Energy Signatures of Dark Matter at the LHC*, arXiv:1109.4398.

[121] J. Jochum *et al.*, *The CRESST dark matter search*, *Prog. Part. Nucl. Phys.* **66** (2011) 202–207.

[122] D. Tucker-Smith and N. Weiner, *Inelastic dark matter*, *Phys. Rev.* **D64** (2001) 043502, [hep-ph/0101138].

[123] S. Chang, G. D. Kribs, D. Tucker-Smith, and N. Weiner, *Inelastic Dark Matter in Light of DAMA/LIBRA*, *Phys. Rev.* **D79** (2009) 043513, [arXiv:0807.2250].

[124] J. Diemand, M. Kuhlen, and P. Madau, *Dark matter substructure and gamma-ray annihilation in the Milky Way halo*, *Astrophys. J.* **657** (2007) 262, [astro-ph/0611370].

[125] J. I. Read, G. Lake, O. Agertz, and V. P. Debattista, *Thin, thick and dark discs in ΛCDM*, *MNRAS* **389** (2008) 1041–1057, [arXiv:0803.2714].

[126] D. Tucker-Smith and N. Weiner, *The status of inelastic dark matter*, *Phys. Rev.* **D72** (2005) 063509, [hep-ph/0402065].

[127] N. Arkani-Hamed, L. J. Hall, H. Murayama, D. Tucker-Smith, and N. Weiner, *Small neutrino masses from supersymmetry breaking*, *Phys. Rev.* **D64** (2001) 115011, [hep-ph/0006312].

[128] J. March-Russell and S. M. West, *A simple model of neutrino masses from supersymmetry breaking*, *Phys. Lett.* **B593** (2004) 181–188, [hep-ph/0403067].

[129] M. C. Smith *et al.*, *The RAVE Survey: Constraining the Local Galactic Escape Speed*, *Mon. Not. Roy. Astron. Soc.* **379** (2007) 755–772, [astro-ph/0611671].

[130] M. Fairbairn and T. Schwetz, *Spin-independent elastic WIMP scattering and the DAMA annual modulation signal*, *JCAP* **0901** (2009) 037, [arXiv:0808.0704].

[131] T. Bruch, J. Read, L. Baudis, and G. Lake, *Detecting the Milky Way's Dark Disk*, *Astrophys. J.* **696** (2009) 920–923, [arXiv:0804.2896].

[132] G. Gelmini and P. Gondolo, *DAMA dark matter detection compatible with other searches*, hep-ph/0405278.

[133] P. Gondolo and G. Gelmini, *Compatibility of DAMA dark matter detection with other searches*, *Phys. Rev.* **D71** (2005) 123520, [hep-ph/0504010].

[134] A. Bottino, F. Donato, N. Fornengo, and S. Scopel, *Do current WIMP direct measurements constrain light relic neutralinos?*, *Phys. Rev.* **D72** (2005) 083521, [hep-ph/0508270].

[135] A. Bottino, F. Donato, N. Fornengo, and S. Scopel, *Interpreting the recent results on direct search for dark matter particles in terms of relic neutralino*, *Phys. Rev.* **D78** (2008) 083520, [arXiv:0806.4099].

[136] C. Savage, G. Gelmini, P. Gondolo, and K. Freese, *Compatibility of DAMA/LIBRA dark matter detection with other searches*, *JCAP* **0904** (2009) 010, [arXiv:0808.3607].

[137] F. Petriello and K. M. Zurek, *DAMA and WIMP dark matter*, *JHEP* **09** (2008) 047, [arXiv:0806.3989].

[138] S. Chang, A. Pierce, and N. Weiner, *Using the Energy Spectrum at DAMA/LIBRA to Probe Light Dark Matter*, *Phys. Rev.* **D79** (2009) 115011, [arXiv:0808.0196].

[139] S. Andreas, T. Hambye, and M. H. G. Tytgat, *WIMP dark matter, Higgs exchange and DAMA*, *JCAP* **0810** (2008) 034, [arXiv:0808.0255].

[140] C. Savage, P. Gondolo, and K. Freese, *Can WIMP spin dependent couplings explain DAMA data, in light of null results from other experiments?*, *Phys. Rev.* **D70** (2004) 123513, [astro-ph/0408346].

[141] R. Foot, *Implications of the DAMA and CRESST experiments for mirror matter-type dark matter*, *Phys. Rev.* **D69** (2004) 036001, [hep-ph/0308254].

[142] R. Foot, *Mirror dark matter and the new DAMA/LIBRA results: A simple explanation for a beautiful experiment*, *Phys. Rev.* **D78** (2008) 043529, [arXiv:0804.4518].

[143] R. Bernabei *et al.*, *New limits on WIMP search with large-mass low-radioactivity NaI(Tl) set-up at Gran Sasso*, *Phys. Lett.* **B389** (1996) 757–766.

[144] R. Bernabei *et al.*, *Possible implications of the channeling effect in NaI(Tl) crystals*, *Eur. Phys. J.* **C53** (2008) 205–213, [arXiv:0710.0288].

[145] N. Bozorgnia, G. B. Gelmini, and P. Gondolo, *Channeling in direct dark matter detection I: channeling fraction in NaI (Tl) crystals*, *JCAP* **1011** (2010) 019, [arXiv:1006.3110].

[146] **DAMA** Collaboration, R. Bernabei *et al.*, *The DAMA/LIBRA apparatus*, *Nucl. Instrum. Meth.* **A592** (2008) 297–315, [arXiv:0804.2738].

[147] **DAMA** Collaboration, R. Bernabei *et al.*, *Performances of the approx. 100-kg NaI(Tl) set-up of the DAMA experiment at Gran Sasso*, . INFN-AE-98-23.

[148] S. Yellin, *Finding an upper limit in the presence of an unknown background*, *Phys. Rev. D* **66** (Aug, 2002) 032005.

[149] **CDMS** Collaboration, D. S. Akerib *et al.*, *First results from the cryogenic dark matter search in the Soudan Underground Lab*, *Phys. Rev. Lett.* **93** (2004) 211301, [astro-ph/0405033].

[150] **CDMS** Collaboration, D. S. Akerib *et al.*, *Limits on spin-independent WIMP nucleon interactions from the two-tower run of the Cryogenic Dark Matter Search*, *Phys. Rev. Lett.* **96** (2006) 011302, [astro-ph/0509259].

[151] G. Angloher *et al.*, *Limits on WIMP dark matter using scintillating CaWO-4 cryogenic detectors with active background suppression*, *Astropart. Phys.* **23** (2005) 325–339, [astro-ph/0408006].

[152] **KIMS** Collaboration, H. S. Lee. *et al.*, *Limits on WIMP-nucleon cross section with CsI(Tl) crystal detectors*, *Phys. Rev. Lett.* **99** (2007) 091301, [arXiv:0704.0423].

[153] H. Park *et al.*, *Neutron beam test of CsI crystal for dark matter search*, *Nucl. Instrum. Meth.* **A491** (2002) 460–469, [nucl-ex/0202014].

[154] **XENON** Collaboration, J. Angle *et al.*, *First Results from the XENON10 Dark Matter Experiment at the Gran Sasso National Laboratory*, *Phys. Rev. Lett.* **100** (2008) 021303, [arXiv:0706.0039].

[155] G. J. Alner *et al.*, *First limits on WIMP nuclear recoil signals in ZEPLIN-II: A two phase xenon detector for dark matter detection*, *Astropart. Phys.* **28** (2007) 287–302, [astro-ph/0701858].

[156] **UK Dark Matter** Collaboration, G. J. Alner *et al.*, *First limits on nuclear recoil events from the ZEPLIN I galactic dark matter detector*, *Astropart. Phys.* **23** (2005) 444–462.

[157] **PAMELA** Collaboration, O. Adriani *et al.*, *An anomalous positron abundance in cosmic rays with energies 1.5.100 GeV*, *Nature* **458** (2009) 607–609, [arXiv:0810.4995].

[158] J. Chang *et al.*, *An excess of cosmic ray electrons at energies of 300.800 GeV*, *Nature* **456** (2008) 362–365.

[159] A. L. Fitzpatrick, D. Hooper, and K. M. Zurek, *Implications of CoGeNT and DAMA for Light WIMP Dark Matter*, *Phys. Rev.* **D81** (2010) 115005, [arXiv:1003.0014].

[160] S. Chang, J. Liu, A. Pierce, N. Weiner, and I. Yavin, *CoGeNT Interpretations*, *JCAP* **1008** (2010) 018, [arXiv:1004.0697].

[161] K. Schmidt-Hoberg and M. W. Winkler, *Improved Constraints on Inelastic Dark Matter*, *JCAP* **0909** (2009) 010, [arXiv:0907.3940].

[162] Y. Cui, D. E. Morrissey, D. Poland, and L. Randall, *Candidates for Inelastic Dark Matter*, *JHEP* **05** (2009) 076, [arXiv:0901.0557].

[163] D. S. M. Alves, S. R. Behbahani, P. Schuster, and J. G. Wacker, *Composite Inelastic Dark Matter*, *Phys. Lett.* **B692** (2010) 323–326, [arXiv:0903.3945].

[164] C. Arina, F.-S. Ling, and M. H. G. Tytgat, *The Inert Doublet Model and Inelastic Dark Matter*, *JCAP* **0910** (2009) 018, [arXiv:0907.0430].

[165] Z. Thomas, D. Tucker-Smith, and N. Weiner, *Mixed Sneutrinos, Dark Matter and the LHC*, *Phys. Rev.* **D77** (2008) 115015, [arXiv:0712.4146].

[166] N. Arkani-Hamed, D. P. Finkbeiner, T. R. Slatyer, and N. Weiner, *A Theory of Dark Matter*, *Phys. Rev.* **D79** (2009) 015014, [arXiv:0810.0713].

[167] I. Cholis and N. Weiner, *MiXDM: Cosmic Ray Signals from Multiple States of Dark Matter*, arXiv:0911.4954.

[168] T. Gherghetta and B. Harling, *A Warped Model of Dark Matter*, *JHEP* **04** (2010) 039, [arXiv:1002.2967].

[169] S. Nussinov, L.-T. Wang, and I. Yavin, *Capture of Inelastic Dark Matter in the Sun*, *JCAP* **0908** (2009) 037, [arXiv:0905.1333].

[170] A. Menon, R. Morris, A. Pierce, and N. Weiner, *Capture and Indirect Detection of Inelastic Dark Matter*, *Phys. Rev.* **D82** (2010) 015011, [arXiv:0905.1847].

[171] J. Shu, P.-f. Yin, and S.-h. Zhu, *Neutrino Constraints on Inelastic Dark Matter after CDMS II*, *Phys. Rev.* **D81** (2010) 123519, [arXiv:1001.1076].

[172] M. McCullough and M. Fairbairn, *Capture of Inelastic Dark Matter in White Dwarves*, *Phys. Rev.* **D81** (2010) 083520, [arXiv:1001.2737].

[173] D. Hooper, D. Spolyar, A. Vallinotto, and N. Y. Gnedin, *Inelastic Dark Matter As An Efficient Fuel For Compact Stars*, *Phys. Rev.* **D81** (2010) 103531, [arXiv:1002.0005].

[174] B. Feldstein, A. L. Fitzpatrick, and E. Katz, *Form Factor Dark Matter*, *JCAP* **1001** (2010) 020, [arXiv:0908.2991].

[175] S. Chang, A. Pierce, and N. Weiner, *Momentum Dependent Dark Matter Scattering*, *JCAP* **1001** (2010) 006, [arXiv:0908.3192].

[176] S. H. Hansen, B. Moore, M. Zemp, and J. Stadel, *A universal velocity distribution of relaxed collisionless structures*, *JCAP* **0601** (2006) 014, [astro-ph/0505420].

[177] A. M. Green, *The WIMP annual modulation signal and non-standard halo models*, *Phys. Rev.* **D63** (2001) 043005, [astro-ph/0008318].

[178] A. M. Green, *Effect of halo modelling on WIMP exclusion limits*, *Phys. Rev.* **D66** (2002) 083003, [astro-ph/0207366].

[179] P. Belli, R. Cerulli, N. Fornengo, and S. Scopel, *Effect of the galactic halo modeling on the DAMA/NaI annual modulation result: an extended analysis of the data for WIMPs with a purely spin-independent coupling*, *Phys. Rev.* **D66** (2002) 043503, [hep-ph/0203242].

[180] J. D. Vergados, S. H. Hansen, and O. Host, *The impact of going beyond the Maxwell distribution in direct dark matter detection rates*, *Phys. Rev.* **D77** (2008) 023509, [arXiv:0711.4895].

[181] W. Dehnen and J. Binney, *Local stellar kinematics from Hipparcos data*, *Mon. Not. Roy. Astron. Soc.* **298** (1998) 387–394, [astro-ph/9710077].

[182] A. M. Green, *Determining the WIMP mass from a single direct detection experiment, a more detailed study*, *JCAP* **0807** (2008) 005, [arXiv:0805.1704].

[183] A. M. Green, *Extracting information about WIMP properties from direct detection experiments: astrophysical uncertainties*, arXiv:1004.2383.

[184] P. J. McMillan and J. J. Binney, *The uncertainty in Galactic parameters*, *MNRAS* **402** (2010) 934–940, [arXiv:0907.4685].

[185] J. Binney, *Distribution functions for the Milky Way*, *MNRAS* **401** (2010) 2318–2330, [arXiv:0910.1512].

[186] R. Schoenrich, J. Binney, and W. Dehnen, *Local Kinematics and the Local Standard of Rest*, *MNRAS* **403** (2010) 1829–1833, [arXiv:0912.3693].

[187] M. J. Reid and A. Brunthaler, *The Proper Motion of Sgr A*: II. The Mass of Sgr A**, *Astrophys. J.* **616** (2004) 872–884, [astro-ph/0408107].

[188] A. M. Ghez *et al.*, *Measuring Distance and Properties of the Milky Way's Central Supermassive Black Hole with Stellar Orbits*, *Astrophys. J.* **689** (2008) 1044–1062, [arXiv:0808.2870].

[189] S. Gillessen *et al.*, *Monitoring stellar orbits around the Massive Black Hole in the Galactic Center*, *Astrophys. J.* **692** (2009) 1075–1109, [arXiv:0810.4674].

[190] S. E. Koposov, H.-W. Rix, and D. W. Hogg, *Constraining the Milky Way potential with a 6-D phase- space map of the GD-1 stellar stream*, *Astrophys. J.* **712** (2010) 260–273, [arXiv:0907.1085].

[191] E. I. Gates, G. Gyuk, and M. S. Turner, *The Local halo density*, *Astrophys. J.* **449** (1995) L123–L126, [astro-ph/9505039].

[192] **Particle Data Group** Collaboration, C. Amsler *et al.*, *Review of particle physics*, *Phys. Lett.* **B667** (2008) 1.

[193] M. Weber and W. de Boer, *Determination of the Local Dark Matter Density in our Galaxy*, *Astron. Astrophys.* **509** (2010) A25, [arXiv:0910.4272].

[194] P. Salucci, F. Nesti, G. Gentile, and C. F. Martins, *The dark matter density at the Sun's location*, *Astron. Astrophys.* **523** (2010) A83, [arXiv:1003.3101].

[195] **CoGeNT** Collaboration, C. E. Aalseth *et al.*, *Results from a Search for Light-Mass Dark Matter with a P- type Point Contact Germanium Detector*, *Phys. Rev. Lett.* **106** (2011) 131301, [arXiv:1002.4703].

[196] A. Bottino, F. Donato, N. Fornengo, and S. Scopel, *Light neutralinos and WIMP direct searches*, *Phys. Rev.* **D69** (2004) 037302, [hep-ph/0307303].

[197] C. Kelso and D. Hooper, *Prospects For Identifying Dark Matter With CoGeNT*, *JCAP* **1102** (2011) 002, [arXiv:1011.3076].

[198] J. I. Collar, *Light WIMP Searches: The Effect of the Uncertainty in Recoil Energy Scale and Quenching Factor*, arXiv:1010.5187.

[199] F. Giuliani, *Are direct search experiments sensitive to all spin- independent WIMP candidates?*, *Phys. Rev. Lett.* **95** (2005) 101301, [hep-ph/0504157].

[200] J. L. Feng, J. Kumar, D. Marfatia, and D. Sanford, *Isospin-Violating Dark Matter*, *Phys. Lett.* **B703** (2011) 124–127, [arXiv:1102.4331].

[201] J. M. Cline, A. R. Frey, and F. Chen, *Metastable dark matter mechanisms for INTEGRAL 511 keV γ rays and DAMA/CoGeNT events*, *Phys. Rev.* **D83** (2011) 083511, [arXiv:1008.1784].

[202] D. Hooper, J. I. Collar, J. Hall, and D. McKinsey, *A Consistent Dark Matter Interpretation For CoGeNT and DAMA/LIBRA*, *Phys. Rev.* **D82** (2010) 123509, [arXiv:1007.1005].

[203] P. W. Graham, R. Harnik, S. Rajendran, and P. Saraswat, *Exothermic Dark Matter*, *Phys. Rev.* **D82** (2010) 063512, [arXiv:1004.0937].

[204] J. P. Filippini, *A Search for WIMP Dark Matter Using the First Five-Tower Run of the Cryogenic Dark Matter Search*, *Ph.D thesis, University of California, Berkeley* (2008).

[205] J. Goodman *et al.*, *Constraints on Light Majorana Dark Matter from Colliders*, *Phys. Lett.* **B695** (2011) 185–188, [arXiv:1005.1286].

[206] J. Goodman *et al.*, *Constraints on Dark Matter from Colliders*, *Phys. Rev.* **D82** (2010) 116010, [arXiv:1008.1783].

[207] A. Aranda and C. D. Carone, *Limits on a light leptophobic gauge boson*, *Phys. Lett.* **B443** (1998) 352–358, [hep-ph/9809522].

[208] M. T. Frandsen, S. Sarkar, and K. Schmidt-Hoberg, *Light asymmetric dark matter from new strong dynamics*, *Phys. Rev.* **D84** (2011) 051703, [arXiv:1103.4350].

[209] R. Kappl and M. W. Winkler, *New Limits on Dark Matter from Super-Kamiokande*, *Nucl. Phys.* **B850** (2011) 505–521, [arXiv:1104.0679].

[210] G. Angloher, M. Bauer, I. Bavykina, A. Bento, C. Bucci, *et al.*, *Results from 730 kg days of the CRESST-II Dark Matter Search*, arXiv:1109.0702.

[211] D. Hooper and C. Kelso, *Implications of CoGeNT's New Results For Dark Matter*, *Phys. Rev.* **D84** (2011) 083001, [arXiv:1106.1066].

[212] R. Foot, *Mirror and hidden sector dark matter in the light of new CoGeNT data*, *Phys. Lett.* **B703** (2011) 7–13, [arXiv:1106.2688].

[213] P. Belli *et al.*, *Observations of annual modulation in direct detection of relic particles and light neutralinos*, *Phys. Rev.* **D84** (2011) 055014, [arXiv:1106.4667].

[214] T. Schwetz and J. Zupan, *Dark Matter attempts for CoGeNT and DAMA*, *JCAP* **1108** (2011) 008, [arXiv:1106.6241].

[215] J. I. Collar, *A comparison between the low-energy spectra from CoGeNT and CDMS*, arXiv:1103.3481.

[216] J. I. Collar, *A Realistic Assessment of the Sensitivity of XENON10 and XENON100 to Light-Mass WIMPs*, arXiv:1106.0653.

[217] J. I. Collar, *Comments on 'Final Analysis and Results of the Phase II SIMPLE Dark Matter Search'*, arXiv:1106.3559.

[218] A. M. Green, *Dependence of direct detection signals on the WIMP velocity distribution*, *JCAP* **1010** (2010) 034, [arXiv:1009.0916].

[219] C. Arina, J. Hamann, and Y. Y. Y. Wong, *A Bayesian view of the current status of dark matter direct searches*, *JCAP* **1109** (2011) 022, [arXiv:1105.5121].

[220] P. J. Fox, J. Liu, and N. Weiner, *Integrating Out Astrophysical Uncertainties*, *Phys. Rev.* **D83** (2011) 103514, [arXiv:1011.1915].

[221] E. Del Nobile, C. Kouvaris, and F. Sannino, *Interfering Composite Asymmetric Dark Matter for DAMA and CoGeNT*, *Phys. Rev.* **D84** (2011) 027301, [arXiv:1105.5431].

[222] G. Plante *et al.*, *New Measurement of the Scintillation Efficiency of Low-Energy Nuclear Recoils in Liquid Xenon*, *Phys. Rev.* **C84** (2011) 045805, [arXiv:1104.2587].

[223] Y. A. Golfand and E. P. Likhtman, *Extension of the Algebra of Poincare Group Generators and Violation of p Invariance*, *JETP Lett.* **13** (1971) 323–326.

[224] D. V. Volkov and V. P. Akulov, *Is the Neutrino a Goldstone Particle?*, *Phys. Lett.* **B46** (1973) 109–110.

[225] J. Wess and B. Zumino, *Supergauge Transformations in Four-Dimensions*, *Nucl. Phys.* **B70** (1974) 39–50.

[226] M. K. Gaillard and B. Zumino, *Supersymmetry and Superstring Phenomenology*, *Eur. Phys. J.* **C59** (2009) 213–221, [arXiv:0805.3726].

[227] J. Wess and J. Bagger, *Supersymmetry and Supergravity*, *Princeton University Press* (1992).

[228] J. Terning, *Modern Supersymmetry: Dynamics and Duality*, *Oxford University Press* (2009).

[229] M. Drees, R. M. Godbole, and P. Roy, *Theory and Phenomenology of Sparticles: An Account of Four-Dimensional N=1 Supersymmetry in High Energy Physics*, *World Scientific Publishing Co Pte Ltd* (2005).

[230] M. Drees, *An Introduction to supersymmetry*, hep-ph/9611409.

[231] S. P. Martin, *A Supersymmetry Primer*, hep-ph/9709356.

[232] R. Haag, J. T. Lopuszanski, and M. Sohnius, *All Possible Generators of Supersymmetries of the s Matrix*, *Nucl. Phys.* **B88** (1975) 257.

[233] A. Salam and J. A. Strathdee, *Supergauge Transformations*, *Nucl. Phys.* **B76** (1974) 477–482.

[234] N. Seiberg, *The Power of holomorphy: Exact results in 4-D SUSY field theories*, `hep-th/9408013`.

[235] J. Wess and B. Zumino, *A Lagrangian Model Invariant Under Supergauge Transformations*, *Phys. Lett.* **B49** (1974) 52.

[236] S. Dimopoulos and H. Georgi, *Softly Broken Supersymmetry and SU(5)*, *Nucl. Phys.* **B193** (1981) 150.

[237] S. Glashow, *Partial Symmetries of Weak Interactions*, *Nucl.Phys.* **22** (1961) 579–588.

[238] S. Weinberg, *A Model of Leptons*, *Phys.Rev.Lett.* **19** (1967) 1264–1266.

[239] H. Fritzsch, M. Gell-Mann, and H. Leutwyler, *Advantages of the Color Octet Gluon Picture*, *Phys. Lett.* **B47** (1973) 365–368.

[240] F. Englert and R. Brout, *Broken symmetry and the mass of gauge vector mesons*, *Phys. Rev. Lett.* **13** (1964) 321–322.

[241] P. W. Higgs, *Broken symmetries and the masse of gauge bosons*, *Phys. Rev. Lett.* **13** (1964) 508–509.

[242] G. S. Guralnik, C. R. Hagen, and T. W. B. Kibble, *Global conservation laws and massless particles*, *Phys. Rev. Lett.* **13** (1964) 585–587.

[243] D. J. Gross and R. Jackiw, *Effect of anomalies on quasirenormalizable theories*, *Phys. Rev.* **D6** (1972) 477–493.

[244] **Super-Kamiokande** Collaboration, H. Nishino *et al.*, *Search for Proton Decay via $p- > e^+\pi^0$ and $p- > \mu^+\pi^0$ in a Large Water Cherenkov Detector*, *Phys. Rev. Lett.* **102** (2009) 141801, [`arXiv:0903.0676`].

[245] L. E. Ibanez and G. G. Ross, *Discrete gauge symmetries and the origin of baryon and lepton number conservation in supersymmetric versions of the standard model*, *Nucl. Phys.* **B368** (1992) 3–37.

[246] Y. Shadmi, *Supersymmetry breaking*, `hep-th/0601076`.

[247] L. Girardello and M. T. Grisaru, *Soft Breaking of Supersymmetry*, *Nucl. Phys.* **B194** (1982) 65.

[248] C. H. Llewellyn Smith and G. G. Ross, *The real gauge hierarchy problem*, *Phys. Lett.* **B105** (1981) 38.

[249] H. Georgi and S. L. Glashow, *Unity of All Elementary Particle Forces*, *Phys. Rev. Lett.* **32** (1974) 438–441.

[250] H. Georgi, H. R. Quinn, and S. Weinberg, *Hierarchy of Interactions in Unified Gauge Theories*, *Phys. Rev. Lett.* **33** (1974) 451–454.

[251] S. Dimopoulos, S. Raby, and F. Wilczek, *Supersymmetry and the Scale of Unification*, *Phys. Rev.* **D24** (1981) 1681–1683.

[252] J. R. Ellis, S. Kelley, and D. V. Nanopoulos, *Probing the desert using gauge coupling unification*, *Phys. Lett.* **B260** (1991) 131–137.

[253] L. E. Ibanez and G. G. Ross, *SU(2)-L U(1) Symmetry Breaking as a Radiative Effect of Supersymmetry Breaking in Guts*, *Phys. Lett.* **B110** (1982) 215.

[254] D. B. Kaplan, *A Single explanation for both the baryon and dark matter densities*, *Phys. Rev. Lett.* **68** (1992) 741–743.

[255] G. R. Farrar and G. Zaharijas, *Dark matter and the baryon asymmetry of the universe*, hep-ph/0406281.

[256] R. Kitano and I. Low, *Dark matter from baryon asymmetry*, *Phys. Rev.* **D71** (2005) 023510, [hep-ph/0411133].

[257] N. Cosme, L. Lopez Honorez, and M. H. G. Tytgat, *Leptogenesis and dark matter related?*, *Phys. Rev.* **D72** (2005) 043505, [hep-ph/0506320].

[258] D. Suematsu, *Dark world and baryon asymmetry from a common source*, *JCAP* **0601** (2006) 026, [astro-ph/0511742].

[259] S. Abel and V. Page, *Affleck-Dine (pseudo)-Dirac neutrinogenesis*, *JHEP* **05** (2006) 024, [hep-ph/0601149].

[260] S. Gopalakrishna, A. de Gouvea, and W. Porod, *Right-handed sneutrinos as nonthermal dark matter*, *JCAP* **0605** (2006) 005, [hep-ph/0602027].

[261] J. McDonald, *Right-Handed Sneutrino Condensate Cold Dark Matter and the Baryon-to-Dark Matter Ratio*, *JCAP* **0701** (2007) 001, [hep-ph/0609126].

[262] V. Page, *Non-thermal right-handed sneutrino dark matter and the Ω_{DM}/Ω_b problem*, *JHEP* **04** (2007) 021, [hep-ph/0701266].

[263] F. Deppisch and A. Pilaftsis, *Thermal Right-Handed Sneutrino Dark Matter in the F_D-Term Model of Hybrid Inflation*, *JHEP* **10** (2008) 080, [arXiv:0808.0490].

[264] G. D. Kribs, T. S. Roy, J. Terning, and K. M. Zurek, *Quirky Composite Dark Matter*, *Phys. Rev.* **D81** (2010) 095001, [arXiv:0909.2034].

[265] T. Cohen and K. M. Zurek, *Leptophilic Dark Matter from the Lepton Asymmetry*, *Phys. Rev. Lett.* **104** (2010) 101301, [arXiv:0909.2035].

[266] N. Arkani-Hamed, L. J. Hall, H. Murayama, D. Tucker-Smith, and N. Weiner, *Neutrino masses at v**(3/2)*, hep-ph/0007001.

[267] F. Borzumati and Y. Nomura, *Low-scale see-saw mechanisms for light neutrinos*, *Phys. Rev.* **D64** (2001) 053005, [hep-ph/0007018].

[268] F. Borzumati, K. Hamaguchi, Y. Nomura, and T. Yanagida, *Variations on supersymmetry breaking and neutrino spectra*, hep-ph/0012118.

[269] T. Hambye, J. March-Russell, and S. M. West, *TeV scale resonant leptogenesis from supersymmetry breaking*, *JHEP* **07** (2004) 070, [hep-ph/0403183].

[270] S. M. West, *Naturally degenerate right handed neutrinos*, *Phys. Rev.* **D71** (2005) 013004, [hep-ph/0408318].

[271] L. J. Hall, T. Moroi, and H. Murayama, *Sneutrino cold dark matter with lepton-number violation*, *Phys. Lett.* **B424** (1998) 305–312, [hep-ph/9712515].

[272] S. Kolb, M. Hirsch, H. V. Klapdor-Kleingrothaus, and O. Panella, *Collider signatures of sneutrino cold dark matter*, *Phys. Lett.* **B478** (2000) 262–268, [hep-ph/9910542].

[273] T. Asaka, K. Ishiwata, and T. Moroi, *Right-handed sneutrino as cold dark matter*, *Phys. Rev.* **D73** (2006) 051301, [hep-ph/0512118].

[274] B. Garbrecht, C. Pallis, and A. Pilaftsis, *Anatomy of F_D-Term Hybrid Inflation*, *JHEP* **12** (2006) 038, [hep-ph/0605264].

[275] T. Asaka, K. Ishiwata, and T. Moroi, *Right-handed sneutrino as cold dark matter of the universe*, *Phys. Rev.* **D75** (2007) 065001, [hep-ph/0612211].

[276] H.-S. Lee, K. T. Matchev, and S. Nasri, *Revival of the thermal sneutrino dark matter*, *Phys. Rev.* **D76** (2007) 041302, [hep-ph/0702223].

[277] C. Arina and N. Fornengo, *Sneutrino cold dark matter, a new analysis: Relic abundance and detection rates*, *JHEP* **11** (2007) 029, [arXiv:0709.4477].

[278] C. Arina, *Sneutrino cold dark matter in extended MSSM models*, arXiv:0805.1991.

[279] C. Arina, F. Bazzocchi, N. Fornengo, J. C. Romao, and J. W. F. Valle, *Minimal supergravity sneutrino dark matter and inverse seesaw neutrino masses*, *Phys. Rev. Lett.* **101** (2008) 161802, [arXiv:0806.3225].

[280] D. G. Cerdeno, C. Munoz, and O. Seto, *Right-handed sneutrino as thermal dark matter*, *Phys. Rev.* **D79** (2009) 023510, [arXiv:0807.3029].

[281] R. Allahverdi, B. Dutta, K. Richardson-McDaniel, and Y. Santoso, *Sneutrino Dark Matter and the Observed Anomalies in Cosmic Rays*, *Phys. Lett.* **B677** (2009) 172–178, [arXiv:0902.3463].

[282] D. G. Cerdeno and O. Seto, *Right-handed sneutrino dark matter in the NMSSM*, *JCAP* **0908** (2009) 032, [arXiv:0903.4677].

[283] D. A. Demir, L. L. Everett, M. Frank, L. Selbuz, and I. Turan, *Sneutrino Dark Matter: Symmetry Protection and Cosmic Ray Anomalies*, *Phys. Rev.* **D81** (2010) 035019, [arXiv:0906.3540].

[284] R. Allahverdi, S. Bornhauser, B. Dutta, and K. Richardson-McDaniel, *Prospects for Indirect Detection of Sneutrino Dark Matter with IceCube*, *Phys. Rev.* **D80** (2009) 055026, [arXiv:0907.1486].

[285] D. G. Cerdeno, *Thermal right-handed sneutrino dark matter with a singlet Higgs*, *AIP Conf. Proc.* **1115** (2009) 163–168.

[286] R. Allahverdi, *Sneutrino dark matter in light of PAMELA*, arXiv:0909.5643.

[287] A. Kumar, D. Tucker-Smith, and N. Weiner, *Neutrino Mass, Sneutrino Dark Matter and Signals of Lepton Flavor Violation in the MRSSM*, *JHEP* **09** (2010) 111, [arXiv:0910.2475].

[288] **WMAP** Collaboration, E. Komatsu *et al.*, *Five-Year Wilkinson Microwave Anisotropy Probe (WMAP) Observations:Cosmological Interpretation*, *Astrophys. J. Suppl.* **180** (2009) 330–376, [arXiv:0803.0547].

[289] W. Hu and J. Silk, *Thermalization constraints and spectral distortions for massive unstable relic particles*, *Phys. Rev. Lett.* **70** (1993) 2661–2664.

[290] L. J. Hall, K. Jedamzik, J. March-Russell, and S. M. West, *Freeze-In Production of FIMP Dark Matter*, *JHEP* **03** (2010) 080, [arXiv:0911.1120].

[291] A. Semenov, *LanHEP - a package for the automatic generation of Feynman rules in field theory. Version 3.0*, *Comput. Phys. Commun.* **180** (2009) 431–454, [arXiv:0805.0555].

[292] A. Strumia and F. Vissani, *Neutrino masses and mixings and.*, hep-ph/0606054.

[293] N. Itoh, H. Hayashi, A. Nishikawa, and Y. Kohyama, *Neutrino Energy Loss in Stellar Interiors. VII. Pair, Photo-, Plasma, Bremsstrahlung, and Recombination Neutrino Processes*, *Astrophys. J. Suppl.* **102** (1996) 411.

[294] H. Yuksel, S. Horiuchi, J. F. Beacom, and S. Ando, *Neutrino Constraints on the Dark Matter Total Annihilation Cross Section*, *Phys. Rev.* **D76** (2007) 123506, [arXiv:0707.0196].

[295] F. Halzen and D. Hooper, *The Indirect Search for Dark Matter with IceCube*, *New J. Phys.* **11** (2009) 105019, [arXiv:0910.4513].

[296] M. Cirelli *et al.*, *Spectra of neutrinos from dark matter annihilations*, *Nucl. Phys.* **B727** (2005) 99–138, [hep-ph/0506298].

[297] H. Kraus *et al.*, *EURECA: The European future of dark matter searches with cryogenic detectors*, *Nucl. Phys. Proc. Suppl.* **173** (2007) 168–171.

[298] E. Aprile, L. Baudis, and f. t. X. Collaboration, *Status and Sensitivity Projections for the XENON100 Dark Matter Experiment*, *PoS* **IDM2008** (2008) 018, [arXiv:0902.4253].

[299] L. W. Kastens, S. B. Cahn, A. Manzur, and D. N. McKinsey, *Calibration of a liquid xenon detector with kr-83m*, *Physical Review C* **80** (2009) 045809.

[300] H. Yamamoto, *Physics at International Linear Collider (ILC)*, *J. Phys. Soc. Jap.* **76** (2007) 111014, [arXiv:0709.0899].

[301] C. Savage, K. Freese, and P. Gondolo, *Annual Modulation of Dark Matter in the Presence of Streams*, *Phys. Rev.* **D74** (2006) 043531, [astro-ph/0607121].

[302] G. J. Feldman and R. D. Cousins, *A Unified approach to the classical statistical analysis of small signals*, *Phys.Rev.* **D57** (1998) 3873–3889, [physics/9711021].

[303] R. W. Ogburn, IV, *A search for particle dark matter using cryogenic germanium and silicon detectors in the one- and two- tower runs of CDMS-II at Soudan*, *Ph.D thesis, Stanford University* (2008).

[304] C. N. Bailey, *The cryogenic dark matter search: First 5-Tower data and improved understanding of ionization collection*, *Ph.D thesis, Case Western Reserve University* (2009).

[305] E. Aprile *et al.*, *New Measurement of the Relative Scintillation Efficiency of Xenon Nuclear Recoils Below 10 keV*, *Phys. Rev.* **C79** (2009) 045807, [arXiv:0810.0274].

[306] P. Sorensen *et al.*, *The scintillation and ionization yield of liquid xenon for nuclear recoils*, *Nucl. Instrum. Meth.* **A601** (2009) 339, [arXiv:0807.0459].

[307] A. Manzur *et al.*, *Scintillation efficiency and ionization yield of liquid xenon for mono-energetic nuclear recoils down to 4 keV*, *Phys. Rev.* **C81** (2010) 025808, [arXiv:0909.1063].